UNIVERSITÀ DEGLI STUDI DI PADOVA

Centro di Ateneo di Studi e Attività Spaziali, CISAS "G. Colombo"

SCUOLA DI DOTTORATO DI RICERCA IN SCIENZE TECNOLOGIE E MISURE SPAZIALI
INDIRIZZO DI MISURE MECCANICHE PER L'INGEGNERIA E LO SPAZIO
CICLO XXVI

# Experimental Characterization of Plasma Sources for Space Propulsion

*

# Caratterizzazione Sperimentale di Sorgenti di Plasma per Propulsione Spaziale

**Direttore della Scuola:** Ch.mo Prof. Giampiero Naletto

**Coordinatore d'indirizzo:** Ch.mo Prof. Stefano Debei

**Supervisore:** Ch.mo Prof. Daniele Pavarin

**Co-supervisore:** Dr. Marco Manente

**Co-supervisore esterno:** Ch.mo Prof. Mark A. Cappelli

**Dottorando:** Andrea Lucca Fabris

## Abstract

The focus of this research program is experimentally characterizing and developing advanced plasma propulsion systems. Experimental measurements have been combined with numerical simulations to examine the physical processes taking place in the analyzed thrusters.

The first part of the project, performed under the EU FP7 HPH.com program, is dedicated to the development of an electrodeless radio-frequency plasma thruster. An experimental facility is designed and constructed, including several plasma diagnostic systems. The plasma properties in the radio-frequency discharge are monitored through optical spectrometers and a microwave interferometer, while the plasma beam is characterized using a retarding potential analyzer and a current probe. Extensive development tests have resulted in an optimized plasma source based on a novel antenna and a particular magnetic field pattern generated by arrays of radially-magnetized permanent magnets. Additionally, the main guidelines for the design of the final prototype of the HPH.com thruster have been determined. The plasma dynamics inside the thruster have been studied by means of the 3D particle-in-cell code F3MPIC, focusing on the ejected plasma plume characterized by the formation of a supersonic ion beam.

In the second part of the project, the Stanford Cylindrical Cusped Field Thruster is experimentally and numerically investigated, with particular attention given to the exit plane acceleration region near the top magnetic cusp. Time-averaged xenon ion laser-induced-fluorescence measurements have mapped the total ion velocity vectors in this region. The velocity field is correlated to the ion beam current profile, the magnetic field and the electrostatic potential field. The thruster is also simulated using F3MPIC. The consistent experimental and numerical results give physical insight into the mechanisms of ion acceleration and the role of the magnetic field topology in determining ion trajectories and plume divergence.

Finally, we propose an innovative dual-stage propulsion system comprised of a traveling magnetic field accelerator. The plasma produced in a primary ionization source is injected into the second stage where it is accelerated by a forward propagating magnetic field. The acceleration mechanism is numerically studied using a 1D particle-in-cell model. Preliminary experiments utilize a microwave source as the primary ionization stage and a transmission line circuit to generate the traveling magnetic field.

## Sommario

Questo progetto di ricerca verte sullo sviluppo e la caratterizzazione sperimentale di avanzati sistemi propulsivi a plasma, utilizzati per applicazioni spaziali. La ricerca si è avvalsa tanto di misure sperimentali quanto di simulazioni numeriche, al fine di acquisire una completa comprensione dei processi fisici che caratterizzano il funzionamento dei propulsori analizzati.

Il progetto è articolato in tre parti, ognuna delle quali dedicata ad uno specifico propulsore.

La prima parte del progetto, svolta nell'ambito del programma di ricerca europeo HPH.com, consiste nello sviluppo di un propulsore in Radio-Frequenza senza elettrodi esposti al plasma. Le attività riguardano la progettazione e la realizzazione di un apparato sperimentale dedicato, comprendente molteplici sistemi di diagnostica. Le proprietà del plasma nella sorgente in Radio-Frequenza sono monitorate mediante spettroscopi ottici ed un interferometro a microonde, mentre il getto di plasma eiettato è caratterizzato tramite un Retarding Potential Analyzer e una sonda di corrente. Un'estensiva campagna di test ha permesso la realizzazione di una sorgente di plasma ottimizzata; la configurazione identificata si basa su un'antenna innovativa ed una particolare struttura magnetica, prodotta da corone di magneti permanenti con magnetizzazione radiale. Inoltre la dinamica del plasma nel propulsore è stata analizzata mediante il codice F3MPIC, di tipo particle-in-cell: le simulazioni mostrano la formazione di un beam ionico supersonico nel plasma eiettato. Infine sono state individuate le linee guida per la progettazione del prototipo finale previsto dal progetto HPH.com.

Nella seconda parte del progetto, è stata svolta un'indagine sperimentale e numerica sul propulsore elettrostatico a cuspidi magnetiche della Stanford University. L'obbiettivo principale di indagine consiste nella comprensione del meccanismo di accelerazione degli ioni. A tal fine, il vettore velocità degli ioni viene misurato in prossimità della sezione di uscita del propulsore, mediante la tecnica "Laser-Induced-Fluorescence". Il campo di velocità ottenuto è quindi correlato alla struttura magnetica, alla distribuzione del potenziale elettrostatico e a misure di corrente svolte nel plasma eiettato. Il propulsore viene inoltre simulato mediante F3MPIC. La combinazione dei risultati numerici con quelli sperimentali, tra loro consistenti, fornisce una descrizione fisica del meccanismo di accelerazione e del ruolo della topologia magnetica nella determinazione della divergenza del getto di plasma eiettato.

Come terza parte, viene proposto un sistema propulsivo innovativo, basato sull'accelerazione di un plasma prodotto da una sorgente primaria mediante un campo magnetico

che si propaga spazialmente. Il meccanismo di accelerazione viene studiato mediante un modello monodimensionale di tipo particle-in-cell. Sono svolti alcuni esperimenti preliminari utilizzando una sorgente a microonde per la ionizzazione ed una linea di trasmissione per la generazione del campo magnetico.

# Contents

# List of Figures

# List of Tables

CHAPTER 1

# Introduction

## 1.1 Project background

### 1.1.1 Electric Propulsion Overview

Jahn [1] defines the electric propulsion (EP) as "the acceleration of gases for propulsion by electrical heating and/or by electric and magnetic body forces". EP systems present as a common feature a transfer of energy provided by an electrical source to the working fluid [2]. This transfer can be physically accomplished in different ways, likewise the acceleration of the outgoing flow is obtained through different mechanisms, e.g. electrothermal, electrostatic, electromagnetic. In electrothermal propulsion the propellant gas is heated by an electrical source and is expanded through a nozzle. In electrostatic propulsion the propellant is ionized and accelerated through electrical body forces. In electromagnetic propulsion the ionized propellant is accelerated through the interactions between electrical currents, flowing through the propellant itself, and external or internal magnetic fields. Operation can be steady or pulsed. Noble gases, different chemical species or mixtures, or even solids can be used as the propellant. The primary attraction of electric propulsion is related to the high exhaust velocity of the propellant which gives an efficient utilization of the propellant mass. The importance of the exhaust velocity $v_{ex}$ appears in the converse Tsiolkovsky rocket equation:

$$\frac{\Delta m}{m_0} = 1 - \exp\left(-\frac{\Delta v}{v_{ex}}\right) \tag{1.1}$$

In the former equation $\Delta m$ is the amount of propellant expended to produce a given velocity increment $\Delta v$ of a rocket with an initial gross mass $m_0$ (including the propellant mass). For a required $\Delta v$ a higher exhaust velocity allows a reduction in the propellant supply.

In general, the main parameters that characterize the propulsive performance of an EP system are the traditional thrust T and specific impulse $I_{sp}$, respectively defined as:

$$T = \dot{m}_i v_i + \dot{m}_n v_n = \dot{m}_{tot}(f_i v_i + (1 - f_i)v_n) \tag{1.2}$$

$$I_{sp} = \frac{\dot{m}_i v_i + \dot{m}_n v_n}{g_0 \dot{m}_{tot}} = f_i \frac{v_i}{g_0} + (1 - f_i)\frac{v_n}{g_0} \tag{1.3}$$

where $\dot{m}_i$, $v_i$ and $\dot{m}_n$, $v_n$ are ionized and neutral mass flow rate and velocity respectively, $\dot{m}_{tot} = \dot{m}_i + \dot{m}_n$ is the overall propellant mass flow rate and $f_i = \dot{m}_i/\dot{m}_{tot}$ is the mass flow ionization fraction.

The specific impulse represents the effective exhaust velocity. EP systems can achieve much higher $I_{sp}$ values (∼1000-10000 s) in comparison with the chemical ones. However electric thrusters are characterized by a low thrust level, due to the limited available electrical power as detailed below.

The total efficiency $\eta$ refers to the ratio of the jet power over the total electric power furnished to the system:

$$\eta = \frac{T^2/2\dot{m}}{P_{el}} \tag{1.4}$$

then:

$$P_{jet} = \eta P_{el} = \frac{T^2}{2\dot{m}} = \frac{1}{2} T I_{sp} g_0 \tag{1.5}$$

$$\frac{T}{P_{el}} = \frac{2}{g_0}\frac{\eta}{I_{sp}} \tag{1.6}$$

Thereby for a given input power and total thruster efficiency, increasing the $I_{sp}$ reduces the thrust available from the electric engine. This trade of thrust for $I_{sp}$ at a constant input power can only be improved through an higher efficiency [2]. Moreover, Eq. 1.5 indicates that for a given constant thrust level and efficiency the required electrical power increases linearly with the specific impulse; as a consequence also the mass of the power supply system scales monotonically with the specific impulse. The mass of the power supply system can become higher than the propellant mass, nullifying the benefit given by the propellant mass saving. Thus for space applications the power supply penalty has to be taken into account in the overall mass budget [1]. Examples of electric thrusters and their performance are reported in table 1.1.

EP thrusters are used in several mission profiles, e.g. long term drag compensation, station keeping in geosynchronous orbits, attitude control, orbit adjustments. An high specific impulse could be beneficial also in interplanetary transfers, orbit raising or lowering (including deorbiting), slow plane change and planetary non-keplerian orbits. The choice of the thruster category depends on the mission profile. A list of operational flights of electric thrusters is provided in Ref. [2].

| Thruster type | Typical power range [W] | Isp [s] (typical) | $\eta$ | Thruster mass [kg/kW] | Power unit mass [kg/kW] |
|---|---|---|---|---|---|
| Resistojet ($N_2H_4$) | 500–1500 | 300 | 80% | 1–2 | 1 |
| Arcjet ($N_2H_4$) | 300–2000 | 500-600 | 35% | 0.7 | 2.5 |
| Hall thruster(xenon) | 300-6000 | 1600 | 50% | 2–3 | 6–10 |
| Ion engine (xenon) | 200-4000 | 2800 | 65% | 3–6 | 6–10 |
| PPT (teflon) | 1–200 | 1000 | 7% | 120 | 110 |
| FEEP (cesium) | $10^{-5}$–1 | 6000 | 80% | — | — |

Table 1.1: Typical electric thruster features (Ref.[2]).

This thesis is focused on the experimental characterization of three EP systems. The three systems under analysis are the following:

- electrodeless Radio-Frequency plasma thruster: the HPH.com thruster;
- magnetized DC discharge: the Stanford Cylindrical Cusped Field Thruster (CCFT);
- traveling magnetic field plasma accelerator.

Besides the experimental characterization, numerical codes based on a particle paradigm are used to provide a more complete picture of the physical processes taking place in the investigated thrusters. An overview of the three different propulsion systems is provided in the following sections. The detailed objectives of the study are defined is section 1.2.

### 1.1.2 Electrodeless Radio-Frequency Plasma Thruster: HPH.com project

Electrodeless propulsion can be considered to be the next step in the technological evolution of EP, since it is able to overcome some critical issues of consolidated propulsion systems, particularly the erosion of electrodes and of the plasma channel wall. Acceleration grid erosion is a lifetime-limiting process in ion thrusters as is wall and cathode erosion in Hall thrusters [3]. The absence of the external neutralizer is another attractive advantage that is offered by electrodeless propulsion systems.

In the last decade several efforts have been dedicated to the development of an electrodeless plasma thruster based on a helicon source [4]. Thanks to their capability to work at different power regimes, helicon thrusters can be a candidate for different mission scenarios: satellites attitude control, drag compensation in LEO orbit, station keeping and orbital transfers.

Roughly a helicon thruster consists of a helicon Radio-Frequency (RF) plasma source, where an injected neutral gas is ionized and heated, and an acceleration stage.

Helicon sources are wave sustained discharges, characterized by an efficient ionization of the operating gas and a power deposition in form of electron heating, leading to the production of higher density plasmas in comparison with other types of discharge (e.g. inductive and capacitive) at the same power level [5, 6]. Helicons are wave modes propagating in a cylindrical, axially magnetized plasma column. Their frequency lies in the frequency region $\omega_{ci} < \omega_{lh} < \omega < \omega_{ce}$ where $\omega_{ce}$ and $\omega_{ci}$ are the ion and electron cyclotron frequencies and $\omega_{lh}$ is the lower-hybrid frequency. The waves propagate along the plasma column and the mode energy is absorbed by electrons through both collisional processes and collisionless damping [5, 4].

The acceleration stage can be a divergent magnetic field (magnetic nozzle) [7], a double-layer [8, 9] or a selective heating system coupled with a magnetic nozzle [10]. The purpose of the magnetic nozzle is to convert plasma internal energy into directed kinetic energy generating thrust for propulsion. The thrust acts on the magnetic field which becomes the mean to transfer the thrust to the spacecraft as in a physical Laval nozzle. However, unlike a conventional nozzle, the magnetic field fills all space and the field lines close themselves. The plasma does not necessarily separate from the magnetic field, following the field lines and returning to the thruster. As a consequence, non-detached plasma does not provide thrust, therefore detachment is a fundamental phenomenon sine qua non issue [11]. Under certain conditions [12] a current-free electric double layer can build up in a helicon plasma expanding in a magnetic field. The double-layer is a plasma structure characterized by a steep potential drop which can provide an ion acceleration up to supersonic velocities [8]. This phenomenon can be exploited for propulsion applications as proposed by Charles [9] at Australian National University.

The physical lay-out of a helicon thruster is simple and made of few elements:

- a feeding system to provide the incoming neutral gas flow;
- a glass tube where the plasma is generated;
- a helicon RF antenna wrapped around the glass tube;
- an externally applied magnetic field generated by either a system of coils or permanent magnets.

The antenna is powered through a RF power network, typically working at 13.56 or 27 MHz. The static magnetic field allows the propagation of electromagnetic waves in the plasma according to proper modes, increasing the plasma source efficiency in terms of power deposition. Moreover it enhances plasma confinement and shapes the magnetic nozzle. The helicon plasma thruster presents several advantages in comparison with the other electrical propulsion systems: the plasma marginally interacts with the structure

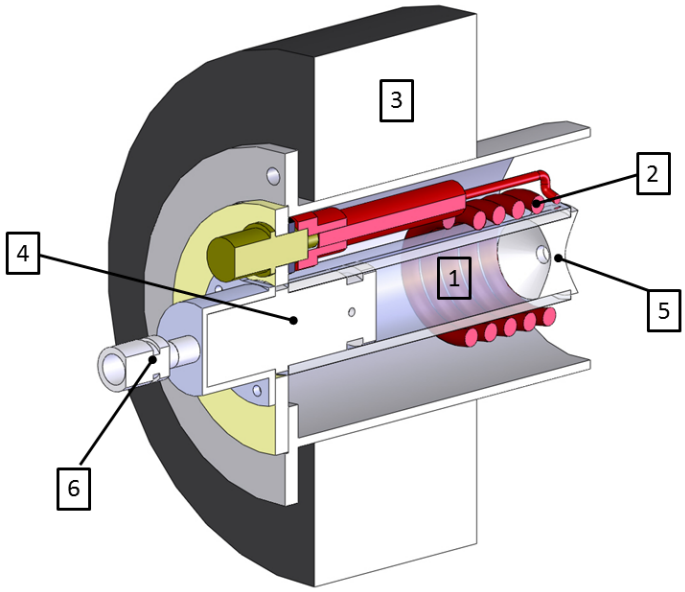


Figure 1.1: Basic scheme of the electrodeless RF plasma thruster: 1) discharge tube; 2) RF antenna; 3) magnetic system; 4) injector; 5) ejection diaphragm; 6) neutral gas feeding pipe.

therefore the erosion is reduced, internal electrodes are absent, the exhaust beam is neutral thus an external neutralizer is not needed, it is light and compact, it can potentially work with different propellants.

Research projects in Australia [9], USA [13, 14, 10], Europe [15] and Japan [16, 17] have been dedicated to this new technology, focusing both on fundamental physics [18] and on engineering aspects [19]. Different operating regimes have been explored in terms of power and mass flow rate.

The researchers of the Australia National University can be considered the pioneers of the helicon plasma thruster since they have been the first to propose the application of a helicon source to space propulsion. They have carried out several studies with different propellants (argon [20] and xenon [6]) in the power range 0.4 - 2 kW, both with electromagnets [20, 6] and permanent magnets [21]. In a recent performance characterization [21], they have obtained a thrust of 15 mN, specific impulse of 2000 s and a thrust efficiency of 8% for 2 kW of input power and a mass flow rate of 24 sccm of argon.

Helicon propulsion technology has been explored also in the high power range, particularly a helicon thruster operating in the range 20 - 100 kW has been developed and tested at Washington University [14], achieving a thrust level of 1N and 2000 s of specific impulse for argon. Other tests with hydrogen have shown a specific impulse up to 8000 s.

A mini-helicon thruster has been studied at Massachusetts Institute of Technology [13] using nitrogen $N_2$ and argon as the propellants (flow rates within the range 10 - 50

sccm) and working in the power range 0.5 - 1 kW. The-mini helicon is characterized by a high-power-density and compactness in comparison with the system developed at ANU. The propulsive performances are: thrust 10 mN, specific impulse 1000-2000 s for Ar and 2000-4000 s for $N_2$ with thrust efficiencies up to 20%.

Finally helicon sources can be exploited as primary source to produce a high-density ion flow in multi-stage thrusters as in VASIMR (Variable Specific Impulse Magneto-plasma Rocket) project [10].

**EU FP7 HPH.com project**

The Helicon Plasma Hydrazine.Combined Micro (HPH.com) is a research project funded by the European Union within the 7th Framework Program and conducted by an international consortium during the period December 2008 - May 2012. The objective of the HPH.com was to design, optimize and develop a space plasma thruster based on helicon-RF technology and to study its application to a mini-satellite for attitude and position control. Moreover, a detailed feasibility study was performed to evaluate the possibility of using the plasma thruster to heat and decompose a secondary propellant in order to develop a two mode thruster, characterized by an high-efficiency low-thrust plasma thruster mode and a low-efficiency high-trust secondary propellant plasma-enhanced mode. The target applications was in the range of 50 - 100 W power. The target thruster performance was: 1 mN of thrust and specific impulse higher than 1200 s. HPH.com project developed through the following steps:

- deep numerical-theoretical investigation through dedicated plasma-simulation tools;
- extensive experimental campaign to validate codes, to develop the thruster, to investigate the physical phenomena involved and to prove the thruster performance;
- the development of a full-scale thruster prototype to be mounted on board of a mini-satellite to demonstrate technology feasibility;
- the study of all the critical issues related to the application to a mini-satellite;
- the design and manufacturing of the mini-satellite mock up including all critical components;
- analysis of scaling law to lower and higher power.

### 1.1.3 Magnetized DC Discharge: the Stanford Cylindrical Cusped Field Thruster

Recent attention given to small, low cost space vehicles has created a need for efficient, low power propulsion technology. Hall thrusters are capable of servicing this low power regime; however, several issues arise when scaling existing models down in power. Increased heat flux to the discharge channel walls, especially the center pole piece in annular Hall thrusters, erodes insulation more quickly and limits the lifetime of the device [22, 23]. Increased ion sputtering to the channel walls has also been shown to reduce the usable life of the thruster [24]. Additionally, it is not well understood how cross-field transport mechanisms, which restrict electron flow to the anode, scale when decreasing thruster size and power requirements.

Several novel designs address these issues inherent with Hall thrusters, including the Cylindrical Hall Thruster (CHT, Princeton) [25], Diverging Cusped Field Thruster (DCFT, MIT) [26], the Cylindrical Cusped Field Thruster (CCFT, Stanford) [27] and the High Efficiency Multistage Thruster (HEMPT, Thales Research Institute and University of Giessen) [28, 29, 30]. The CHT design mitigates heat loading and erosion by retracting the overloaded center pole piece and pushing the ion acceleration region largely outside the discharge channel [31, 32, 33]. The CHT has demonstrated $\sim 25\%$ anode effeciencies when operating with xenon between 100 and 200 W [34]. The DCFT has a conical discharge channel with three permanent magnetic cusps that diminish in strength towards the exit plane. Magnetic bottles between cusps increase electron residence time, creating efficient ionization regions; mitigate electron flow directly to the anode; and minimize wall interactions through the mostly axial magnetic field [35]. The DCFT has demonstrated around 40% anode efficiency at 200 W [26]. The CCFT employs a cusped permanent magnetic field profile that weakens towards the exit plane to qualitatively reproduce the diverging DCFT magnetic profile. CCFT studies with krypton demonstrated anode efficiencies of around 23% when operated between 40 to 240 W [27]. The HEMPT concept [28] exploits a system of magnets with alternating polarity to form magnetic cells with a cusp-mirror configuration to trap electrons and to reduce the plasma flow to the wall. Different HEMPT models have been developed covering a broad power range from 75 W to 10 kW [29]. The HEMPT 2050 DM9-1 model is designed to operate in the 400 W - 2000 W power range, generating a thrust of 15 - 70 mN with an $I_{sp}$ within the range 2500 - 3000 s. At the low power point (400W) this model has demonstrated an anode efficiency of 36% [28]. Finally a down-scaled configuration of HEMPT thruster for $\mu$N applications, with a power level below 10 W, has been developed at University of Giessen [30], showing an $I_{sp}$ of 270 - 350 s.

### Stanford Cylindrical Cusped Field Thruster (CCFT)

The design and operating principles of the CCFT, developed by the Stanford Plasma Physics Laboratory group, have been described in detail elsewhere [27, 36, 37] and are reviewed briefly here. A schematic of the Stanford CCFT appears in Fig. 1.2a, with the magnetic field profile simulated by finite element method magnetics (FEMM)[38] superimposed. The magnetic topology is generated by three samarium cobalt permanent magnets of alternating polarity that decrease in strength moving downstream away from the anode, separated by 1018 steel spacers to shape the field. This arrangement produces the diverging magnetic profile seen in the DCFT [26] even though the channel is cylindrical. The maximum magnetic field strength at the cusps is 0.45 T.

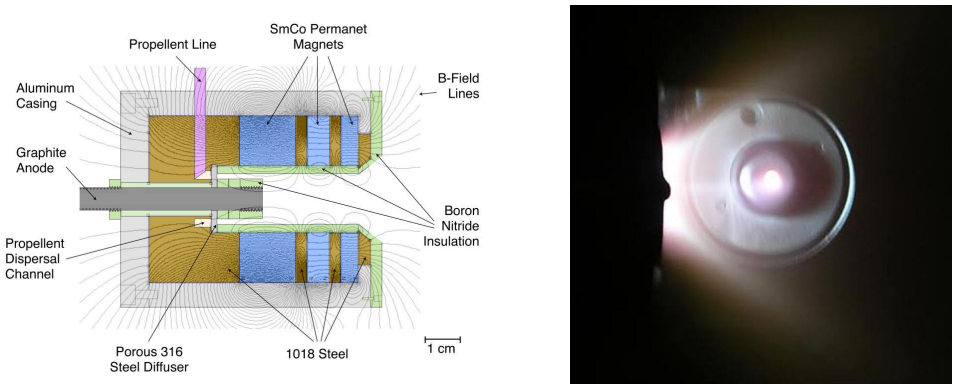


(a) (b)

Figure 1.2: (a) Design schematic of the CCFT with magnetic topology superimposed, illustrating magnetic cusps of decreasing strength moving downstream from the anode. (b) The Stanford Cylindrical Cusped Field Thruster operating on krypton in the Stanford Plasma Physics Laboratory. The external cathode operating on argon is pictured behind the thruster, facing the camera.

Electrons are emitted by the external cathode (not pictured in Fig. 1.2a but seen in the background of Fig. 1.2b) and may either travel along magnetic field lines towards the thruster anode, biased at high positive potential relative to the grounded cathode body, or be ejected with the plume of ionized propellant atoms, neutralizing the ejected ion flow. Those electrons entering the discharge channel are impeded by the magnetic field structure, which is designed to trap electrons through magnetic mirroring between adjacent cusps and restrict electron flow to the graphite anode (located in a region of converging magnetic field). This resistance to electron migration establishes a primarily axial electric field that accelerates thrust-producing propellant ions away from the device. High energy electrons that overcome the sheath potential of the ceramic insulating wall and scatter may end up on magnetic field lines leading to an upstream cusp, or eventually to the anode.

Regions between cusps with parallel magnetic field lines to the channel wall seek to reduce erosion by keeping particles away from the wall.

The propellant is injected at the base of the channel through a porous steel diffuser. As propellant atoms encounter electrons with sufficient energy gained from the electric field, ionization events may occur. These secondary electrons may also become trapped in the magnetic cusps, increasing their residence time in the channel, and contribute to avalanche ionization. The resulting xenon ions are not affected by the magnetic field due to their high mass; however, the complicated interplay between the magnetic topology, ionization regions, and acceleration zones observed in the thruster may in fact produce an indirect link between the magnetic structure and eventual ion trajectories.

The thruster is encased in an aluminum cylinder 7 cm in length with a 6 cm outer diameter. The boron nitride cylindrical discharge channel is 1.4 cm in diameter and 4 cm in length up to the chamfered edge near the exit plane. This angled edge ensures that electrons traveling along magnetic field lines from the external cathode have a means of entering the channel without excessively impacting the front face of the thruster [27]. The anode is a partially threaded 0.64 cm diameter graphite rod.

The CCFT operating on krypton propellant is shown in Fig. 1.2b, where the conical plume of visible plasma (similar to that observed in the DCFT) suggests the beam angle is determined by the diverging magnetic field profile rather than the geometry of the channel. When operating on krypton, the CCFT demonstrated good performance in the 40 - 240 W range. With krypton flow rates of 5.9 - 8.9 sccm, the generated thrust is between 2-5 mN with specific impulse values up to 1200 s and total efficiencies up to 23% [27].

### 1.1.4 Traveling Magnetic Field Plasma Accelerator

As previously mentioned, several research efforts are dedicated to the development of new electrodeless propulsion concepts. Helicon thrusters are a promising technology (section 1.1.2). Other more unconventional solutions have been proposed in the last few years, such as ion acceleration with beating electrostatic waves [39] or plasma acceleration produced by a rotating electric field [40]. Another electrodeless system is the pulsed inductive thruster (PIT) [41]. In this device a strong current is pulsed through a flat coil discharging a bank of capacitors. The effect is a strong azimuthal field which breaks down the neutral gas and gives rise to an azimuthal current in the opposite direction relative to that flowing through the coil. The azimuthal current interacts with the radial component of the magnetic field giving an axial thrust component. Efficiencies up to 50% and $I_{sp}$ up to 2240 s have been achieved for 4 kJ energy pulses. An evolution of this concept is represented by the FARAD (Faraday Acceleration with Radio Frequency Assisted Discharge) [42] thruster developed at Princeton University which consists of a double stage system with: 1) a

helicon discharge for primary ionization, 2) an inductive flat coil for plasma acceleration, relying on the same principle as that of the PIT. In the PIT the strong azimuthal field both ionizes and accelerates the propellant, whereas in the FARAD these two stages take place separately (partially, since the azimuthal field provides an additional ionization). As a result, accelerated current sheets form at lower pulse energies (down to 44 J). A sheet velocity of 12000 m/s has been measured for a 78.5 J pulse.

During the 1960s and 1970s several studies [43, 44, 45, 46, 47, 48, 1, 49, 50] were carried out on plasma acceleration by means of propagating magnetic fields. In the most typical configuration, the plasma is injected in a cylindrical dielectric tube surrounded by an array of coaxial coils with currents progressively phase-shifted according to the target propagation velocity of the magnetic field, usually within the range $10^4 - 10^5$ m/s. The magnetic field acts as a piston pushing the plasma downstream and accelerating it at velocities close to the traveling velocity of the fields. Both theoretical analysis and experimental tests were performed demonstrating the viability and effectiveness of the concepts. Propagating fields with various configurations (flat, mirror shaped, cusped shaped) were tested and the effect of an additional magnetostatic background field was also investigated [47]. Typically, the coils are powered by polyphase networks [44, 45, 48, 49] or are integrated into a transmission line circuit [43, 50]. The operating mode can be pulsed [47, 50] or with continuous power application [43, 44, 45, 46, 48, 49]. The traveling velocity can be varied along the acceleration direction by tuning the values of the circuit elements. For instance, Haldeman's system [43] presents a linear increase of the phase velocity of the propagating field (from 4000 to 12000 m/s) along the acceleration channel in order to optimize the energy transferred to the gas flow per unit length. The system consists of a sequence of coils with currents progressively phase-shifted (Fig. 1.3) and operated in continuous power mode at 30 kHz. The chosen circuit scheme is a slow transmission line operating in ring mode. In a transmission line the wave travels with a velocity depending on the inductance and capacitance per unit length. Thus the phase velocity can be varied regulating those parameters along the accelerator. The experimental results along with a mathematical model demonstrate the feasibility of coupling the plasma to the traveling magnetic field giving an acceleration effect.

The effect of an additional background field on the overall plasma acceleration is explored by Light [47], focusing particularly on its magnitude and its direction (parallel or antiparallel relative to the acceleration direction). This uniform axial magnetic field affects the shape of the "'magnetic piston"' and enhances the plasma confinement from the accelerator walls. Light's system is operated in pulsed mode (2.5 kJ/pulse), discharging a bank of capacitors on a transmission line network with a constant propagation velocity to produce a field traveling at $1.1 \times 10^5$ m/s. The magnetic piston has a strength of 6000 G

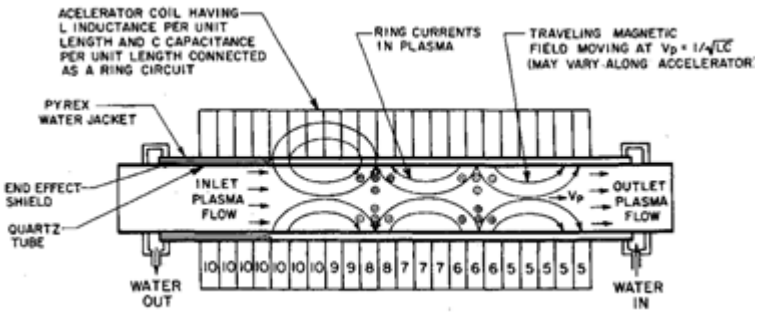


Figure 1.3: Haldeman's traveling magnetic field plasma engine with variable phase velocity.

and the additional field has a magnitude of up to 4000 G. The position of the magnetic piston is monitored through radial B-field probes and the position of the pushed plasma is detected by means of photomultiplier tubes along the acceleration channel. The experiments demonstrate that the magnetic piston is effectively accelerating the plasma and the velocity of the plasma increases with the strength of the static background field both in the parallel and antiparallel configuration.

A research program aimed at the development of a traveling magnetic wave plasma engine was carried out at NASA Lewis Research Center [44, 45, 46]. Experiments with both four and ten-coil configurations were performed. The velocity of the magnetic wave is 46500 m/s in both cases. The power for the coils is supplied by two 13 kW generators operating at 150 kHz. A pendulum momentum probe is placed at the exhaust of the accelerator to provide an estimation of the thrust. The operating propellants are xenon and argon with mass flow rates within the range $0.2-2.6\times10^{-6}$ kg/s and input power of 1-5 kW. The axial magnetic field strength on the axis is about 70 - 80G. The measured thrust spans from 0.8 up to $2.5 \times 10^{-2}$ N. For the four-coil configuration, a propulsive efficiency of 0.1 and a specific impulse of 3200 s are measured for argon and 0.23 and 4200 s for xenon, respectively. The effect of a coaxial ferrite core is also investigated in an attempt to increase the the strength of the radial component of the magnetic field. However, the overall effect is negative because of the drag and heat losses due to the core.

An alternative configuration is proposed by Heflinger [49], characterized by a rectangular duct with a transverse geometry of the magnetic field which is perpendicular to the traveling direction (Fig. 1.4). The magnetic field has an intensity of about 500 G, travels with a velocity of 54000 m/s, and is generated by four coils powered at 480 kHz. The neutral gas is ionized by the electric field associated with the propagating magnetic field. Several propellants are tested. The best performance is obtained with helium, showing a specific impulse up to 6000 s and an efficiency of about 0.5 for a power of 160 kW and a

mass flow of $5 \times 10^{-5}$ kg/s.

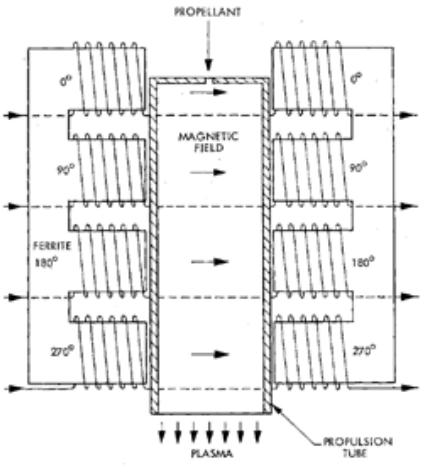


Figure 1.4: Heflinger's traveling magnetic field thruster with rectangular duct.

Despite the significant prior history and promising results of these traveling wave concepts, this propulsion concept is still in a proof-of-concept phase. Particularly, its application to space propulsion in the low power range ($<$ 250W) has never been explored. We aim to propose an electrodeless plasma thruster based on a axially-propagating magnetic field. The accelerator is intended to be used as an acceleration stage in a multi-stage thruster, using a RF plasma source or a microwave cavity as primary ionization stage. The target propagation velocity of the field is within the range 15000 - 30000 m/s.

## 1.2 Objectives and Methodology

Three different plasma propulsion systems are analyzed in this project: the electrodeless RF plasma thruster (HPH.com thruster), the magnetized DC discharge (Stanford Cylindrical Cusped Field Thruster) and the traveling magnetic wave plasma accelerator. The activities performed on each of them are of different nature due to the different aims of the investigations, as described below. The investigation methodology is mainly experimental. For each analyzed thruster a dedicated experimental test-bed has been setup and different diagnostics have been used to characterize the plasma properties. Additionally, the experimental measurements have been combined with numerical simulations to give a more complete picture of the physical processes taking place in the thrusters.

### 1.2.1 Electrodeless Radio-Frequency Plasma Thruster

The work on the RF plasma thruster has been carried out in the frame of the EU FP7 HPH.com project, particularly we have been responsible for the experimental activities at Center of Studies and Activities for Space of University of Padova. The experimental campaign is aimed to develop a RF plasma thruster in the class 50 W - 1 mN. The design of the experimental apparatus, the analysis and the installation of the measurement systems, the tests for the thruster development are part of this PhD project. Non-intrusive diagnostics have been privileged for the RF plasma source characterization to avoid the perturbation of the RF source operation. Electrostatic probes have been used to characterized the plasma beam. Summarizing, the objectives are:

- to design and build a dedicated experimental setup to develop the RF thruster;
- to analyze and install non-intrusive plasma diagnostic systems (e.g. optical spectrometers and microwave interferometer) to characterize the plasma in the RF source;
- to design and build electrostatic probes for the plasma beam characterization (e.g. Retarding Potential Analyzer and current probes);
- to identify the thruster critical parameters and to experimentally determine their influence on the thruster performance;
- to identify the main design guidelines for the HPH.com thruster prototype.

Finally, particle-in-cell simulations have been performed to understand the physical processes taking place in the thruster, particularly the plasma acceleration mechanism: an existing 3D PIC code, called F3MPIC, has been used to analyze the plasma dynamics forced by a novel RF antenna developed during HPH.com project.

### 1.2.2 DC Magnetized Discharge

The activities on the Stanford Cylindrical Cusped Field Thruster are aimed to provide an insight of the ion acceleration mechanism. Pursuing this goal, the ion velocity field in the region close to the thruster exit plane has been measured through a Laser-Induced-Fluorescence technique. The CCFT has been also simulated using the 3D PIC code F3MPIC to validate and extend the experimental measurements. Finally, a novel technique for ion velocimetry based on the optogalvanic method is proposed. Summarizing, the objectives are:

- to analyze the LIF technique and its application to ion velocity measurements;
- to tune the LIF measurement system;
- to characterize the ion velocity field (both magnitude and direction) in the region surrounding the thruster exit plane;
- to simulate the thruster with the 3D PIC code F3MPIC with particular focus on the resulting ion velocity distribution on the exit plane to be compared with LIF measurements;
- to provide a physical insight of the plasma acceleration mechanism combining LIF measurements, previous plasma potential measurements and 3D PIC simulations;
- to study the feasibility of a novel ion velocimetry method based on an optogalvanic technique.

### 1.2.3 Traveling Magnetic Field Plasma Accelerator

This study is focused on the exploitation of a traveling magnetic field to accelerate plasma in a dual-stage propulsion system. The main goals of the analysis are the understanding of the plasma dynamics forced by the traveling field and the achievement of an experimental proof-of-concept. In detail, the objectives are:

- to provide a physical insight of the acceleration mechanism through analytical and numerical models;
- to design and build a system of coils able to produce a traveling magnetic field in the target velocity range (15000 - 30000 m/s), working either in a steady or in a pulsed mode;
- to design and setup an experiment to test the traveling field accelerator installing proper probes to detect an accelerated plasma sheet.

## 1.3 Thesis Outline

The thesis outline is the following:

- In chapter 2 the investigation tools, both experimental and numerical, are described into detailed. The plasma diagnostic systems are analyzed defining their characteristics, uncertainty sources and identified measurement procedures.
- Chapter 3 is dedicated to the description of the work performed on the RF plasma thruster. Particularly the experimental design, the guidelines followed during the test campaigns, the main results are described. Furthermore the results of the numerical analysis are illustrated.
- Chapter 4 is focused on the physical investigation on the acceleration mechanism in the Stanford CCFT. The LIF ion velocity measurements are reported along with the numerical analysis carried out through the 3D PIC code. Experimental and numerical results are compared and combined together giving an overall picture of the ion acceleration region.
- The traveling magnetic field plasma accelerator is described in Chapter 5. An insight of the plasma acceleration mechanism is given through 1D PIC analysis. The system designed and built to generate the traveling field is described along with some preliminary experimental results.

CHAPTER 2

# Physical Investigation Tools

This chapter is dedicated to the description and analysis of the tools, both experimental and numerical, employed to investigate the plasma propulsion systems.

Two optical spectrometers, a microwave interferometer, a Retarding Potential Analyzer and a current probe have been employed to characterize the Radio-Frequency plasma thruster developed at University of Padova during the EU FP7 HPH.com project.

Laser-Induced-Fluorescence velocimetry has been used to measure the ion velocity field in the plume of the Stanford Cylindrical Cusped Field Thruster at the Stanford Plasma Physics Laboratory. The application of the optogalvanic technique for the ion velocity measurement is an original idea born at the Stanford Plasma Physics Laboratory.

Additionally, the propulsion systems have been simulated by means of particle codes entirely developed at University of Padova by the plasma propulsion group.

## 2.1 Experimental Diagnostic Systems Survey

### 2.1.1 Optical Spectrometers

Two optical spectrometers are used to acquire the emission spectrum of the plasma, in order to extrapolate information on the ratios between atomic excitation and ionization as well as on the electron temperature:

- an Ocean Optics HR4000 spectrometer, with a wavelength range 380-830 nm, a slit width of 25$\mu$m and a resolution of 0.54 nm;
- an Ocean Optics HR4000 spectrometer with a wavelength range 220-575 nm, a slit width of 5$\mu$m and a resolution of 0.24 nm.

The spectrometers have been used in the experimental characterization of the RF plasma thruster operating with argon. The coupled employment of these devices allows the obser-

vation of a broad band of the emission spectrum from the near UV to the near IR.

Both the spectrometers are interfaced to the plasma source by means of an optical fiber, 2 m long and with a 600 $\mu$m core diameter; during the various tests, the optical fibers heads usually look the same source section and are oriented in order to point the plasma core. Spectrometers measurements are affected by the presence of the Pyrex glass tube (i.e. the plasma source tube), which is responsible of a wavelength-dependent attenuation of spectrum intensity, particularly below 300 nm. A dedicated calibration deuterium-halogen light source, emitting a known spectrum, is used to determine the response of the overall system (comprised of spectrometer, optical fiber and Pyrex layer) in function of the wavelength. The elaboration of the acquired data then requires: the subtraction of the background light in the absence of plasma, the superimposition of the calibration curve and a preliminary comparison with the theoretical spectrum to individuate a possible wavelength shift. The uncertainty on the spectral intensity is within 5%, considering the uncertainty resulting from the calibration process and the spectrometers specifications. An argon lines database is incorporated in a MATLAB post-processing tool which identifies the argon ion and neutral lines in the spectra.

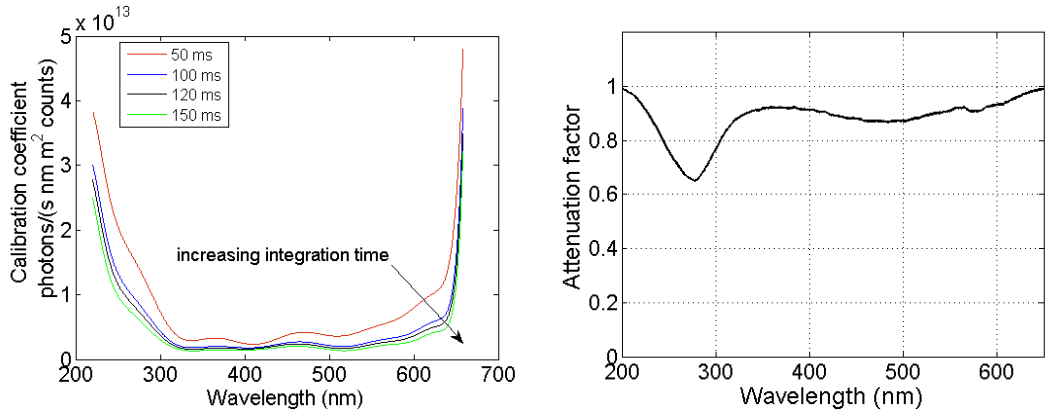


(a) (b)

Figure 2.1: a) Example of calibration curves for the Ocean Optics spectrometer operating in the range 220-575 nm (without Pyrex contribution). b) Wavelength-dependent attenuation introduced by the Pyrex glass.

The measured optical spectra can be coupled to a Collisional-Radiative (CR) model to obtain an estimation of the plasma temperature and density. The specific case of the RF thruster under testing presents particular complexities since the plasma can't be considered properly homogeneous, stationary and in a local thermodynamic equilibrium (LTE) condition. The lack of a complete LTE condition has been demonstrated by comparing the acquired spectra with those of an Ar hollow cathode lamp near equilibrium [51]. The

development of a complete interpretative model for an in-depth spectra analysis is outside the goals of this thesis, nevertheless the spectra are used for qualitative comparisons among different configurations of the thruster. The ionization level is qualitatively evaluated by means of four ArII to ArI lines ratios. The considered lines are 420, 452.2, 355.9, 434.8, 488 nm. The first couple of values corresponds to the neutral argon while the last three values identify the ionized argon; then the ratios E(355.9)/E(420), E(434.8)/E(420), E(488)/E(420), E(488)/E(452.2) are calculated to trace their dependency on the key parameters changed during the thruster investigation. The set of measures gains reliability if all the ratios show an equal trend, condition which is satisfied in most of the cases. For these qualitative analysis, the calibration coefficient is applied in dimensionless form, normalized respect to the mid-range value, in order to compensate the wavelength-dependent response of the spectrometer and the glass filtering effect.

Even if a detailed model for the spectral analysis has not been developed within this thesis, during the HPH.com program we have been supported by a partner of the program who developed a dedicated global model giving an evaluation of the electron temperature and density. Particularly, the model takes into account that the optical path encompasses an external cold plasma region, where the abundance of Ar I prevails, and a central core, where the bulk of the Ar II amount is concentrated. A detailed description of the model is reported on Ref. [52] and some of the results are mentioned in section 3.3.

### 2.1.2 Microwave Interferometer

#### Basic Theory and Overall Description

The microwave interferometer is used for a nonintrusive measurement of the electron plasma density in the Radio-Frequency discharge of the HPH.com thruster. The interferometry overcomes some of the issues associated with the use of electrostatic probes in plasma thrusters of small dimensions. In this case the use of electrostatic probes is critical since both the probes themselves and above all their housings have a dimension comparable with the inner discharge channel diameter inducing a significant spurious effect on the discharge properties; moreover, if the thruster is based on a RF technology, the control electronics of the probe and the interpretation of the collected data increase in difficulty due to the RF environment; finally their metal components can interfere with the RF antenna. The microwave interferometry has been already successfully applied to the measurement of the plasma densities in the plasma discharge and in the ejected plume of space propulsion systems, e.g. Hall thrusters [53] and arcjets [54]. The microwave interferometer used in this study has been designed and built by ENEA[1] laboratories during the HPH.com project.

[1] Agenzia Nazionale per le Nuove Tecnologie. l'Energia e lo Sviluppo Economico Sostenibile, Frascati, Italy

The working principle of this instrument is based on the phase difference between a microwave reference signal propagating along a waveguide and a microwave beam which crosses the plasma. The phase shift between the signals driven through the different paths depends on the plasma refractive index R, therefore on the plasma density. In the case of magnetized plasma the wave propagation mode depends on the polarization relative to the magnetic field. Assuming a propagation perpendicular to the external magnetic field B, if the electric field is parallel to B the mode is the ordinary mode (O-mode), otherwise the mode is extraordinary (X-mode) [55]. In the latter case the refractive index becomes:

$$R_x^2 = \frac{[(\omega+\omega_{ci})(\omega-\omega_{ce})-\omega_p^2][(\omega-\omega_{ci})(\omega+\omega_{ce})-\omega_p^2]}{(\omega^2-\omega_{ci}^2)(\omega^2-\omega_{ce}^2)+\omega_p^2(\omega_{ce}\omega_{ci}-\omega^2)} \tag{2.1}$$

where $\omega_{ce}$, $\omega_{ci}$, and $\omega_p$ are the electron cyclotron frequency, ion cyclotron frequency and the plasma frequency respectively. The refractive index for an O-mode wave propagation can be expressed by:

$$R_O^2 = 1 - \frac{\omega_p^2}{\omega^2} \tag{2.2}$$

In the case of $\omega >> (\omega_p, \omega_{ce}) >> \omega_{ci}$ the previous equations can be simplified and developed in series, giving the following expression valid for both the O-mode and the X-mode propagation:

$$R_x \approx R_O \approx 1 - \frac{\omega_p^2}{2\omega^2} \tag{2.3}$$

This approximation is satisfied for the considered range of plasma parameters and the operating frequency of the interferometer; indeed, considering a background magnetic field of 0.1 T and an expected density of $\sim 5 \times 10^{18}$ m$^{-3}$ the ion cyclotron, the electron cyclotron and the plasma frequencies are 40 kHz, 2.8 GHz and 20 GHz respectively, whereas the operating frequency is 75 GHz. Furthermore, the cutoffs in the dispersion relation must be considered to assess whether the wave propagates or is reflected by the plasma. For an O-mode propagation the cutoff takes place at $\omega = \omega_p$, which corresponds to a density of $7 \times 10^{19}$ m$^{-3}$ for $\omega/2\pi = 75$ GHz. In the case of X-mode propagation the cutoffs are expressed by $\omega \approx \omega_{pe} \pm 1/2\ \omega_{ce}$ corresponding to a density of 6.7-7.2 $\times 10^{19}$ m$^{-3}$.

It is worth mentioning that we are operating in the low collisional limit, otherwise for high electron collision frequency the previous relation must be modified [56]. For a density of $10^{19}$ m$^{-3}$ and a temperature of 5 eV the expected electron-ion collision frequency, estimated through the Spitzer relation, is about 34 MHz and can reach a value as high as 380 MHz for a temperature equal to 1 eV. Moreover the background neutral pressure in the plasma source ranges from $3.6 \times 10^{-2}$ up to $6 \times 10^{-2}$ mbar, giving an electron-neutral collision frequency $\nu \approx 3 \times 10^{9}$p (in Torr) lower than 113 MHz. Thus the effective collisional frequency $\nu_e$ has a negligible effect on the phase shift since $\nu_e \ll (\omega, \omega_p)$.

Assuming a slab geometry, the phase shift due to the plasma can be estimated as:

$$\Phi = \frac{2\pi}{\lambda} \int_0^D (1 - R) dl \tag{2.4}$$

Introducing the Eq. 2.3, the previous relation becomes:

$$\Phi = \frac{e^2}{4\pi c^2 \epsilon_0 m_e} \lambda \int_0^D n dl \tag{2.5}$$

where $e$ is the elementary charge, $m_e$ the electron mass, $\epsilon_0$ the vacuum permittivity, $\lambda$ and $\omega/2\pi$ the vacuum wavelength and frequency of the wave, n the electron density and D the plasma thickness (i.e. the plasma column diameter). Finally we obtain:

$$\Phi = Q \overline{n} D \tag{2.6}$$

where we have introduced the mean electron density $\overline{n}$ calculated along the plasma column diameter and the constant $Q$, defined as:

$$Q = \frac{e^2}{4\pi c^2 \epsilon_0 m_e} \lambda \tag{2.7}$$

Eq. 2.7 and 2.6 indicate that the sensibility of the instrument is proportional to the wavelength: a longer wavelength provides a higher sensibility. On the other hand, the slab approximation in the case of a cylindrical plasma with a constant density can be applied when the condition $D/\lambda > 3$ is satisfied. The diameter of the RF plasma source of the HPH.com thruster is 19 mm and the chosen wavelength is 4 mm (f = 75 GHz) giving $D/\lambda = 4.75$. A phase shift of $2\pi$ is produced by a plasma of $2.8 \times 10^{19}$ $m^{-3}$, assuming a plasma filling the whole source cylinder (D = 19 mm). The resolution of the interferometer depends on the accuracy of the phase detection as described in the following paragraph.

**Interferometer Hardware**

The interferometer presents an heterodyne configuration [57]. Two microwaves signals at $f_1$ = 75 GHz and $f_2$ = 75.1 GHz are generated by two oscillators (osc1 and osc2) and propagate along the two branches of the instrument, made of WR12 waveguide. The oscillators are made up of two stages: two phase-locked dielectric resonators generate 9.375 and 9.3875 GHz signals and two 8-times frequency multipliers give the final 75 GHz and 75.1 GHz signals. The two resonators are locked in phase to a 100 MHz crystal oscillator. Two directional couplers split the power of each interferometer branch into two parts. A pair of signals at $f_1$ and $f_2$ are combined in a mixer (Mixer 2) to provide a local reference signal (LO). The remaining $f_1$ power is driven across the plasma through a couple of radiating/receiving standard gain horns and is combined with the $f_2$ signal in

a second mixer (Mixer 1) giving in output the measurement signal (RF). The presence of the plasma introduces the aforementioned phase shift on the crossing microwave beam. The LO and RF signals are then amplified, filtered with a central frequency equal to the beating frequency $f_2$-$f_1$ = 100 MHz and 3 MHz of bandwidth, and their relative phase $\phi$ is measured through a digital phase detector. This lay-out allows to compensate slow frequency drifts of the two oscillators since they produce the same effect on the two input signals of the digital phase detector. The latter is a digital vector voltmeter operating a 100 MHz which gives the quadrature components I = A cos$\phi$, Q = A sin$\phi$ of the two signals. The overall bandwidth of the phase detection system is 11.4 kHz at 3 dB and presents a noise of 0.02°, corresponding to a density of 1.6 × $10^{15}$ $m^{-3}$ for a plasma thickness of 19 mm. This interferometer configuration satisfies the challenging requirements of the

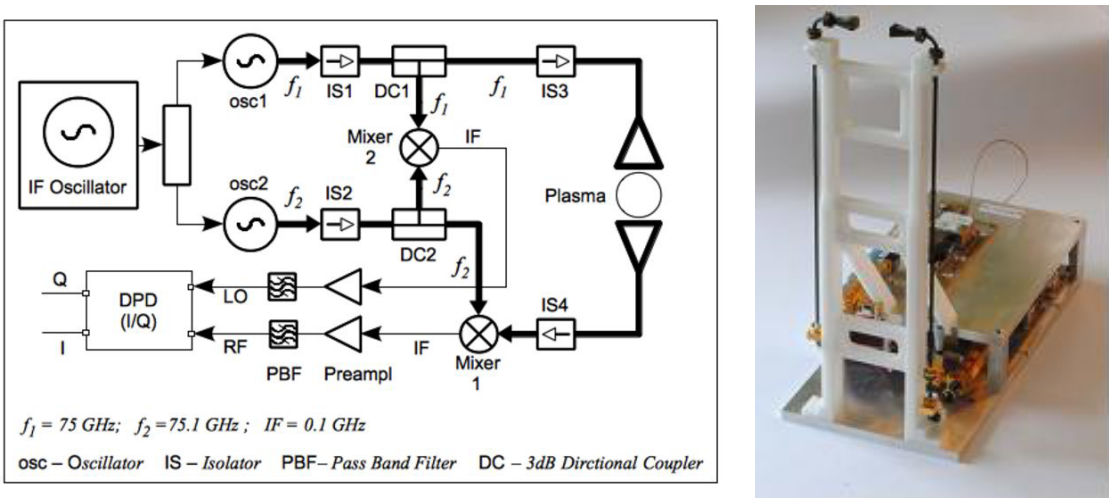


(a) (b)

Figure 2.2: a) The microwave interferometer schematic. b) Picture of the microwave interferometer.

broad density range ($10^{16}$ - $10^{19}$ $m^{-3}$) and the small size of the plasma source. The small size of the plasma limits the value of the wavelength, limiting also the value of the gain factor Q, where $\Phi = Q\overline{n}D$. As a consequence, the high-sensitivity low-noise phase detector is used to provide a measurement of the lowest density value. The noise spectrum of the interferometer without plasma when installed in the experiment presents a standard deviation of 0.33° considering the full bandwidth, but this value reduces to 0.06° (corresponding to a density of 5 × $10^{15}$ $m^{-3}$ for a plasma thickness of 20 mm of diameter) applying a low pass filter with a cutoff frequency at 100 Hz and a notch filter to remove a strong 20 Hz oscillation (probably due to mechanical vibrations).

### Method for Different Diameters of the Plasma Column

In some operating modes of the Radio-Frequency plasma thruster, the plasma does not fill the whole source cylinder but is confined in the central region around the axis of the system. In such cases the slab approximation is not longer valid since D/$\lambda \approx 1$ and some corrections have to be applied for the calculation of the density from the phase shift. In Ref. [58] an analytical approach to estimate the phase shift introduced by a small plasma cylinder between the emitting and receiving horn is presented. The plasma cylinder behaves as a divergent lens on the microwave beam: part of the incoming beam crosses the plasma column and is detected by the receiving horn, another part is steered outside the collecting angle and a third part does not cross the plasma. Only the collected component crossing the plasma gives a contribution to the phase shift, equal to $2\pi$(R-1)D/$\lambda$. Following a geometrical method, the resulting phase shift can be expressed as a function of the geometrical properties of the horns and of the plasma density and diameter. Fig. 2.3a shows the reference configuration along with the involved geometrical parameters: the distance between the horns 2B, the horns aperture A and their length L. D is the plasma column diameter and R the plasma refractive index.

$$\Phi = \tan^{-1}\left[\frac{\alpha^{0.5}\sin[2\pi(R-1)D/\lambda]}{\alpha^{0.5}\cos[2\pi(\mu-1)D/\lambda] + \left(1-\frac{D}{w}\right)^{0.5}}\right] \tag{2.8}$$

$$w = \frac{L+B}{L+2B}A \tag{2.9}$$

$$\alpha \approx \frac{AD[(L+B)-D/2]}{4\left(\frac{1}{R}-1\right)B(L+B)+D(L+2B)}\frac{1}{w} \tag{2.10}$$

In order to validate this method we have carried out a sequence of measurements of the phase shift introduced on the microwave beam by a Plexiglas cube with a central cylindrical hole. The Plexiglas cube has been located between the emitting horn and the receiving one. The diameter of the central hole has been increased from few millimeters up to 15 mm. The central hole generates an effect similar to that of the plasma cylinder. Indeed, in the case of the Plexiglass blocks, the microwave beam run into a cylindrical region (the hole) with a refractive index lower than the surrounding medium ($R_{plex}$=1.61). Similarly, in the case of the plasma cylinder the microwave beam propagates through a cylindrical plasma whose refractive index is lower than 1. The obtained phase shifts have been compared with those calculated through Eq. 2.8. The analytical and the experimental results are in good agreement revealing the effectiveness of the method (Fig. 2.3b). Furthermore the data highlight that for diameters higher than 7.8 mm the slab approximation represents properly the phase shift.

Figure 2.4 illustrates the application of Eq. 2.8 to the case of a plasma cylinder of

various densities and diameters. Particularly, figure 2.4b highlights again the failure of the slab approximation for plasma columns of small diameter.

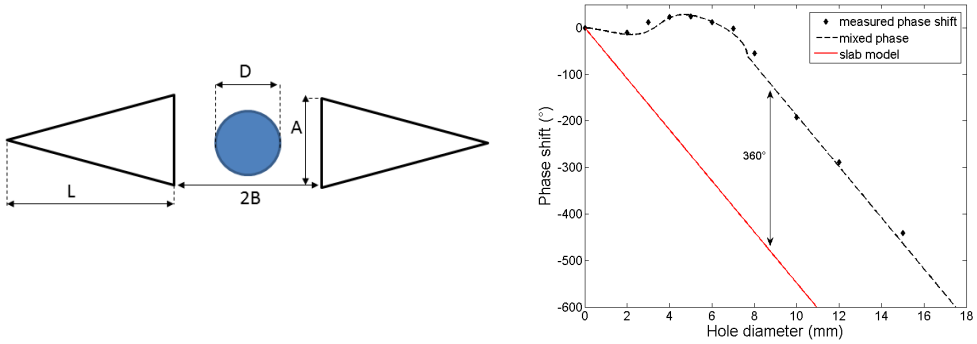


(a) (b)

Figure 2.3: a) Small plasma column between the interferometer horns. b) Phase shift introduced by a hole of different diameters in a Plexiglass block. The mixed phase is calculated through the relation 2.8.

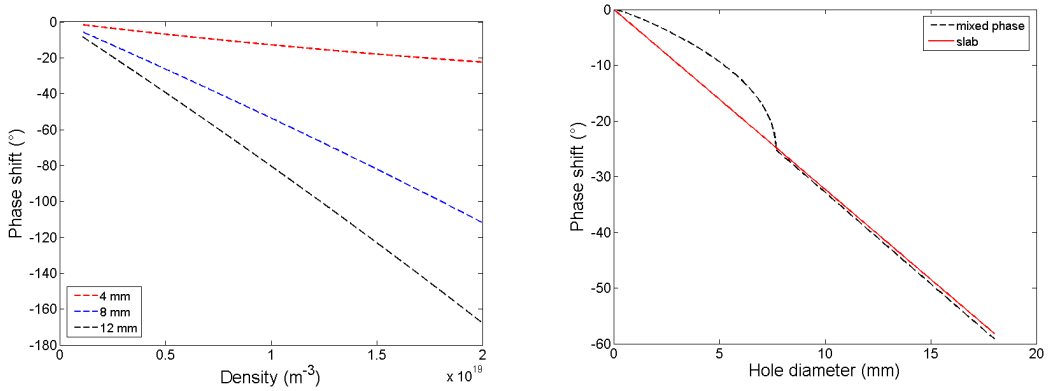


(a) (b)

Figure 2.4: a) Phase shift in function of the plasma density and for different values of the plasma column diameter. b) Phase shift in function of the plasma column diameter and for a fixed density of $5 \times 10^{18}$ m$^{-3}$.

### Data Analysis

Figure 2.5 illustrates the phase difference step due to the powering off of the plasma discharge. In the validity range of the slab approximation, this step is a linear function of the plasma density according to Eq. 2.6:

$$\overline{n} = \frac{\Phi}{QD} \tag{2.11}$$

The procedure carried out for each acquisition is the following:

1. the plasma discharge is switched on and led to the wanted conditions
2. the acquisition through the microwave interferometer is started
3. the plasma discharged is switched off
4. the acquisition through the microwave interferometer is stopped.

The powering off of the plasma produces this phase step which is dependent on the density. A MATLAB post-processing tool has been developed in order to analyze the data. The data are numerically low-pass filtered with a cutoff frequency of 10 Hz. The routine automatically individuates the step and calculates its magnitude:

$$\Phi = \phi_1 - \phi_2 \tag{2.12}$$

where $\phi_1$ and $\phi_2$ are the mean values of the phase difference before and after the switching off of the plasma, respectively.

$$\phi_1 = \frac{1}{N_{plasma\ on}} \sum_{1}^{N_{plasma\ on}} \phi_j \tag{2.13}$$

$$\phi_2 = \frac{1}{N_{plasma\ off}} \sum_{1}^{N_{plasma\ off}} \phi_j \tag{2.14}$$

The standard deviations are evaluated as:

$$\sigma_{\phi_1} = \left[ \frac{1}{(N_{plasma\ on} - 1)} \sum_{1}^{N_{plasma\ on}} (\phi_j - \phi_1)^2 \right]^{1/2} \tag{2.15}$$

$$\sigma_{\phi_2} = \left[ \frac{1}{(N_{plasma\ off} - 1)} \sum_{1}^{N_{plasma\ off}} (\phi_j - \phi_2)^2 \right]^{1/2} \tag{2.16}$$

and finally:

$$\sigma_{\Phi} = \sqrt{\sigma_{\phi_1}^2 + \sigma_{\phi_2}^2} \tag{2.17}$$

The standard deviations $\sigma_\phi$ are representative of the dispersion of the sampled data due to the noise, which is the main source of phase uncertainty for the considered case.

The deviation on the density is finally given by:

$$\sigma_n = \sqrt{\left(\frac{\sigma_\Phi}{QD}\right)^2 + \left(\frac{\Phi}{QD^2}\sigma_D\right)^2} \tag{2.18}$$

The uncertainty on the measured density is evaluated as $3\sigma_n$, considering the 99.7% confidence interval. In the previous relation the uncertainty of the constant Q (Eq. 2.7) can be neglected since the main sources of uncertainty originate from the determination of the phase shift and of the plasma column diameter. All the physical constants included in $Q$ are known with a high accuracy and the uncertainty on the wavelength $\lambda$ can be neglected due to the high microwave source stability.

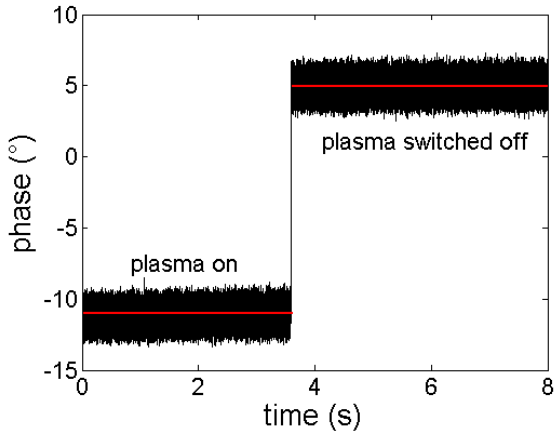


Figure 2.5: The step of the phase difference due to the switching off of the plasma.

Figure 2.5 illustrates an example of the phase difference versus the acquisition time. The mean values $\phi_1$ and $\phi_2$ respectively before and after the switching off the plasma are shown. The estimated density is $\overline{n}$=(2.7 $\pm$ 0.64)$\times$ $10^{18}$ $m^{-3}$ for a plasma column diameter equal to (9.2 $\pm$ 0.25) mm.

In the case of small plasma diameters the uncertainty analysis becomes more complicated, because of the nonlinearity of the problem and the increased number of variables involved in the calculation. The plasma density is calculated from equation 2.8 written in the form $f(n, \Phi, D, L, B, A) = 0$ and solved for the density $n$ through a bisection algorithm. In order to analyze the uncertainty of the resulting plasma density the Monte-Carlo method [59] is applied. The Monte-Carlo method consists in the generation of $M$ values of the variables $x_j$ involved in the model $f(x_1..x_j..)$ for the measurement process. A probability distribution function (PDF) is associated at each variable for the generation of the

random values. In this analysis we assume a Gaussian PDF whose standard deviation $\sigma_x$ satisfies the relation $3\sigma_j$=$\Delta x_j$ where $\Delta x_j$ is the 99.7% confidence uncertainty of the variable $x_j$. Let's consider a test case for the application of the method. The measured phase shift is equal to (51 ± 6.3)°. The diameter of the plasma column is (7 ± 0.25) mm. The geometric parameters of the interferometer horns are L = (33 ± 0.05) mm, A = (11 ± 0.05) mm B = (50 ± 0.5) mm. The frequency distribution of density values produced by the Monte Carlo method (100000 trials) is shown in Fig. 2.6. The resulting density is (1.51 ± 0.24) × $10^{19}$ $m^{-3}$, thus a percentage uncertainty of about 16%.

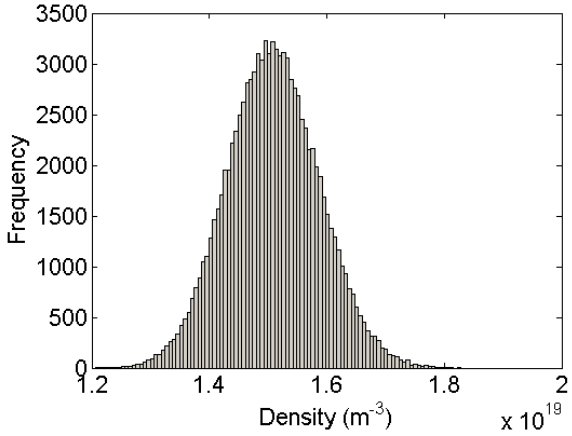


Figure 2.6: Frequencies of the values generated by the Monte Carlo method: the mean value is 1.51 × $10^{19}$ $m^{-3}$ and the standard deviation 0.08 × $10^{19}$ $m^{-3}$.

In order to employ the relations 2.11 or 2.8 it is necessary to know the value of the effective discharge diameter D, which, during the usual operating mode, is considerably smaller than the inner diameter of the glass tube housing the plasma source. In order to estimate D, an image processing technique is employed: by means of a Basler scA1400-30FC CCD camera with focusing lenses (1388 x 1038 pixel sensor) two pictures are taken for each discharge, one with a 488BP10 bandpass filter (center frequency 488 nm, bandwidth 10 nm) in order to observe the distribution of the ions, which are concentrated in the cylinder of diameter D, and an unfiltered one, acquired from the same point of view. A MATLAB script is then used to analyze the two pictures, calculating the scale in mm/pixel from the unfiltered one referring to the glass tube outer diameter and then using it to estimate D from the other. We calculate the radial light intensity profile at each axial position under the interferometer horns. The plasma column diameter is then calculated as the diameter which encompasses the 99% of the integrated light intensity. The uncertainty is calculated considering the change of the diameter along the axial direction and the uncertainty on the scale. An example of this process can be seen in figures 2.7a and 2.7b.

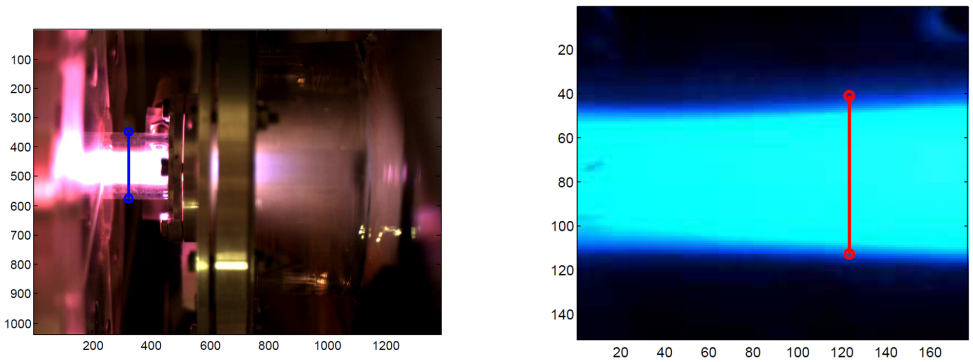


(a) (b)

Figure 2.7: a) Unfiltered image of the plasma discharge. The blue line indicates the outer diameter of the source tube (24 mm), which is used to calculate the scale of the picture. b) Particular of the plasma discharge. Image resolution: 0.105 mm/pixel, plasma discharge diameter: (9.2± 0.24) mm.

### 2.1.3 Retarding Potential Analyzer

#### Basic theory and overall description

In electric propulsion testing the Retarding Potential Analyzer (RPA) is widely used to estimate the local ion velocity distribution function (IVDF) in the plasma. The main application of the probe is the measurement of the ion acceleration in the plume downstream the exit plane of the thruster, even though it is sometimes used inside the discharge channel. The RPA allows to identify the mean ion velocity, the width of the distribution function and can reveal the presence of multiple populations, allowing the comprehension of their influence on the thruster performance. This probe presents a system of grids at different electric potentials plus a collector. This system produces a selective filtering of the ions based on their energy. The classical grid lay-out is the following:

- an outer screen grid to isolate the analyzer from the plasma;
- a grid with a negative potential to repel the unwanted incoming electrons;
- a positively polarized grid to energetically discriminate the ions by means of a potential sweep;
- a grid with a negative potential to rebound secondary electrons emitted from the collector which can falsely increase the ion current; in some RPAs this grid is not used;
- a collector C to detect the incoming current.

The collected current is given by:

$$I_c = \tau^3 e n_0 A_c \langle v_i \rangle \tag{2.19}$$

where $n_0$ is the density of the incident ion flow, $\tau$ is grid transparency, $A_c$ the effective colletion area, $\langle v_i \rangle$ the average velocity of the collected ions and $e$ the elementary charge. The ion flux can be expressed through the ion velocity distribution function:

$$n_0 \langle v_i \rangle = \int_{v_c}^{\infty} v f(v) dv \tag{2.20}$$

where $v_c$ is an equivalent velocity that represents the same energy than the retarding potential $V_p$ expressed relative to the plasma potential. All the ions with a velocity above $v_c$ have enough kinetic energy to reach the collector, all the ions with a velocity below $v_c$ are repelled by the potential barrier. The boundary velocity $v_c$ for an ion mass $m_i$ is then associated to the retarding potential $V_p$:

$$\frac{1}{2} m_i v_c^2 = -eV_p \tag{2.21}$$

The derivative of the collected current $I_c$ in function of the retarding potential $V_p$ gives a direct estimation of the ion velocity distribution function according to the following relation, as derived in Ref. [60]:

$$f(v) = -\frac{m_i}{\tau^3 e^2 A_c} \frac{dI_c}{dV_p} \tag{2.22}$$

The previous relation has been obtain in a simplified frame neglecting some physical processes which can alter the collected current. Such effects include charge exchange collisions, secondary electron emission from the collector, ionization processes inside the RPA channel and losses at the channel walls due to a diverging lens effect of the grids on the ion trajectories. Moreover different polarization configurations of the grids can introduce different effects on the collected current.

Bohm in Ref. [60] illustrates how the various phenomena can alter the RPA characteristic curve. For his study Bohm uses a RF plasma source operating with argon at a pressure of 0.025 Torr. Figure 2.8a illustrates the benchmark I-V characteristic curve obtained through the most classical polarization pattern, made by an entrance grid #0, an electron repeller #1, an ion discriminator #2 and a secondary electron emission suppressor #3. If the electron repulsion grid is set grounded or removed we observe a linear increase of the ion collected current for filter energies higher than the maximum ion kinetic energy (Fig. 2.8b). In contrast, this segment is constantly zero in the benchmark curve (Fig. 2.8a), since no ion has enough energy to overcome the potential barrier generated by the ion discriminator. The linear increase is due to ionization in the analyzer channel by

electron-neutral collision; this effect is enhanced for higher voltage differences between the grids. The I-V curve shown in Fig. 2.8c, obtained through the grounding of the suppression grid #4, highlights the effect of secondary electron emission from the collector, mainly due to ion bombardment. In this case a current peak takes place before the decreasing segment of the curve, i.e. at the low-energy limit of the IVDF. Additionally an offset of the curve is observed due to a spurious secondary electron current escaping from the collector in the direction opposite to the ion movement. In this case the current detected at the collector is made of an ion component and a secondary electron component. The presence of these two contributions is pointed out sweeping grid #3 from -200 V to 200 V together with grid #2 (Fig. 2.8d). If the grid #2-3 potential $V_r$ is lower than the collector potential $V_c$ the collected current is carried only by incoming ions since the emitted secondary electrons are rejected to the collector. For $V_c < V_r < 0$ both an ion and a secondary electron component are collected, giving an higher value of the measured current. For a certain potential $V_r > 0$ the ions become to be energetically filtered and as a consequence the ion current decreases. For high positive grids potential all the incoming ions bounce back and the residual current is carried exclusively by the emitted secondary electrons. The constancy of the residual current suggests the absence of additional ionization between the collector and the grid; indeed the effect of the ionization would produce a linear increase of the current with the voltage as shown in Fig. 2.8b.

Another issue originates from practical difficulties to determine the overall effective transparency, which is a combination of the grids transparency and possible misalignments due to assembling imperfections. The result is a higher uncertainty in the determination of the absolute value of the plasma density obtained from the integration of the IVDF, nevertheless the energy distribution is not significantly affected. The problem can be faced carrying out a calibration with a known monoenergetic ion-beam source or auxiliary probes [61].

Inaccuracies of the energy filter could be introduced by possible potential depressions between the grid wires. Ions with an energy lower than the retarding potential can penetrate through the grid because of the lower effective potential in the grid holes. The energy resolution of the analyzer is affected also by the steering of the ion trajectories before being filtered by the discrimination grid.

Finally the RPA is an intrusive probe which can create a spurious perturbation of the surrounding plasma. In this work the RPA has been used to detect the presence of an accelerated ion beam downstream the Radio-Frequency plasma source developed during the HPH.com project following a comparative approach, i.e. determining how the most probable ion energy is affected by the discharge parameters. Due to the aforementioned issues we don't extend the analysis to the calculation of the absolute value of the plasma

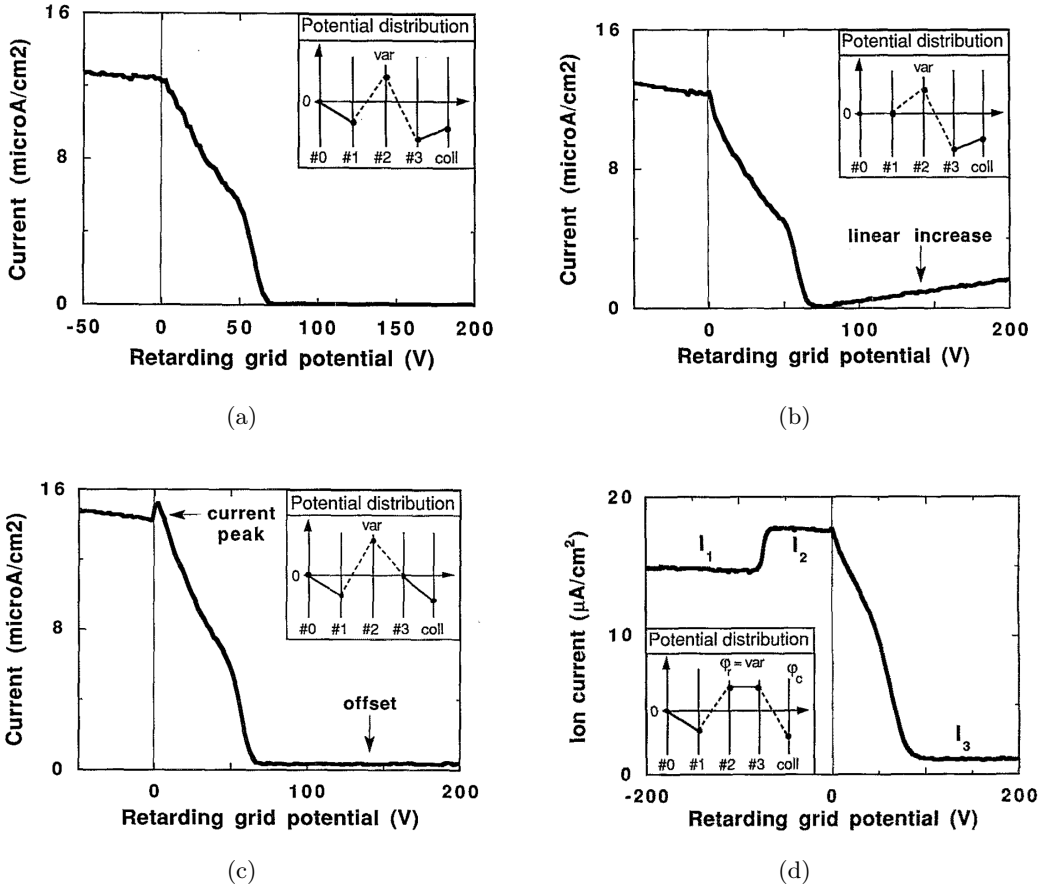


Figure 2.8: RPA characteristic curves resulting from different grid polarizations obtained by Bohm [60].

density. RPA ion energy measurements have already been performed on RF-based plasma thrusters by other research groups [18, 62] even if operating at higher power.

### Retarding Potential Analyzer hardware

The RPA used in this study has been designed according to the guidelines described by Hutchinson [63]. The main requirement deals with the spacing between the electron repelling and the ion retarding grids: in order to avoid space charge limitations the spacing should be lower than 4 Debye lengths. The probe has been designed considering an optimal operating point n = $5 \times 10^{15}$ $m^{-3}$, $T_e$ = 2 eV, giving $\lambda_{De} \sim 0.21$ mm. The mesh size is a trade-off choice since a small size of the holes (which usually gives a lower transparency) is preferable to have a uniform potential throughout the grid whereas a higher transparency is preferable to enhance the signal-to-noise ratio.

The RPA has a three-grids configuration. The polarization pattern is different from the classical configuration. The first grid G1 is grounded, the second grid G2 is the ion discriminator, the third one G3 is negatively polarized to repel primary electrons coming from the plasma and simultaneously bounce back secondary electrons coming from the collector. This configuration allows to use only one grid (G3) to both repel primary and secondary electrons. The use of only three grids allows to obtain a lower overall transparency with a consequent increase of the output current signal. The electron repulsion grid is kept to a constant voltage of -120 V using an array of batteries. The intense negative value of the repulsion potential is set to repel the high energy electrons ejected from the thruster. As described later in Ch. 3, the operating principle of the RF thruster is characterized by the ejection of high energy electrons along with the accelerated ions. Thus the required repulsion potential is higher in comparison with other propulsion systems, such as Hall thrusters, in which the neutralizing electrons in the plume are usually at lower energy. Finally, the positive potential is usually swept within the range 0 - 300 V.

The grids are made of a 30 $\mu m$ square mesh of nickel welded between two copper annular supports in a sandwich-like configuration. The transparency of the grids is equal to 0.6. The cylindrical central channel presents a diameter of 2.5 mm. The RPA front aperture is a stainless steel disk with a 2mm-diameter central hole. This disk is held in contact with the first grid to produce a uniform sheath throughout the entrance slit. The grids are spaced by some ring insulators made of MICA. The spacings between the grids are: 0.4 mm between G1 and G2, 0.8 mm between G2 and G3, 0.6 mm between G3 and the collector. All these components are housed in a peek cylinder to insulate the inner grids from the external case made of stainless steel.

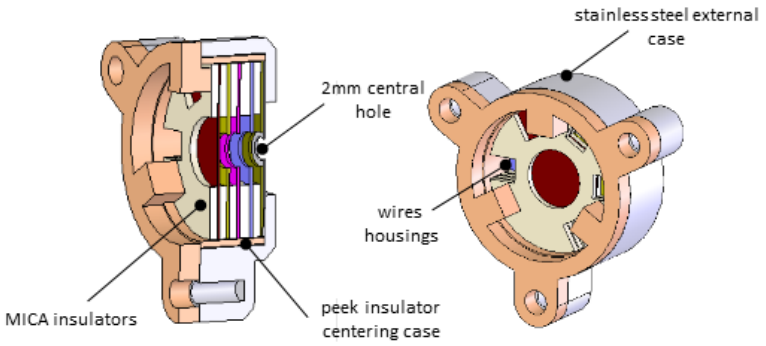


(a)

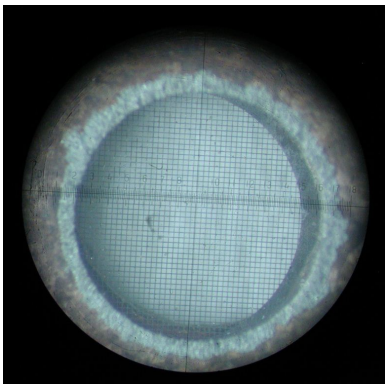

(b)

Figure 2.9: a) Design of the RPA head; b) picture of an RPA grid realized through an optical microscope.

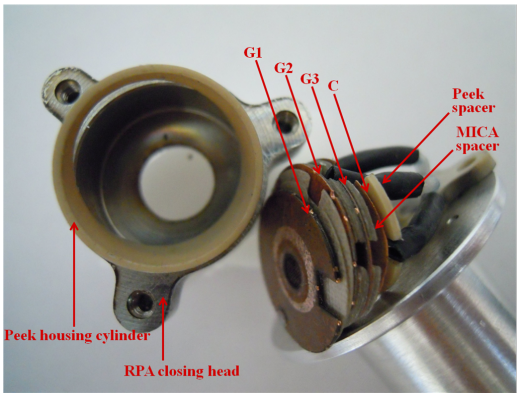


(a)

(b)

Figure 2.10: a) A picture of the grids and the insulator rings of the RPA; b) the RPA installed in a fixed position 100 mm downstream the RF plasma source outlet.

### Data acquisition and analysis

As previously discussed, the IVDF is represented by the derivative of the collected current $I_c$ in function of the retarding potential $V_p$ relative to the plasma potential:

$$f(v) = -\frac{m_i}{\tau^3 e^2 A_c}\frac{dI_c}{dV_p} \tag{2.23}$$

where $m_i$ is the ion mass, $\tau$ the grids transparency, $A_c$ the collecting area and $e$ the elementary charge. The second grid presents a positive bias and only the ions energetically able to overcome the potential barrier can pass over. Therefore a potential sweep yields a selective collection and gives the energy distribution of ions through the curve $I_c$ vs $V_p$.

The current is acquired and converted in a voltage signal through an ad hoc electronics with a tunable gain factor. In this case the selected one is 300 V/mA. The overall uncertainty on the read current is below 2%. The retarding potential of the second grid is acquired through a 10:1 probe with an uncertainty of 5%. The analogue signals are then digitized by means of a DAQ platform Yokogawa WE7000. Subsequently the signal coming from the DAQ is numerically low-pass filtered with a cut-off frequency of 10 Hz to reduce the high frequency noise.

Assuming an accelerated Maxwellian ion population, the ion velocity distribution function can be expressed as:

$$f(v) = n_0 \left(\frac{m_i}{2\pi K T_i}\right)^{1/2} \exp\left[-\frac{m_i(v-v_b)^2}{2KT_i}\right] \tag{2.24}$$

where $v_b$ represents the mean velocity of the accelerated beam, corresponding to a retarding potential $eV_b = 1/2 m_i v_b^2$. $T_i$ and $n_0$ are the ion temperature and density in the incoming flow. The collected current in function of the retarding potential can be properly fitted with a function in the following form [64], obtained combining Eqn. 2.19, 2.20, 2.21 and 2.24:

$$I_i(V_p) = J\left[\sqrt{KT_i}\exp\left[-\frac{\left(\sqrt{eV_p}-\sqrt{eV_b}\right)^2}{KT_i}\right] + \sqrt{eV_b\pi}\,\mathrm{erfc}\left[\frac{\sqrt{eV}-\sqrt{eV_b}}{\sqrt{KT_i}}\right]\right] \tag{2.25}$$

where

$$J = A_c\tau^3\sqrt{\frac{n_0^2 e^2}{2m_i\pi}} \tag{2.26}$$

Indeed, the derivative of Eq. 2.25 gives:

$$\frac{dI_i}{dV_p} = -A_c\tau^3 n_0 e^2\sqrt{\frac{1}{2m\pi KT_i}}\exp\left[-\frac{(\sqrt{eV_p}-\sqrt{eV_b})^2}{KT_i}\right] \tag{2.27}$$

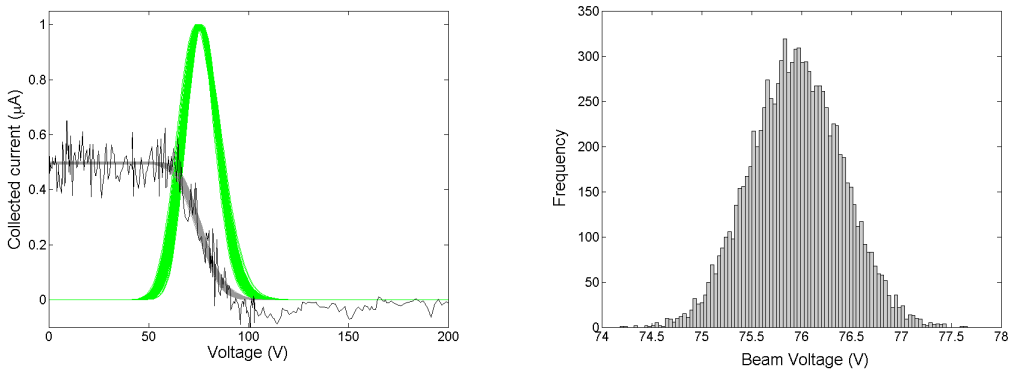


(a) (b)

Figure 2.11: a) RPA characteristic curves (grey) and consequent ion energy distribution functions (green) generated by the Monte-Carlo method, along with the initial rough data b) Frequency distribution of the values of the mean retarding voltage of the energy distribution.

The unknown parameters ($n_0$, $T_i$, $V_b$) are then calculated from the fitting of the experimental data ($I_{ck}$,$V_k$) through the least square method, which solves the problem $\min(\sum \epsilon_k^2)$ where:

$$\epsilon_k = I_{ck} - I_i(V_k) \tag{2.28}$$

The set of parameters ($n_0$, $T_i$, $V_b$) fully characterize the collected current profile and give a direct indication of the most probable energy of the beam and the width of the energy distribution. This procedure can be easily extended to multiple ion populations.

An uncertainty ($\Delta$V,$\Delta$I) is associated to the voltage and current acquisitions of each experimental point ($V_k$,$I_{ck}$). In order to estimate the resulting uncertainty of the target values $V_b$ and $T_i$ given by the fitting process, we have applied a Monte-Carlo method. Each experimental point can be located in a 2D region of the V-I plane with a certain probability; we assume a 2D Gaussian PDF whose widths are defined by the uncertainties of the voltage $\Delta$V and current $\Delta$I. A number N of V-I curves are produced through the random generation of $(V_k,I_{ck})_j$, j = 1...N values for each experimental point according to the assumed PDF. From each V-I curve a value of $V_b$ and $T_i$ is obtained. Fig. 2.11a illustrates the cloud of fitting V-I curves generated for an analyzed test case (N = 10000 trials), along with the initial rough data. In this case, a single Maxwellian population properly represents the ion energy distribution function. The mean retarding voltage associated to the accelerated population is (75.9 $\pm$ 1.5) V, and the ion temperature (0.52 $\pm$ 0.18) eV. The fitting provides also an estimation of the density $n_0 \sim 10^{15}$ $m^{-3}$, however this value is not reliable due to the difficulties in the determination of the grid transparency and the effective collecting area. Finally, the maximum ion current $I_0$, i.e. the current collected when all the ions

overcome the potential barrier of the retarding grid, is $I_0 = (0.49 \pm 0.06)\mu A$.

### 2.1.4 Beam Current Probes

#### Stanford Current Probe

The current probe consists of a 11 mm (± 3%) diameter aluminum collector with a guard ring. This probe is used to measure the ion current in the plume of the Stanford CCFT. Both the collector and the guard ring are polarized at the same voltage, usually 15 V, to repel electrons and collect ions. The ion current is detected by means of a Keithly 485 Picoammeter with an accuracy of 1%. The guard ring limits possible fringe effects creating a uniform sheath throughout the collecting area. The probe is mounted in a fixed position and angular scans are obtained through a rotation of the thruster. The integration of the current density over the angular scan gives an estimation of the ion flow ejected by the thruster.

#### CISAS Current Probe

The probe is used for the RF thruster characterization. The current probe consists of a 3 mm (± 2%) diameter nickel plate encased in an alumina tube. The plate is located 1 mm inside the tube to avoid collection of particles from the edges. The collector can be negatively or positively polarized in order to measure the electron or ion current ejected by the thruster. The current is read by means of a current-voltage conversion electronics in combination with a 34401A Agilent multimeter, with an overall accuracy of 5%. In the case of ion current detection, the typical probe polarization is -150 V. This polarization value is high in comparison with that used for other types of thrusters ($\sim$ 15 - 20 V), such as the CCFT or Hall thrusters; the reason is related to the higher energy of electrons ejected by the RF thruster. However, the high polarization voltage of the probe may introduce an increase of the effective collection area, due to the deflection of ion trajectories traveling nearby the probe and the consequent collection of these ions. Through single-ion orbit simulations, we have estimated that for a monoenergetic ion beam of $\sim$ 80eV ($\sim$ 20000 m/s for argon) the effect of the high probe polarization is negligible. However, for a beam of 50 eV the effective collection area increases of a factor 1.7. These estimations give a qualitative description, however the simulation of simple ion orbits is limiting if we aim to obtain an accurate value of the effective collection area. Based on this considerations, the estimation of the ejected ion flow from the integrated current density is prone to inaccuracies; as a consequence, we will use current measurements only to obtain information on the plasma plume shape and comparisons among different thruster configurations.

The probe can be mounted both in fixed position or on a micrometric three-axis move-

ment system composed of two axial stages (with range 200 mm and 300 mm respectively), for axial and radial scans of the plume, and a 360° rotational stage. The system allows to map the ejected current, giving information about the shape of the plume and allowing to estimate its overall value.

### 2.1.5 Laser-Induced-Fluorescence Ion Velocimetry

#### General description

This ion velocimetry method involves measuring a Doppler shift in the laser-induced fluorescence spectrum of a moving species as compared with a stationary reference. Typically this method consists of two stages:

- The ions are optically pumped through a laser from the initial state (1) to an excited state (2)
- The ions spontaneously decay from the excited state to a third state (3) with the emission of photons (fluorescence).

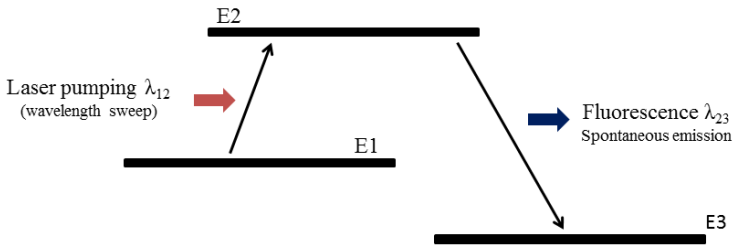


Figure 2.12: Basic scheme of the LIF diagnostic.

The initial state is the ground state or a metastable state. The laser wavelength $\lambda_{12}$ to obtain the ion excitation depends on the energy gap between the first and the second state:

$$h\frac{c}{\lambda_{12}} = E_2 - E_1 \tag{2.29}$$

where $h$ is the Planck constant and $c$ the light speed. Similarly the spontaneous fluorescence is emitted at a wavelength $\lambda_{23}$ which satisfies the relation:

$$h\frac{c}{\lambda_{23}} = E_2 - E_3 \tag{2.30}$$

If an ion has a velocity component $v$ in the same direction as the exciting laser, the incoming laser wavelength $\lambda_{ex}$ is Doppler shifted (by an amount $\lambda_D$) in the ion frame; now the ion

will only absorb an exciting photon whose energy with the Doppler correction is equal to the requisite $hc/\lambda_{12}$ for the transition. This amounts to a change in the exciting laser wavelength $\lambda_{ex}$ that is absorbed by the moving ion, as compared with $\lambda_{12}$ that is absorbed by a stationary ion:

$$\lambda_{ex} = \lambda_{12} - \lambda_D \tag{2.31}$$

In the previous equation $\lambda_{ex}$ is the effective excitation wavelength and $\lambda_D$ the Doppler shift depending on the relative velocity of the ions along the laser direction:

$$\lambda_D = -\frac{v}{c}\lambda_{12} \tag{2.32}$$

For example, if the ion is moving in the opposite direction than photons, the wavelength in the ion frame is lower than the absolute one, so the laser should be tuned at a higher wavelength than the stationary $\lambda_{12}$ to excite ions, i.e the effective exciting wavelength it is red-shifted.

LIF applied to the measurement of ion velocity exploits the Doppler effect. A laser wavelength scan is performed with a central value equal to $\lambda_{12}$ and a range $\Delta\lambda$. The emitted fluorescence is then collected by dedicated optics and a sensor, typically a photomultiplier tube. A bandpass filter with a central wavelength $\lambda_{23}$ is placed in front of the sensor in order to detect exclusively the light coming from the transition 2-3. When the laser wavelength is equal to the effective excitation wavelength $\lambda_{ex}$ a relatively high number of ions are pumped from the initial state 1 to the excited state 2 and subsequently decay to the third state, giving a peak in the emitted fluorescence. The fluorescence wavelength $\lambda_{23}$ is Doppler shifted as well, however this effect is compensated since the light is integrated over the whole bandwidth of the filter. We obtain the profile of the integrated fluorescence signal as a function of the laser wavelength. As previously stated, the peak of the fluorescence takes place when the laser is tuned on the ion absorption line shifted from the atomic value $\lambda_{12}$ because of the Doppler effect; therefore the velocity of the ions can be calculated from equation 2.32. In real conditions, a distribution of ion velocities exists in the plasma and the fluorescence profile will properly represent this distribution.

It is worth mentioning that the laser plays the role of fine wavelength discriminator, not the collection system. The resolution on the measured velocity depends on the laser linewidth and tuning resolution. The collection system has a broad wavelength bandpass (given by the filter) compared to the Doppler wavelength shift. The employment of different atomic transitions, i.e. 1-2 for the excitation and 2-3 for the fluorescence collection, in combination with the bandpass filter allows to drastically reduce the scattered light coming from the laser, indeed the laser wavelength (from $\lambda_{12}$-$\Delta\lambda/2$ to $\lambda_{12} + \Delta\lambda/2$) is outside the permitted wavelength range by the filter centered around $\lambda_{23}$. An important issue is to isolate the induced fluorescence signal from the background noise due to the photons emit-

ted by the plasma with wavelengths inside the bandpass of the filter. A chopper is used in order to modulate the laser at a given frequency; as a consequence the fluorescence induced by the laser excitation is modulated at the same frequency; then only the component at the chopping frequency is extract from the overall signal coming from the photomultiplier tube.

The LIF diagnostic is reliable and by nature nonintrusive, avoiding perturbation of the surrounding plasma that can occur with probe-based techniques. Since the ionic transitions are narrow, LIF can nominally measure velocities at 100 m/s resolution. The measurement volume is defined by the intersection of the laser beam and collection optical path, allowing for fine spatial resolution. These advantages make LIF uniquely suited for characterizing the ejected plasma from a thruster or obtaining the local ion velocity distribution function in a plasma discharge. The most common implementation of LIF is time-averaged: the fluorescence photons are collected and integrated over a given time interval. However, time-synchronized measurements have also been conducted, locking the measurement into a specific phase of a periodic phenomena (e.g. the oscillating current mode observed in the DCFT) [65, 66]. The measurements presented in this thesis are time-averaged.

### LIF Equipment

This LIF system has been setup for measurements in plasma sources operating with xenon. Both xenon neutrals and ions can be probed according to the schemes reported in Fig. 2.13.

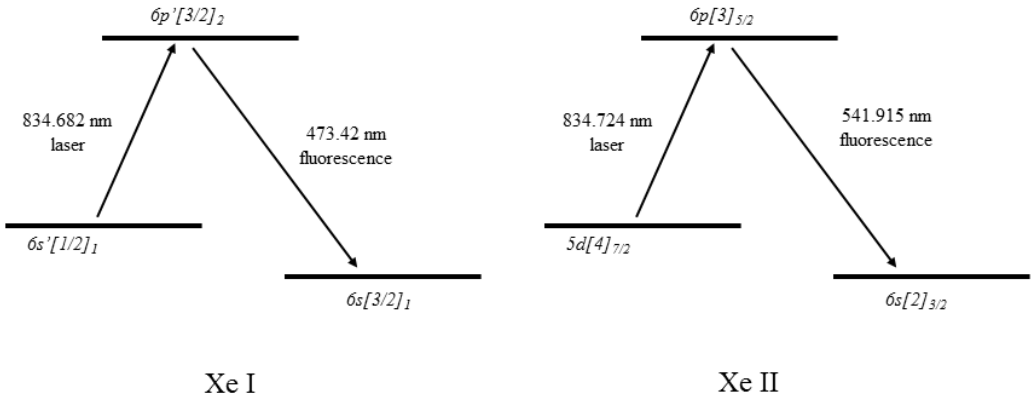


Figure 2.13: LIF schemes for XeI and Xe II (air wavelengths).

**Diode Laser** The laser used to excite the xenon neutrals (in case of XeI LIF) or xenon ions (in case of XeII LIF) is the Vortex-New Focus 6017 external cavity diode laser. The laser nominal wavelength is 834.7 nm (air wavelength) and the maximum output power

is 20 mW. The most important characteristic of the laser is the wavelength tuning range without mode hops, which must be wider than the Doppler shift due to the expected particle velocity. The employed laser presents a fine tuning range without mode hops of 50 GHz, i.e. about 0.12 nm at 834.7 nm, and a linewidth narrower than 300 kHz. The velocity corresponding to a Doppler shift of $\sim$25 GHz is about 20000 m/s at 834.72 nm, which represents the highest measurable velocity. The wavelength tuning is performed through a built-in diffraction grating and a rotating mirror moved by a piezoelectric actuator. The latter is piloted through an externally supplied voltage with a maximum modulation frequency of 3.5 kHz. Typically, the voltage for the wavelength sweep is a triangular signal provided by a function generator, adjusting the amplitude in order to obtain the wanted wavelength range. The selection of the scanning frequency is a trade-off choice influenced by several factors. The scanning velocity (in terms of nm/s) must be slow in comparison with the collection system time response, characterized by the lock-in amplifier time constant, otherwise spurious frequency shifts can be calculated due to the time delay between the laser actual frequency and the lock-in amplifier output signal. In the case of low density ion population a long time constant and thus a low scanning rate are required. On the other hand, a slow scanning velocity implies a longer time to take the measurement and the behavior of the plasma source can change during the measurement interval. The wavelength is also affected by the current flowing through the diode with a maximum rate of 150 MHz/mA, however this contribution is negligible when the laser operates in constant current mode.

In thruster experiments the exciting laser beam is amplified by a New Focus TA-7600 semiconductor tapered amplifier, seeded by the diode laser through a polarization-maintaining optical fiber. The maximum amplifier output power is 1 W; however, we limit the power to the 40 - 90 mW range to avoid saturating the transition.

**Wavelength Scale Reconstruction** The actual wavelength of the laser during the scanning is obtained through the combined use of a xenon reference lamp and a Fabry-Perot interferometer. The xenon lamp provides a stationary reference; the reference transition can be the same than the probed one or a different one. In our case the reference lamp is a Heraeus xenon hollow cathode lamp powered by an high voltage power supply at 250 V - 4 mA. Two different types of reference can be used:

- Absorption reference. A sample of the laser beam passes through the lamp and it is detected by a photodiode; when the laser wavelength is tuned at the XeI line 834.68 nm a strong absorption takes place and the laser light detected by the photodiode results strongly attenuated. This dip in the signal represents the reference for the wavelength scale reconstruction.

- Optogalvanic reference. A sample of the laser beam is chopped at a frequency $f_r$ and passes through the xenon lamp. Here, neutrals excited by the laser are more likely to become ionized and create free electrons in electron impact ionization events; the resulting extra electrons produce more free electrons in an avalanche ionization process which causes a temporary spike in discharge current in the lamp. The resulting perturbations of the lamp current, occurring at the chopping frequency $f_r$, are detected through a 10 k$\Omega$ shunt resistor and a 700 nF capacitor to block the DC signal component. A lock-in amplifier then isolates the AC component at the chopping frequency $f_r$.

The Fabry-Perot interferometer consists of two semi-reflecting surfaces separated by a fixed distance so that many waves of light, derived from the same incident wave, can interfere in the cavity. The transmission spectrum is characterized by a sequence of peaks, equispaced in terms of frequency. The distance between two peaks is called free spectral range FSR. The finesse is the ratio between the FSR and the peak width, expressed as full width at half maximum. In the experimental setup here presented, a Thorlabs SA200-8B Fabry-Perot interferometer is employed, characterized by a FSR equal to 1.5 GHz (corresponding to 0.0035 nm at 834.7 nm), a finesse of 200 and a working wavelength range 820 - 1275 nm. During the scan of the laser wavelength, the output signal of the Fabry-Perot is a sequence of peaks, which occur every 0.0035 nm of wavelength change.

An example of the signals during the wavelength sweep is illustrated on figure 2.14. The time $t_0$ which corresponds to the known reference is individuated, and then the actual laser wavelength is calculated at each time instant through the count of the number of peaks of the Fabry-Perot interferometer signal. The wavelength scale is reconstructed with an accuracy of 0.001 nm. The associated velocity calculated from the Doppler shift formula is 360 m/s.

**Fluorescence Collection System** The fluorescence is collected through a proper system of lenses and mirrors, which focus the light on the aperture of a photomultiplier tube (PMT). A bandpass filter is installed in front of the PMT aperture in order to detect only the light coming from the induced fluorescence transition. The filter used for XeI LIF has a bandwidth of 10 nm centered on 473 nm. In the case of XeII LIF, the central wavelength of the filter is 540 nm and the bandwidth 10 nm. A 3 mm iris rejects background emission from the plasma outside of the target measurement volume to increase the signal to noise ratio. A shortpass filter with a 750 nm cutoff is used to reject any scattered laser light at 834-835 nm. The weak fluorescence light is detected by means of a PMT.

PMTs are vacuum tubes used as light detectors in the ultraviolet, visible and near infrared wavelength ranges. These devices provide high sensitivity and ultra-fast response.

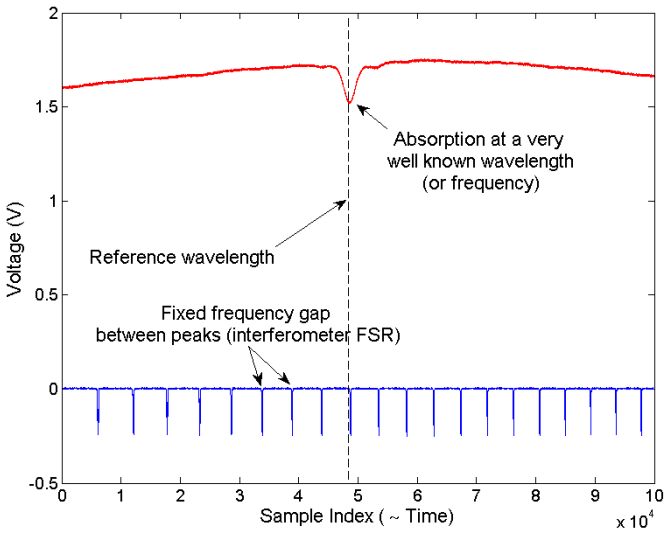


Figure 2.14: Absorption reference dip and Fabry-Perot interferometer signal used for the reconstruction of the wavelength of the laser during the sweep.

The basic structure consists in three stages:

- *A photocathode.* The photocathode exploits the photoelectric effect in order to emit electrons when the light photons strike its surface.
- *An electron multiplier.* The electron multiplier consists in several dynodes that allow a progressive multiplication of the electrons coming from the photocathode, exploiting the secondary electron emission.
- *An anode.* The anode collects the electrons coming from the last dynode.

The overall scheme of such a device is illustrated on figure 2.15.

The cathode and the dynodes are housed inside a vacuum glass tube. The incoming photons pass through the input window and strike the photocathode with a consequent emission of electrons. The emitted electrons are then driven by an electrode and focused on the first dynode. Thanks to the secondary electrons emission effect, the incident electrons are multiplied and driven to another dynode. A PMT contains several dynodes in order to obtain a multiplication in cascade. Each dynode is held at a positive potential in comparison with the previous one in order to force the electron flow and to accelerate the electrons. The purpose is to obtain impacts with enough energy to produce an effective secondary electron emission. Finally, the electrons are collected by the anode, giving the output current signal. The output signal due to a photon is a sharp current pulse, produced by the emission from the photocathode, the electron multiplication through the dynodes and the

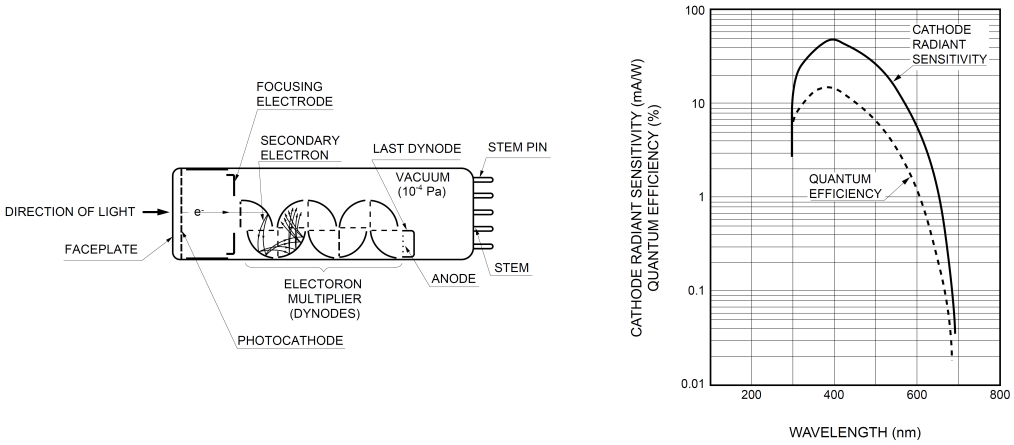


Figure 2.15: Overall structure of a photomultiplier tube and typical quantum efficiency and cathode sensitivity for a Hamamatsu 1P21 PMT.

charge accumulation at the anode. In the experimental setup a Hamamatsu 1P21 PMT is used with optimal operative range 350 - 500nm, maximum quantum efficiency (figure 2.15) of 13% at 350 nm and cathode radiant sensitivity of 48 mA/W at 400 nm. The time response mainly depends on the travel time of the progressively multiplied electron current across the various dynodes of the system. The electron transit time in the Hamamatsu 1P21 PMT is 22 ns.

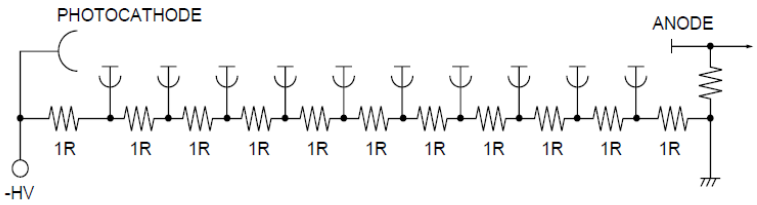


Figure 2.16: Dynodes electrical scheme.

The electron flow is driven by the voltage difference between consecutive dynodes, progressively increasing from the photocathode to the anode. The required voltage is supplied by an external power supply and is properly distributed to the dynodes by means of a voltage divider, consisting of a sequence of series-connected resistors, with the negative pole at the photocathode. The output current from the anode is linear with the divider current for low incident light fluxes. When the incident light increases a deviation from linearity occurs and the output anode current saturates to a value close to the divider current, since the externally supplied current just compensates the electrons emitted for secondary emission from the dynodes. In order to operate in the linear region a practical

rule suggests to maintain the divider current $i_s$ (acting on the divider voltage) at least 10-20 times higher than the output current flowing from the anode $i_a$. In our case the external power supplied voltage is 800 - 1000 V giving a current of $i_s$= 0.37 - 0.46 mA flowing through the divider. We have verified the condition $i_a \ll i_s$ is satisfied. The current is converted in a voltage signal by means a 1.5 kΩ load and is subsequently plotted on a scope or becomes the input of the lock-in amplifier.

**Noise rejection** A key task is the identification of the weak fluorescence signal induced by the laser in the overall light collected by the PMT. The induced fluorescence can be thousands of times smaller than the background noise due to the photons spontaneously emitted by the plasma in the allowed wavelength range of the filter. A Stanford Research SR850 lock-in amplifier is used to address this issue, exploiting a phase-sensitive detection. This technique is based on the modulation of the target phenomenon (in our case the induced fluorescence) at a known frequency $f_c$, and the extraction of the component at that specific frequency $f_c$ from the collected signal. This modulation is obtained through the mechanical chopping of the exciting laser. The overall collected signal is made of several harmonics:

$$V_t = \sum_j V_j \sin(\omega_j t + \phi_j) \tag{2.33}$$

where $\omega_j$=$2\pi f_j$. Among all the j-components the target one is $V_c \sin(\omega_c t)$. In the lock-in amplifier the collected signal is amplified and then multiplied by a reference sinusoidal signal at the modulation frequency $V_r \sin(2\pi f_c t + \phi_c)$, obtaining:

$$V_o = \sum_j \frac{1}{2} V_j V_r \cos\left[(\omega_j - \omega_c)t + \phi_j - \phi_c\right] + \frac{1}{2} V_j V_r \cos\left[(\omega_j + \omega_c)t + \phi_j + \phi_c\right] \tag{2.34}$$

The multiplication, carried out by a phase sensitive detector (PSD), gives a signal made of various components at frequencies $(\omega_j - \omega_c)$ and $(\omega_j + \omega_c)$. If $\omega_j = \omega_c$ the difference frequency component is a DC signal proportional to the amplitude of the component at the modulation frequency $f_c$:

$$V_{of} = \frac{1}{2} V_c V_r \cos\left(\phi_j - \phi_c\right) \tag{2.35}$$

The use of a low pass filter after the multiplication cuts the components with $(\omega_j - \omega_c) \gg 0$ and $(\omega_j + \omega_c)$. In other words, the filter allows the selection of the components of the collected signal with frequencies close to $f_c$ and cuts all the remaining noise spectrum. The noise components close to $f_c$ give low frequency AC components whose rejection depends on the filter attenuation and bandwidth. The reference signal is provided by an internal oscillator locked to an external signal by means of a phase-locked-loop. The external signal is provided by the chopper electronics. In order to eliminate the phase dependency in the

output signal (eq. 2.35), a second PSD is introduced, which multiplies the overall signal with the reference signal shifted of $90^o$:

$$V_{of90^o} = \frac{1}{2} V_c V_r \sin(\phi_j - \phi_c) \tag{2.36}$$

Finally combining the two quadrature outputs:

$$V_o = \sqrt{V_{of}^2 + V_{of90^o}^2} = \frac{1}{2} V_c V_r \tag{2.37}$$

Therefore the final output represents the amplitude of the component of the collected signal at the modulation frequency. The ratio between the largest noise signal to the full scale target signal is called dynamic reserve, expressed in dB. The SR850 lock-in amplifier presents a dynamics reserve of 100 dB and a full scale variable sensitivity from 2 nV to 1 V. The laser beam is mechanically modulated by means of a chopper at a frequency $f_c$ in the range 0.8 - 2 kHz.

The processing time of the lock-in amplifier takes about 5 times the time constant of the inner low-pass filter. This can produce a significant delay between the processed LIF signal and the reference absorption signal which has to be compensated in the post-processing of the data. Differently, the optogalvanic reference requires the use of another lock-in amplifier, thus this issue can be solved by setting the same time constant in both the lock-in amplifiers.

### Preliminary System Testing on a 60 Hz Xenon Tube

Preliminary experiments have been performed on a 60 Hz xenon plasma discharge, in order to individuate the proper settings of the diagnostic system and to estimate the accuracy of the wavelength scale reconstruction. The plasma source consists of a glass tube with a central 10 cm long capillary region (Fig. 2.19) filled by xenon. The ends of the tube are sealed by the electrodes powered through a 60Hz oscillating high voltage. Each electrode acts alternatively as an anode and as a cathode during each cycle.

LIF has been applied both to neutral excited xenon (XeI) and xenon ions (XeII). The neutral xenon is laser-pumped from the $6s'[1/2]_1^0$ state up to the $6p'[3/2]_2$ state. The wavelength associated to this transition is 834.6822 nm - air wavelength (834.9116 nm - vacuum wavelength). In the the spontaneous decay from the $6p'[3/2]_2$ state down to the $6s[3/2]_1^0$ state, photons at 473.42 nm are emitted (fluorescence). In the case of XeII, the laser pumping takes place at 834.724 nm - air wavelength (834.953 nm - vacuum wavelength), corresponding to the transition from the $5d[4]_{7/2}$ state up to the $6p[3]_{5/2}$ state, and the fluorescence emission at 541.92 nm (from $6p[3]_{5/2}$ down to $6s[2]_{3/2}$ states).

The experimental setup is represented in figure 2.17 and a picture is shown in figure 2.18. The beam emitted by the Vortex-New Focus 6017 laser (lb1) passes through two beam

samplers (BS1 and BS2) and is steered to the target 60Hz Xe tube through a sequence of mirrors. A laser beam sample (lb2, 10% of the main beam) is splitted into two minor beams (lb2a and lb2b) by means of a 50-50% beam splitter (BS3). Beam lb2a is directed to a Burleigh WA-1500 wavemeter for a rough wavelength measurement while tuning the laser parameters; we do not use the wavemeter for an exact determination of the laser wavelength during the scan as it is prone to inaccuracies and drift. The second minor beam (lb2b) passes through the xenon hollow cathode lamp and is detected by a photodiode to provide an absorption reference line. Another beam sample (lb3) is steered to a Fabry-Perot interferometer. The combined use of the xenon hollow cathode lamp for the reference line and the Fabry-Perot interferometer allows a fine reconstruction of the wavelength scale (see paragraph *Wavelength scale reconstruction* for the details). We use the xenon neutral transition at 834.9116 nm as the reference. The main beam is modulated through a mechanical chopper and focused on the target plasma. An optical system collects the fluorescence photons and focuses them on the aperture of a photomultiplier tube (PMT) employed for the detection. In front of the PMT a bandpass filter allows the exclusive detection of photons coming from the fluorescence transition. Moreover an iris diaphragm improves the rejection of the laser scattered light and reduces the sampling volume of the collection system. The signal is finally processed by a lock-in amplifier which extracts the component at the chopping frequency.

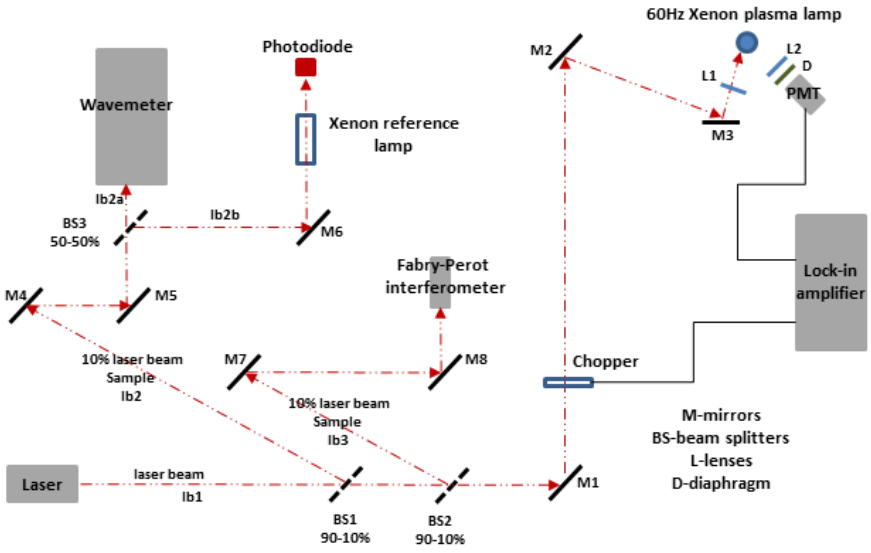


Figure 2.17: Scheme of Laser Induced Fluorescence experimental setup.

We have carried out LIF measurements both on xenon neutrals and xenon ions. The laser beam power is 10 mW. The main beam is chopped at a frequency of 1.5 kHz, giving

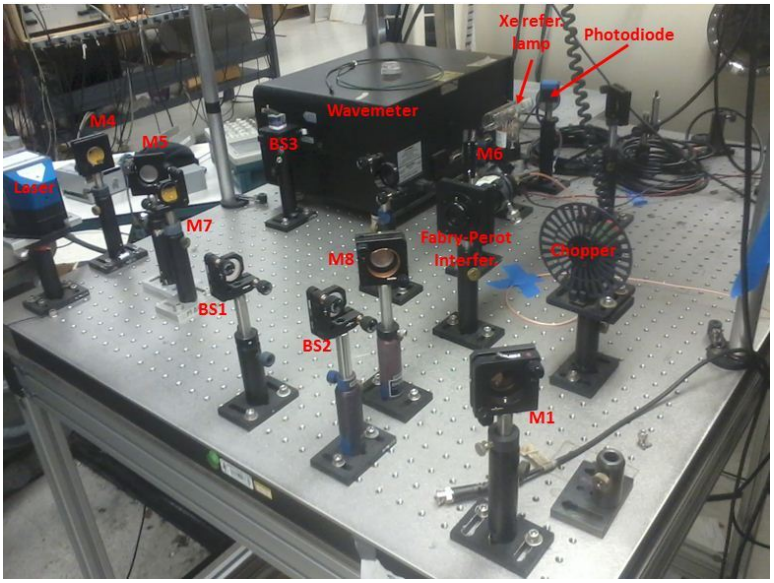


Figure 2.18: Laser Induced Fluorescence experimental setup.

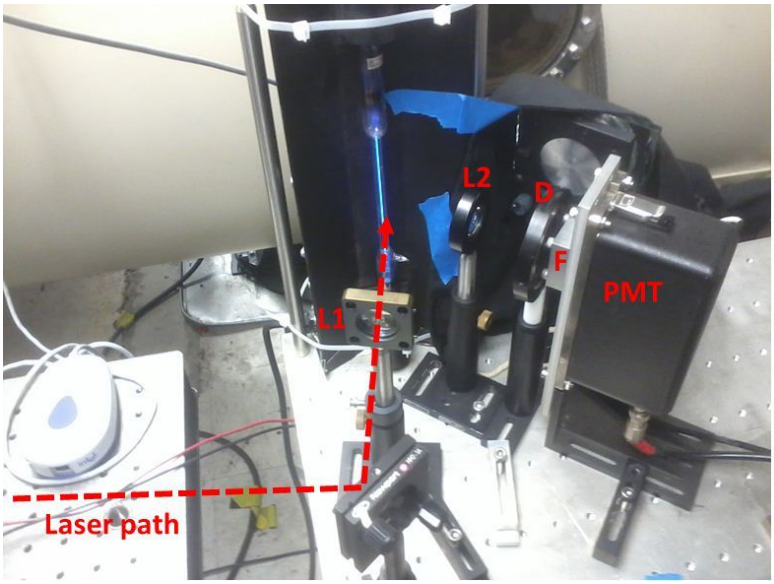


Figure 2.19: Xe 60 Hz tube with the focusing and collection optics: L1 focusing lens, L2 collection lens, D iris diaphragm, F bandpass filter housing and photomultiplier tube (PMT).

an amplitude modulation of the LIF signal at the same frequency. Figures 2.20a and 2.20b report the frequency spectrum of the PMT output signal without and with the laser excitation of the 834.68 nm neutral transition, respectively; the spectrum is calculated through a Fast Fourier Transform (FFT) of the rough PMT signal. The 60 Hz harmonics of the xenon tube are apparent in both the plots. Figure 2.20b highlights the collection of the laser induced fluorescence photons at the chopping frequency 1.5 kHz. This frequency component is afterwards isolated by the lock-in amplifier, setting a sensitivity of 20 mV and a 300 ms time constant of the low-pass filter. The signal processing in the lock-in introduces a delay of the LIF signal relative to the reference absorption signal of about 5 time constants of the low-pass filter. This delay is compensated in post-processing.

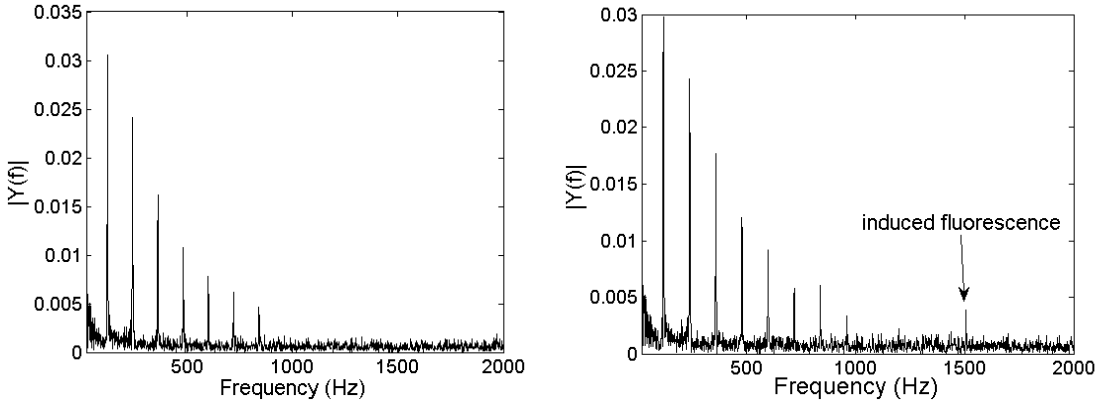


Figure 2.20: a) FFT of the PMT output signal without laser-induced-fluorescence photons. b) FFT of the PMT signal with the collection of laser-induced-fluorescence photons at the chopping frequency 1.5 kHz.

Figure 2.21a illustrates the rough signals acquired in the Xe I LIF measurement. Particularly, the reference absorption, the Fabry-Perot and the LIF signals are shown. As expected, the fluorescence peak and the absorption dip coincide since we are pumping the same transition both in the hollow cathode lamp and in the Xe 60 Hz tube. We can assume stationary xenon neutrals in both the plasmas. Figure 2.21b shows the LIF signal in function of the detuning frequency. The origin of the frequency scale coincides with the absorption dip and the detuning frequency has been calculated through the counting of the Fabry-Perot peaks, located 1.5 GHz apart. The resulting LIF peak is located at 0.12 GHz ($\sim$ 0.0003 nm) relative to the absorption dip, which can be consider the error introduced by the measurement system and post-processing method.

A similar measurement has been performed also on the XeII population in the xenon tube. The lock-in amplifier sensitivity and time constant are 100 $\mu$V and 3 s respectively.

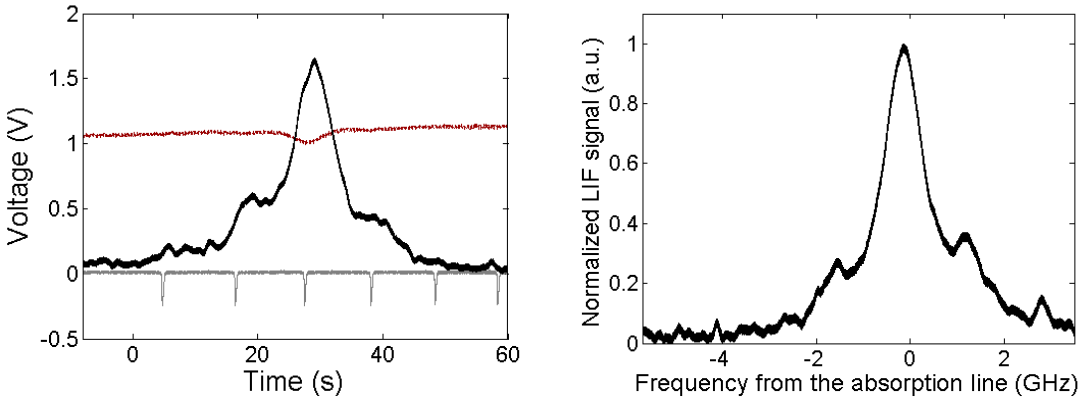


(a) (b)

Figure 2.21: a) Signals acquired during the XeI LIF measurement on the xenon 60 Hz tube: absorption reference (red dotted line), Fabry-Perot (grey line) and LIF (black line) signals. b) LIF signal in function of the detuning frequency. The origin of the frequency scale is located at the absorption dip.

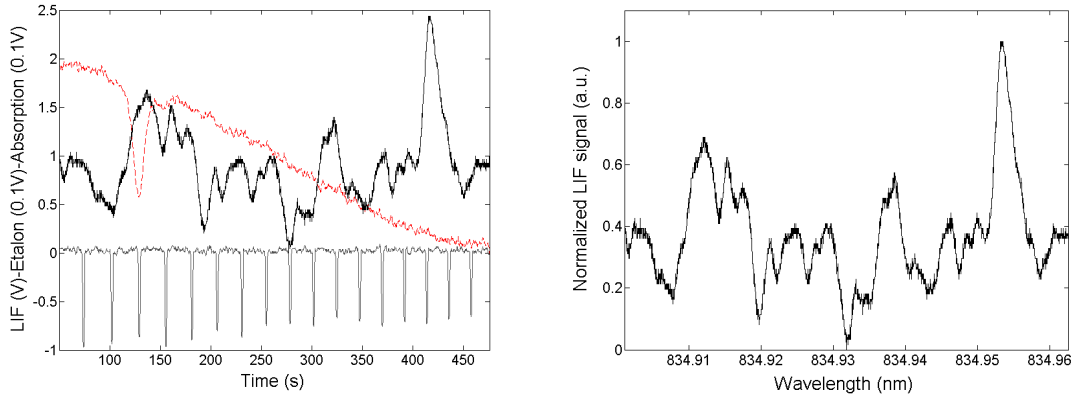


(a) (b)

Figure 2.22: a) Signals acquired during the XeII LIF measurement on the xenon 60 Hz tube: absorption reference (red dotted line), Fabry-Perot (grey line) and LIF (black line) signals. b) XeII LIF signal in function of the wavelength (vacuum wavelength).

Figure 2.22a shows the absorption profile, the Fabry-Perot peaks and the LIF intensity. In this case the absorption dip and the LIF maximum are wavelength shifted, since the former takes place at the XeI transition whereas the latter occurs at the XeII transition. Considering stationary ions, we expect a fluorescence peak at 834.953 nm (vacuum wavelength), i.e. at the Doppler-free atomic transition. The assumption of ion stationarity is

appropriate in this case since the laser penetrates the tube in the radial direction and the 60 Hz oscillating electric field creates mainly an axial motion. Moreover we are performing a time-averaged measurement, as a consequence a possible oscillating velocity along the laser direction gives a null mean Doppler shift. The reconstructed LIF profile in function of the wavelength (Fig. 2.22b) presents the maximum intensity for a wavelength of 834.9524 nm (vacuum wavelength) which is $\sim 0.0006$ nm apart from the theoretical value.

The uncertainty on the measured ion velocity in a thruster is influenced mainly by the uncertainty on the wavelength. The analysis above, demonstrates the high reliability of the implemented wavelength reconstruction method with an uncertainty below 0.001 nm giving a consequent uncertainty on the velocity below 360 m/s.

### 2.1.6 Novel Optogalvanic Technique for Ion Velocimetry

The optogalvanic (OG) effect consists in a change of the electrical characteristics of a plasma source induced by a radiation having a wavelength corresponding at an atomic or molecular transition of the gas species in the discharge. This method has been applied extensively to spectroscopic studies of neutral or ionized species [67, 68, 69, 70]. In this section we propose the exploitation of the optogalvanic effect to measure the velocity of ions emitted from a DC plasma thruster. The potential advantages of this novel diagnostic method are remarkable: it is local and non-intrusive and does not require an optical collection system as in the case of Laser-Induced-Fluorescence technique. A laser beam is split into two beams of equal intensity. Thanks to a proper setup of mirrors, the optical paths of the two beams intersect in the measurement volume in the thruster plume with the same angle relative to the target velocity component. Before the intersection the two beams are mechanically chopped at two different frequencies $f_1$ and $f_2$. Small perturbations of the thruster current are induced by the laser beams at the frequencies $f_1+f_2$ and $f_1-f_2$ as well as at $f_1$, $f_2$. The perturbations modulated at combined frequencies $f_1+f_2$ and $f_1-f_2$ are due to the non-linear interaction of the two beams with the same group of ions. The perturbation at $f_1$ originates from the plasma illuminated by the first beam, the perturbation at $f_2$ originates from the plasma illuminated by the second beam, and the perturbation modulated at a combined frequency originates at the intersection volume of the two beams giving a local measurement.

A lock-in amplifier is used to pick the $f_1+f_2$ component out. The wavelength of the laser is scanned around a transition of the ions and the OG signal is monitored during the scan. If the ions are moving in the laser direction, the wavelength in the ion frame is Doppler shifted depending on their velocity; as a consequence, the collected OG signal is representative of the ion velocity distribution function. The directions of the two laser beams have to be at the same angle $\theta$ relative to target ion velocity direction thus the laser

beams excite simultaneously the same velocity class of ions.

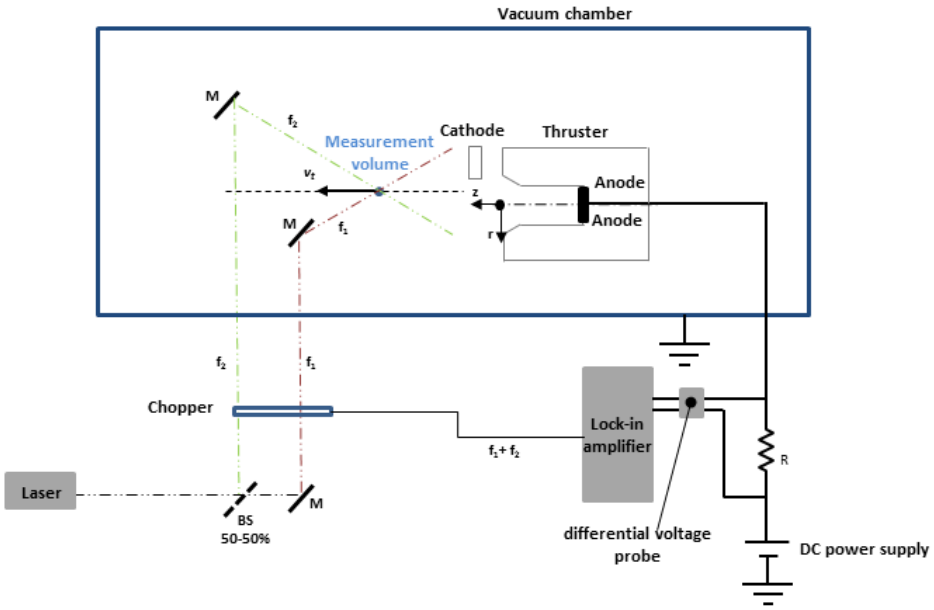


Figure 2.23: Basic scheme of optogalvanic ion velocimetry.

Preliminary optogalvanic measurements have been performed on a xenon DC hollow cathode lamp, operating at 240 V - 3.8 mA. The 834.682 nm XeI transition and the 834.724 nm XeII transition are excited by means of the Vortex-New Focus 6017 diode laser operating at 20 mW. The laser beam is mechanically chopped at a frequency $f_c$ = 1.3 kHz before passing through the lamp. The optogalvanic perturbation of the discharge current is monitored using a 10 kΩ shunt resistor and a 700 nF capacitor to filter out the DC component. Finally, a lock-in amplifier extracts the component at the chopping frequency $f_c$: a full-scale sensitivity of 10 $\mu$V and a time constant of 1 s have been set for the XeI optogalvanic detection, whereas the respective values for the XeII are 50 nV and 3 s. The amplitude of the detuning frequency is given by the interference peaks of the Fabry-Perot interferometer. Figures 2.24a and 2.24b illustrate the XeI and XeII spectral lines profiles measured through the optogalvanic method.

A second measurement of the XeI 834.682 nm spectral line has been carried out applying an intermodulated optogalvanic method. The main laser beam is split into two minor beams through a 50-50% beam splitter. One minor beam is chopped at $f_1$ = 1 kHz and enter the discharge from one direction while the other beam is chopped at $f_2$ = 1.3 kHz and sent through the discharge in the opposite direction. The lock-in amplifier detection takes place at the sum of the chopping frequencies $f_1 + f_2$ = 2.3 kHz. This technique

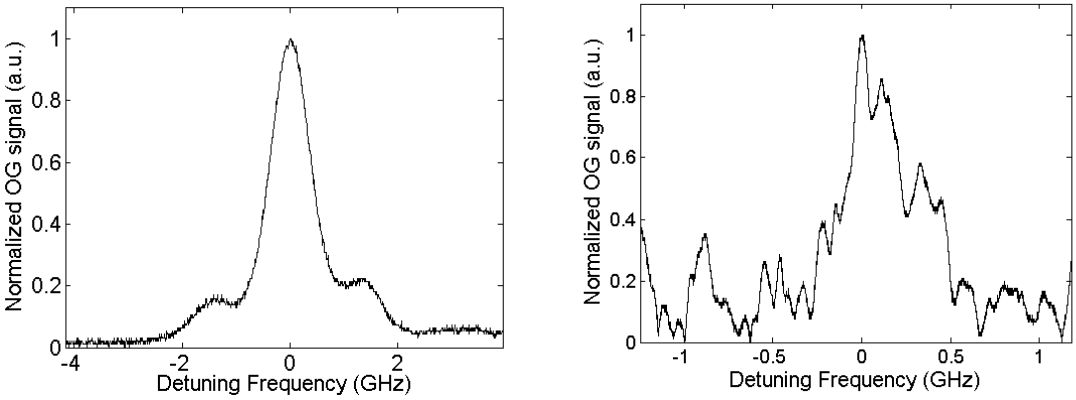


(a) (b)

Figure 2.24: Profiles of: a) XeI 835.682 nm spectral line, b) XeII 835.724 nm spectral line obtained through the optogalvanic method.

allows a Doppler-free characterization of the spectral line, i.e. the Doppler broadening is compensated. Since the two beams propagate in opposite directions they excite different groups of atoms, characterized by opposite velocities under the Doppler-broadened profile of the transition. Only when the laser wavelength coincides with the line center the two beams interact with the same group of atoms giving a combined effect at $f_1 + f_2$. The compensation of the Doppler broadening can be observed comparing the Xe I spectral line obtained through the standard optogalvanic method (Fig. 2.24a) and the intermodulated technique (Fig. 2.25b). In the former measurement the broadness (evaluate as full width at half maximum) of the spectral line is 0.92 GHz, in the latter is 0.56 GHz.

We have attempted to apply the optogalvanic method to measure the velocity of ions ejected from the Stanford Cusped Field Thruster. Unfortunately we have not remarked any reliable optogalvanic signal; the experimental details, possible motivations and proposed improvements will be discussed in section 4.3.

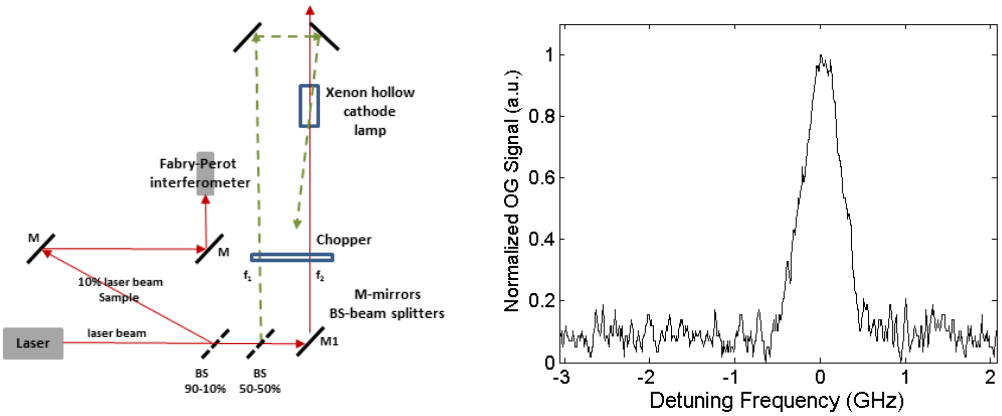


(a) (b)

Figure 2.25: a) Schematic of the optical setup used for the intermodulated optogalvanic measurements. b) Doppler-free profile of the XeI 835.682 nm spectral line.

## 2.2 Particle Codes for Plasma Simulation

In parallel with the experimental activity, simulation codes have been used for a in-depth investigation of the characteristic physical phenomena. The simulations results combined with the experimental measurements allow for a more complete physical picture of the thrusters behavior. The codes are particle-in-cell (PIC) type. The PIC method [71] is a common approach for simulating a broad range of plasma phenomena, including plasma propulsion systems [72, 73, 74]. These codes can treat both ions and electrons as particles or can be based on a hybrid method in which ions are treated kinetically in a surrounding electron fluid, removing the need to resolve the system at the much faster time scale of electron motion. In the simulations presented in this thesis both ions and electrons are treated as particles. The used codes are:

- **1D PIC code** is a one-dimensional plasma PIC code with a finite-difference electrostatic solver for the Poisson equation solution. It has been developed by the author with the help of a MSc student during his final thesis [75].
- **F3MPIC** is a three-dimensional plasma PIC code, built on an unstructured mesh of tetrahedra, coupled with a FEM electrostatic and electromagnetic solver. It has been developed by CISAS plasma propulsion group (in particular M. Manente, D. Rondini and D. Curreli) during EU FP7 HPH.com project.

### 2.2.1 1D Particle-In-Cell Code

The code is based on a 1D electrostatic particle-in-cell model for the simulation of plasmas. Similar codes have been developed in the past even if with slightly different approaches [76, 77]. For instance, a 1D PIC electrostatic hybrid model with particle ions and Boltzmann fluid electrons is described in Ref. [77]. The effect of a divergent magnetic field is taken into account through a magnetic mirror term. Differently, the code presented in Ref. [76] treats both ions and electrons as particles and models the plasma expansion in a divergent magnetic field introducing a particle loss process along the axis of the simulation.

In our 1D PIC code the plasma behavior is described using a particle approach both for ions and electrons. Following the classical PIC approach, physical particles are aggregated in computational macroparticles in order to reduce the computational effort. A macroparticle is treated as a single particle but owns the extensive properties of the group of particles it represents, i.e. mass and charge for the peculiar case. Macroparticles move in a continuum space, in this case one-dimensional, forced by the electric and magnetic fields. The fields are instead calculated in the nodes of a discrete grid. The cell dimension is a parameter correlated to the specific simulated plasma. The macroparticles motion obeys to

the Newton-Lorentz equations and the force acting on them is computed by interpolating the fields between the closest grid points. The effect of magnetic gradients on particles motion is included through the force term $-\mu\nabla B$ along the considered dimension, where $\mu$ is the magnetic moment defined as:

$$\mu = \frac{mv_{\perp}^2}{2B} \tag{2.38}$$

In the last equation $v_{\perp}$ is the velocity component perpendicular to the field lines, $m$ is the particle mass, and $B$ the magnetic field magnitude. The introduction of the magnetic moment and the assumption of its conservation allows to take into account the shape of the magnetic field, in particular the axial variation of its intensity. With these assumptions the ion and electron equations of motion become:

$$m_e\frac{dv_{ze}}{dt} = -e\frac{d\phi}{dz} - \mu_e\frac{dB}{dz} \tag{2.39}$$

$$m_i\frac{dv_{zi}}{dt} = e\frac{d\phi}{dz} - \mu_i\frac{dB}{dz} \tag{2.40}$$

The equations of motion are integrated through a leapfrog algorithm, where the location of the particle is evaluated at whole time steps, whereas the velocity is offset by half a time step:

$$v_z^{(n+1/2)} = v_z^{(n-1/2)} + \frac{F(z^{(n)})}{m}\Delta t \tag{2.41}$$

$$z^{(n+1)} = z^{(n)} + v_z^{(n+1/2)}\Delta t \tag{2.42}$$

The electric field is expressed as the gradient of the potential $E_z$ = - $d\phi/dz$, while the potential is related to the charge density by the Poisson equation.

$$\frac{d^2\phi}{dz^2} = -\frac{\rho}{\epsilon_0} \tag{2.43}$$

The Poisson equation is solved at the nodes of the grid using a central finite difference method:

$$\frac{\phi_{j-1} - 2\phi_j + \phi_{j+1}}{dz^2} = -\frac{\rho_j}{\epsilon_0} \tag{2.44}$$

The boundary conditions at the edges of the simulation domain are Dirichlet type. The electric field is calculated from the potential applying a five point stencil method:

$$E_j = -\frac{-\phi_{j+2} + 8\phi_{j+1} - 8\phi_{j-1} + \phi_{j-2}}{12\Delta x} \tag{2.45}$$

The force is interpolated linearly to the particle location from the adjacent cell boundaries. Similarly, the charge density is calculated on the grid knowing the number of particles in the adjacent cells and weighting their contributions depending on their distance from

the grid nodes. The particles are initially loaded in a random position of the simulation domain according to a uniform spatial distribution and with a random velocity according to an overall Maxwellian population. The plasma is considered initially quasi-neutral, so ion - electron pairs are loaded in the same position. The overall computational scheme is reported in Fig. 2.26.

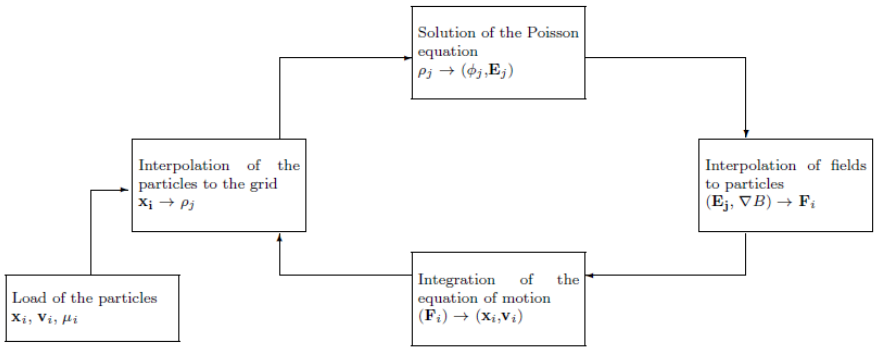


Figure 2.26: 1D PIC code basic scheme.

The code has been validated comparing the results to theoretical models. This methodology has been applied both to the subroutines of the code and to the overall code. The validation benchmark for the code has been the simulation of a standard unmagnetized sheath. In order to have a consistent comparison with the standard sheath theory [78, 79] a collisionless, fully-ionized, unmagnetized plasma has been simulated and the electron velocity distribution function has been forced to be Maxwellian with constant temperature $T_e$. The simulation domain is a 10 cm length, 1 cm radius cylinder. The simulations have been performed for different combinations of electron temperatures ($T_e$ = 1-7 eV), plasma densities (n = $10^{13}$-$10^{15}$ $m^{-3}$) and different gas species (argon and hydrogen). We simulate low-density plasmas to reduce the computational effort. The macroparticle weight is 10000, i.e. 10000 physical particles are aggregated in a numerical macroparticle. The cell dimension $\Delta$x is set to solve the Debye length in the simulated plasma ($\Delta x < \lambda_{De}$). The plasma is initially quasi-neutral. Subsequently, during the time evolution, the quasi-neutrality is locally lost and the sheath begins to form at the boundaries. Here, the difference between ion and electron densities leads to a positive net charge and an electric field arises to damp electron outward motion and to accelerate ions, until the balance of fluxes is reached. We report an example of charge density distribution in fig.2.27a.

Figure 2.28a illustrates the profile of the potential along the domain for a plasma with an electron temperature equal to 7 eV and a density of $10^{13}$ $m^{-3}$. As previously described, the formation of the sheath gives raise to a potential drop at the exit boundaries of the

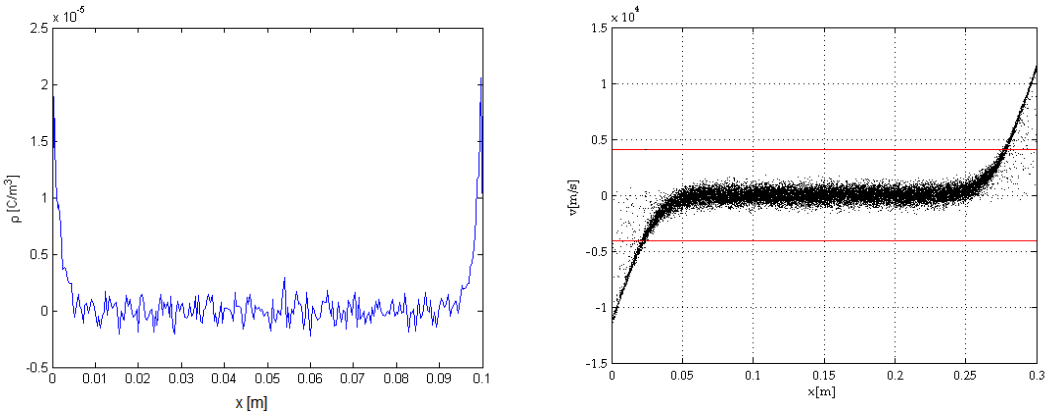


(a) (b)

Figure 2.27: a) Example of the charge density along the system. At the edges the positive charge arises due to electron losses and an electric field forms, while in the bulk plasma quasi-neutrality is preserved. b) Ions phase space for a bulk density of n = $10^{13}$ $m^{-3}$ and an electronic temperature $T_e$ = 7 eV; the red lines highlight the Bohm velocity.

system which accelerates the ions through the exit while rejecting the electrons, except the more energetic that are able to overcome the potential barrier. The sheath thickness resulting from the simulation is $\sim 5\lambda_D$. The magnitude of the potential drop from the bulk plasma to the wall obtained through the 1D PIC code simulations fully agrees with that estimated through the analytical equation given in Ref. [78]:

$$\Delta\Phi_T = \frac{T_e}{2}\left[1 + \ln\left(\frac{m_i}{2\pi m_e}\right)\right] \tag{2.46}$$

where $m_i$ is the ion mass, $m_e$ the electron mass and $T_e$ is the electron temperature in eV. In figure 2.28b the sheath potential drops obtained by the code for different electron temperature and ion species are shown, along with the values predicted by the sheath theory (blue line for argon, red line for hydrogen). Moreover the acceleration of ions (ion phase space, figure 2.27b) satisfies the Bohm sheath criterion, since their velocity overcomes the Bohm velocity.

### 2.2.2 F3MPIC Code

F3MPIC [80] was developed for the detailed design and optimization of helicon and general-purpose plasma thrusters and has been validated both numerically and experimentally under the HPH.com project. The code has been tested on High Performance Computing (HPC) facilities and can be run in serial or parallel mode, with a GPU version now under testing.

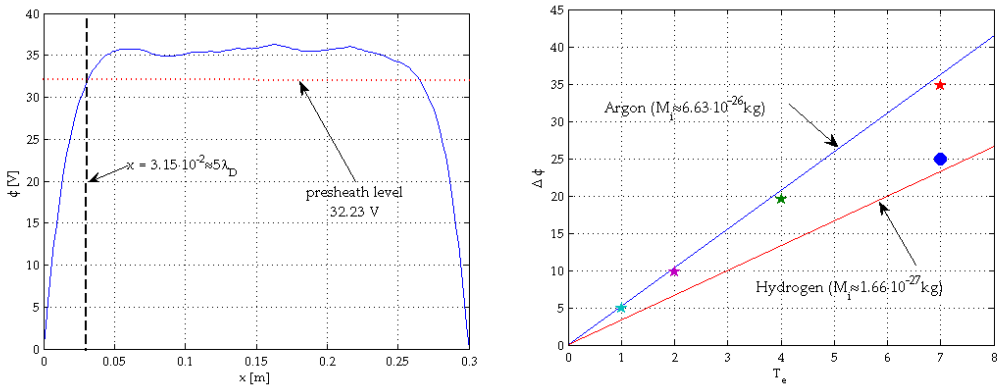


(a) (b)

Figure 2.28: a) Potential profile for a bulk density n = $10^{13}$ $m^{-3}$ and an electron temperature $T_e$ = 7 eV. b) Values of the total sheath potential drop for different electron temperatures, different gases and a density of n = $10^{13}$ $m^{-3}$. The stars and circles represent the values obtained through the 1D PIC simulations. The lines represent the values predicted by the sheath theory.

Developed originally for plasma propulsion applications, F3MPIC has also been successfully applied to other plasma systems such as ion sources for the selective production of exotic species [81].

In F3MPIC, the classical PIC algorithm is coupled with a 3D finite element electrostatic solver in time. The code is built on an unstructured mesh of tetrahedra, allowing for arbitrary geometries, and the PIC core is comprised of a Boris-Leapfrog scheme that can manage multiple species, both charged and neutral. A magnetic field with an arbitrary topology can be imposed to study magnetized particle dynamics. Particles are tracked inside the tetrahedra using a fast priority-sorting algorithm and charge density is assembled on the nodes of the mesh at each time step.

The electrostatic fields are then computed by solving Poisson's equation or the full set of Maxwell's equations including both plasma source terms (charge density and plasma currents) and external source terms (e.g. a polarized electrode). The electrostatic field can be solved in either 2D axisymmetry or full 3D via a finite element method. Non-plasma regions (e.g. vacuum, conducting elements) may also be incorporated. Plasma currents are treated in a tensor representation (the Stix tensor), and oscillating current sources like antenna and electromagnetic emitters can be readily incorporated using an external electromagnetic FEM solver.

A Monte-Carlo collision (MCC) method treats neutral-charged particle collisions based on the proper cross-sections of the chemical species involved.

Simulated surfaces may be designated conductors, dielectrics, exit ports, neutral emit-

ters, or charged particle emitters.

Spatial distributions of plasma properties, electric and magnetic fields can be recorded at user-defined time steps. Arbitrary control surfaces can record the positions and velocities of passing particles, allowing computation of distribution functions, mass flow rates, thrusts and beam divergence angles.

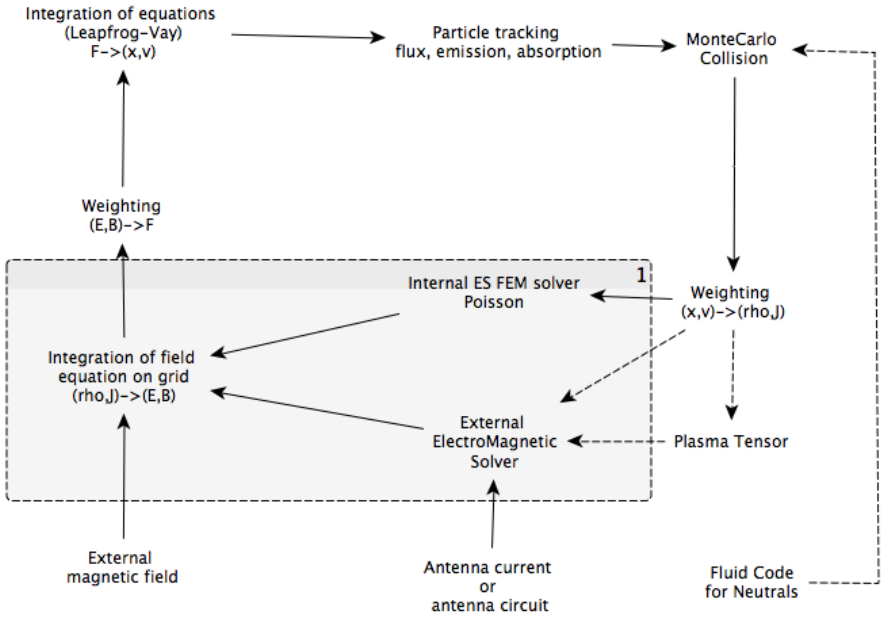


Figure 2.29: Overall schematic of the F3MPIC code.

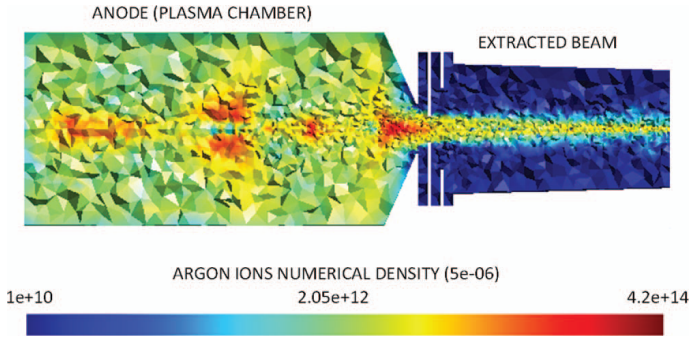


Figure 2.30: Example of application of F3MPIC to the calculation of the emittance for an electrode-ion-source used to produce exotic species [81].

CHAPTER 3

# Electrodeless Radio-Frequency Plasma Thruster Investigation

This chapter is dedicated to the description of the experiments carried out to develop the electrodeless RF plasma thruster of the project HPH.com. The design and the installation of the experiment have been essential parts of this work. The starting point has been the identification of the critical parameters affecting the thruster performance. The experiment has been designed to allow a certain variability of these parameters in the limits defined by the goals of the project.

In parallel with the experimental investigation, auxiliary PIC simulations have been performed to complete the characterization.

## 3.1 Experimental Design and Setup

### 3.1.1 Preliminary Assessment on the Thruster Performance

We aim to develop a thruster working in the range 1 – 3 mN, with a specific impulse of at least 1000 s, and an input RF power within the range 50 – 100 W.

The thrust is given by:

$$T = \dot{m}_i v_i + \dot{m}_n v_n \tag{3.1}$$

where $\dot{m}_i$ and $\dot{m}_n$ are the ejected ion and neutral mass flows, and $v_i$ and $v_n$ are the ion velocity achieved through the acceleration mechanism and the neutral velocity. Neglecting the contribution of neutrals the thrust is expressed by T$\approx \dot{m}_i v_i$. The ion mass flow can be properly represented as:

$$\dot{m}_i \approx \beta n_0 A_e c_s M_i \tag{3.2}$$

where $n_0$ is the ion density in the bulk plasma in the region just upstream the outlet section, $A_e$ is the exit orifice area, $c_s$ is the Bohm velocity $c_s = \sqrt{K_B T_e / M_i}$ for an electron temperature $T_e$ and an ion mass $M_i$. For these preliminary calculations we assume an outgoing ion flow equal to that flowing through a classical sheath, following the description provided by Chen in his study of a plasma expansion through a diverging magnetic field [82]. The consequent value of $\beta$ is $\exp(-1/2) = 0.61$.

The ion velocity can be associated to the Bohm velocity as:

$$v_i = \alpha c_s \tag{3.3}$$

As detailed in the introduction, different acceleration mechanisms can be considered, such as a magnetic nozzle, a double layer or an additional heating system. Based on experimental and theoretical studies reported in bibliography, reasonable values of the acceleration coefficient $\alpha$ are within 2–8. For instance, Chen [82] describes the ion acceleration as predictable from classical sheath theory. In this frame, the achievable energy of the ion beam is $E_b \sim 5.18 K_B T_e$ for argon; the equivalent acceleration coefficient, given by $v_i = \sqrt{2E_b/M_i}$, is $\alpha \sim 3.2$. Charles [8] has experimentally measured a supersonic ion beam ($\sim$2.1 $c_s$) downstream a helicon sustained argon plasma source. In another theoretical study, Ahedo [83] analyzes the effect of a hot electron tail on the electrostatic acceleration of a plasma through a convergent-divergent magnetic nozzle. Acceleration coefficients as high as 8 can be reached. Also, we have simulated the thruster developed during the HPH.com project through the 3D PIC code (section 3.5). The simulation gives $\alpha \approx 5.2$, consistently with the aforementioned range.

Fig. 3.1a and 3.1b report the achievable thrust levels as a function of the plasma properties ($n_0$ and $T_e$) in the RF discharge for two different outlet diameters, 5 and 10 mm respectively. The calculation considers an acceleration coefficient $\alpha = 5$ and argon as the propellant. The plasma properties needed to generate the target thrust level are inferable from the plots: a plasma density of at least $\sim 5 \times 10^{18}$ m$^{-3}$ for the 10 mm outlet diameter and $\sim 2 \times 10^{19}$ m$^{-3}$ for the 5 mm outlet diameter, and an electron temperature higher than 4 eV. Even if these estimations result from approximations, they give useful indications on the RF plasma properties we should aim for.

A final consideration concerns the mass flow ionization fraction $f = \dot{m}_i/(\dot{m}_i + \dot{m}_n)$, indeed a low ionization fraction can drastically decrease the specific impulse:

$$I_{sp} = f_i \frac{v_i}{g_0} + (1 - f_i) \frac{v_n}{g_0} \tag{3.4}$$

Since the neutral velocity is significantly lower than the ion velocity, an efficient ionization of the propellant flow is crucial to reach a specific impulse of at least 1000 s. In this study the explored range of total propellant flow is 0.1 - 0.3 mg/s.

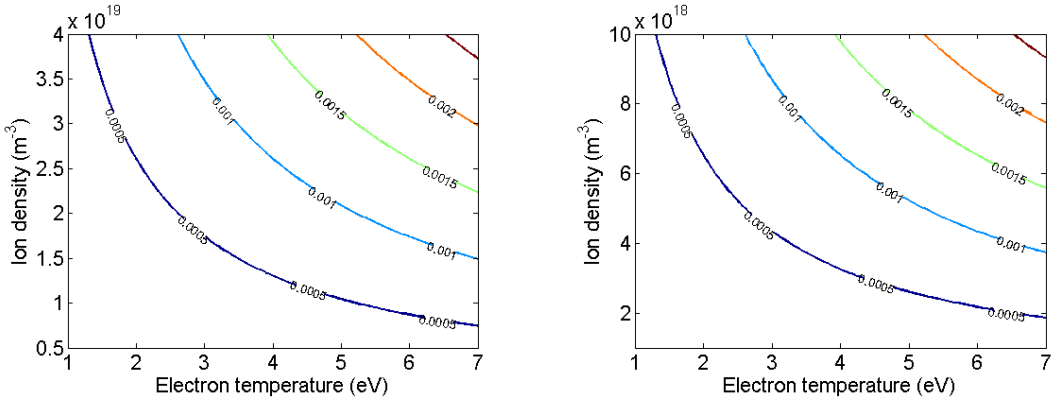


(a) Outlet diameter 5 mm

(b) Outlet diameter 10 mm

Figure 3.1: Thrust levels (in N) obtained for different plasma density and electron temperature assuming an acceleration coefficient $\alpha = 5$. The two figures refer to two different outlet diameters.

### 3.1.2 Thruster Critical Parameters

The propulsive performance of the RF plasma thruster is influenced by several parameters which are interdependent. An overview of the effect of each parameter on the source performance is reported below. A detailed analysis, accomplished coupling a wave propagation code with a source fluid model, is reported in Ref. [84] by Curreli.

**Antenna, power network and operating frequency** Each RF antenna is characterized by its own spectrum, determining the plasma wave coupling and thus the power deposition profile in the plasma. This depends also on the operating frequency.

The RF power network efficiency influences the overall performance of the propulsion system so should be taken into account in the thruster development stage. In general, higher frequencies generate higher parasitic losses. The power dissipation in the RF network has to be minimized in comparison with the power coupled into the plasma.

**Magnetic field** The magnetic field influences the wave propagation mode, both in radial and axial direction, and thus the power deposition. Moreover a higher magnetic field enhances particles confinement reducing the wall losses. Finally, if the magnetic nozzle is the main acceleration mechanism the magnetic field plays a fundamental role also in the plasma acceleration.

**Plasma source radius** The plasma source radius influences the wave propagation into the plasma, the wall losses, the volume and the mass of the thruster. In general, a higher radius implies a heavier magnetic system to produce a certain magnetic field level.

**Plasma source length** A higher source length entails a more extended surface exposed to the plasma. The volume and the mass of the thruster increase with the source length as well. The resident time of particles depends on the length of the system affecting the excitation, ionization and recombination probabilities. Finally, it affects the axial modal propagation and the power deposition.

**Ejection orifice** The ejection orifice diameter plays a fundamental role in the ejected particle flows, both charged and neutral. As a consequence, for a given mass flow rate it determines the pressure regime inside the discharge channel, influencing the power deposition and the ionization level. Finally, a smaller outlet diameter gives higher wall losses on the inner diaphragm surface exposed to the plasma.

**Mass flow rate** As reported above, the combination of mass flow rate and ejection orifice determines the pressure regime inside the discharge channel. In a thruster-like configuration, the background neutral density level is affected also by an additional pumping effect produced by ionization and consequent ejection of ions; thus the resulting neutral density is lower in comparison with the case of a simple neutral gas flow.

**Power** The power deposition into the plasma is not a linear function of the power level: there can be power thresholds, i.e. a minimum power required to trigger efficient propagation modes.

### 3.1.3 Experimental Setup

#### Vacuum Facility

The experiments have been carried out at CISAS plasma propulsion laboratory. The vacuum facility consists of a 2 m length, 0.6 m diameter vacuum chamber evacuated by a turbo-molecular pump and a diffusive one, with the relative back-pumping system. The overall pumping capacity is 12600 L/s. A gate valve is mounted at the interface between the external plasma thruster setup and the vacuum chamber in order to reduce the contamination of the chamber because of the frequent venting. This methodology allows to constantly maintain the vacuum chamber in a high or medium vacuum level, even when the plasma source is disassembled for servicing. Five Pirani gauges are employed to measure the pressure in several points along the pumping circuit and in the chamber itself, with a measuring range from $10^{-4}$ mbar to 1 bar. A Penning gauge is used to monitor the pressure in the chamber in high vacuum regime (operating range from $10^{-8}$ mbar to $10^{-4}$ mbar). In absence of a mass flow injection the background pressure level in the chamber is $5{\times}10^{-7}$ mbar, while during thruster operations its value typically varies from $3 \times 10^{-5}$ mbar to

$10^{-4}$ mbar depending on the working mass flow rate, which ranges from 0.1 mg/s to 0.4 mg/s of propellant gas. The presence of contaminants is monitored by means of a mass spectrometer capable of detecting mass to charge ratios up to 300. During the experiments both the pumping lines are connected to the vacuum chamber, whereas during stand-by or servicing time only the turbo-molecular is employed.

### Geometry

The thruster development model is mounted externally to the vacuum tank, connected through its exhaust section. This set-up, although not representative of a fully space-like environment, allows a fast and flexible change of the geometric, magnetic and electric configuration of the source. The main components of the model are (Fig. 3.2, 3.3, 3.4):

1. a **Pyrex expansion bell** where plasma is ejected from the RF discharge; it is a bell-shaped glass component installed between the RF plasma source and the vacuum chamber; this component allows the visual observation of the plasma beam;
2. a **Pyrex tube** (i.e. the plasma source) with a inner diameter of 19 mm and an outer diameter of 24 mm where the plasma is generated;
3. a **ceramic outlet diaphragm** that can be changed in order to test different outlet diameters; the diaphragm thickness is 4 mm;
4. a **ceramic injector** with a 2 mm central axial hole;
5. an **injection system**, responsible of gas feed into the source; a stainless steel piston mechanism allows to change the source length; the mass flow is regulated through a MKS feedback controller in the range from 0.1 up to 0.4 mg/s with an accuracy of $\pm$(0.008+0.1% rv) mg/s, where rv stands for reading value; the mass flow controller is electrically decoupled from the piston by a ceramic breaker;
6. an **antenna for plasma generation**, coaxial to the plasma source, and a RF power supply network able to operate at different frequencies;
7. a **magnetic system**, coaxial to the plasma source and axially movable along the source; the magnetic field is generated by either electromagnets or permanent magnets.

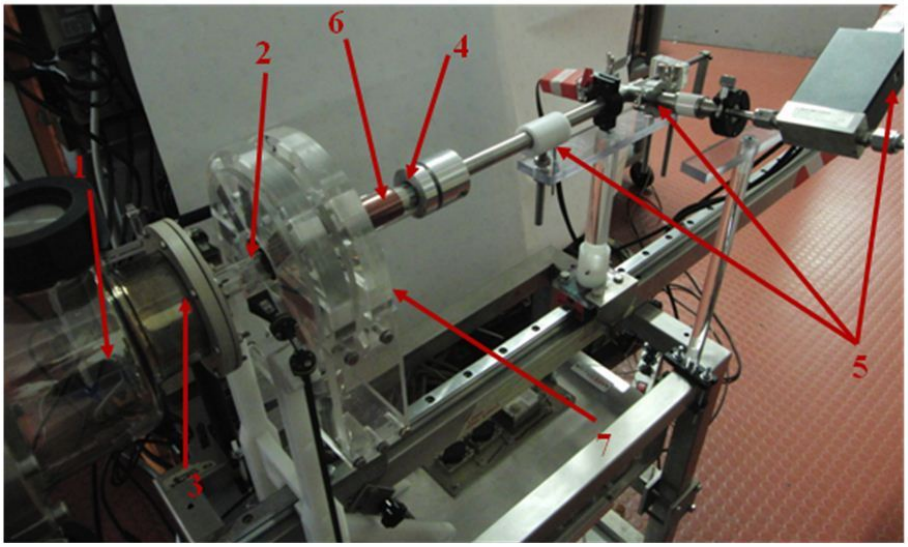


Figure 3.2: Main components of the thruster development model: 1) Pyrex expansion bell; 2) Pyrex tube (i.e. plasma source tube); 3) outlet diaphragm; 4) ceramic injector; 5) injection system; 6) antenna; 7) magnetic system. A detailed CAD of the system is reported in Fig. 3.3.

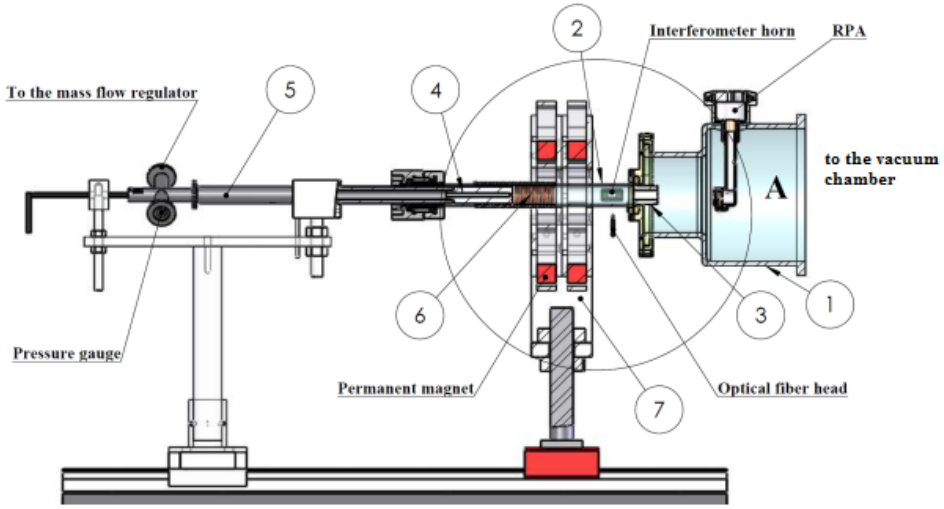


Figure 3.3: Overall CAD view of the experiment and its main components: 1) Pyrex expansion bell; 2) Pyrex tube (i.e. plasma source tube); 3) outlet diaphragm; 4) ceramic injector; 5) injection system; 6) antenna; 7) magnetic system. The location of diagnostics (microwave interferometer, RPA and optical fibers) is also shown.

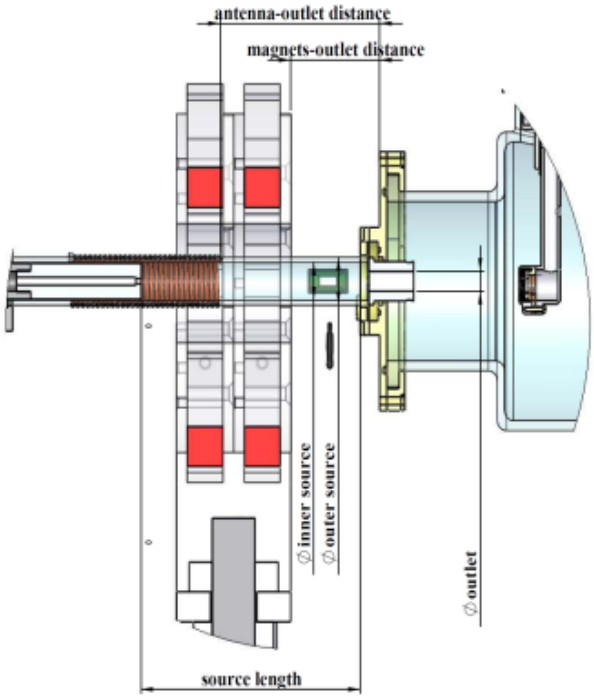


Figure 3.4: Detailed view of the plasma source region with the main geometrical features highlighted.

### Magnetic Field

The magnetic field is generated either by electromagnets or permanent magnets. The former allow to modify the magnetic field during the experiments and thus are suitable for the first development stage. The latter are advantageous if compared to electromagnets in terms of weight and power consumption, although being much less flexible. The employed magnetic systems are the following:

- **Electromagnets** The system consists of four independently powered electromagnets, mounted on two axially-movable supports housing two electromagnets each. Different field patterns can be generated, acting on the current flowing through the windings of each electromagnet and on their relative position. Each electromagnet has an inner diameter of 82 mm, an outer diameter of 320 mm, a length of 27.6 mm, a total of 628 copper wire windings, giving a resistance of 2 Ω. A single electromagnet generates at its center approximately 40 G of axial magnetic field for every Ampere of current flowing through its windings. The magnetic field intensity produced by the overall system ranges from 0 up to 1250 G.

- **Permanent magnets** The magnetic field is generated by samarium-cobalt (SmCo5) cubic permanent magnets with a size of 20 mm. The housings of the magnets consist of plastic disks with radial grooves where the magnets are located at the proper radial position and held by Teflon spacers. The magnetization vector can be oriented both in the axial and in the radial direction. Moreover the whole frame, being mounted on a carriage, can be axially translated along the source. The design of magnets layouts, supported by FEM magneto-static simulations, has initially been aimed at the reproduction of the fields obtained with electromagnets, while further optimization has led to the investigation of other configurations as well, in order to identify the most performing ones.

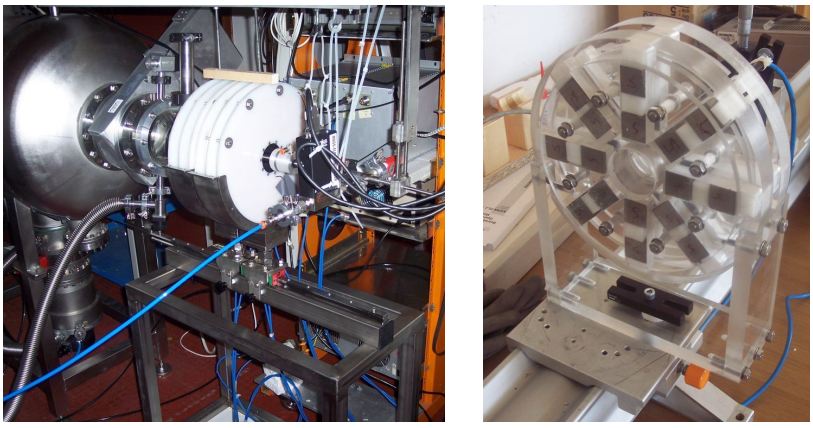

(a) (b)

Figure 3.5: a) System of four electromagnets, independently powered and mounted on two axially-movable supports housing two electromagnets each. b) Samarium cobalt cubic permanent magnets with a size of 20 mm housed in plastic disks with radial grooves where the magnets are located at the proper radial position and held by Teflon spacers.

### Definition of the Variability Ranges

The variability ranges for the main parameters are the following:

1. power: 40 W - 100W;
2. mass flow rate: 0.1 mg/s - 0.3 mg/s, using argon as the propellant;
3. source length: 50 mm - 150 mm;
4. diameter of the outlet orifice: 5 mm, 10 mm, 15 mm;

5. magnetic field: both the magnetic lines pattern and the intensity (up to 1250 G) are changed;

6. antenna type and RF frequency: within the range 3 MHz - 13 MHz;

7. the plasma source diameter has a fixed value equal to 19mm; this value has been identified during a previous study [84] combining a global fluid model of the plasma source with a 1D wavecode.

#### Diagnostic Systems

The following plasma diagnostic systems have been employed:

1. microwave interferometer to measure the electron density;

2. optical spectrometers to detect the plasma emission spectrum;

3. RPA to estimate the ion energy downstream the plasma source;

4. beam current probe to measure the ejected current.

#### Radio-Frequency Power Network

The RF signal is generated by an HP 8640B RF generator and amplified by means of a Spin HFPA-300 RF amplifier, whose characteristics are:

1. working range between 2 MHz - 30 MHz;

2. 300 W maximum output power;

3. $Z_a = 50\ \Omega$ internal impedance.

Since the output signal of the generator is too weak to pilot the amplifier, an IntraAction PA-4 low-power RF amplifier is employed as a pre-amplification stage. The matching system depends on the antenna type and will be discussed later in sections 3.2 and 3.3. All the power connections between the amplifier and the antenna employ RG214 cables (with a capacitance per unit length of 1 pF/cm) terminated with N connectors, while low-power signals are carried by RG58 cables with BNC connectors.

The parameters of the Radio-Frequency power network are monitored through an analogue device (designed and built by RESIA[1]) which measures the voltage and the current at the output of the RF power amplifier. Particularly:

[1] Realizzazioni Elettroniche Selmo ing. Antonio, San Bonifacio, Verona, Italy - HPH.com project partner

1. a compensated resistive voltage divider is used for the measurement of the voltage. The divider consists in a 5 kΩ load terminated by a 50 Ω load giving a ratio 100:1;

2. a ferrite toroid core transformer is used for the current sensing, giving an output voltage signal of 500 mV/A.

The compensation capacitors are calibrated for a specific length of the RG58 cables between the voltage-current measurement device and the reading instrument (e.g an oscilloscope), equal to 150 cm. The output signals of the device are read through an oscilloscope or a vector voltmeter. Both the voltage channel and the current one require to be terminated on a 50 Ω load.

The RF voltage and current traces give an indirect measurement of the instantaneous power (both real and reactive components), along with an indication of the circuit matching. The real power $P_f$ is calculated as:

$$P_f = \frac{V_0 I_0}{2} \cos\phi \tag{3.5}$$

where $V_0$ and $I_0$ are the amplitude of the voltage and the current respectively, and $\phi$ their relative phase. Considering the uncertainties on the voltage and current readings and on their relative phase, the uncertainty on the calculated power is 10%. In order to operate in proper matching conditions the voltage and the current must be in-phase and the overall load $Z_L$ of the RF network downstream of the amplifier output must be equal to the internal impedance of the amplifier itself $Z_L = Z_a = 50\ \Omega$. The impedance $Z_L$ includes the impedance of the transmission lines, of the matching system and of the antenna coupled with the plasma.

## 3.2 Experiments with a Standard Radio-Frequency Source

The experimental campaign described in this section has been carried out employing a four-loops antenna requiring a standard matching network. In order to obtain the proper coupling between RF power amplifier and the antenna, a matching box has been manufactured according to the classical scheme with two variable capacitors, one of them connected in series and the other one in parallel. Variable in-vacuum capacitors have been employed, with values in the range 40-1250 pF. An additional degree of freedom is given by the capability to tune the RF frequency, piloting the amplifier with the external RF generator. A strong effort has been dedicated to the minimization of spurious impedances: all the connections are made of copper plates to exploit the skin effect and an aluminum case covered by a copper layer is used as the common conductor. A picture of the matching box is shown in Fig. 3.6. The overall scheme of the power network is illustrated in Fig. 3.7.

Figure 3.6: Picture of the inside of the matching box: two variable in-vacuum capacitor are used. All the connections are made by copper plates to exploit the skin effect.

Hereafter we describe the characterization of the plasma generated by the four-loops antenna wrapped around the 19 mm-diameter Pyrex tube. The overall antenna length is 25 mm. The magnetostatic field is produced by an electromagnet coaxial to the source tube and located all around the antenna. This arrangement allows the generation of a uniform axial field under the antenna and a slowly divergent field downstream, as in the classical helicon thruster configuration [9, 84]. A ceramic diaphragm with a 5 mm-diameter orifice narrows the outlet section area determining a higher neutral pressure regime inside the source. The resulting neutral pressure in the source is $4.7 - 9 \times 10^{-2}$ mbar (for the explored mass flow rate range 0.15 – 0.3 mg/s), whereas the vacuum chamber pressure is 3.4 – $8.3 \times 10^{-5}$ mbar. The distance between the ceramic injector and the outlet diaphragm

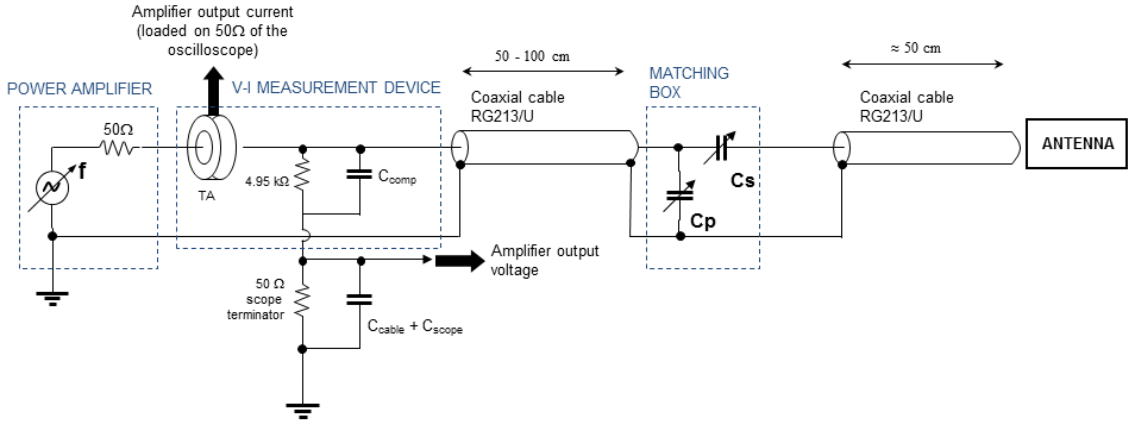


Figure 3.7: Schematic of the RF power network. The main components are: variable frequency RF generator, RF voltage-current measurement device, matching box and antenna.

is 75 mm. The plasma source configuration is shown in Fig. 3.8 along with the generated magnetic field pattern. The plasma density and the plasma emission spectrum have been measured through the microwave interferometer and the optical spectrometer for different operating conditions. The microwave horns and the optical fiber head are placed 25 mm downstream the antenna.

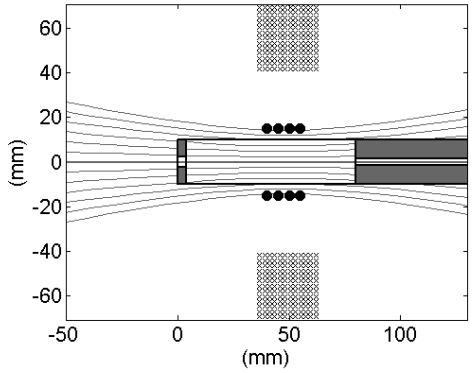


Figure 3.8: Configuration of the RF plasma source based on the four-loop antenna. The magnetic field, generated by an electromagnet, is also shown.

Fig. 3.9b shows the density as a function of the magnetic field intensity for a RF power of 55 W a mass flow rate of 0.23 mg/s. The plot highlights the presence of an optimal magnetic field equal to $\sim$ 160 G. The corresponding maximum density is 2.57 $\times 10^{17}$ m$^{-3}$. For a magnetic field intensity lower than 120 G and higher than 250 G, the interferometer phase shift is too low in comparison with the phase noise to estimate a reliable density

value, which would be lower than $5 \times 10^{16}$ m$^{-3}$ anyway. Fig. 3.9c reports the density as a function of the mass flow rate for a magnetic field of 160 G and a power of 70 W. A maximum density 6 $\times 10^{17}$ m$^{-3}$ is measured for a mass flow rate of 0.23 mg/s. Finally a power scan has been performed for the optimal magnetic field and mass flow rate values. The density increases monotonically with the power, from a value 2.57 $\times 10^{17}$ m$^{-3}$ for 55 W up to 1.22 $\times 10^{18}$ m$^{-3}$ for 155 W.

The optical emission spectrum in the range 200 - 650 nm relative to the operating point 160 G - 0.23 mg/s - 155 W is shown in Fig. 3.9a. ArI and ArII lines are identified in the plot as red and blue lines respectively. The predominant species is the Ar I, which is symptomatic of a low ionization level and a low electron temperature (approximatively lower than 2 eV, according to an estimation made through a C-R model).

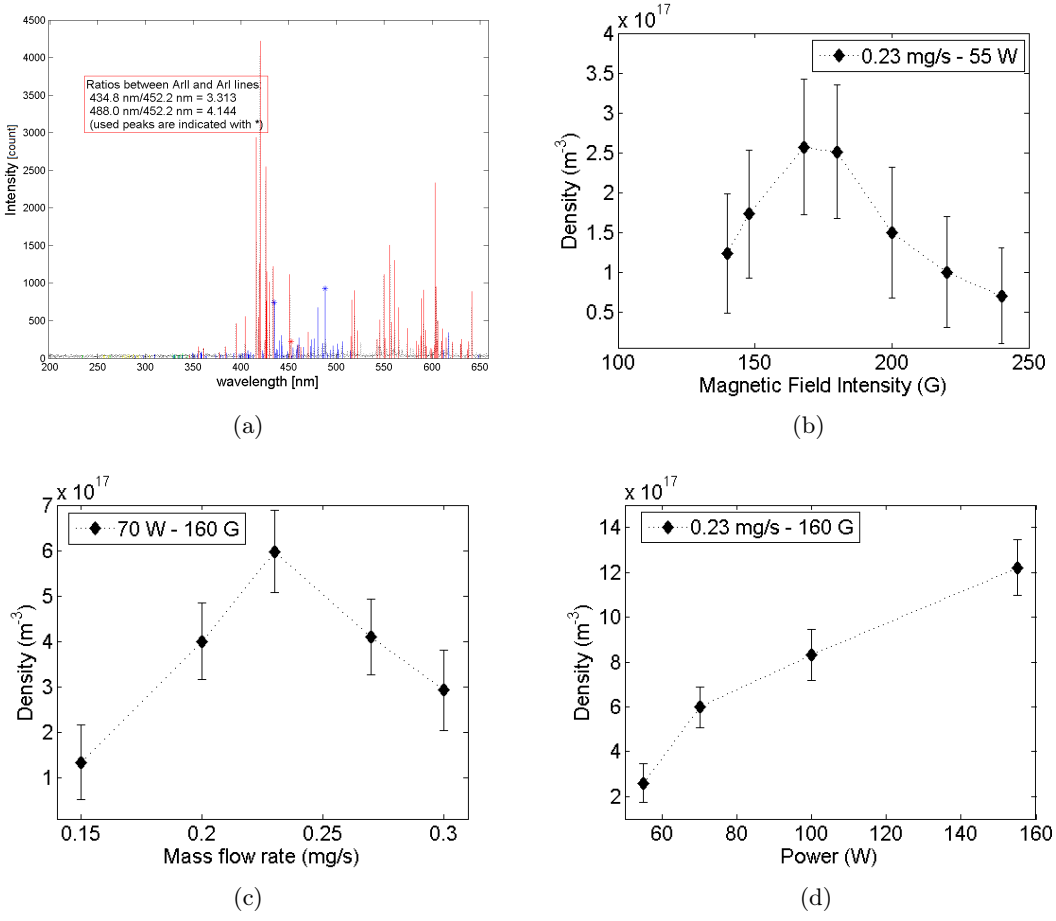


Figure 3.9: a) Optical emission spectrum acquired for 160 G - 0.23 mg/s - 155 W b) Plasma density as a function of the magnetic field intensity. c) Density as a function of the mass flow rate. d) Density as a function of the RF power.

The measured plasma properties are below the expected performance values required to produce the target thrust. Other experiments have been performed with different outlet diameters, antennas types, source lengths, injector types (i.e with radial holes instead of axial) and magnetic field patterns. However, in the explored power and mass flow rate ranges we could not observe an efficient plasma ionization. The maximum measured plasma density has been 3.5 $\times 10^{18}$ $m^{-3}$ (at $\sim$ 80 W - 0. 27 mg/s) and the electron temperature has never exceeded 2 eV. Possible reasons are the following: the presence of a higher power threshold to trigger an efficient discharge mode; the identified variability ranges of the various parameters; high power losses in the RF network. Additional considerations concern the matching system. Indeed, stray impedances in the circuit can introduce a sensible change of the matching condition; particularly this effect becomes relevant and difficult to predict for the inductance range ($\sim 0.5\mu$H) of the used antenna [84]. These considerations have led to a change of the development strategy, focusing on a novel type of antenna proposed by RESIA during the HPH.com project. This antenna is able to ignite a higher-density discharge mode in the power and mass flow rate ranges under consideration; furthermore it works through a different matching concept, based on a frequency tuning. The description of the antenna, the following development of the RF discharge and its experimental characterization are presented in the next section.

## 3.3 Experiments with a Novel Radio-Frequency Antenna Configuration

The experiments described in this section are performed with a novel RF antenna developed by RESIA[2] during the HPH.com project. This system is under patenting process. The antenna is made of a multi-loop inductive part and two coaxial annular electrodes connected at the extremities, as shown in the scheme 3.10. The electrodes are not exposed to the plasma so the "electrodeless" definition of the thruster is not altered. The antenna is designed to work at a specific frequency and does not require a matching network with tunable components as traditional systems do. The proper matching is obtained by means of frequency adjustments around the nominal working value (Fig. 3.11). Indeed the presence of the plasma changes the equivalent impedance of the antenna shifting the operating frequency. At the operating frequency with plasma the antenna presents a pure resistive behavior and an equivalent impedance in the 60-90 Ω range. In order to characterize the plasma behavior at different frequencies different antennas have been built working in the range 3 MHz-13 MHz. Typically, the antenna overall length is 12 cm, the electrodes are 15 - 25 mm wide and the central inductor is made of 30-40 turns depending on the target operating frequency. The antenna working at the lowest frequency (3 MHz) has a particular configuration characterized by a single electrode located on the ejection side of the thruster.

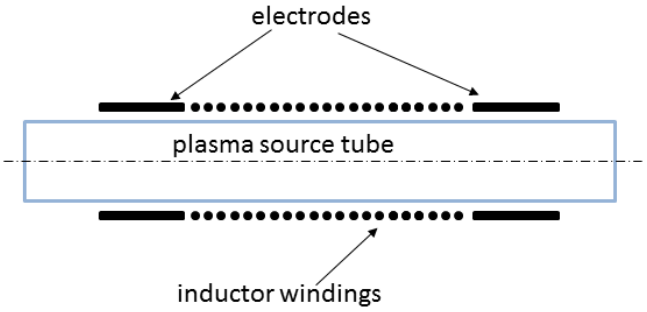


Figure 3.10: Schematic of the novel RF antenna: the central multi-loop inductor and the electrodes at the extremities are shown.

### 3.3.1 Experiments with Electromagnets

The novel RF antenna has been initially tested using the electromagnets for the generation of the magnetic field due to their higher versatility in comparison with permanent magnets. The antenna, working at 13 MHz, has been placed between the two pairs of electromagnets. Preliminary tests have been carried out sweeping independently the currents of the

[2]Realizzazioni Elettroniche Selmo ing. Antonio, San Bonifacio, Verona, Italy - HPH.com project partner

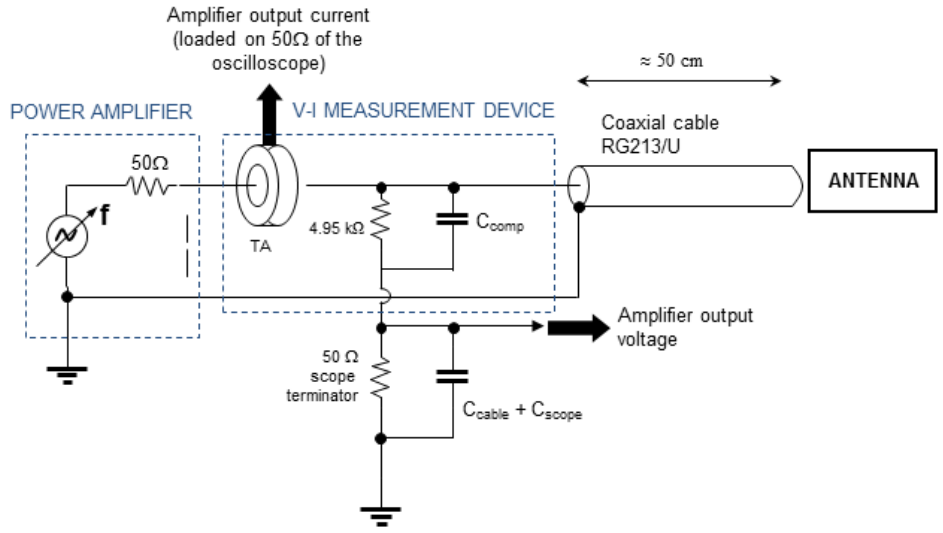


Figure 3.11: Schematic of the RF power network with the novel RF antenna. The main components are: variable frequency RF generator, RF voltage-current measurement device and the antenna. Note that a matching box is not required.

electromagnets. Examples of the generated magnetic field patterns are reported in Fig. 3.12a and 3.12b. Fig. 3.12a illustrates a uniform magnetic field obtained powering all the electromagnets with the same current value, whereas Fig. 3.12b illustrates the magnetic field structure powering only electromagnet #4. In the former case the magnetic field is nearly uniform under the antenna and slightly diverges downstream; in the latter the magnetic field lines present a convergent region followed by a divergent region and the magnetic field intensity is characterized by a steeper gradient in comparison with the first case. Indeed the high magnetic intensity is localized under the operating electromagnet.

Among the explored magnetic configurations, we have observed the strongest power coupling in the case of an intense magnetic gradient inside the source and a magnetic peak localized between the antenna and the source outlet (this is the case of Fig. 3.12b, obtained activating only electromagnet #4). Recall that the RF network is monitored through the measure of the RF voltage and RF current at the RF amplifier output, giving the forward and reflected power along with the matching status of the circuit. In the case of weak power coupling into the plasma the resulting active power at the amplifier output is really low since the equivalent resistive load absorbing active power is negligible. On the contrary, in the case of proper coupling the active power is significant since it is efficiently deposited into the plasma.

In the best operating conditions, visual observation of the discharge shows that the effective plasma discharge diameter appears to be smaller than the glass tube diameter

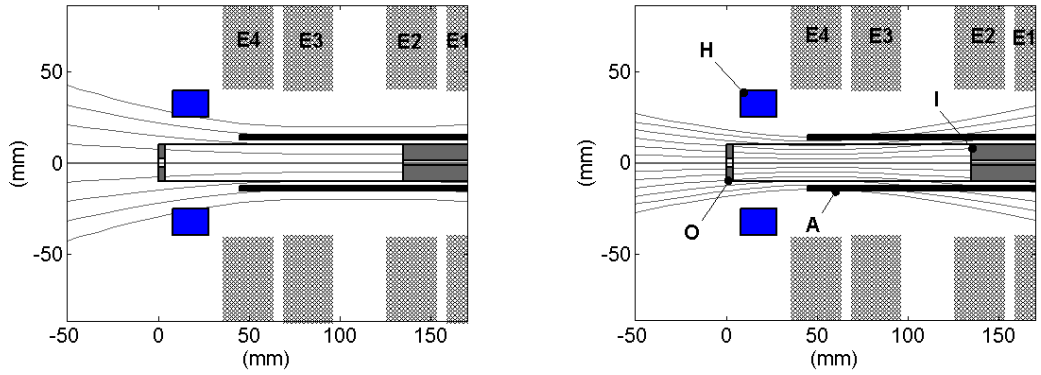


(a) (b)

Figure 3.12: a) Magnetic field pattern generated by the electromagnets powered with he same current value b) Magnetic field structure generated by the single electromagnet #4. The main components are reported in figures: E - electromagnets, A - antenna, I - injector, O - outlet diaphragm, H - interferometer horns.

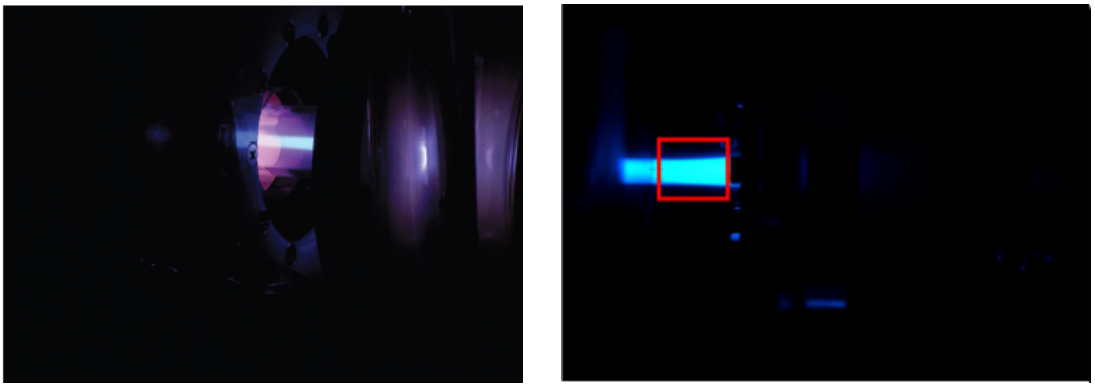

(a) (b)

Figure 3.13: a) Picture of the plasma discharge produced by the novel RF antenna and using electromagnets for the generation of the magnetic field: the plasma seems concentrated in the central region around the axis of the source; b) picture acquired through a CCD camera applying an optical bandpass filter with a 10 nm band centered on the 488 nm ArII line: the image confirms the ions are mainly located in a cylindrical region around the axis of the system.

(Fig. 3.13a). This structure is confirmed by the analysis of ionized particles distribution by means of the 488 nm (ArII line) filter-equipped CCD camera (Fig. 3.13b): the acquired pictures show that the ions are mainly located in a cylindrical region around the axis of the system ("blue core") whose diameter is strongly dependent on the outlet hole diameter and more weakly on the magnetic field.

Once identified this particular magnetic field pattern, the effect of its intensity has been investigated for various mass flow rates within the range 0.15 mg/s – 0.3 mg/s, employing a fixed power of 60 W and a fixed geometrical configuration. For each mass flow rate, a magnetic intensity sweep has been performed after the plasma ignition acting on the current flowing through electromagnet #4 in order to maximize the plasma density, monitoring it in real time through the interferometer. During the magnetic intensity sweep small frequency adjustments are implemented to "chase" the proper matching conditions. Indeed the change of the magnetic field induces changes of the plasma properties and thus of the equivalent impedance, producing a shift in the antenna working frequency. The emission spectrum corresponding to the highest density is acquired. The optical emission is collected by means of an optical fiber positioned in order to observe the source core region 10 mm upstream the outlet diaphragm. The microwave horns are located in the same position. The source configuration presents a length of 130 mm and an outlet diameter of 5 mm. The active electromagnet and the antenna are located 35 mm and 45 mm from the exit plane, respectively. The choice of such a distance is due to the presence of the microwave interferometer horns. The experimental parameters are summarized in table 3.1.

| **Parameter** | **Value** |
|---|---|
| Outlet diameter | 5 mm |
| Source length | 130 mm |
| Electromagnet #4 - outlet plane distance | 35 mm |
| Antenna - outlet plane distance | 45 mm |
| Mass flow rate | 0.15-0.3 mg/s (argon) |
| Power | 60 W |
| Vacuum chamber pressure | 3.5 – 8 $\times 10^{-5}$ mbar |
| Pressure inside the source | 4.7–9 $\times 10^{-2}$ mbar |
| Antenna operating frequency | 13 MHz |

Table 3.1: Operating parameters for the thruster configuration with 13 MHz antenna and 5 mm outlet diameter. The magnetic field is produced by electromagnets.

Fig. 3.14a shows the maximum densities measured during the magnetic intensity sweep for each mass flow rate. The peak value of the generated magnetic field is shown for each point. Similarly Fig. 3.14b shows the 488 nm(ArII)/452.2 nm(ArI) lines intensity ratio which, although not giving a quantitative indication of the actual ionization level, can be used to achieve a qualitative idea of its trend as the various source parameters are varied. It can be observed that both the density and the lines ratio exhibit a similar trend as a function of the mass flow rate. The measured density values are within the range 0.67 –

$1.44 \times 10^{19}$ m$^{-3}$. A maximum density is observed with 0.25 mg/s and 20 A flowing through electromagnet #4 (corresponding to a field of approximately 800 G). This current level is the maximum achievable with the available power supplies so we can not exclude higher performance in the case of an increased magnetic field.

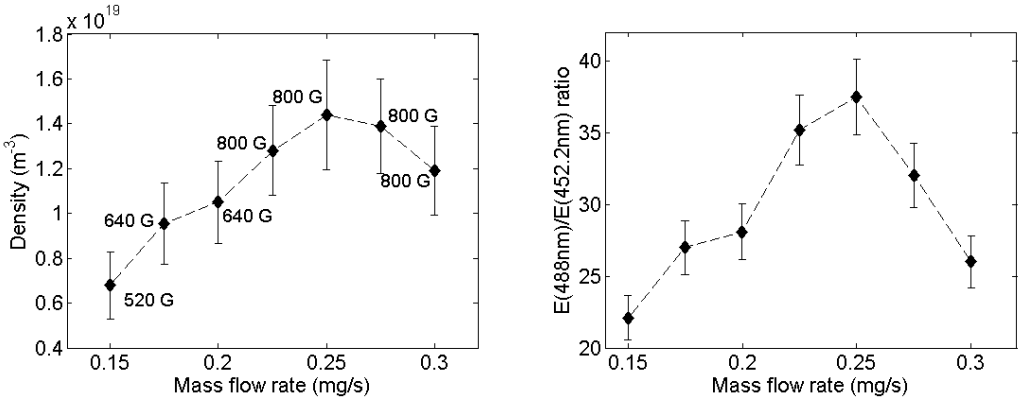


(a) (b)

Figure 3.14: Plasma density (a) and ArII/ArI lines intensity ratio (b) for different mass flow rates and a fixed power of 60 W. For each mass flow rate the magnetic field intensity has been swept in order to maximize the plasma density. The identified magnetic field value is reported in figure (a).

This sequence of experiments has demonstrated that the magnetic field is one of the most critical features for this type of thruster, both in terms of intensity and field lines patterns. The effect of the magnetic field intensity can be remarked observing the sequence of spectra in the 200-650 nm range reported in Fig. 3.15a-3.15d, acquired in a series of tests performed with the same source geometry, a power of 60 W and a fixed mass flow rate of 0.25 mg/s. For the lowest magnetic field intensity (160G) ArII lines appear to be weak, then their intensity progressively increases while the magnetic field value is enhanced. The trend of ArII/ArI lines intensity ratio is plotted in Fig. 3.16: the ratio increases as the magnetic field intensity is progressively raised, symptomatic of an increased ionization level. These observations can be also associated to the analysis of these spectra performed by Katsonis and Berenguer (Ref. [52], [51]) by means of a dedicated Collisional-Radiative model which indicates an electronic temperature ranging from 2.5 eV for the lower magnetic field magnitude up to 4.5 eV for the higher.

In summary, these experiments demonstrate that a plasma density $\sim 1.5 \times 10^{19}$ m$^{-3}$ and an electron temperature of 4.5 eV are achievable at a power of 60 W and a mass flow rate within 0.2 – 0.25 mg/s, using the novel RF antenna in combination with a particular magnetic field configuration. The identified magnetic topology is characterized by an intensity of $\sim$ 800 G with a peak located between the antenna and the thruster exit plane.

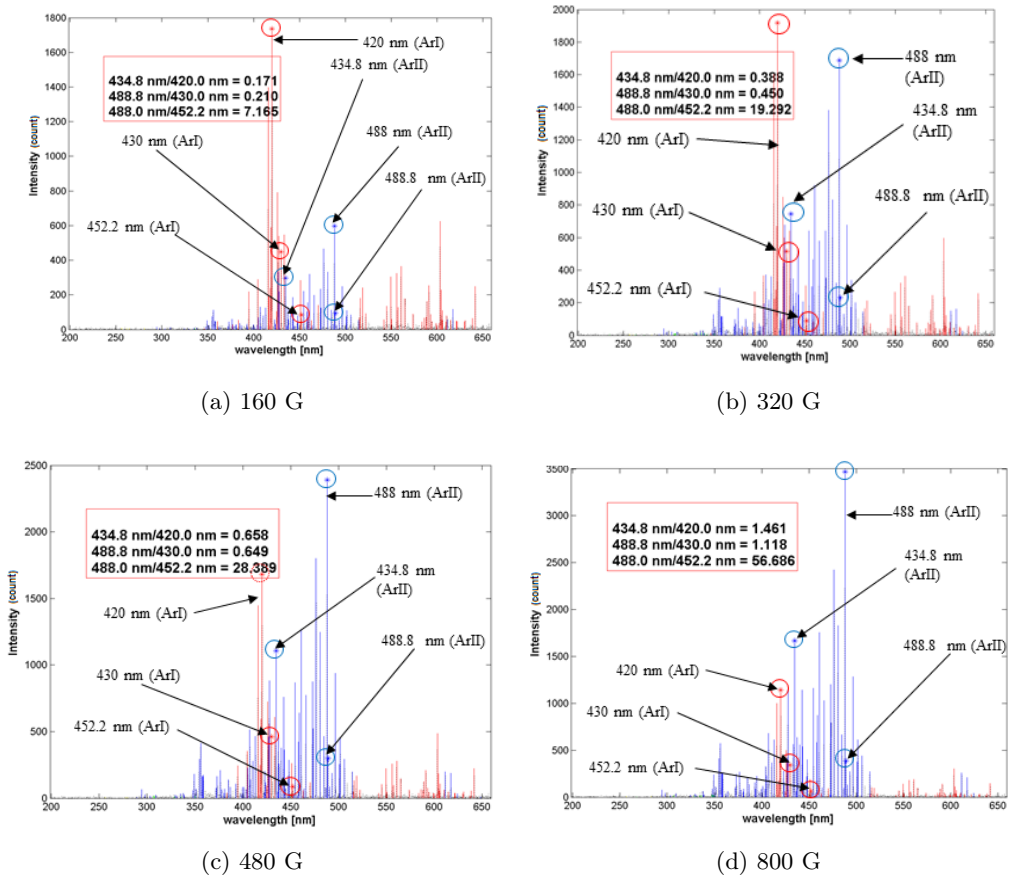


(a) 160 G

(b) 320 G

(c) 480 G

(d) 800 G

Figure 3.15: Optical emission spectra in the 200-650 nm range obtained for different magnetic field intensities (160, 320, 480, 800 G). The RF power is 60 W and the mass flow rate is 0.25 mg/s. ArI (red) and ArII (blue) lines are highlighted.

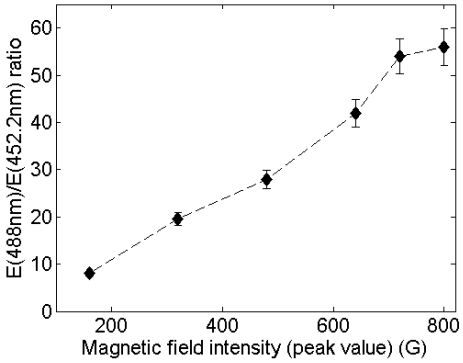


Figure 3.16: Trend of ArII/ArI lines intensity ratio in function of the magnetic field intensity. The magnetic field is produced by the electromagnet #4, generating the field configuration shown in Fig. 3.12b.

### 3.3.2 Experiments with Permanent Magnets

The target magnetic system to be used in the final thruster prototype is made of permanent magnets, due to the lower mass, volume and power consumption in comparison with electromagnets. These engineering advantages become particularly significant when a high magnetic field level is required for an efficient power coupling into the plasma and when the electromagnets power consumption is a significant fraction of the overall power budget of the thruster. Different permanent magnets configurations have been developed and tested. The features identified during the experiments with electromagnets have been taken into account, reproducing a strong gradient inside the source and an intense (higher than 800 G) peak located between the antenna and the outlet section. We aim to produce plasma properties (in terms of density and temperature) equal to or higher than those measured in the RF discharge with electromagnets.

The RF discharge properties have been characterized for each employed permanent magnets system. The first tests have been performed orienting the magnetization vector along the axial direction. With this configuration the plasma density and temperature have shown much lower values in comparison with those obtained employing the electromagnets. An improved performance is achieved employing the mixed axial-radial and fully radial configurations which are described in the following paragraphs.

#### Axial-Radial Permanent Magnets

The magnetic field is generated by two axial-symmetric arrays of samarium-cobalt 2cm-size cubic permanent magnets with radial and axial magnetization, arranged as illustrated in Fig. 3.17a. The axially-oriented magnets are arranged in two rings with inner radii equal to 38 mm and 68 mm. The radially-oriented magnets form another 38 mm-radius ring. Each ring comprises 8 magnets. Fig. 3.17b illustrates the magnetic profile on the axis measured by means of a Hall probe. This permanent magnets lay-out produces an axial field exhibiting a strong ($\sim$1400 G) central peak with two inversion zones and two secondary peaks of different intensity ($\sim$800 G and $\sim$200 G). The peak of 800 G is located on the outlet side, whereas the antenna is located on the 200 G peak side. The permanent magnets supporting structure is located $\sim$ 40 mm from the outlet because of the presence of the interferometer horns. The antenna position depends on the geometric constraints defined by the magnetic system geometry.

The RF plasma source lay-out is shown in Fig. 3.17a with the magnetic field topology superimposed. The tested configurations include two different antennas, operating at 10 MHz and 3 MHz and three different outlet diameters, namely 5, 10, 15 mm. Scans in terms of power and mass flow rate have been carried out for each configuration. Spectral emission data are combined with interferometer measurements to get a sense of what is the

global performance of the RF plasma discharge. The probed plasma region is located 10 mm upstream the exit plane. Plasma behavior sensibly changes varying outlet diameter and antenna operating frequency, as shown by the measurements reported in the following paragraphs.

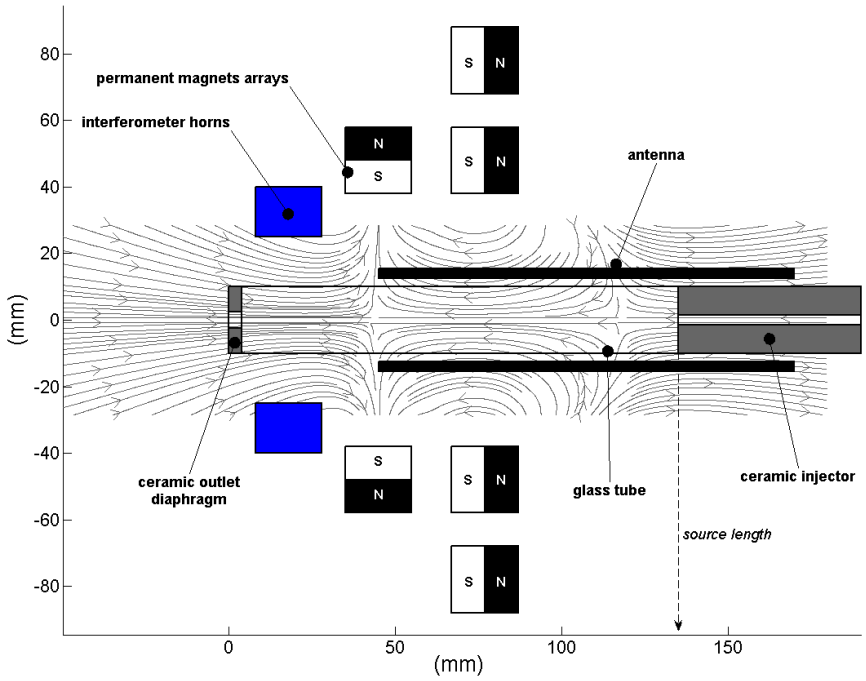


(a)

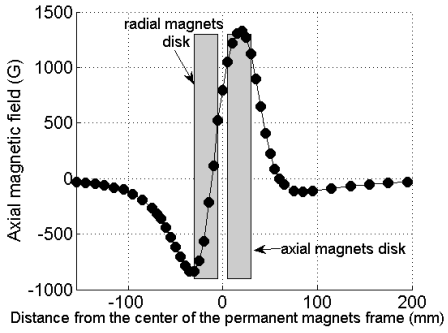


(b)

Figure 3.17: a) Schematic of the RF plasma thruster configuration used for these development tests with the magnetic field pattern superimposed; b) axial component of the magnetic field along the axis measured by means of an Hall probe.

**10 MHz antenna** Hereafter we present a set of measurements relative to the RF discharge produced by a 10 MHz antenna. Different outlet diameters are tested: 5, 10, 15 mm. The explored mass flow rate range is 0.167 – 0.25 mg/s. The value 0.167 mg/s is the minimum mass flow to sustain the discharge. For this mass flow rate range the background neutral pressure in the vacuum chamber is 4–6 $\times 10^{-5}$ mbar, whereas the pressure in the source tube is dependent on the outlet diameter; approximately, the order of magnitude is $\sim 10^{-2}$ mbar. Table 3.2 reports the main experimental parameters. The discharge structure is similar to that observed with electromagnets, characterized by a high-density central core as shown in the picture of the discharge (Fig. 3.18). The width of the core is dependent on the outlet diameter, being more condensed in the case of a 5 mm diameter and broadening for the 15 mm one. Roughly we can assess $d_{core} \sim d_{outlet}$. The source length has been determined moving progressively the injector towards the outlet diaphragm and monitoring the plasma density. The selected length is the maximum length which allows the ignition of this high density discharge mode. We have selected the maximum length rather than a shorter one to avoid that the stainless steel piston structure which moves the injector gets too close to the antenna causing a spurious load.

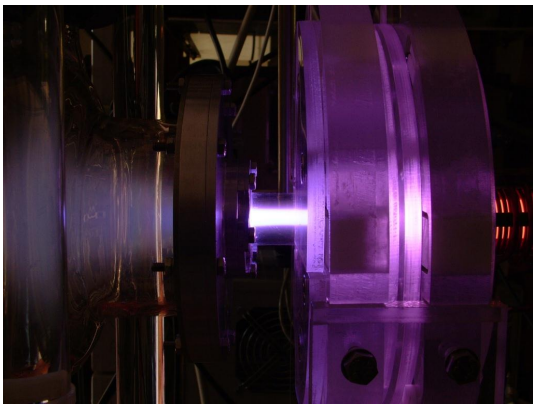

Figure 3.18: Picture of the discharge.

Fig. 3.19a shows an example of a typical Ar spectrum acquired and elaborated, where lines of ArI (red ones) and ArII (blue ones) can be distinguished in the wavelength region from 290 nm to 650 nm. Some ArIII lines can be identified in the region from 320 to 350 nm: their intensities are remarkably weaker that those of ArI and ArII, so a conspicuous increase of the spectrometer integration time is needed to achieve a notable size of them even thought this solution may easily cause a loss of information due to the saturation of other lines. In the spectrum we highlight the five lines previously described in section 2.1.1 adopted for the ArII to ArI ratios calculations. The various lines ratios, plotted in Fig. 3.19b, show the same trend in function of the mass flow rate for each value of power.

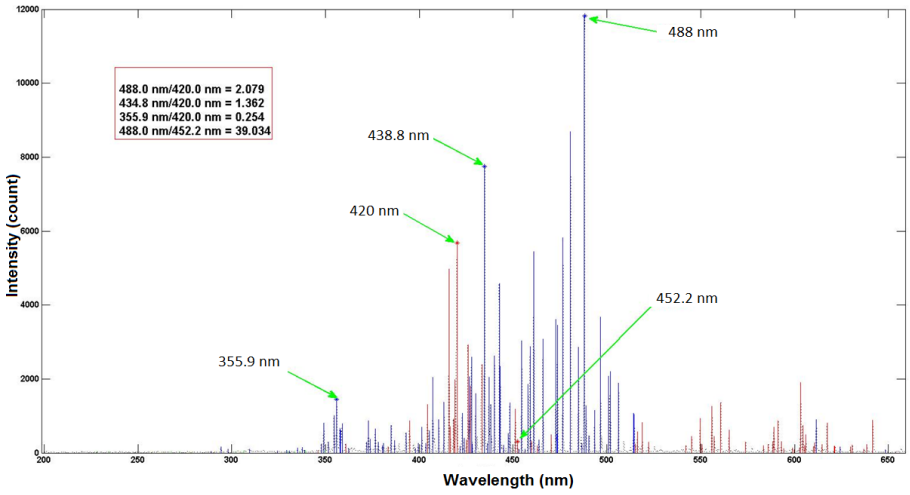


(a)

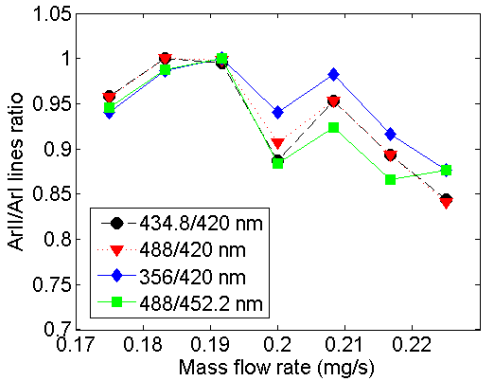


(b)

Figure 3.19: a) Argon plasma emission spectrum: ion (blue) and neutral (red) lines are highlighted in the plot. b)Comparison between four ArII to ArI lines ratios: all of them show the same trend.

Fig. 3.20c and 3.20d report the experimental results for an outlet diameter of 10 mm. Both the ionization level and the density grow with the electrical power. The spectral ratio decreases monotonically with the increase of the mass flow rate, while the density exhibits a maximum value at an intermediate mass flow. The maximum density takes place at 0.2 mg/s for 50, 65, 75 W of power and 0.225 mg/s for 90 W. Considering a mass flow rate of 0.2 mg/s, the plasma density is equal 2.38 $\times 10^{18}$ $m^{-3}$ for 50 W and rises up to 2.81 $\times 10^{18}$ $m^{-3}$ for 90 W. For a fixed power, this configuration produces a smaller quantity of ions when the mass flow rate is lower (i.e. 0.167 mg/s), so the remaining coupled power goes into temperature rise. As the mass flow rate increases, the contribution given to enhance the amount of ions becomes more significant till a maximum is reached. Higher mass flow

| Parameter | Value |
|---|---|
| Outlet diameter | 5, 10, 15 mm |
| Source length | 135 mm |
| Magnets - outlet plane distance | 40 mm |
| Antenna - outlet plane distance | 45 mm |
| Mass flow rate | 0.167-0.25 mg/s (argon) |
| Power | 50-90 W |
| Vacuum chamber pressure | 4–6 $\times 10^{-5}$ mbar |
| Pressure inside the source (5mm outlet) | 5.2–7.5 $\times 10^{-2}$ mbar |
| Pressure inside the source (10mm outlet) | 1.3–1.95 $\times 10^{-2}$ mbar |
| Pressure inside the source (15 mm outlet) | 0.6–0.9 $\times 10^{-2}$ mbar |
| Antenna operating frequency | 10 MHz |

Table 3.2: Operating parameters for the thruster configuration with a 10 MHz antenna. The magnetic field is produced by permanent magnets with axial-radial configuration.

rates cause a performance fall both in terms of density and ArII/ArI lines ratio, revealing that a higher fraction of power is spent for neutral excitation rather than ionization.

Similar trends can be identified using the 15 mm outlet (Fig. 3.20a and 3.20b): the ArII/ArI lines ratio decreases for increasing mass flow rates and the density is characterized by a maximum value for an intermediate mass flow rate of 0.2 mg/s. A different trend is observed for the density profile at 90 W: it increases monotonically with the mass flow rate. For a fixed mass flow rate, an increase of the electrical power produces a growth of both the parameters. Considering a mass flow rate of 0.2 mg/s, the measured densities at 50 and 90 W are 7.1 and 8.7 $\times 10^{17}$ m$^{-3}$, respectively. The density values are lower of a factor of 3 than those measured in the case of a 10 mm outlet diameter. The ArII/ArI lines ratio are lower as well. The results indicate that such a configuration produces a less ionized plasma, i.e. with a higher fraction of excitation processes relative to the ionization processes.

The 5 mm outlet diameter configuration has been characterized for a fixed power, equal to 50 W, and a restricted mass flow rate interval within the range 0.167 – 0.225 mg/s. An unequivocal trend can not be identified for the ArII/ArI lines ratio (Fig. 3.20f). A maximum density of 1.54 $\times 10^{19}$ m$^{-3}$ is measured for a mass flow of 0.19 mg/s (Fig. 3.20e), revealing a higher plasma density than the 10 mm outlet case. These measurements are in good agreement with those obtained with electromagnets for a peak field of 800 G: indeed, using an outlet diameter of 5 mm a density of 1.45 $\times 10^{19}$ m$^{-3}$ was observed and the emission spectra featured the same characteristics.

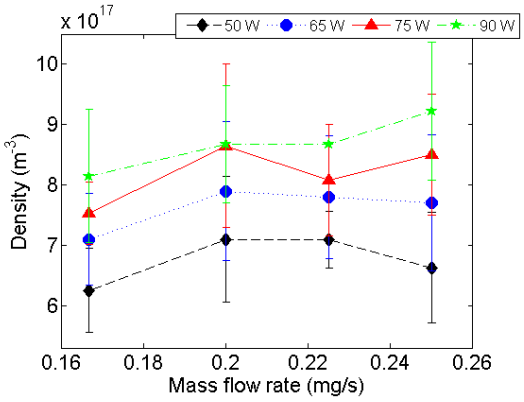


(a) 10 MHz - 15 mm

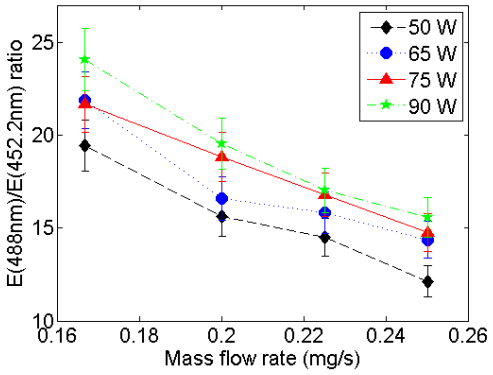


(b) 10 MHz - 15 mm

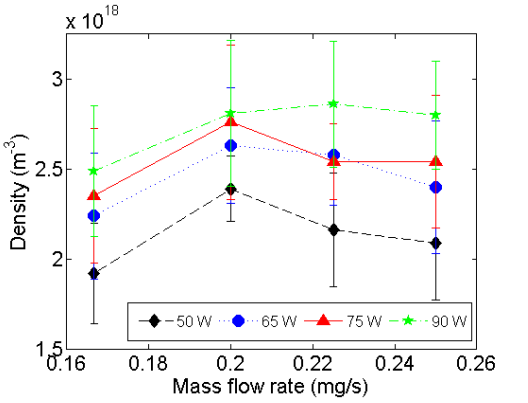


(c) 10 MHz - 10 mm

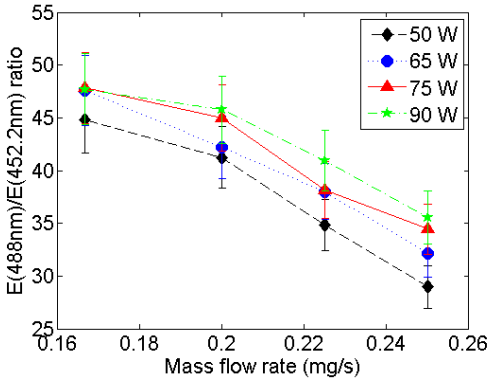


(d) 10 MHz - 10 mm

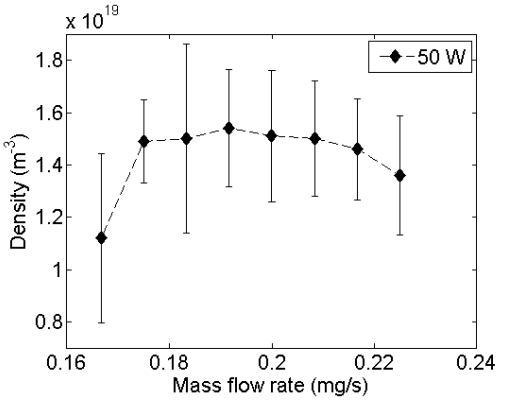


(e) 10 MHz - 5 mm

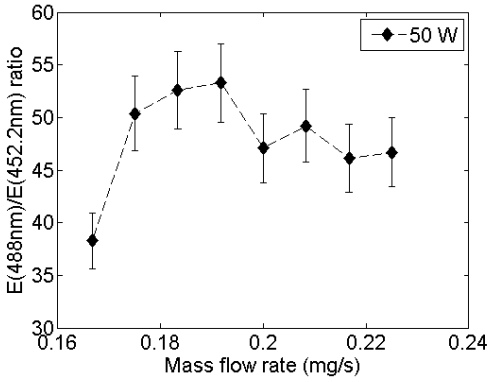


(f) 10 MHz - 5 mm

Figure 3.20: RF plasma source properties using a 10 MHz antenna and different outlet diameters in function of the mass flow rate and power.

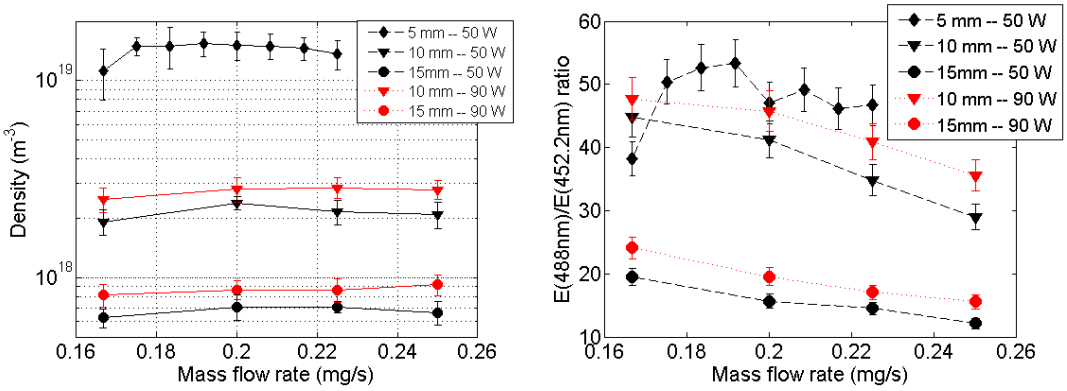


(a) (b)

Figure 3.21: Comparison of the plasma discharge properties measured for different outlet diameters and using a 10 MHz antenna.

Finally, Fig. 3.21a and 3.21b report a comparison of the plasma properties for the three different outlet diameters. We can observe that the highest density and ArII/ArI lines ratio are produced by the configuration with the 5 mm orifice; however the highly positive factor on the plasma density must be tempered by considerations about the general behavior of the thruster. Indeed the use of a 5 mm outlet diameter implies higher losses on the outlet diaphragm inner surface and a smaller exhaust section which scales as $(d_1/d_2)^2$, giving a factor of 4 in the case $d_1/d_2$=2. The measurements in the plasma source have to be combined with measurements in the plasma beam to provide a complete assessment of the system performance.

**3 MHz antenna** The properties of the plasma generated by the 3 MHz antenna have been characterized for different outlet diameters (5 and 10 mm) and operating conditions. Recall that the novel RF antenna works at a fixed frequency thus changing the operating frequency coincides with replacing the antenna. The experimental parameters are reported in Table 3.3. The explored mass flow rate range is 0.167 – 0.25 mg/s. The maximum power is limited to 75 W for the 5 mm outlet diameter and to 60 W for the 10 mm outlet diameter because of the difficulties with maintaining the proper matching conditions. Moreover spurious harmonics have been observed in the RF current and voltage traces for increasing power, probably due to the operating frequency close to the lower limit of the working frequency range of the RF pre-amplifier.

Fig. 3.22a and 3.22b illustrate the plasma density and the ArII/ArI lines ratio for the 10 mm outlet diameter. The density increases monotonically in function of the mass flow rate. This trend is different from the profile observed in the 10 MHz antenna configuration,

| Parameter | Value |
|---|---|
| Outlet diameter | 5, 10 mm |
| Source length | 145 mm |
| Magnets - outlet plane distance | 40 mm |
| Antenna - outlet plane distance | 55 mm |
| Mass flow rate | 0.167-0.25 mg/s (argon) |
| Power | 50-75 W |
| Vacuum chamber pressure | 4–6 $\times 10^{-5}$ mbar |
| Pressure inside the source (10 mm outlet) | 1.3–1.95 $\times 10^{-2}$ mbar |
| Pressure inside the source (5 mm outlet) | 5.2–7.5 $\times 10^{-2}$ mbar |
| Antenna operating frequency | 3 MHz |

Table 3.3: Operating parameters for the thruster configuration with a 3 MHz antenna. The magnetic field is produced by permanent magnets with axial-radial configuration.

which was characterized by a maximum density at an intermediate mass flow rate. On the contrary, the ArII/ArI line ratio decreases if a higher mass flow is injected. As in the other analyzed cases, a higher electrical power induces a growth of both the parameters. A maximum density of 1.9 $\times 10^{18}$ m$^{-3}$ is measured in the point 60 W-0.25mg/s.

The profiles obtained in the case of the 5 mm orifice present a different behavior: both the density (Fig. 3.22e) and the ArII/ArI lines ratio (Fig. 3.22f) exhibit a maximum for a mass flow of 0.2 mg/s. The density presents an order of magnitude of $\sim 10^{19}$ m$^{-3}$. The comparisons among the plasma properties identified for the different source outlet diameters are shown in Fig. 3.22e and 3.22f, which highlight the improvement of the parameters in the case of the 5 mm hole.

Finally, Fig. 3.23a and 3.23b report the comparison between the plasma densities produced by the two characterized antennas, working at 3 MHz and 10 MHz. The figures correspond to a 5 and 10 mm outlet diameter respectively. In the case of a 5 mm orifice, the 3 MHz antenna generates a denser plasma in comparison with the 10 MHz one in the considered mass flow rate range. For both the antennas the density presents a maximum for a mass flow of ∼0.2–0.225 mg/s. Moreover the plasma produced by the 3 MHz antenna is characterized by higher ArII/ArI lines ratios, as shown by Fig. 3.20f and 3.22d. In the case of a 10 mm outlet diameter, the situation is reversed: the 10 MHz antenna produces a denser plasma. As previously stated, the trend of density in function of the mass flow is slightly different between the two antennas: the density increases monotonically for the 3 MHz antenna and exhibits a maximum in the case of the 10 MHz antenna.

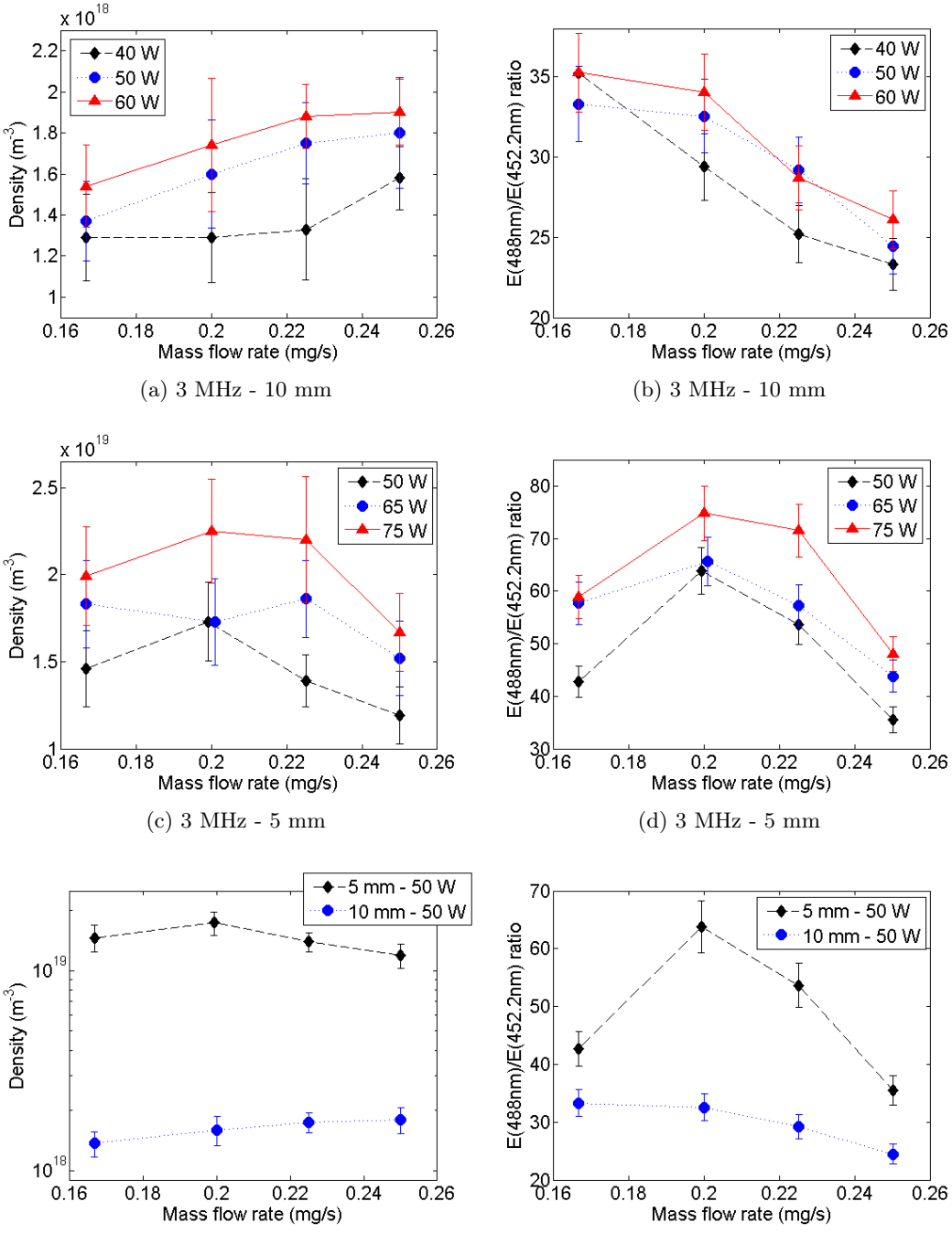


(a) 3 MHz - 10 mm

(b) 3 MHz - 10 mm

(c) 3 MHz - 5 mm

(d) 3 MHz - 5 mm

(e) 3 MHz - 5,10 mm

(f) 3 MHz - 5,10 mm

Figure 3.22: RF plasma source properties using a 3 MHz antenna and different outlet diameters in function of the mass flow rate and power.

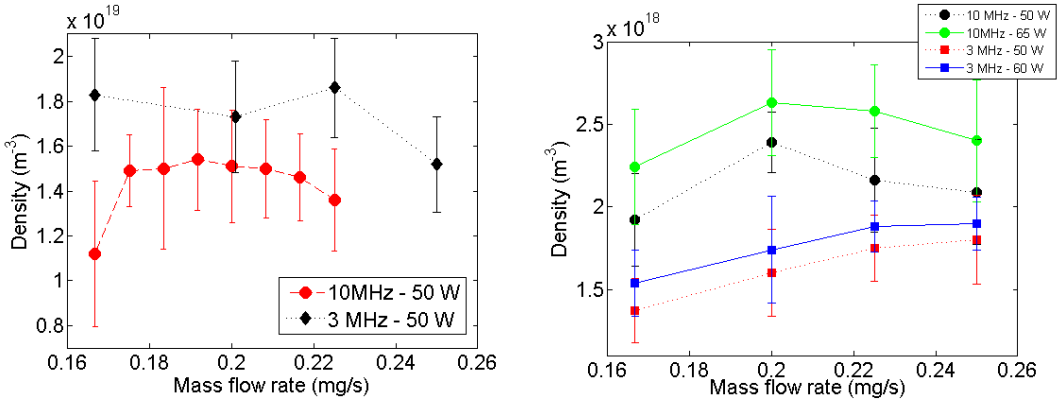


(a) 5 mm (b) 10 mm

Figure 3.23: Comparison of the plasma density measured for the 10 MHz and 3 MHz antennas for two different outlet diameters.

**Plasma beam properties** The plasma beam ejected by the RF plasma source has been characterized through the RPA and the current probe. The investigated region is located downstream the discharge channel exit plane, inside the glass bell which connects the source tube to the vacuum chamber (the reader is referred to the scheme 3.3). The 3 mm diameter current probe is mounted on a two-axis horizontal motorized stage to map the target region both in the axial and radial direction. The probe collector is polarized at -150 V; this high polarization voltage is required to repel the high energy electrons ejected from the thruster. The presence of this high energy population is due to the high electric field produced by the novel antenna, as highlighted in the results of the particle-in-cell simulations presented in section 3.5. The RPA is installed in a fixed location 10 cm downstream the exit plane. Details on the current probe and RPA are given in sections 2.1.4 and 2.1.3 respectively. The measurements have been performed on the 10 MHz RF plasma source whose geometrical parameters and pressure levels are summarized in table 3.2. Both the 5 mm and the 10 mm outlet diameter configurations have been investigated.

The RPA characteristic curve, namely the collected ion current in function of the retarding voltage, has been acquired for different operative conditions in terms of mass flow rate and power. Fig 3.24 illustrates the characteristic curve relative to an outlet diameter of 10 mm, a mass flow rate of 0.167 mg/s and a power equal to 90 W, along with the estimated ion energy distribution function (IEDF). The curve reveals a strong acceleration mechanism with the energy peak for a retarding voltage higher than 100 V. This voltage includes the contribution of the plasma potential which should be subtracted to estimate the purely kinetic component. However in the RPA position, located 10 cm

downstream the plasma source, we can assume a low potential component since we expect a strong potential drop nearby the discharge exit plane, where the plasma production region interfaces with the vacuum region as shown by the PIC simulations. The trend of ion energy in function of the mass flow rate is highlighted in the plots shown in Fig. 3.25a and 3.25b, corresponding to outlet diameters of 10 mm and 5 mm respectively: in both cases a decrease of the energy is observed for an increasing mass flow rate at the same power level. On the contrary, any effect of the power is not remarked.

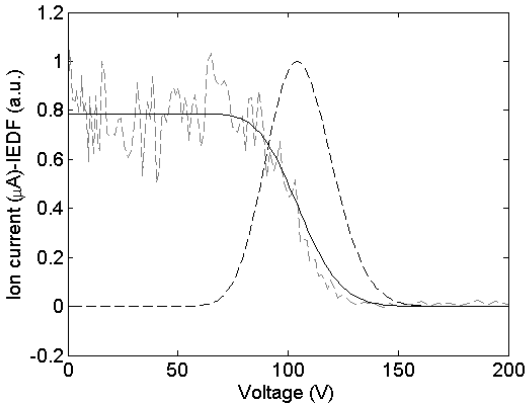


Figure 3.24: RPA characteristic curve and resulting IEDF for an outlet diameter of 10 mm, a mass flow rate of 0.167 mg/s and a power of 90W. The rough data are plotted as a dashed gray line.

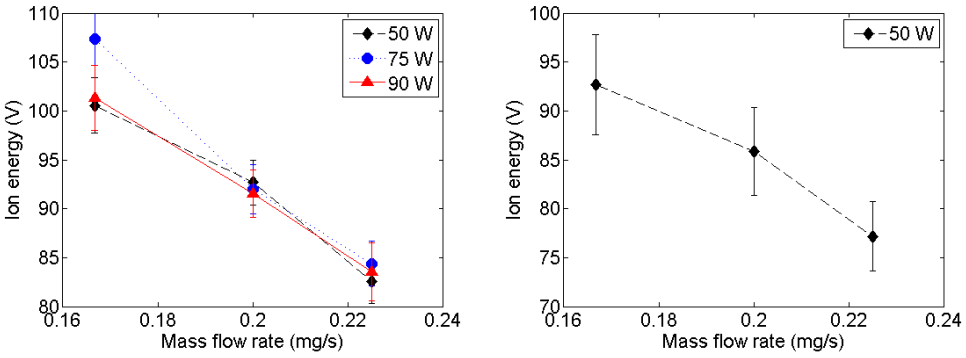


(a) 10 mm

(b) 5 mm

Figure 3.25: Retarding voltages corresponding to the IEDF peak in function of the mass flow rate and for various power level. The RPA is installed in a fixed position, 10 cm downstream the exit plane of the RF discharge. Figures (a) and (b) refers to an outlet diameter of 10 mm and 5 mm respectively.

The ion current has been measured at fixed operating conditions: 50 W of power and 0.2 mg/s of mass flow. Fig. 3.26a shows the current density map in a region starting from Z = 73 mm downstream the RF source exit plane and extended until Z = 150 mm. The map is obtained for a 10 mm outlet hole. The measurement grid spacing is 2 cm in the axial direction and 5 mm in the radial one. We can observe that the current density progressively decreases moving downstream due to the plume divergence. The radial profiles, plotted in Fig. 3.26b, show the presence of two maximum values, symmetric respect to the axis and located at about R = 20 mm for Z = 73 mm. This radial profile identifies a hollow conical plume shape with a lower current density in the central region. This effect becomes weaker moving downstream, indeed the current profile becomes flatter with a smoothing of the aforementioned bulges. The integration of the radial current profile gives $(0.12 \pm 0.015)$ A, considering the effective collection area equal to the physical collector area. As already described in section 2.1.4, the effective collection area may be higher because of the high polarization of the probe. We use anyway the integrated current to compare the 5 mm and 10 mm configurations; indeed, for the same probe polarization and comparable ion velocities, the difference of the effective collection area is negligible. In the case of a 5 mm outlet diameter the current profile does not present the bulges even if a certain asymmetry is remarked, probably due to misalignments in the system. The current density level observed for the 5 mm outlet is higher and narrower in comparison with the 10 mm case, indicating an enhanced focusing of the plume. The current integration gives $(0.096 \pm 0.012)$ A, again considering the effective collection area equal to the physical collector area.

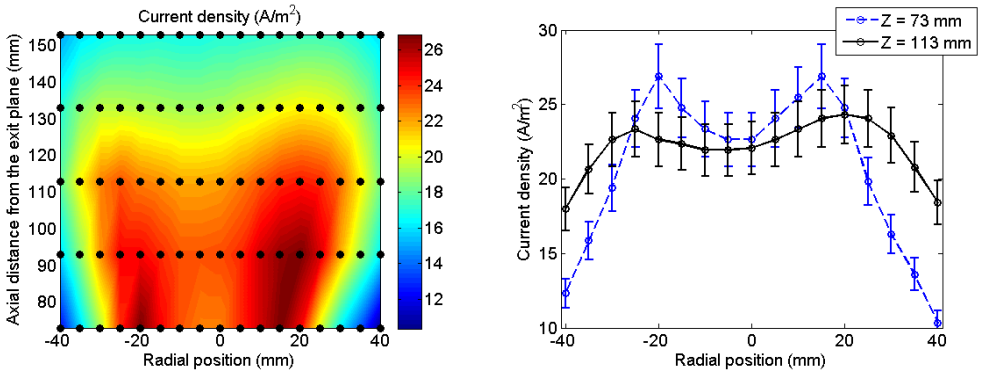


(a) Current map - 10 mm outlet diameter (b) Current profiles - 10 mm outlet diameter

Figure 3.26: a) Current map downstream the exit plane for the following operative conditions: mass flow rate 0.2 mg/s, power 50W, outlet diameter 10 mm. b) Radial profiles of the current at the same operative conditions.

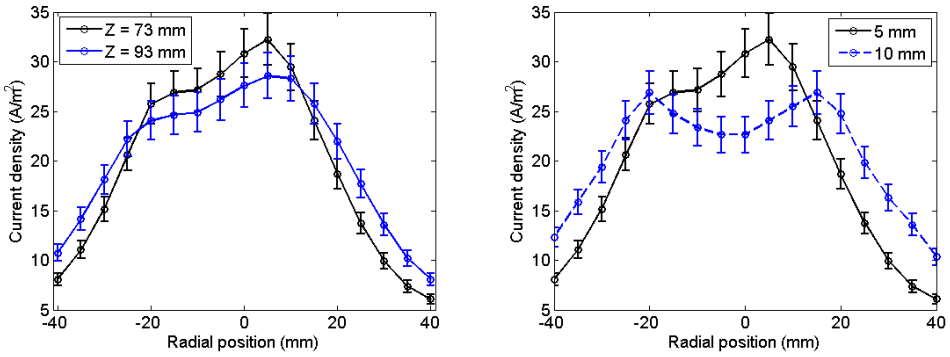


(a) 5 mm outlet diameter

(b) 5 and 10 mm outlet diameter

Figure 3.27: a) Current radial profiles for an outlet diameter of 5 mm, a mass flow rate equal to 0.2 mg/s and a power of 50W. b) Comparison among the current radial profiles corresponding to the two different outlet diameters at a distance of 73 mm downstream the exit plane of the RF discharge.

### Radial-Radial Permanent Magnets

Additional experiments have been performed with two rings of radially oriented permanent magnets. The two rings have different diameters, with the smaller one located on the outlet side. This configuration maintains a strong magnetic field gradient inside the source and an intense peak concentrated near the outlet section, as it has been confirmed both by magnetostatic simulations and experimentally (Fig. 3.28a and 3.28b). Moreover in the source region the axial magnetic field exhibits a single inversion point. Electron temperature and density in the source and ion beam energy are in the same ranges of those obtained with the axial-radial lay-out.

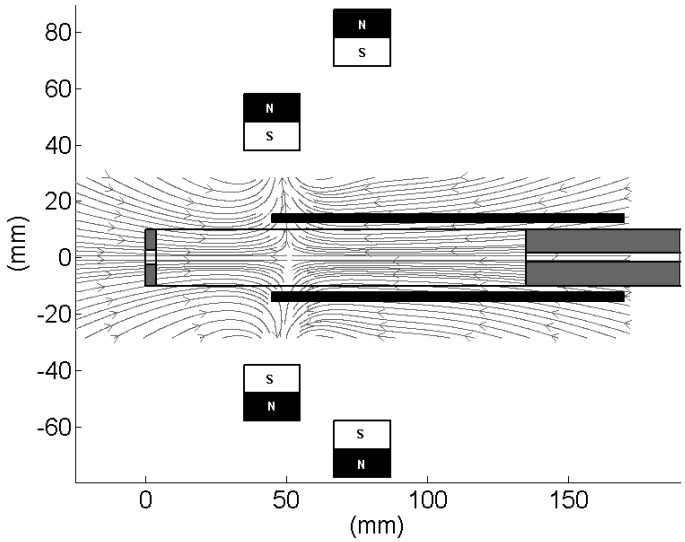


(a)

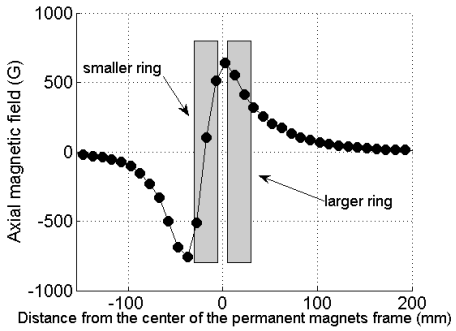


(b)

Figure 3.28: a) Magnetic field pattern produced by the radial-radial configuration; b) axial component of the magnetic field along the axis measured by means of an Hall probe.

A sequence of measurements has been carried out in order to identify the effect of the antenna and magnetic field position on the ejected current. The current probe has been located in a fixed location 110 mm downstream the exit plane of the source tube on the axis of the system. The microwave interferometer horns have been disassembled in order to move the magnetic system closer to the exit plane. A spectrometer has been used to verify the emission spectrum during the measurements. The optical fiber head looks at a position 10 mm upstream the exit plane as in the other experiments. The minimum allowed distance between the magnets supporting structure and the exit plane is 25 mm. The tests have been carried out using a 13 MHz antenna, a 5 mm outlet diameter and a source length of 120 mm. The operating point is 0.2 mg/s - 60 W for all the measurements. Fig.

3.29a reports the current and the ArII/ArI lines ratio trends as a function of the antenna position for a fixed magnets position, located 25 mm from the exit plane. Each curve is normalized to unit for plotting convenience. We can observe that both the lines ratios and the current present the same trend, thus in this case the measured value of the current is determined by changes in the discharge conditions rather than by changes of the exhausting conditions. Fig. 3.29b illustrates the current trend as a function of the antenna position for different magnets locations relative to the exit plane. In general, the current density increases when the magnets are closer to the exit plane. The current density increases for antenna positions closer to the exit plane as well, with the exception of the profile relative to the 25 mm magnets location, which is nearly independent on the antenna position.

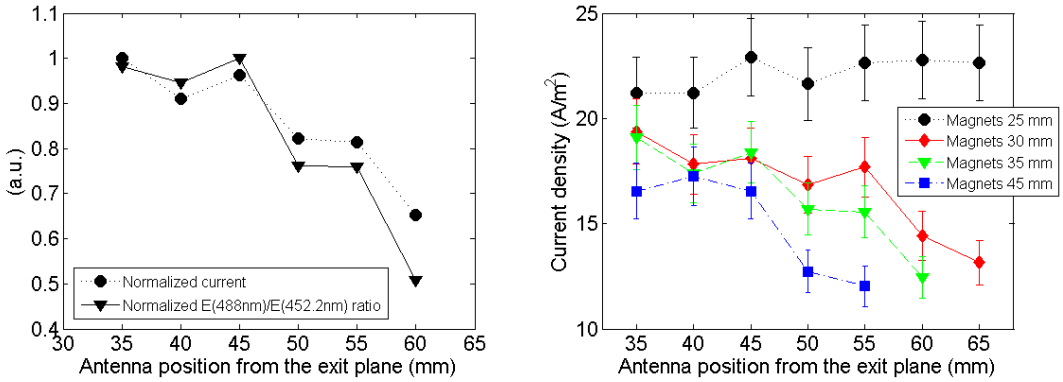


(a) (b)

Figure 3.29: a) Normalized current density and ArII/ArI lines ratio as a function of the antenna distance from the RF source exit plane; the magnets are located 35 mm from the exit plane and the current probe is installed on the axis 110 mm downstream. b) Current density as a function of the antenna position for different magnets locations.

### Conclusions

Summarizing, the developed plasma source produces a plasma density up to $\sim 10^{19}\mathrm{m}^{-3}$ and an electron temperature of $\sim 4.5$ eV. Ion energies as high as 100 eV have been measured in the ejected plume. The plasma source is based on a novel RF antenna combined with a particular magnetic field pattern generated by arrays of radially-oriented permanent magnets. After the characterization outside the vacuum tank, the repeatability of the plasma properties has been verified in a fully space-like environment, mounting the thruster inside the vacuum tank. The vacuum chamber has been equipped with electrical feedthroughs and feedthroughs for the gas feed line and the optical fiber. The design of the in-vacuum experiment has been part of this project.

A dielectric screen has been installed around the plume: the aim is to break possible particles paths along the magnetic field lines, forcing their detachment from the field lines and preventing a back flow. Furthermore, the screen prevents the rise of currents between the ejected plasma and the antenna. For the same reason the antenna have been encased in an insulating screen.

The plasma source has been monitored through the measurement of the optical emission spectrum and the ejected current has been measured by means of the current probe. The tests entirely in vacuum have confirmed the previous results: the acquired spectra and the current levels are compatible with those observed outside the vacuum chamber.

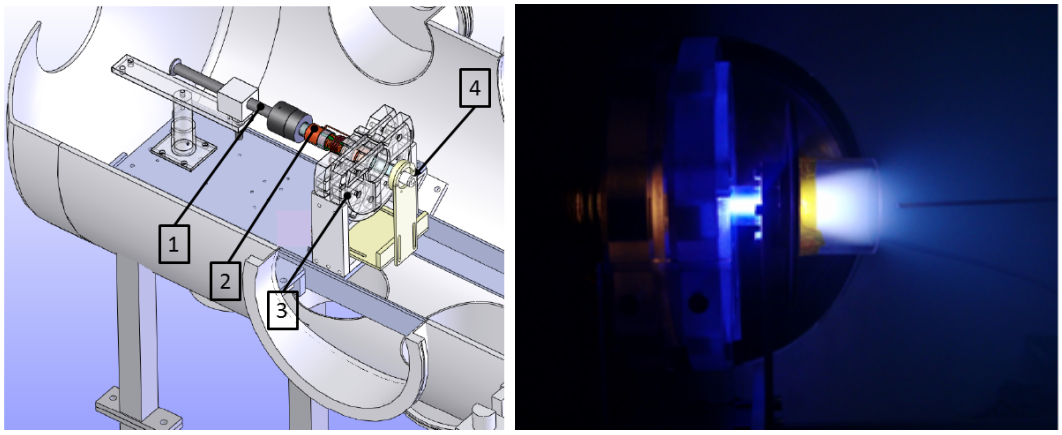


(a) (b)

Figure 3.30: a) Schematic of the RF plasma thruster mounted completely inside the vacuum chamber: 1) neutral gas injection system, 2) antenna, 3) permanent magnets arrays, 4) ejection orifice. b) Picture of the experiment: a cylindrical plume screen presents a diameter of 50 mm and a length of 50 mm is installed downstream the RF discharge. The 3 mm current probe is facing the ejection section of the thruster.

These experimental studies have determined the following guidelines, used for the design of the HPH.com thruster prototype:

1. In the target mass flow rate and power ranges (0.1-0.25 mg/s, 50-90 W) and for the identified source radius, the novel RF antenna produces a higher density and higher electron temperature plasma in comparison with standard RF systems.

2. The magnetic configuration is critical: a proper power coupling in the plasma is achieved only in the case of particular magnetic field patterns. Two permanent magnets lay-outs have been identified, made of two circular arrays of permanent magnets. The first lay-out consists of an axially-oriented magnets array followed by

a radially-oriented magnets array; in the second lay-out the permanent magnets are radially-oriented in both the arrays.

3. The use of a ceramic diaphragm to reduce the outlet diameter allows to work in different pressure regimes inside the source tube. The highest ionization in the source is achieved for an outlet diameter of 5 mm. The integrated ejected current values are comparable in the case of a 5 mm outlet diameter and a 10 mm outlet diameter. The ion energy is slightly higher for the latter.

4. Comparable plasma properties have been measured for antennas working at different frequencies in the range 3 - 13 MHz. However a lower frequency is preferable to reduce strain impedances and losses in the RF network. At lower frequencies the RF amplifier efficiency can be enhanced as well.

5. The use of a dielectric screen around the ejected plasma plume can be an effective method to force particle detachment from the field line and to avoid the rise of parasitic currents to the antenna.

## 3.4 HPH.com thruster prototype

The thruster prototype has been built by the plasma propulsion group of the Kharkiv Aviation Institute (KhAI - Kharkiv, Ukraine) which was a HPH.com project partner. The final configuration has been designed based on the results previously described in this chapter and those obtained at KhAI during a parallel experimental campaign. The thruster core is the novel RF antenna combined with a magnetic field produced by two circular arrays of radially magnetized samarium-cobalt permanent magnets. The axial component of the resulting magnetic field presents two peaks ($\sim$ 900 G) located at the inlet and outlet sections. In order to reduce the overall thruster volume, the length of the antenna has been reduced to 55 mm and only the electrode on the ejection side is used. The plasma source presents the same length of 55 mm. Experimental tests have been carried out to verify the proper behavior of the system with this antenna. The operating frequency is 13 MHz. The 18 mm-diameter discharge chamber is made of quartz; the outlet diameter is equal to 4 mm and the injector presents four radial channels; both the outlet diaphragm and the injector are made of alumina. The thruster case is made of fiberglass. Finally the thruster presents a conical screen around the plume.

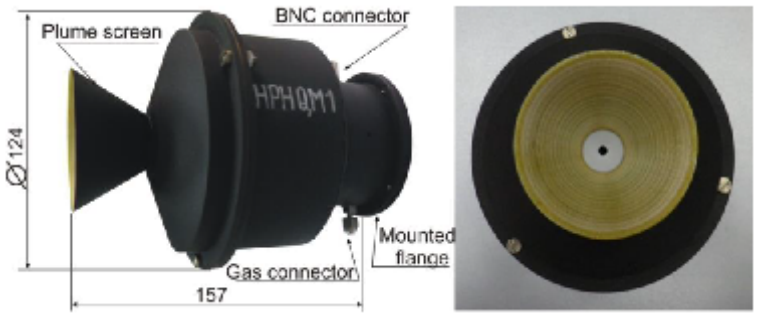


Figure 3.31: Picture of the HPH.com thruster prototype built at Kharkiv Aviation Institute.

The propulsive performance of the thruster prototype has been characterized by means of a pendulum thrust balance by the KhAI electric propulsion group. Previously, this thrust balance was used for the extensive characterization of Hall thrusters [85]. Thrust measurements on a RF thruster are challenging due to the RF interferences on the instrumentation and the issue associated with powering the thruster. Indeed RF power cables present a nonlinear elastic constant which changes during the operations due the temperature rise. Thus the overall elastic constant of the balance can change during the tests and also a spurious force component can be induced by thermal effects. Moreover the length of

the cables should be minimized to reduce resistive losses and parasitic impedances, which can alter the proper matching condition. To face these issues, a dedicated RF amplifier for in-vacuum operation has been built and mounted on the thrust balance together with the thruster. In this way the whole system mounted on the balance is powered in DC; only a low-power RF signal is transmitted through a coaxial cable to pilot the amplifier. Finally, the RF effective power has been limited below 10 W to limit the spurious RF interferences on the balance electronics. Fig. 3.32 shows the results obtained at KhAI: the highest propulsive efficiency, 13%, is achieved for a mass flow rate of 0.12 mg/s. For this mass flow rate the measured thrust is 0.5 mN giving a specific impulse of 422 s.

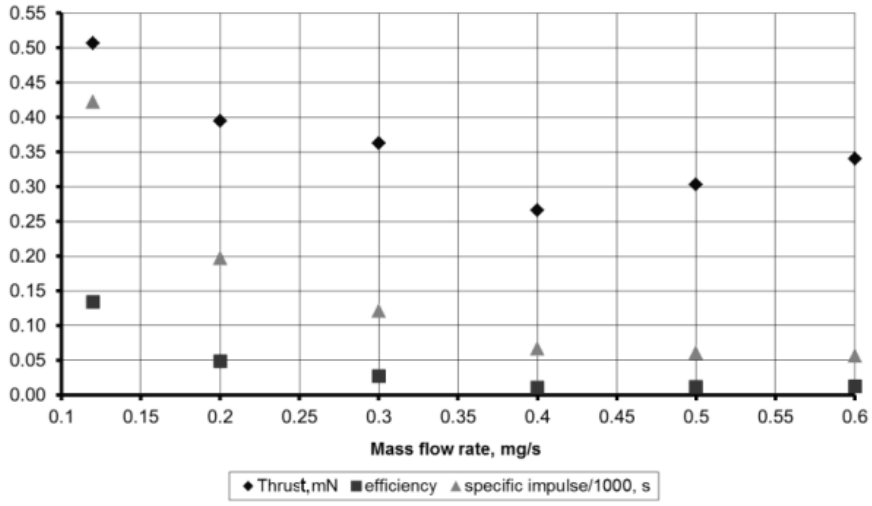


Figure 3.32: Thrust, specific impulse and propulsive efficiency of the HPH.com RF thruster prototype. The measuremnts have been performed by the KhAI electric propulsion group by means of a pendulum balance.

## 3.5 3D PIC Simulations of the Novel Radio-Frequency Antenna

In this section we investigate the performance parameters of the thruster in case of exploitation of the novel RF antenna technology. The investigation tool is the 3D PIC code F3MPIC. A detailed model of the plasma generation mechanism and heating is here neglected, since the analysis is focused on the particles dynamics inside the source and on the capability of the thruster to eject and to accelerate the plasma into vacuum. Electron and ion populations are imposed in the simulations according to plasma properties measured in experimental tests. An external magnetic field is provided according to the permanent magnets configuration used in the final prototype of the thruster.

The important role of the RF oscillating electric field in the exhaust region is investigated. The electric field periodically forces the particle motion, particularly the electron one, and influences the properties of the ejected plasma beam. In the simulations the electric field is generated by the antenna electrodes. The field is considered purely electrostatic. The simulations give both a physical insight of the plasma ejection mechanism and an estimation of the propulsive parameters of the thruster.

### 3.5.1 Definition of the Numerical Problem

The axial-symmetric geometry is made of two main regions: 1) the plasma source, 2) the ejection region. The plasma source is a cylindrical region which represents the thruster discharge chamber. The ejection region is a wider region downstream the plasma source in which the plasma expands. The radius of this region is at least double the radius of the source. The plasma produced in the source is exhausted into the ejection region through a narrow circular aperture placed at one end of the source tube, which represents the hole of the diaphragm used in the thruster to determine the neutral pressure regime inside the discharge chamber.

The geometry has been modeled by means of the 3D grid generator GMSH [86], defining all the physical entities required by the simulations. The geometrical dimensions reproduce those of the HPH.com thruster prototype: the source region is a 55 mm-length 18 mm-diameter cylinder, the outlet orifice has a diameter of 4 mm, whereas the ejection volume is 59 mm long and 54 mm wide.

The unstructured tetrahedral mesh is also generated by GMSH. The tetrahedra size $\Delta$x is set to satisfy the condition $\Delta x < \lambda_{De}$, where $\lambda_{De}$ is the Debye length. Different mesh sizes are used in the different regions of the system: a finer mesh in the plasma source and in the ejection orifice, a coarser mesh in the expansion volume, where the plasma density is orders of magnitude lower than in the source. On the other hand, $\Delta x$ should be

large enough to have a statistically significant number of numerical macroparticles in each tetrahedron. The final mesh size becomes a trade-off choice among the aforementioned issues with typical ratio $\lambda_{De}/\Delta x \approx 1.5 - 2$. The mesh (Fig. 3.33a) comprises $\sim$1.9 $\times 10^6$ tetrahedra.

All the physical walls are defined as particles removing elements, i.e. each particle impacting the wall is removed from the simulation domain.

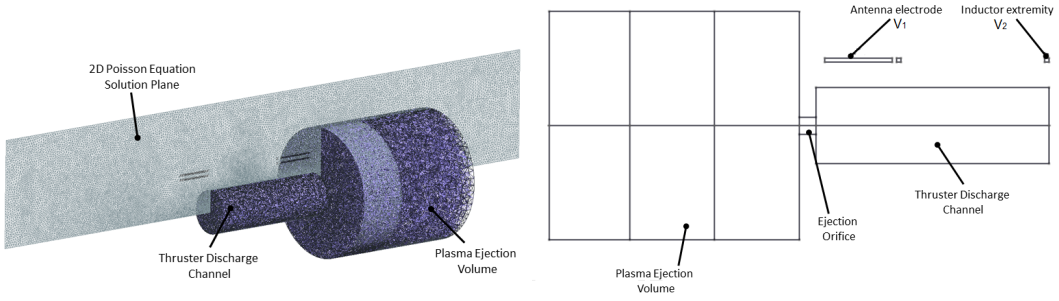


(a) (b)

Figure 3.33: a) View of the tetrahedral mesh generated by means of GMSH to simulate the RF thruster. b) Schematic of the simulated geometry.

F3MPIC is used in its 2D-3D electrostatic version. The Poisson equation is solved in a 2D domain, exploiting the axial-symmetry of the system. The domain for the solution consists of a plane which cuts longitudinally the 3D geometry.

The HPH.com prototype is based on the novel RF antenna with a single electrode on the ejection side. As previously mentioned, the antenna produces a strong RF axial electric field which forces particles motion. In order to reproduce the same electric field pattern the electrode itself is introduced in the simulations. Since the electrostatic potential is solved on a 2D plane which cuts longitudinally the simulation geometry, the annular electrode is represented as a thin rectangular surface. Similarly, the extremity of the inductor on the injection side is included as a small surface and properly polarized to reproduce the potential difference at the antenna edges. The electrode length is 15 mm, whereas antenna overall length is 55 mm. The proper electric potentials $V_j$ have been applied to the electrode and to the inductor extremity, according to the the harmonic relation:

$$V_j = V_{0j} \sin(2\pi f t + \phi) \tag{3.6}$$

where $V_j$ is the potential amplitude, t is the simulation time, f the operating frequency and $\phi$ the phase. The amplitudes are calculated through the antenna circuital modeling and are equal to $V_1$ = 1000 V and $V_2$=500 V for the electrode and the inductor extremity

respectively (Fig. 3.33b). Finally, a potential equal to 0 has been set on the boundaries of the Poisson solution plane.

The static magnetic field is generated by two permanent magnet rings with radial magnetization. The rings present an inner diameter of 55 mm, an outer diameter 95 mm and a width of 20 mm. The resulting magnetic field is plotted on Fig. 3.34. The axial component presents two peaks of $\sim$ 900 G located at the ejection orifice and at the opposite side, i.e. at the injector wall. Differently, in the central source region the magnetic field is mainly radial.

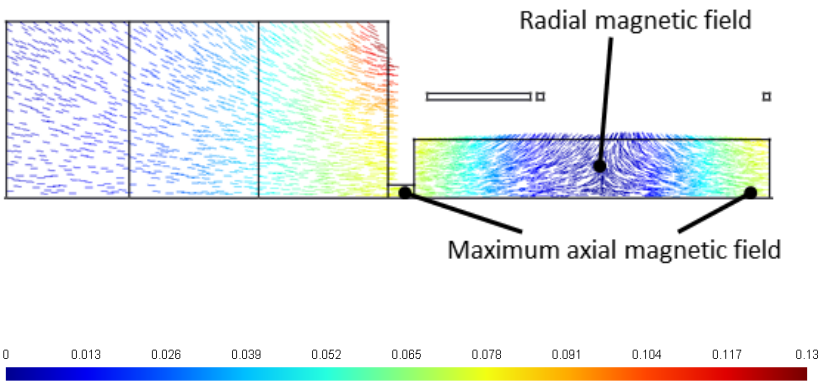


Figure 3.34: Magnetic field topology (in T) of the RF thruster: the peaks of the axial component occur at the outlet diaphragm and at the injection wall.

A fully ionized plasma made of two particle species (ions and electrons) is simulated. The weight of a numerical macroparticle is 1000, i.e. 1000 physical particles are aggregated in a numerical macroparticle. The number of macroparticles initially loaded is $10^6$ for each species. The electron temperature is set to 4 eV and the ion temperature to 300 K. The ion species is made of single-charged argon ions. The macroparticles are continuously loaded in the source region with a constant rate of 2.5 $\times$ $10^{12}$ macroparticles/s, and with a velocity distribution according to a Maxwellian population. The load of macroparticles is spatially uniform. Collisional effects are not included. The simulation consists of two stages: 1) we simulate 10 $\mu$s using a rough time step of $10^{-9}$s to let ions leave the plasma source and fill the downstream volume; 2) we simulate additional 1$\mu$s using a finer time step of $10^{-10}$s to solve the electron cyclotron period, equal to 0.36 ns for a maximum magnetic field of 1000 G. The overall simulation time has been set in order to reach a steady condition, continuously monitoring the number of computational particles in the domain, whose final value is 3 $\times 10^6$. The mean plasma density reached at steady state condition is $\sim 1.5 \times 10^{14} \mathrm{m}^{-3}$. We choose to simulate this lower density level in comparison

with the real thruster since higher densities imply a drastic increase of the computational time.

### 3.5.2 Simulation Results

The simulation gives a physical insight of the plasma behavior forced by the electrostatic fields generated by the novel antenna operating at 13 MHz. The geometrical features of the 3D simulation domain, the magnetic topology, the simulation settings and the constraints for the Poisson solver have been described in the previous sections.

Fig. 3.35 illustrates the ion density evolution during the first simulation stage using the rough time step $10^{-9}$ s. Ions start leaving the source region after about $1\mu$s and reach the end of the simulation volume in about $6\mu$s. Electrons present a higher mobility and are ejected from the plasma source in a shorter time scale. Furthermore, the electron dynamics is strongly dependent on the forcing RF field as detailed below.

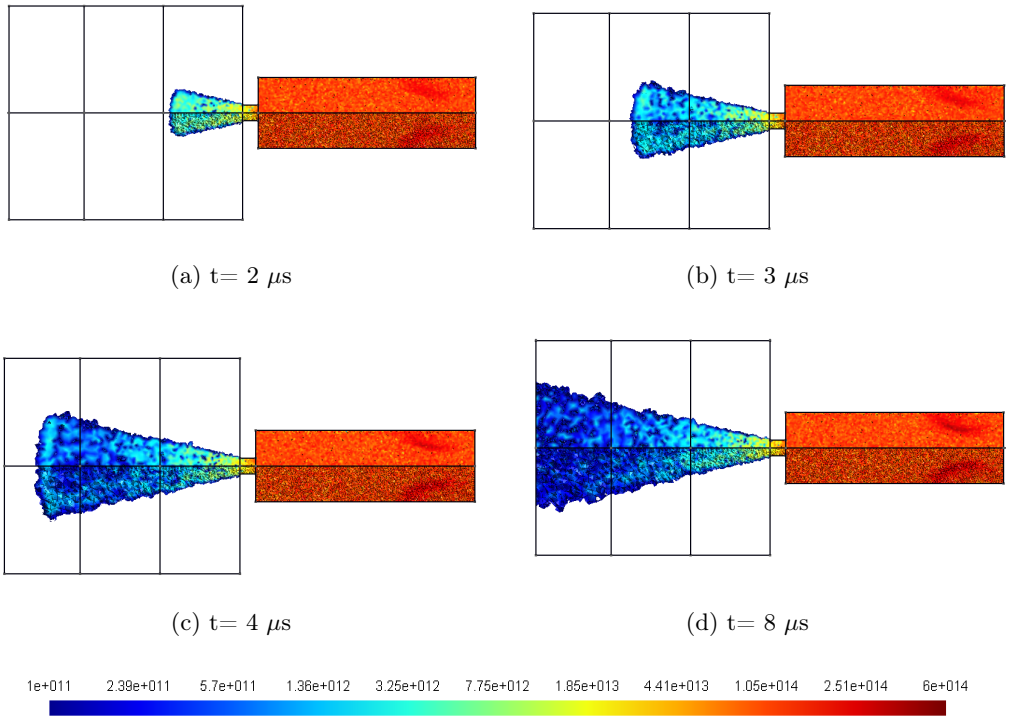


(a) t= 2 $\mu$s (b) t= 3 $\mu$s

(c) t= 4 $\mu$s (d) t= 8 $\mu$s

Figure 3.35: Ion density ($m^{-3}$) evolution during the first simulation stage with a time step of $10^{-9}$s.

Fig. 3.36 illustrates the electric field pattern and the potential changes in a RF period generated by the novel antenna. The electric field presents a strong oscillating axial component in the central region of the source. Another characteristic of the field is the radial component which arises in the region under the electrode during the negative and positive half-cycles, due to electric field lines terminating on the electrode. This peculiar oscillating electric field deeply affects electron motion and more weakly ion motion. Fig. 3.37 shows the electron density for different phases within the RF cycle. Electrons are pushed back and forth along the source in a RF period. Particularly, they are repelled by the electrode during the negative half-cycle as shown in Fig. 3.37a, 3.37e and 3.37f. On one side they are pushed upstream towards the source end, on the opposite side they are pushed downstream into the vacuum volume through the ejection orifice. On the contrary, electrons are spread throughout the discharge chamber as the electrode is positively polarized. The overall effect is periodically-forced ejection of electrons.

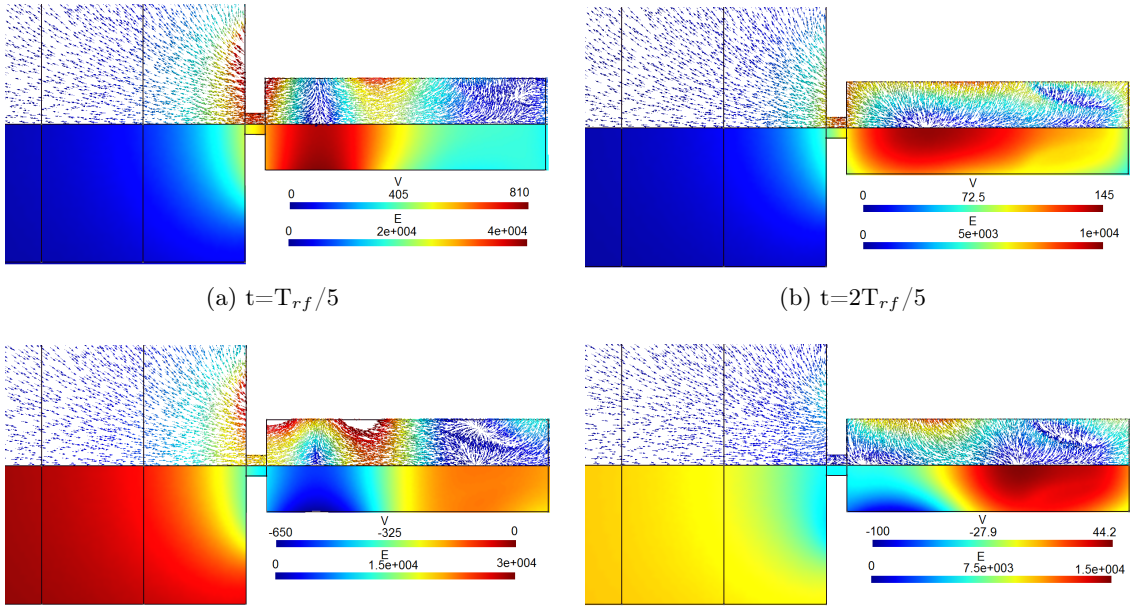


(a) t=$T_{rf}/5$ (b) t=$2T_{rf}/5$

(c) t=$3T_{rf}/5$ (d) t=$T_{rf}$

Figure 3.36: Electrostatic potential (V) and resulting electric field at different time frames within the RF period.

During the whole RF period, a high electron density region can be observed close to the source end. This region presents a hollow shape whose borders follow the magnetic field lines curvature. The electrons are here confined by the magnetic field cusp produced by the permanent magnets. This effect takes place only on the upstream side of the magnets since downstream the predominant effects are produced by the electric field generated by the

electrode. Furthermore, during the positive RF half-cycle the electron spatial distribution is characterized by a higher density cylindrical core, located around the axis just before the ejection orifice. Electrons can produce a higher ionization in this region, creating a plasma structure similar to the experimentally observed high density central core. However, a final assessment requires the use of a collisional ionization model in the simulation.

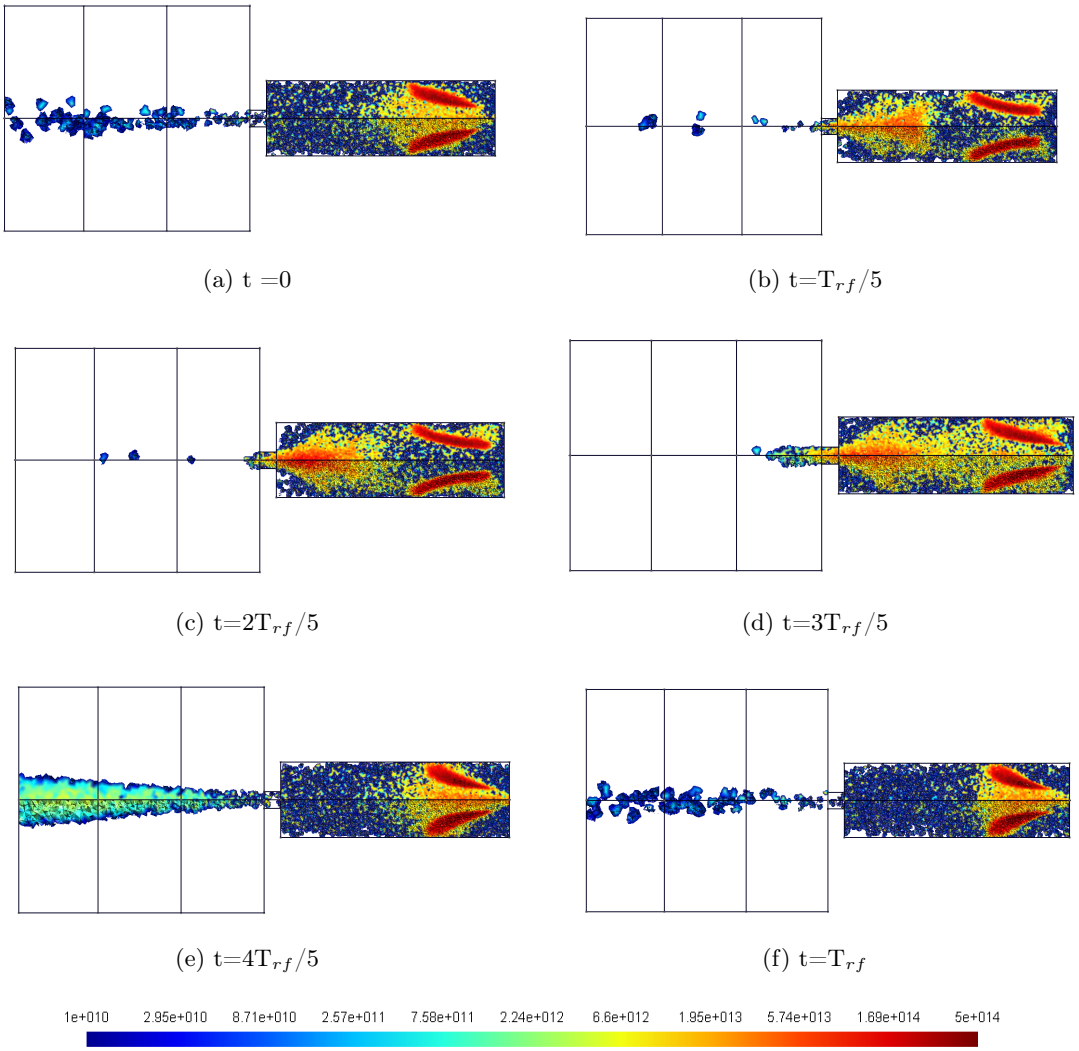


(a) t =0 (b) t=$T_{rf}/5$

(c) t=$2T_{rf}/5$ (d) t=$3T_{rf}/5$

(e) t=$4T_{rf}/5$ (f) t=$T_{rf}$

Figure 3.37: Electron density ($m^{-3}$) at different time frames within the RF period. This results refer to the simulation stage with the finer time step ($10^{-10}$s).

The ion response to the oscillating electric field is less evident than the electron one due to the different dynamics timescales of the two particle species. The ions are scattered along the entire discharge chamber without a net RF-forced motion and progressively expand in the vacuum region (Fig. 3.38). However, both the ejected ion mass flow and the ion velocity in the beam present fluctuations around a mean steady value according to the RF period. During the simulation we record position and velocity of the particles crossing a control surface located 2 cm downstream the exit plane at each time step. Then the recorded data are post-processed to estimate the ejected mass flow rate and particles velocity distribution functions. The periodic fluctuations of the ion mass flow rate and velocity can be observed in the plots shown in Fig. 3.39c and 3.39d. The reason is related to the periodic polarization of the electrodes at the extremities of the antenna which periodically alters the potential distribution inside the plasma. Indeed, the time delay between two peaks in the plots is $7.7\times10^{-8}$s equal to the RF period.

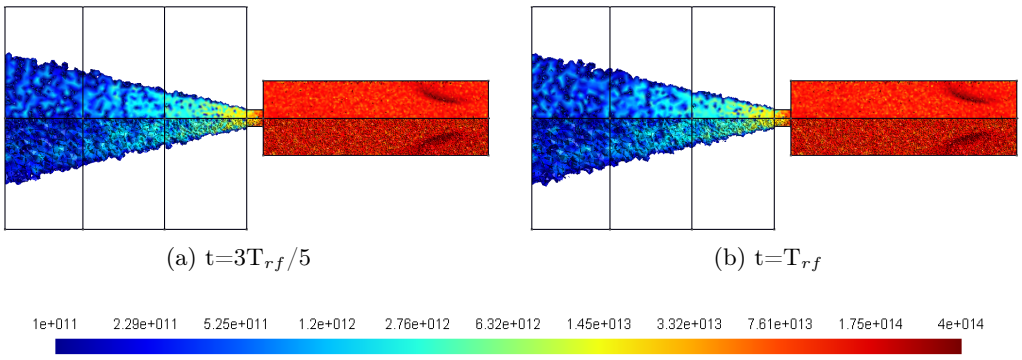


(a) t=3T$_{rf}$/5 (b) t=T$_{rf}$

Figure 3.38: Ion density (m$^{-3}$) at different time frames within the RF period. This results refer to the simulation stage with the finer time step ($10^{-10}$s).

Fig. 3.39b and 3.39a illustrate the electron and ion axial velocity distribution functions (EVDF and IVDF) through the same surface. An electron drift velocity can be observed showing the electron outward motion previously described. The most-probable kinetic energy is ∼280 eV. The distribution appears asymmetric respect to its peak value with a steep drop above a certain velocity threshold. This effect is probably due to the depletion of electrons to be ejected. Referring to the electron dynamics (Fig. 3.37), electrons are distributed throughout the source when the electrode is positively polarized, comprising the region under the electrode itself. When the polarization becomes negative, electrons are progressively repelled upstream and downstream, and the electron density under the electrode progressively decreases. The velocity distribution of ejected electrons is directly related to a combination of electrode potential, electron density and velocity distribution

in the region before the outlet orifice, giving this asymmetric shape with a steeper slope for velocities higher than the most probable one. Finally, a small number of electrons presents negative velocity values: these few electrons are low-energy electrons recalled during the positive electrode polarization intervals. Similarly, ions present a drift outward velocity in the axial direction with a mean value of 16100 m/s. This value is about 5 times the Bohm velocity ($\alpha \approx 5.2$). Finally, Fig. 3.39e and 3.39f highlight the radial distribution of the velocity components of ions. The axial velocity distribution is uniform along the radial direction. On the other hand the average radial velocity of ions increases with the radius.

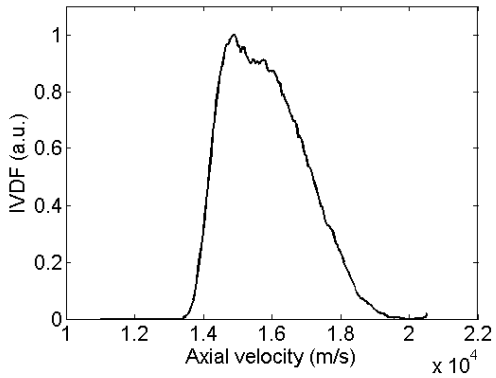


(a) Ion Velocity Distribution

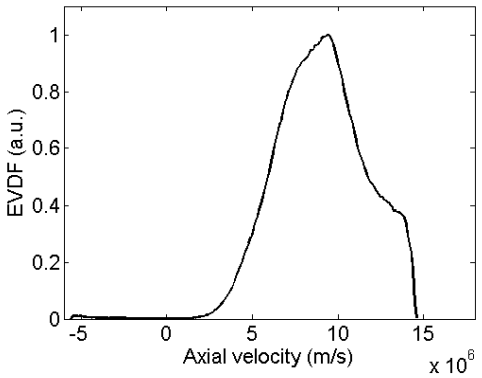


(b) Electron Velocity Distribution

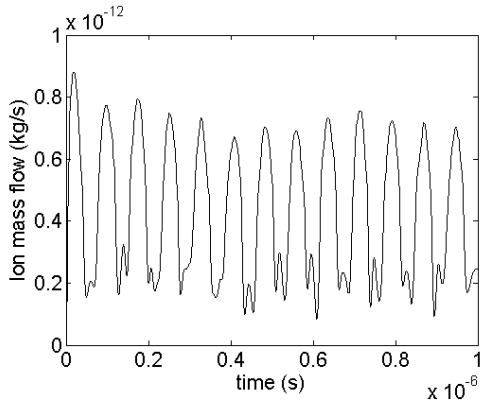


(c) Ion mass flow

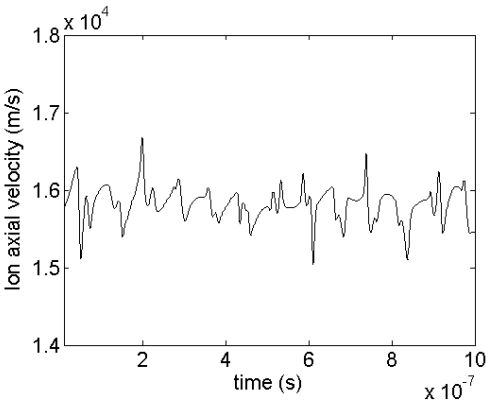


(d) Ion velocity

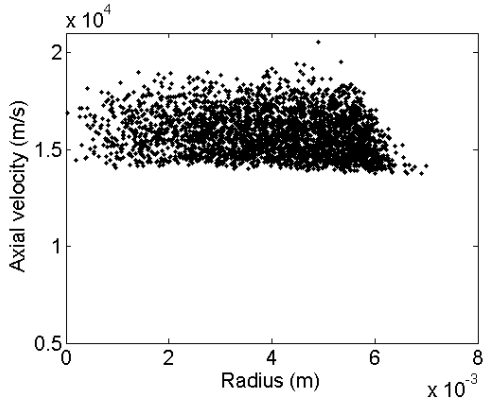


(e) Ion axial velocity

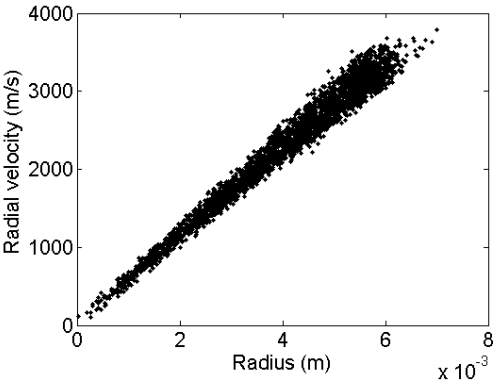


(f) Ion radial velocity

Figure 3.39: Properties of the plasma beam crossing a control surface located 2 cm downstream the thruster exit plane. The position and velocity of particles crossing the control surface have been recorded during the $1\mu$s simulation with the fine time step equal to $10^{-10}$s. The data have been post-processed to estimate the distribution functions, mass flow rates and velocities.

CHAPTER 4

# Magnetized DC Discharge Investigation

The ion velocity field in the plume of the Stanford Cylindrical Cusped Field Thruster (CCFT) has been characterized through Laser-Induced-Fluorescence measurements. We aim to obtain a picture of the physical processes taking place in the thruster with a particular focus on the acceleration mechanism and on the origin of the hollow conical plume observed in such category of thrusters. The experimental results have been correlated to previous measurements and their interpretation has been supported by dedicated 3D particle-in-cell simulations.

## 4.1 Laser-Induced-Fluorescence Ion Velocimetry

### 4.1.1 Experimental Lay-out

#### Vacuum Facility

The measurements have been carried out at the Stanford Plasma Physics Laboratory vacuum facility, which consists of a stainless steel chamber (4 m long and 1.25 m in diameter), equipped with a two-stage cryogenic cooling system. The first stage is two shrouds cooled with a Polycold Fast Cycle Water Vapor Cryopump (PFC, Model 1100), and the second stage consists of two cryopanels cooled to 16 K with cryogenic helium. A rotary pump and a blower provide the initial rough vacuum. The chamber achieves a background pressure of $5 \times 10^{-7}$ mbar and maintains a pressure of $2.6 \times 10^{-5}$ mbar while operating the thruster. The pressure is measured by means of a ionization gauge.

**Laser-Induced-Fluorescence Setup**

The Laser-Induced-Fluorescence method applied to ion velocimetry has been extensively described in section 2.1.5. We summarize below the main features of the system used to characterize the ion velocity field in the plume of the Stanford Cusped Field Thruster.

The Xe II (ion) $5d[4]_{7/2}$ – $6p[3]_{5/2}$ transition is laser-pumped and the resulting fluorescence to the $6s[2]_{3/2}$ state at $\lambda_{23} = 541.915$ nm is collected for determining the Doppler shift in the absorbed laser radiation. This LIF scheme has been used previously for xenon ion velocity measurements in different types of plasma thrusters [87, 88, 89]. The Xe I (neutral) $6s'[1/2]_1$ – $6p'[3/2]_2$ transition at 834.682 nm is used in an optogalvanic (OG) stationary reference measurement on a xenon hollow cathode lamp. The observed OG peak is known to be located at $\lambda_{12} = 834.682$ nm during the laser scan. We utilize the Xe I line for the stationary reference because the much higher neutral xenon population in the lamp provides a stronger OG signal than the sparser xenon ion population. Figure 4.1 shows the two aforementioned schemes for the LIF and the optogalvanic stationary reference.

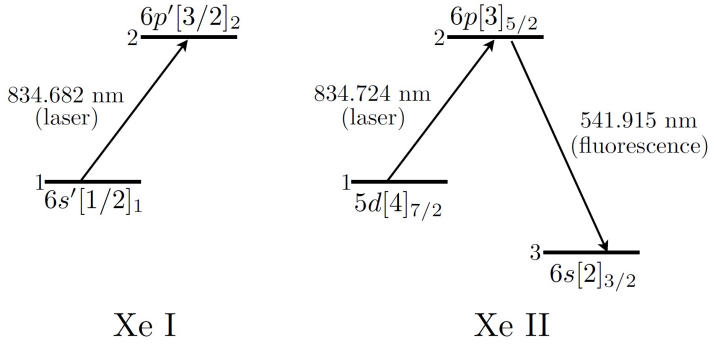


Figure 4.1: Xenon atomic transitions used in this work and the respective wavelengths in air. Xe I (neutrals) in a hollow cathode lamp are used as an optogalvanic stationary wavelength reference when probing moving Xe II (ions) in the thruster plume.

A schematic of the LIF experimental setup is illustrated in Fig. 4.2. The exciting laser beam is generated by a New Focus TA-7600 semiconductor tapered amplifier which is seeded by a 20 mW tunable external-cavity diode laser (New Focus, Model TLB-6017) through a polarization-maintaining optical fiber. The laser beam power is within the 40-90 mW range avoiding to saturate the transition. Wavelength modulation of the diode is obtained with a voltage ramp from a function generator (SRS Model DS345).

The beam emitted by the laser amplifier (lb1) passes through two beam samplers (BS1 and BS2) and enters a vacuum chamber window via a sequence of mirrors. The first beam sample (lb2, 10% of the main beam) is further separated into two minor beams (lb2a and lb2b) by means of a 50-50% beam splitter (BS3). Beam lb2a is directed to a Burleigh

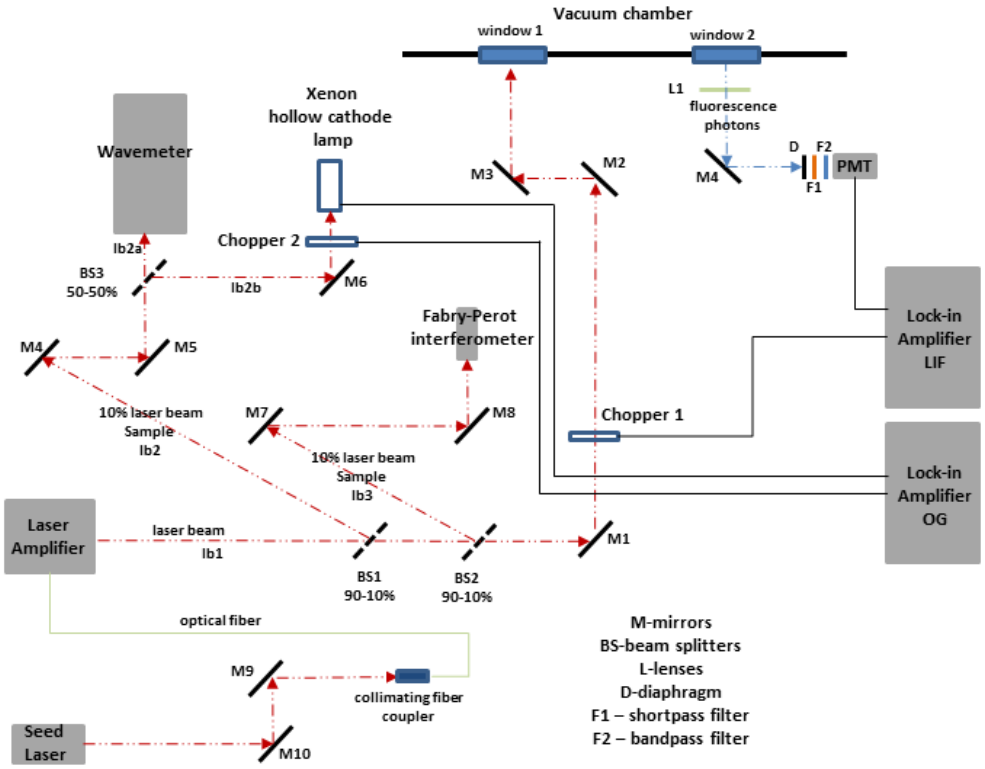


Figure 4.2: Schematic of laser induced fluorescence experimental setup.

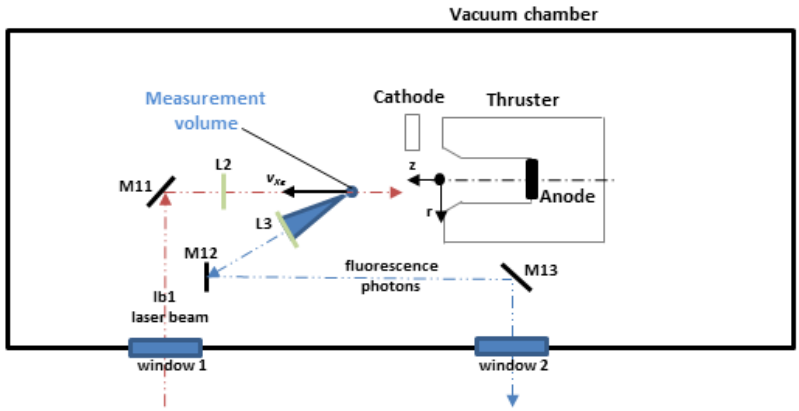


Figure 4.3: LIF experimental setup inside the vacuum chamber.

WA-1500 wavemeter for a simple wavelength reading while tuning the laser parameters. The second minor beam (lb2b) is mechanically chopped (Chopper 2) and passes through a xenon hollow cathode lamp for a zero-velocity optogalvanic reference signal. The current in the lamp is detetected through 10 kΩ shunt resistor and a 700 nF capacitor to block the DC signal component. A lock-in amplifier then isolates the AC component at the chopping frequency. Another beam sample (lb3) is steered to the Fabry-Perot interferometer (FSR = 1.5 GHz). As described in section 2.1.5, the combined use of the xenon hollow cathode lamp for the reference line and the Fabry-Perot interferometer allows a fine reconstruction of the wavelength as a function of time throughout the scan. Before entering the vacuum chamber, the main beam (lb1) is mechanically chopped (Chopper 1) at 1.5 kHz.

Once inside the chamber (Fig. 4.3), the beam is focused on the target plasma by a system of mirrors and lenses. Fluorescence photons are collected through a lens, directed back out of the chamber, and focused on the aperture of a photomultiplier tube (PMT) (Fig. 4.2). In front of the PMT the following components are installed: a 3 mm iris to shadow background emission from the plasma outside of the target measurement volume, a shortpass filter with a 750 nm cutoff to reject any scattered laser light at 834-835 nm, and a 10 nm bandpass filter centered at 540 nm further restricts the collection system to detect only photons originating from the desired fluorescence transition at 541.92 nm. The collection system is aligned by firing a helium neon laser backwards through the collection path. The measurement volume is defined as the intersection between the main beam and the collection optical path (accounting for the iris), which is estimated to provide a spatial resolution of about 1 mm. Finally, the collected fluorescence signal from the PMT is processed by a second lock-in amplifier which extracts the signal component at the chopping frequency.

### Thruster Setup Description

The thruster is mounted on a two-axis horizontal motorized stage plus a 360° rotation stage for obtaining spatially resolved measurements – the LIF measurement volume remains fixed in space. A previous study [37] conducted axial LIF ion velocity measurements at several points near the CCFT exit plane in an 18 mm axial and 12 mm radial range. The current work extends these measurements to fully specify the velocity vectors, i.e. both magnitudes and directions, at a subset of points near the magnetic separatrix of the top cusp. This is accomplished through two LIF measurements at each point, one with the incident beam parallel to the thruster axis and one with the thruster rotated 30° off-axis. We choose 30° rather than a full 90° radial measurement based on geometrical constraints and the need to access inside the discharge channel. All data are taken on the cathode side of the plume, again for geometrical reasons. The CCFT is operated with a xenon mass flow rate of 0.586

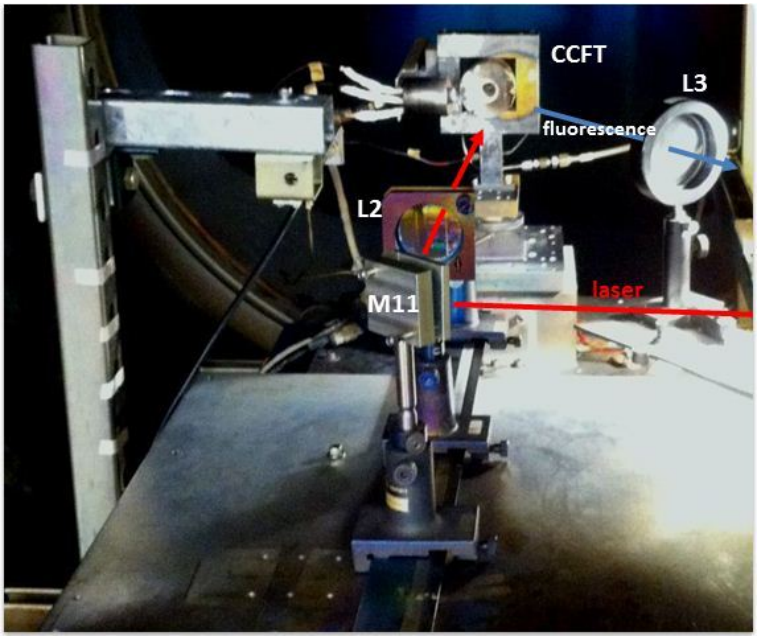


Figure 4.4: Picture of the CCFT and the LIF optical system inside the vacuum chamber.

mg/s and applied anode potential of 300 V, drawing ∼0.4 A of current and 120 W of power from a Sorenson DCS-600-1.7 DC power supply. An IonTech (Model HCN-252) cathode is used as the electron source. The cathode, installed 28.3 mm downstream of the exit plane at a radius of 30 mm, is operated on argon propellant with a mass flow rate of 0.14 mg/s. The cathode keeper is operated in current limited mode at 0.25 A and the nominal heater current is 7 A. The operating conditions are summarized in table 4.1. The thruster body is kept electrically floating, using an insulating component between the thruster itself and the metallic support.

### 4.1.2 Experimental Measurements

LIF measurements have been carried out in the points of a spatial grid in order to provide a spatially resolved characterization of the ion velocity field. The spacing between points is 2 mm both in the radial and in the axial direction with the exception of the region nearby the exit plane where we have used a finer grid with 1 mm axial spacings. The uncertainty on the thruster position relative to the laser direction is ± 1mm. The probed region extends from Z = -4 mm to Z = 4 mm in the axial direction and from 0 to 12 mm in the radial direction, where the reference frame origin is located at the thruster centerline on the exit plane (Fig. 4.5a). We have obtained a reliable LIF signal in the points reported as diamond markers in Fig. 4.5b, whereas we can't determine an unequivocal peak in the

| Parameter | Value |
|---|---|
| Anode flow | 0.586 mg/s (xenon) |
| Anode voltage | 300 V |
| Anode current | 0.4 A |
| Anode power | 120 W |
| Cathode flow | 0.14 mg/s (argon) |
| Keeper voltage | 24 V |
| Keeper current | 0.25 A |
| Heater voltage | 9.7 V |
| Heater current | 7 A |

Table 4.1: Operating parameters of the thruster during the experiments.

LIF profile in the remaining points (reported as circles). We suppose the main reason is the lower plasma density in the latter points, which are located close to the wall inside the discharge channel and nearby the centerline downstream the exit plane. This is consistent with a hollow conical plume with a low-density central region and two high density wings. This particular plume shape will be described later.

An example of LIF, optogalvanic reference and Fabry-Perot signals is shown in Fig. 4.6. A time constant of 3 s is set in both the lock-in amplifiers employed for LIF and optogalvanic detection; thus, both the signals present the same processing time with a negligible relative delay. The lock-in amplifier sensitivity used for LIF detection ranges from 10 $\mu$V to 200 $\mu$V. The sensitivity set for optogalvanic detection is 500 $\mu$V.

Acquired LIF profiles at a given axial position Z = 1 mm and different radii are shown in Fig. 4.7a: the Doppler shift increases in the outer radii region, revealing an ion acceleration. This effect is highlighted by Fig. 4.8a which reports the ion most probable velocity in function of the radial position. Similarly, Fig. 4.7b illustrates two LIF profiles characterized by different Doppler shifts due to the different axial locations. Fig. 4.8b shows the accelerating front is located between Z = -2 mm and Z = 1 mm; furthermore the exact location of the accelerating front is dependent on the considered radial position. Recall that the most probable velocity is taken at the observed Doppler shifted peak in the XeII fluorescence signal relative to the optogalvanic stationary XeI reference; additional smaller peaks in the acquired signal may be indicative of multiple ion velocity classes present at the measurement location. Double ion populations (Fig. 4.9) are observed in the acceleration region, where already accelerated ions coexist with low velocity new-born ions.

A complete picture of the ion velocity field appears in Fig. 4.10-4.11, mapping the most probable ion velocities in the vicinity of the last CCFT cusp. The uncertainty on

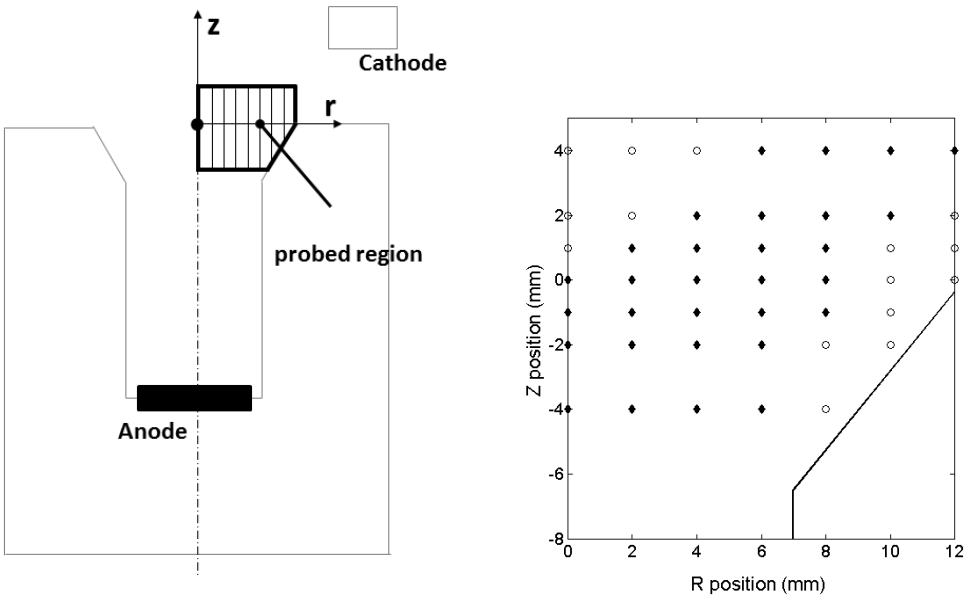


(a) (b)

Figure 4.5: a) Investigated region nearby the exit plane of the thruster; b) measurement grid: reliable measurements have been obtained in the points with filled diamond markers, whereas in the remaining points (empty circles) a clear peak in the LIF signal has not been identified.

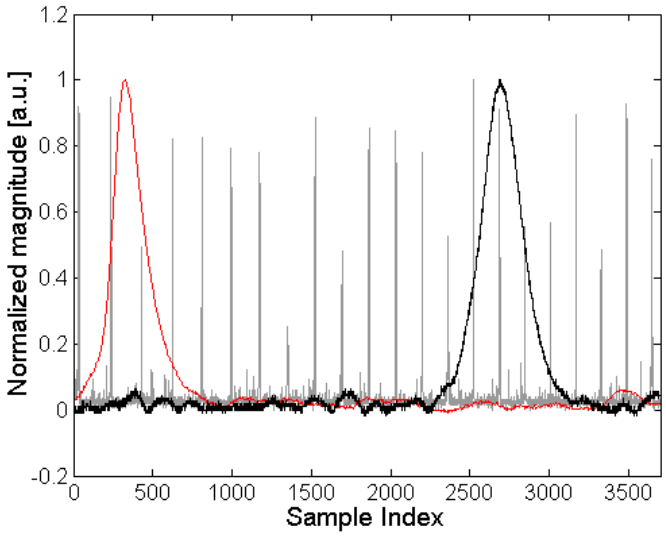


Figure 4.6: XeI optogalvanic reference (red), F-P interferometer (gray), XeII LIF (black) acquired signals showing an ion population of about 2000 m/s.

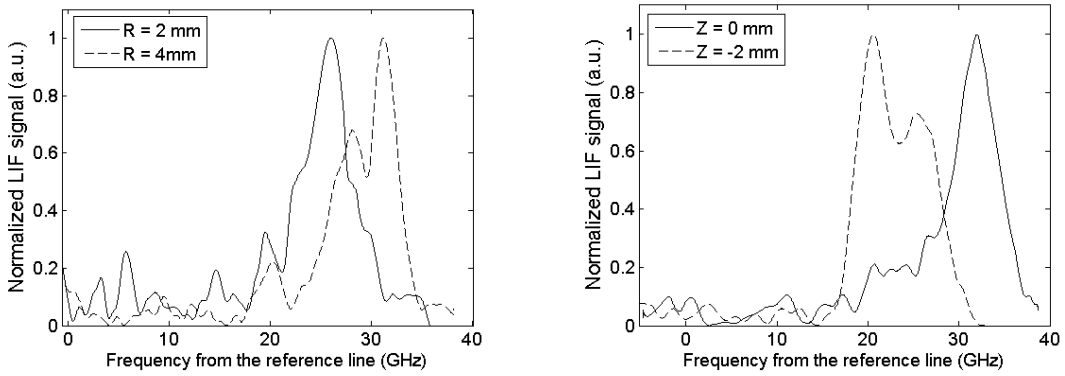


(a) (b)

Figure 4.7: a) LIF measurements at a fixed axial position Z = 1 mm and two different radial positions: the profiles remark a higher velocity for the outer radii region ; b) measurements at fixed radial position R = 4 mm: the ions accelerate between Z = -2 mm and Z = 0 mm.

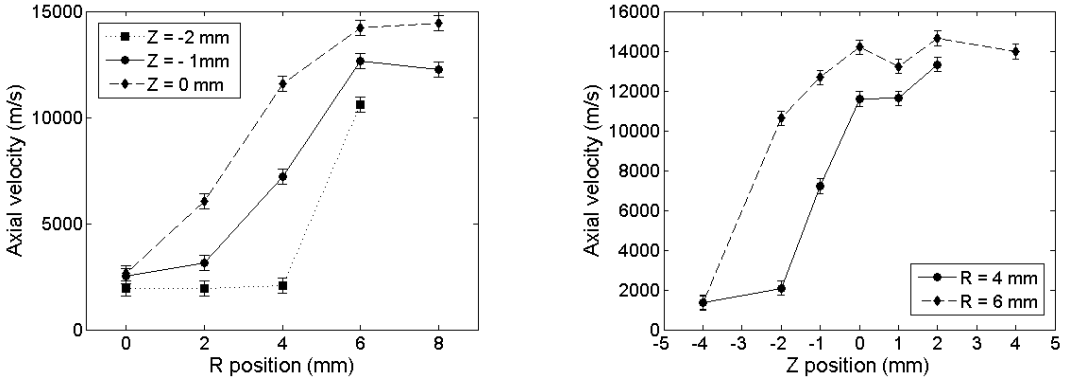


(a) (b)

Figure 4.8: a) Ion most probable velocities in function of the radius for different axial positions; b) Axial evolution of the ion velocity for different radial positions.

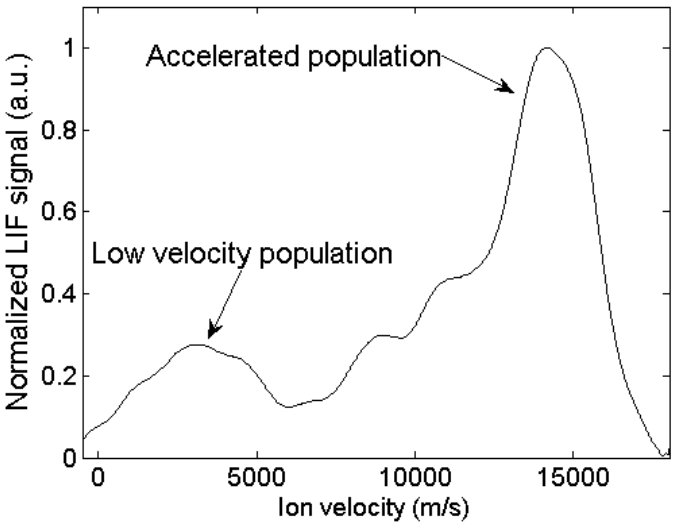


Figure 4.9: Multiple ion populations at Z = 0 mm and R = 6 mm.

the measured velocity is 360 m/s, derived from the wavelength shift uncertainty obtained through our preliminary tuning process (section 2.1.5).

Points where LIF traces are taken are indicated by $\Delta$ symbols. The acquired velocities are interpolated throughout the remainder of the domain using an inverse-distance method [37] where $\phi_s$ are the measured source point velocities and $\phi_d$ is the interpolated destination point velocity:

$$\phi_d = \frac{\sum w_s \phi_s}{\sum w_s} \tag{4.1}$$

$$w_s = D^{-E}. \tag{4.2}$$

The weighting function $w_s$ is determined by the distance $D$ between the source and destination points and a weighting factor $E$ chosen here to be 3.5. This value gives more weight to immediately adjacent source points and yields good smoothing. The white area in the lower right hand corner of the plots represents the angled thruster face near the exit plane ($Z = 0$, see Fig. 4.5). Magnetic field lines calculated from FEMM [38] are indicated with dotted lines.

Figures 4.10a and 4.10b illustrate the measured velocity components with the exciting laser beam oriented parallel to the thruster axis ($R = 0$) and at a 30° counterclockwise rotation relative to the thruster axis, respectively. The uncertainty on the initial alignment between thruster axis and laser direction is ± 3° due possible misalignments of the structure supporting the thruster. Inside the thruster discharge channel, the ions exhibit relatively slow axial velocities of about 2000 m/s. The axial acceleration begins to occur

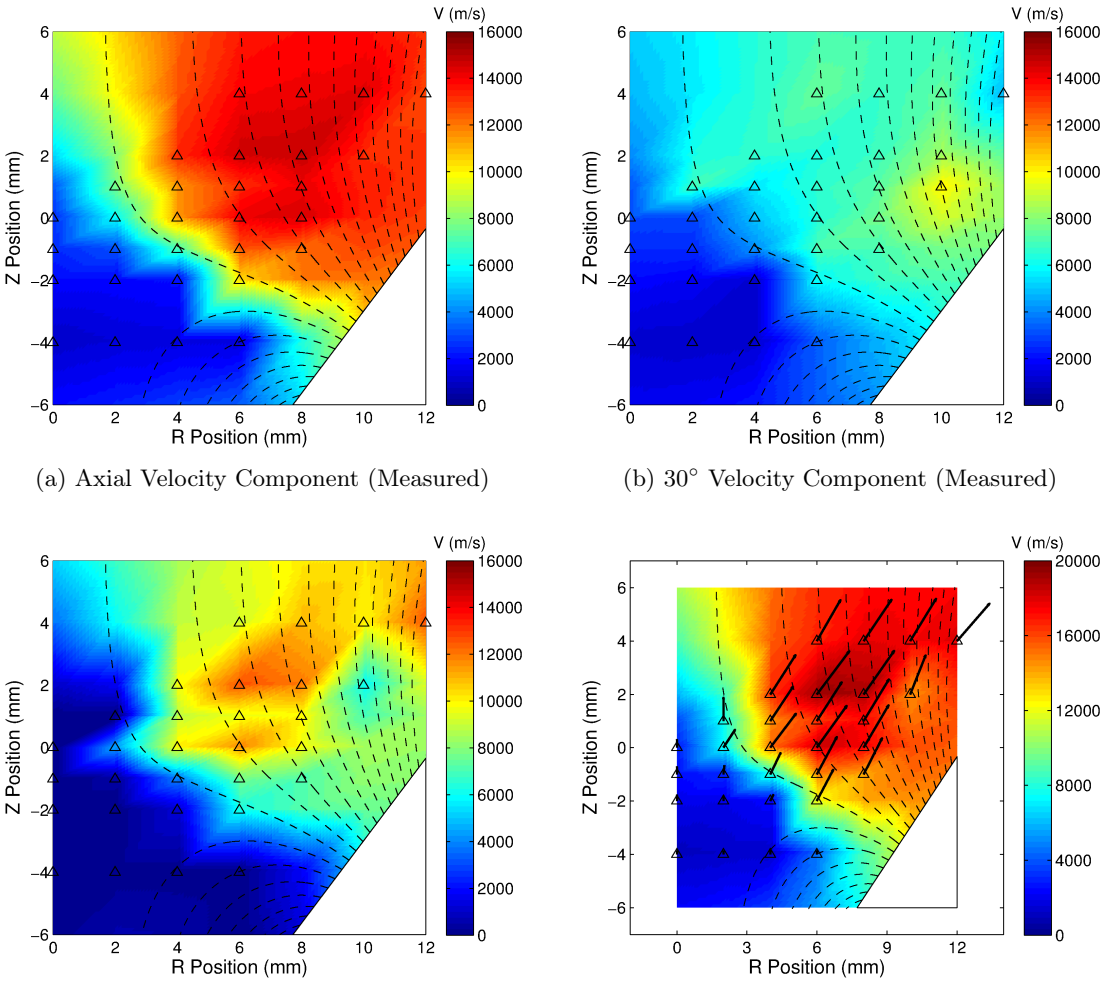


(a) Axial Velocity Component (Measured)

(b) 30° Velocity Component (Measured)

(c) Radial Velocity Component (Calculated)

(d) Total Velocity (Calculated)

Figure 4.10: Compiled LIF data for the CCFT operating at 300 V anode potential and 0.586 mg/s xenon mass flow rate. Calculated (dotted) magnetic field lines from FEMM [38] are indicated. LIF scans are taken with the exciting beam (a) parallel to the main axis (R = 0) and (b) 30° from R = 0 in a CCW rotation. The two data sets permit calculation of the (c) radial velocity components and (d) total velocity vector magnitudes and directions.

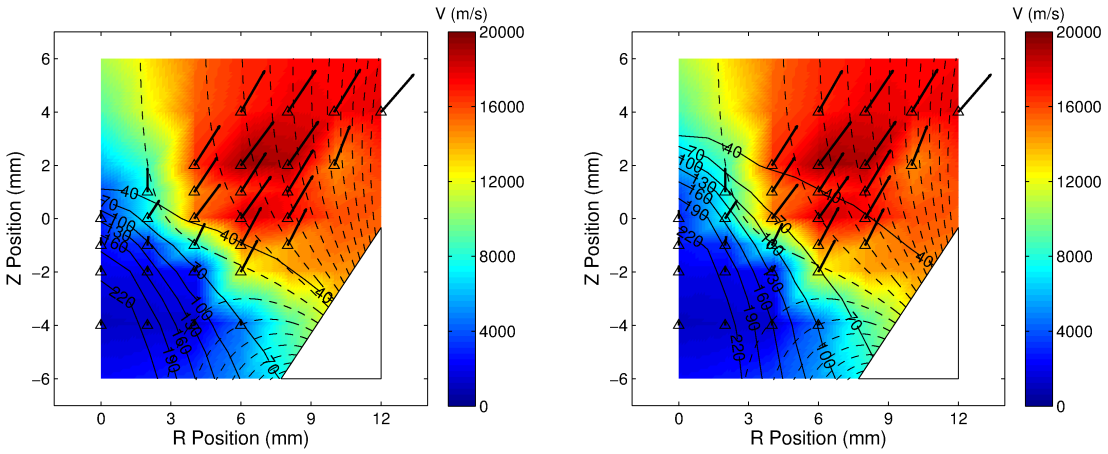


(a) Total Velocity with Measured Potential

(b) Total Velocity with Adjustusted Potential

Figure 4.11: Compiled LIF data for the CCFT operating at 300 V anode potential and 0.586 mg/s xenon mass flow rate. Previously measured potential data are superimposed in (a). Adjusting the measured potential 2 mm in the $+Z$ direction in (b) illustrates how ions are most likely accelerated by the steep potential drop in directions orthogonal to the equipotential lines.

at Z = -2 mm, especially at radii close to the channel wall. Moving downstream, the axial acceleration front progressively penetrates towards the centerline. Figure 4.10a highlights the correspondence between the measured velocity profile and the magnetic field structure in this region: the acceleration takes place orthogonal to the angle of the magnetic separatrix of the last cusp. In the investigated region the ions reach a maximum axial velocity of 14800 m/s. The combination of the axial and 30° velocity components ($v_{ax}$ and $v_{30}$, respectively) permits calculation of the total ion velocity ($v_t$) at each point, plotted in Fig. 4.10d:

$$\tan(\theta) = \frac{1}{\tan(30°)} - \frac{v_{30}}{v_{ax}\sin(30°)} \tag{4.3}$$

$$v_t = \frac{v_{ax}}{\cos(\theta)} \tag{4.4}$$

where $\theta$ is the total velocity vector angle from the thruster axis. The uncertainty on the calculated angle is ± 6° in the accelerated flow, i.e. in the region downstream Z = -1 mm excluding the centerline. Differently, in the discharge channel (Z ≤ -1 mm) and nearby the centerline the calculated angle $\theta$ is very sensitive to small variations in the measured values because of the low velocities; thus, the determination of angles is prone to a higher uncertainty giving also unreliable negative values. Angles calculated to be slightly negative are anyway shown in Fig. 4.10d forced to zero for a physical result. The relative uncertainty on the total velocity magnitude is below 9% throughout the accelerated plasma

region, whereas it significantly increases in the low-velocity region. These estimations are obtained propagating the uncertainties on the measured velocity components and on their angles relative to the thruster axis.

The radial velocity can be estimated by the measured components as well:

$$v_r = v_{ax} \tan(\theta) \tag{4.5}$$

The radial velocities (Fig. 4.10c) follow the same general pattern as the axial components, starting at low values in the thruster discharge channel and increasing in magnitude after the acceleration zone along the magnetic separatrix. As required for efficient conversion of ion momentum to thrust, the axial velocity components are greater in magnitude than the radial components.

The total calculated velocity vectors are shown in Fig. 4.10d. The ions slowly move downstream inside the discharge channel until they are sharply accelerated in the vicinity of the last magnetic cusp at a mean angle of 31.2°, roughly orthogonal to the first magnetic field line to bend out of the channel. The ion velocity angle increases to 36.6° if only the accelerated flow (i.e. for Z > -1 and excluding the centerline) is considered. The maximum measured velocity of 19300 m/s occurs at the point ($R$ = 8 mm, $Z$ = 2 mm). Previous plasma potential measurements in this region [37] obtained with a floating emissive probe, reproduced in Fig. 4.11a, show consistency with the measured velocity profile. Equipotential lines indicate about a 180 V potential drop through the separatrix, leading to a theoretical increase in xenon ion velocity of $\Delta v = \sqrt{2q\Delta\phi/M_i} = 16255$ m/s – which is in good agreement with the measured velocity values. We note that by adjusting the measured potential 2 mm in the $+Z$ direction (Fig. 4.11b), we achieve an even more physically consistent picture where accelerated ions are traveling nearly orthogonal to the 40 V equipotential line by the end of the potential drop. This small shift in position could be accounted for uncertainties in emissive probe position and LIF system alignment between the two distinct experiments, as well as the intrusive nature of the emissive probe that could push a measured potential drop upstream.

Note that for $Z \geq 1$ near the centerline, the signal-to-noise ratio (SNR) substantially drops and the determination of a reliable peak in the fluorescence signal is more difficult. This low SNR region continues while moving downstream for radii less than that of the high velocity conical region. A possible explanation is the lower ion density here in comparison with the high velocity region (which emits strong visible radiation, see Fig. 4.20). This feature has been identified in beam current measurements (section 4.2) which show two large peaks in the collected ion current density at angles corresponding to the high velocity conical plume.

These experimental measurements highlight how the ion velocity field, the magnetic field and the the electrostatic potential field are all correlated. Magnetized electrons,

influenced by the magnetic cusp geometry, set up the electrostatic field that in turn sets the acceleration regions and shapes the final ion trajectories. Since the ions are unmagnetized (with Larmor radii much larger than the thruster dimensions), the ion motion may be considered to be indirectly determined by the magnetic field topology. In the section 4.4 we investigate these relationships further through a numerical approach.

## 4.2 Beam Current Measurements

The ion current in the CCFT plume has been measured by means of a current probe (described in section 2.1.4). The thruster operating point is 0.586 mg/s(xenon) - 120 W (see table 4.1 for details). The probe is mounted in a fixed position located 20.3 cm downstream the exit plane of the thruster. Both the collector and the guard ring are polarized at -15 V. The current measurements have been carried out at different angular positions rotating the thruster as shown in figure 4.12a. The resulting current density in function of the rotation angle is illustrated in Fig. 4.12b. The profile presents two peaks located at an angle of $-28°$ on the cathode side and of 35.5° on the opposite side. These values are in agreement with the angles of the ion velocities observed nearby the exit plane through LIF measurements. An asymmetry of the peaks relative to the thruster axis is observed due to the presence of the cathode. Indeed on the cathode side the maximum current density is lower than on the opposite side and the current drops for angles higher than 45° due to a shadowing effect introduced by the cathode itself.

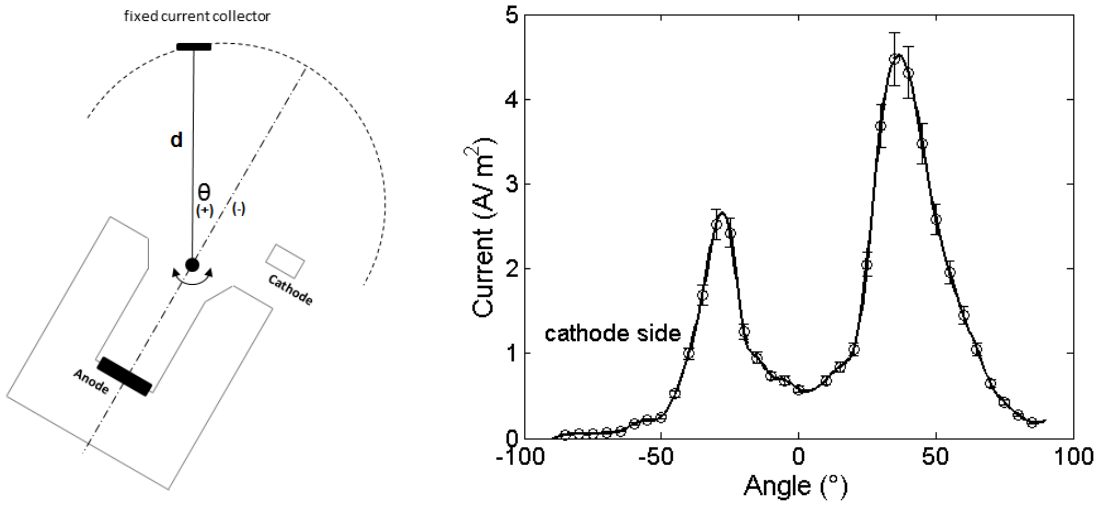


(a) (b)

Figure 4.12: a) Lay-out used for the beam current measurements: the probe is located d = 20.3 cm downstream the thruster exit plane and is fixed; the thruster is rotated as shown in the figure to perform the angular scan. b) Current density in function of the angular coordinate.

The integration of the current density profile permits the estimation of the total ejected ion current in the assumption of azimuthal uniformity:

$$I_i = 2\pi d^2 \int_0^{\pi/2} J(\theta)\sin(\theta)d\theta \tag{4.6}$$

where J($\theta$) is the ion current density which is evaluated averaging the values at $\theta$ and $-\theta$. The previous integration gives an ion current of (0.27 $\pm$ 0.03) A which corresponds to a xenon ion flow of (0.37 $\pm$ 0.04) mg/s. The uncertainty on the integrated ion current includes the uncertainty on the measured current density and that on the angular position. Finally, Fig. 4.13 illustrates the cumulative profile of the integrated current in function of the collecting angle: the 90% of the total beam current is encompassed within and angle of 62°.

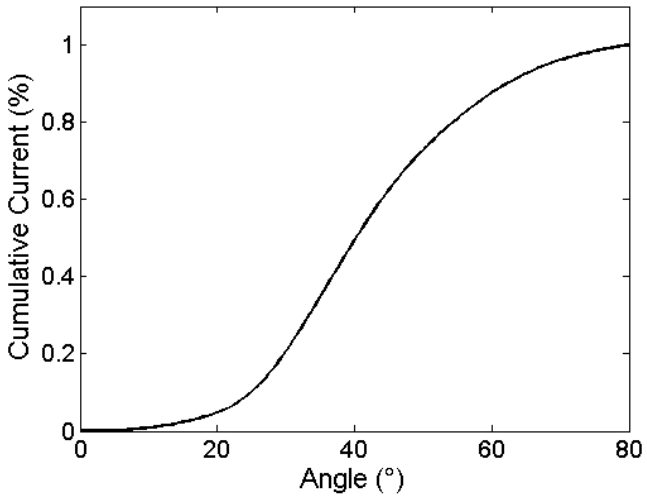


Figure 4.13: Cumulative integrated ion current in function of the collecting angle: the 75% of the total current is encompassed within an angle of 50°, the 90° within an angle of 62°.

## 4.3 Optogalvanic Velocimetry Testing

The optogalvanic ion velocimetry concept has been described in section 2.1.6. Since this is the first application of an optogalvanic method to a plasma thruster, the first step involves the generation of a simple optogalvanic perturbation in the thruster discharge channel. The operating parameters of the thruster are those reported in table 4.1. A laser beam generated by the laser amplifier has been directed inside the thruster discharge channel along the axial direction as shown in Fig. 4.14. Before entering the vacuum chamber the laser is mechanically chopped. The laser wavelength is tuned around the neutral or ion transition in order to produce a change in the neutral or ion energy states and induce small changes in the thruster anode current at the chopping frequency. In case, the effective excitation wavelength is Doppler-shifted if the particles have a velocity component along the laser direction. The thruster anode current is monitored through a shunt resistor in combination with an Analogue Devices AD8479 high common-mode voltage difference amplifier (common mode voltage up to 600 V and offset voltage up to 15 V). Different shunt resistors in the range 0.5 - 12.5 Ω have been tested. A 700 nF capacitor is used to block the DC component of the signal and a lock-in amplifier isolates the component at the chopping frequency. The laser power has been increased up to 300 mW.

In the traces of the processed signal we could not observe any evidence of an optogalvanic perturbation of the thruster current. The radial location of the laser has been changed moving the thruster to probe different regions. An attempt has been also made with an increased mass flow rate to enhance the neutral population. Possible explanations of the absence of the OG effect are the following:

- A not-optimized detection circuit. Since the DC component of the current is ∼0.4 A the value of the shunt resistor has to be chosen within the few Ohms range, limiting also the gain in the current-voltage conversion. Thus a small optogalvanic current becomes really hard to be detected. The thermal noise of the shunt resistor can be higher than the signal itself and the voltage difference amplifier itself can be a source of noise.

- The noise in the thruster current. Even if we are operating in DC, the thruster discharge channel can present spurious harmonics generated by the thruster operation itself; additionally, stray impedances - inductances and capacitances - in the power circuit can amplify or damp some of these harmonics. The current noise can be reduced operating in a different mode (e.g. at a different power level) and/or optimizing the DC power circuit (e.g. reducing the cables length).

- Sputtering on the mirrors and lenses inside the vacuum chamber. A sputtered layer

was observed on the mirrors and lenses after venting the vacuum chamber. This results in an attenuation of the effective laser power.

Therefore further investigation is needed in order to validate this novel method. Particular attention will be focused on the detection circuit configuration. A possible solution can be decoupling the DC component and the AC components of the discharge current dividing the circuit in a L-R branch and a C-R branch.

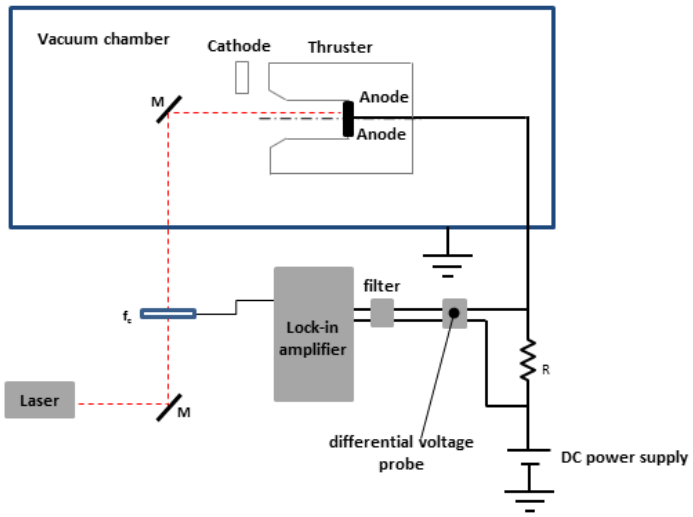


Figure 4.14: Setup used to induce an optogalvanic effect in the thruster discharge channel: a laser is fired in the discharge channel along the axial direction. Small changes of the anode current are monitored through a shunt resistor and a differential voltage amplifier.

## 4.4 3D PIC Simulation of the Magnetized DC discharge

### 4.4.1 Definition of the Numerical Problem

The geometry of the CCFT, including the external cathode, has been mapped to a tetrahedral mesh by the 3D finite element grid generator GMSH [86] (see Fig. 4.15a). The simulation domain is comprised of two main cylindrical regions: the thruster discharge channel and the vacuum ejection volume. The former is 14 mm in diameter and 36 mm long, while the latter is 40 mm in diameter and 84 mm long. The cathode is modeled as a cylindrical cavity in the ejection volume located 35 mm downstream of the thruster exit plane. The mesh size $\Delta x$ is chosen in each simulation to satisfy the condition $\Delta x < \lambda_{De}$, where $\lambda_{De}$ is the Debye length. Differently sized tetrahedra are used throughout the domain: the mesh is denser in the thruster channel to account for higher plasma density and is coarser in the expansion volume. The mesh consists of about 850,000 tetrahedra.

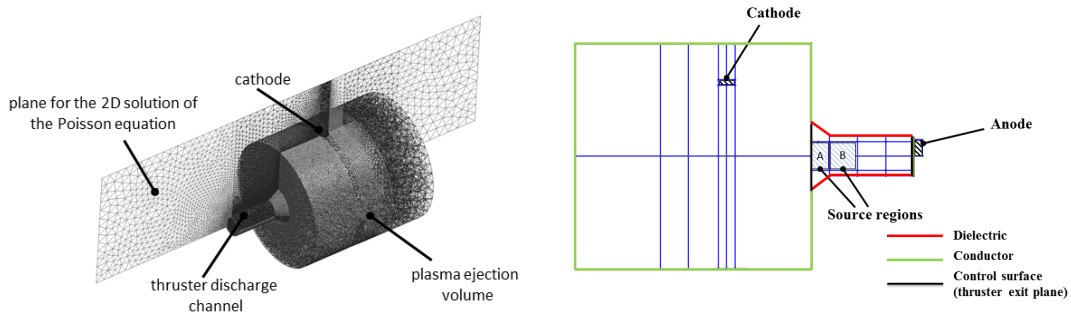


Figure 4.15: a) Generated 3D tetrahedral mesh over the computational domain with the 2D Poisson solution plane superimposed. b) Simulated thruster geometry with electron emitting cathode, electron and ion source regions, and anode indicated.

The simulated magnetostatic field topology reproduces the two cusps located inside the discharge channel and the magnetic separatrix at the diverging channel exit (see Fig. 4.16). The magnetic field is calculated through the code FEMM at each mesh node of a 2D radial-axial plane exploiting its axial-symmetry. We simulate a fully ionized collisionless plasma comprised of electrons and singly charged xenon ions. Both ions and electrons are treated kinetically with a simulation time step set to resolve the fastest characteristic plasma period (in this case the electron cyclotron period). A detailed model of the ionization mechanism is neglected here; rather, the effect of ionization is represented by loading a certain number of both ions and electrons in defined source regions ($A$ and $B$) at each time step (see Fig. 4.15b). The source rates in regions $A$ and $B$ are $0.5 \times 10^{12}$ macroparticles/s and $0.25 \times 10^{12}$

macroparticles/s, respectively. A higher source rate is used close to the exit plane near the final cusp where we expect strong ionization and previous measurements indicate a steep potential drop (see section 4.1.2).

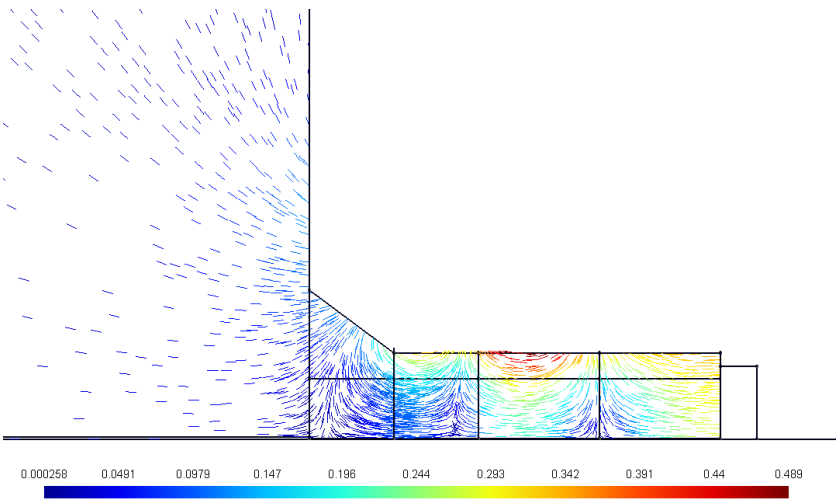


Figure 4.16: Magnetic field topology (in T) of the CCFT: it is characterized by two cusps located inside the discharge channel and the magnetic separatrix at the diverging channel exit.

The electrons and ions are generated according to a Maxwellian distribution with temperatures of 2 eV and 300 K, respectively. The cathode is represented by an electron emitting surface that ejects 25 eV particles according to the applied experimental keeper potential. The discharge channel walls are represented as dielectrics that specularly reflect incident particles, while the plasma ejection volume boundary and anode are defined as conductors that remove incident particles from the simulation domain. Note that the F3MPIC conductor boundary condition applies to particles reaching the physical device walls only and does not influence the electrostatic field solver, whose constraints are defined separately. The simulation is purely electrostatic. Although the code can compute electrostatic fields in 3D, these simulations solve the Poisson equation on a 2D (radial-axial) plane (pictured in Fig. 4.15a) to reduce computation time. The cathode and anode appear as polarized rectangular surfaces on this 2D longitudinal plane. The fields are then applied at the nodes of the 3D mesh through an axisymmetric (azimuthal) revolution of the plane. Note that in the continuum space where particles move, the cathode volume is not revolved in this manner and is located at a given azimuthal position as in the real device. To represent the experimental operation conditions with 300 V anode potential and $\sim$ 25 V plasma potential near the cathode, the simulated anode is given 275 V and the simulated cathode is given 0 V. An issue originates from the significantly different ion and the electron time scales. Due to the high magnetic field intensity in the cusps (0.45

T), the minimum electron cyclotron period is relatively fast (about $8 \times 10^{-11}$ s), requiring a time step of at least $4 \times 10^{-11}$ s. The ions need on order of a few microseconds to exit the discharge channel and fill the ejection volume. The required number of time steps is then $2.5 \times 10^5$, leading to an impractically long run time for the simulations. To address this issue, simulations are advanced for about 10 $\mu$s with a rough time step ($10^{-9}$ s), followed by an additional 1 $\mu$s with a refined time step of $4 \times 10^{-11}$ s. The number of computational particles in the domain is continously monitored to determine when a steady condition is reached; at each time step we verify that the number of particles exiting the domain is balanced by the number of particles loaded. The simulations presented here comprise about $6 \times 10^6$ particles. In the thruster discharge channel, the steady state plasma density is about $4 \times 10^{15}$ m$^{-3}$. Simulations with higher densities imply either a greater number of simulated macroparticles, increasing the computation time, or a higher weight per particle which can increase the numerical noise. Moreover, higher densities require a denser mesh to satisfy the Debye length restriction. Thus, we accept a lower simulated density than observed in the real thruster to limit the computational effort.

### 4.4.2 Simulation Results

We record the position and velocity of the particles crossing the exit plane at each time step. Post-processing tools are then used to estimate mass flow rates, currents and velocity distribution functions in the thruster plume. Figures 4.17 and 4.18 illustrate the ion and electron densities at different times throughout the simulation. We observe an initial outward flow of electrons from the discharge channel, followed by the slower ions. The latter take about 2 $\mu$s to begin leaving the channel and 5 $\mu$s to reach the opposite boundary of the ejection volume.

Apparent in the ion density plot (Fig. 4.19) is the presence of a higher density conical region with a divergence angle between $30^\circ - 40^\circ$ relative to the thruster axis, originating near the exit plane. A cross section taken about 2 cm downstream the exit plane into the plume in Fig. 4.21 confirms the thin annular area of elevated ion density. This feature is characteristic of the cusped field thrusters and can be visually observed during thruster operation. The simulated divergence angle of the plume is in agreement with the experimentally determined ion velocity vector angle of $\sim 35^\circ$ and the visible plume in Fig. 4.20. A similar value can also be derived from beam current probe measurements of the CCFT (section 4.2).

The electrons emitted by the cathode are mainly guided by the magnetic field lines towards the cusp near the exit plane. In the discharge channel, electrons are strongly magnetized and become trapped by the magnetic cusps; higher electron density is thus observed in these regions, which is readily apparent in Fig. 4.22 where the magnetic field

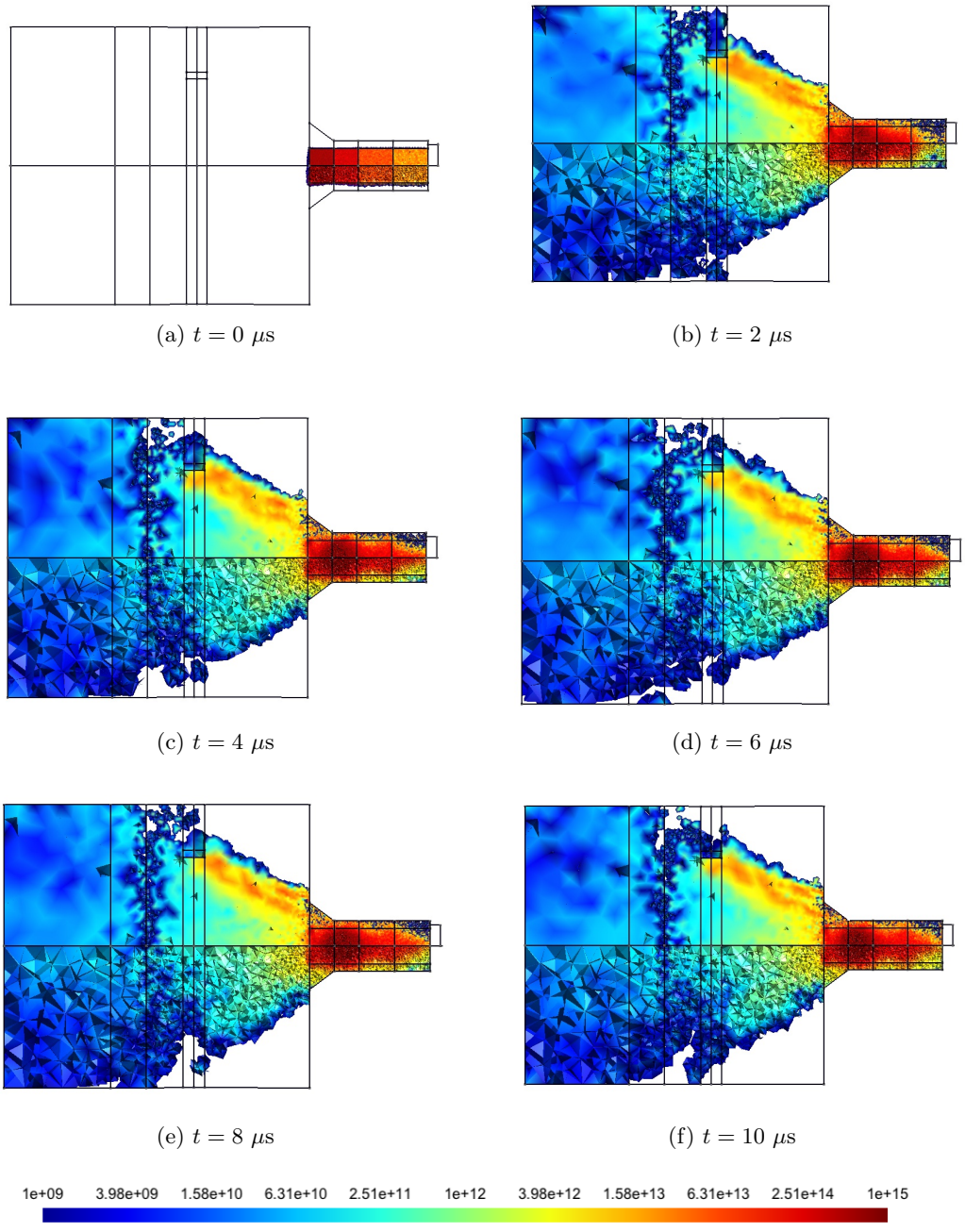


(a) $t = 0$ $\mu$s (b) $t = 2$ $\mu$s

(c) $t = 4$ $\mu$s (d) $t = 6$ $\mu$s

(e) $t = 8$ $\mu$s (f) $t = 10$ $\mu$s

Figure 4.17: Computed electron density profiles (in $m^{-3}$) at various time steps. This time evolution of the electron density has been obtained during the first simulation phase with a time step of $10^{-9}$s.

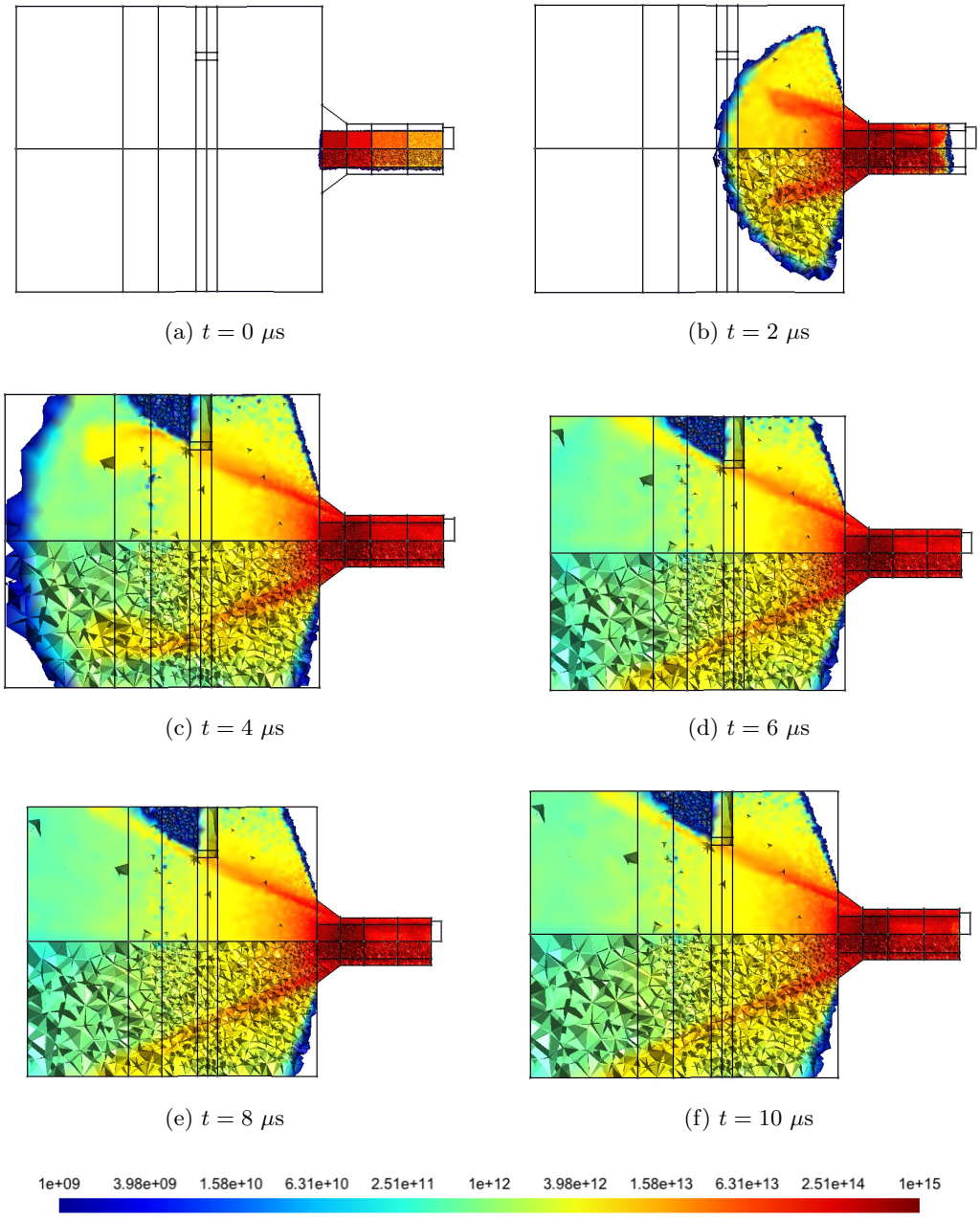


(a) $t = 0$ $\mu$s (b) $t = 2$ $\mu$s

(c) $t = 4$ $\mu$s (d) $t = 6$ $\mu$s

(e) $t = 8$ $\mu$s (f) $t = 10$ $\mu$s

Figure 4.18: Computed ion density profiles (in $m^{-3}$) at various time steps. The ions lag the electrons leaving the thruster discharge channel. This time evolution of the ion density has been obtained during the first simulation phase with a time step of $10^{-9}$s.

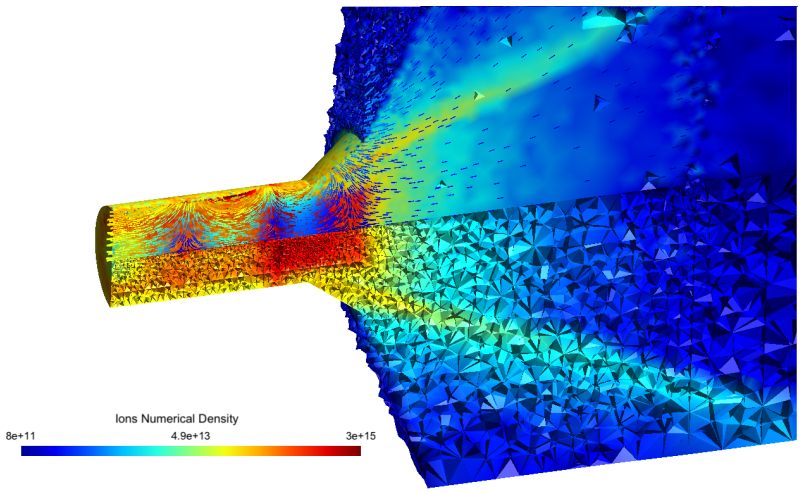


Figure 4.19: Ion density (in $m^{-3}$) in the discharge channel with magnetic field lines superimposed. The plume presents a hollow conical shape.

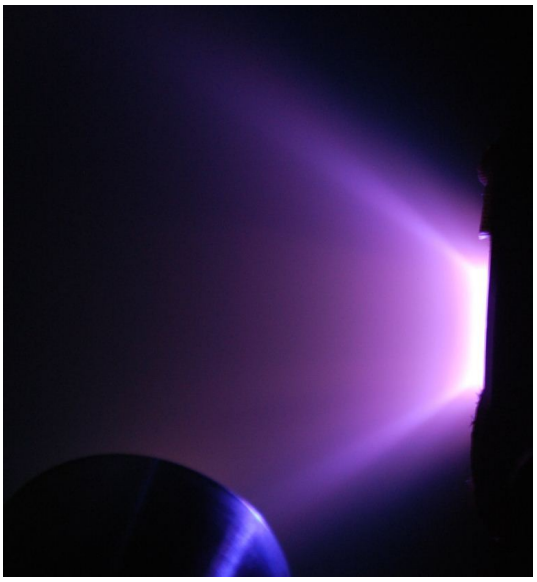

Figure 4.20: Picture of the thruster plume: the hollow conical shape of the plume can be remarked also by visual observation.

lines have been superimposed. The magnetic field confines electrons in the central region of the discharge channel, with the exception of the cusps.

The calculated electrostatic potential is presented in Fig. 4.23. The plot shows a strong potential drop located near the thruster exit plane which strongly accelerates ions downstream. This feature has also been observed experimentally with a floating emissive probe [37], where potential changes of >180 V occur within a few millimeters. In contrast, the

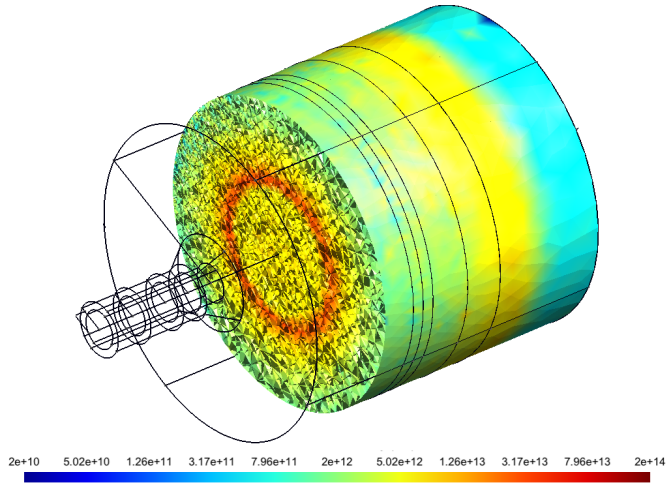


Figure 4.21: Cross section of the plume ion density distribution (in $m^{-3}$) highlighting the presence of a higher density annular region.

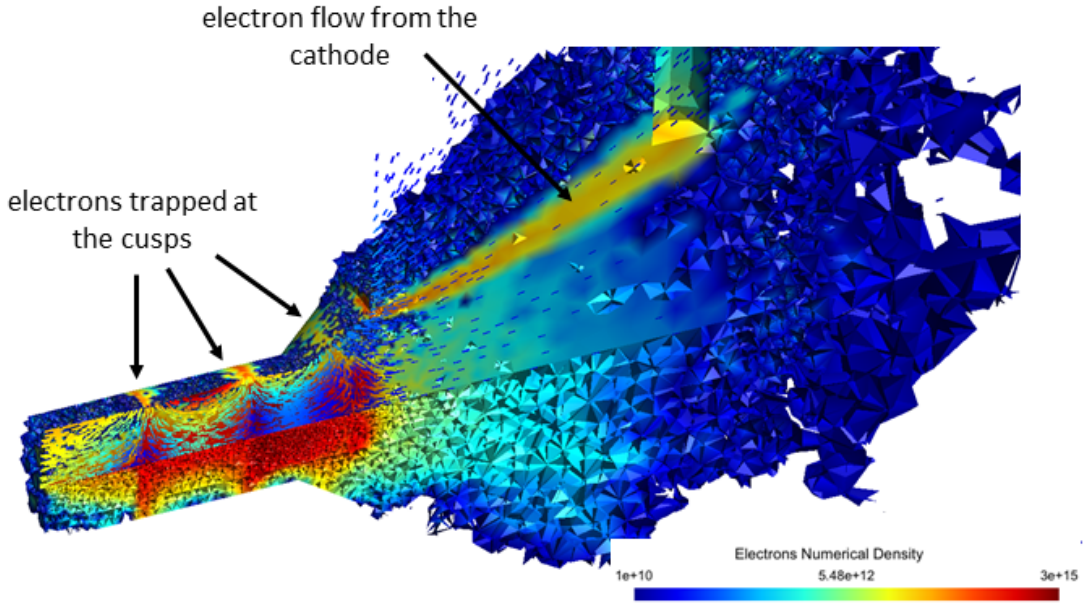


Figure 4.22: Electron density (in $m^{-3}$) in the discharge channel with magnetic field lines superimposed illustrating electrons collecting near the cusps.

simulated potential drop takes place over a few centimeters. A possible reason for this discrepancy is the lower plasma density present in the simulation in comparison with the real system. The spatial scale of the potential drop (and sheath thickness) can be considered proportional to the Debye length, which increases as density decreases.

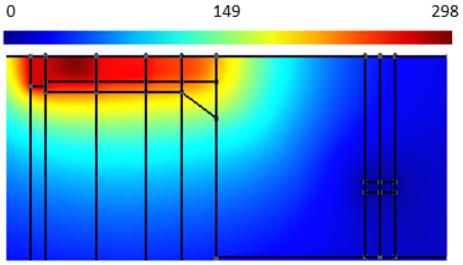


Figure 4.23: (a) Simulated potential distribution (in V) in the thruster discharge channel.

The positions and velocities of particles crossing the exit plane have been recorded during the last 10 ns of the simulation in order to determine the radial velocity distributions. The collected axial and radial ion velocity components as a function of radius are plotted in Fig. 4.24. The axial component is characterized by two different populations: a low velocity population present throughout the plane and a high velocity population located at radii greater than 8 mm, which is apparent in the ion velocity distribution functions (IVDFs) shown at two radial positions in Fig. 4.24c. At $R = 2$ mm a dense low velocity population is observed. In contrast, by $R = 10$ mm the predominant population has been accelerated to 12000 m/s and a sparse low velocity population persists near 4500 m/s. The double ion population is given by the simultaneous presence of accelerated ions and new-born ions. Such IVDF shape has been observed also in the LIF measurements. The simulated IVDFs qualitatively agree with the LIF velocity measurements performed here, which show strong ion acceleration in the outer part of the channel and observed velocities up to 14000 m/s. Finally, Fig. 4.24d illustrates the calculated ion current density at the exit plane as a function of radius. The calculation include all the particles with a given radius $|R| \pm \epsilon$, thus it is an average value on a 360° ring and does not distinguish the cathode side from the opposite side. The curve is then mirrored on the negative R values. The profile exhibits the high density wings of the divergent thruster plume discussed above. Note the presence of a central swell. This particular shape has been remarked in several beam current measurements carried out in thrusters of the same category, such as the MIT DCFT [90], the University of Giessen micro-HEMPT [30] and the Stanford CCFT itself operating with krypton [27].

The results highlight that the fully kinetic 3D PIC simulations reproduce several char-

acteristics of the CCFT discharge observed experimentally. The code proves to be an effective tool for investigating thruster behavior and supporting the interpretation of the experimental measurements.

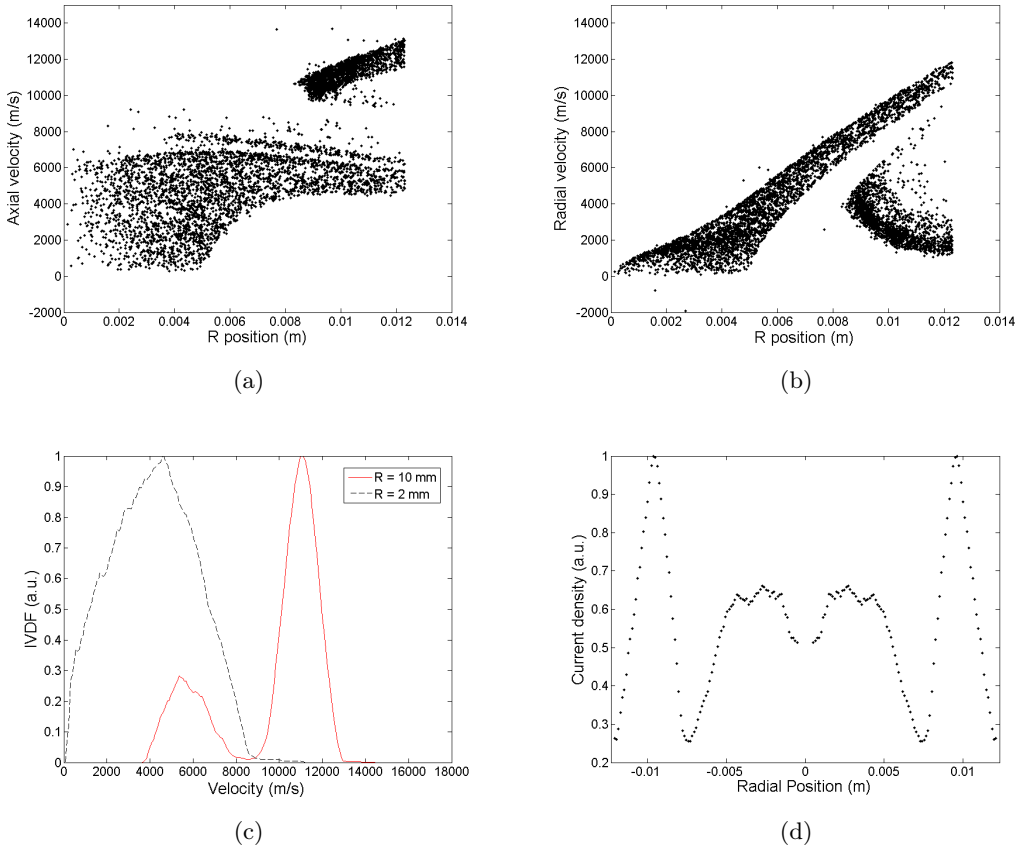


Figure 4.24: (a) Axial and (b) radial velocity components of ions crossing the exit plane as a function of radius. c) Calculated ion velocity distribution functions at the exit plane for two radial positions, 2 mm and 10 mm. (d) Calculated ion current density at the exit plane as a function of radius demonstrating the high density wings observed in the plume.

CHAPTER 5

# Investigation on a Traveling Magnetic Field Plasma Accelerator

This chapter describes our preliminary studies on a traveling magnetic field plasma accelerator, focusing on the understanding of the basic physics of the device through the numerical simulation of the plasma acceleration process. Along with the numerical analysis, we have designed a system of coils able to produce a magnetic field traveling with a velocity of about 20000 m/s. Preliminary operation of this design includes a neon plasma source driven by an Evenson microwave cavity [91] as the primary ionization stage.

The analysis is structured as follow: an overview of the propulsion system is given in section 5.1; 1-D particle-in-cell code simulations aimed to provide physical insight of the acceleration mechanism are described in section 5.2 ; the preliminary experiment set up to characterize the accelerator's operation is illustrated in section 5.3.

This project has been developed at the Stanford Plasma Physics Laboratory.

## 5.1 Propulsion System Overview

The thruster consists of a dual-stage system:

- a plasma source stage to ionize the neutral propellant flow;
- a plasma accelerator which exploits a traveling magnetic field to accelerate and eject the plasma, generating thrust.

Different types of plasma sources can be employed as the first stage. Due to the high efficiency a helicon source is the best candidate as used in the FARAD concept [42]. An alternative solution is a microwave discharge operating in the electron cyclotron resonance mode.

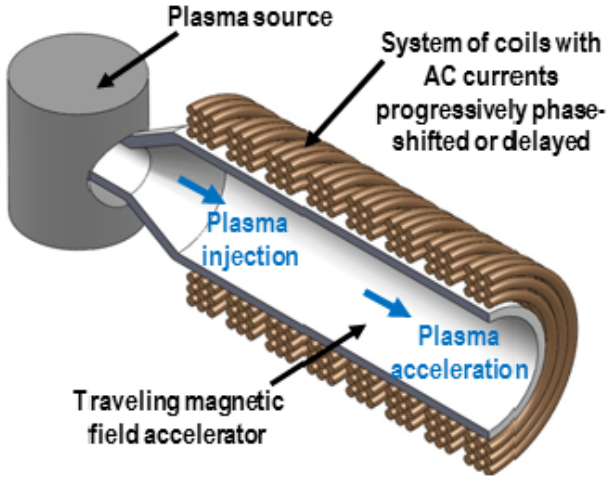


Figure 5.1: Propulsion system schematic.

The plasma produced in the source stage is injected into the acceleration channel, which consists of a cylindrical quartz tube. A sequence of coaxial coils with currents progressively phase-shifted or delayed is located around the tube in order to generate the traveling field. According to Faraday's law, an azimuthal electric field is associated to the time-varying magnetic field, generating an azimuthal current $J$ in the plasma (Ohm's law) [1].

$$\nabla \times \mathbf{E} = -\frac{\partial \mathbf{B}}{\partial \mathbf{t}} \tag{5.1}$$

$$\mathbf{J} = \sigma \mathbf{E} \tag{5.2}$$

This azimuthal current interacts with the radial component of the magnetic field giving a force term in the axial direction.

$$\mathbf{f} = \mathbf{J} \times \mathbf{B} \tag{5.3}$$

where $\sigma$ is the plasma conductivity. Among the different configurations of circuits able to produce a traveling magnetic field, we have selected a matched transmission line. The coils of the accelerator constitute the inductors of the transmission line. Capacitors are connected in parallel in the junctions between the inductors. The velocity of a wave propagating along a transmission line (considered lossless in this preliminary description) depends on the inductance $l$ and capacitance $c$ per unit length. The velocity of the traveling wave can be imposed selecting the proper values of $l$ and $c$.

$$v_t = \frac{1}{\sqrt{lc}} \tag{5.4}$$

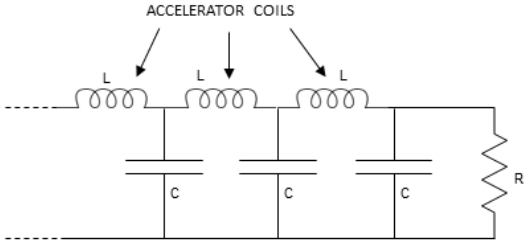


Figure 5.2: Transmission line.

The transmission line can be closed by a resistive load equal to its intrinsic load $Z_0 = \sqrt{l/c}$ or operated in a ring configuration [43]. Moreover the mode of operation can be either continuous or pulsed. In the former case a Radio-Frequency power supply is used, the currents in the coils are sinusoidal and progressively phase-shifted, as illustrated in Fig. 5.3. In the pulsed mode a capacitor is discharged to produce a current pulse traveling along the line. The current peak in each coil is delayed relative to the previous one according to the wave speed.

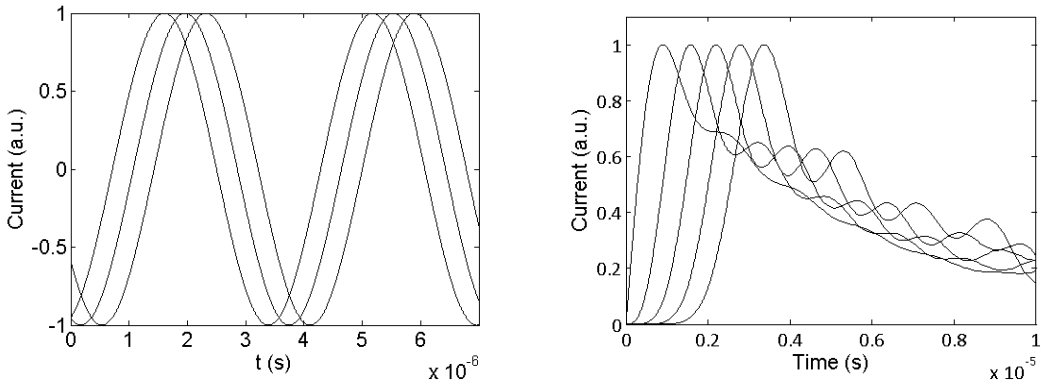


Figure 5.3: a) Currents in three consecutive coils of a transmission line powered through a 280 kHz RF generator; b) current pulse propagating through five consecutive coils.

The shape of the magnetic field generated by the transmission line strongly depends on the mode of operation, continuous or pulsed. The field on a longitudinal plane (r,z) of the accelerator at a given time can be estimated exploiting the magnetostatic approximation, based on the instantaneous currents flowing in each coil at the considered time. An example of a traveling magnetic field pattern produced by a transmission line powered by an RF power supply is depicted in Fig. 5.4. The field presents radial cusped-shaped regions alternating with regions in which the field is mainly axial. The field direction (both of

the radial and axial component) changes along the accelerator, however the induced electric field and the associated plasma azimuthal current also reverse, giving an axial force component that always points downstream.

In contrast, the field generated by a current pulse (Fig. 5.5) has a simple mirror shape and does not present inversions along the accelerator. The magnetic field propagates along the accelerator and acts as a piston on the plasma.

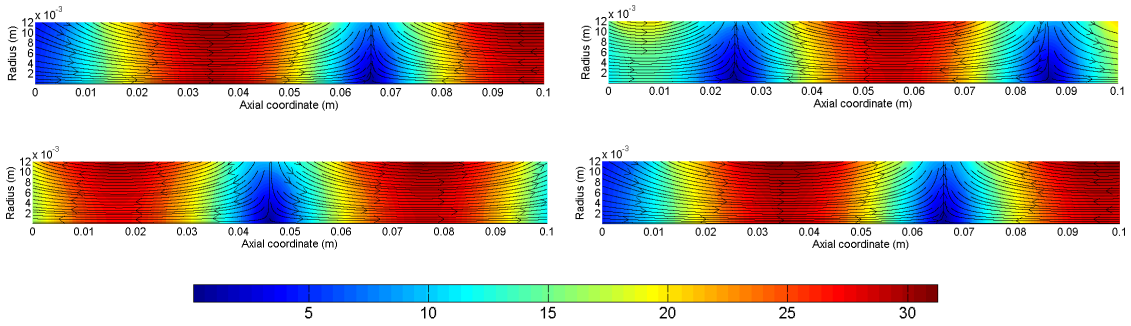


Figure 5.4: Example of magnetic field (in G) generated by a transmission line powered through a 280 kHz RF generator at different time frames: 1, 3, 5, 7 $\mu$s. The propagation velocity is 22500 m/s.

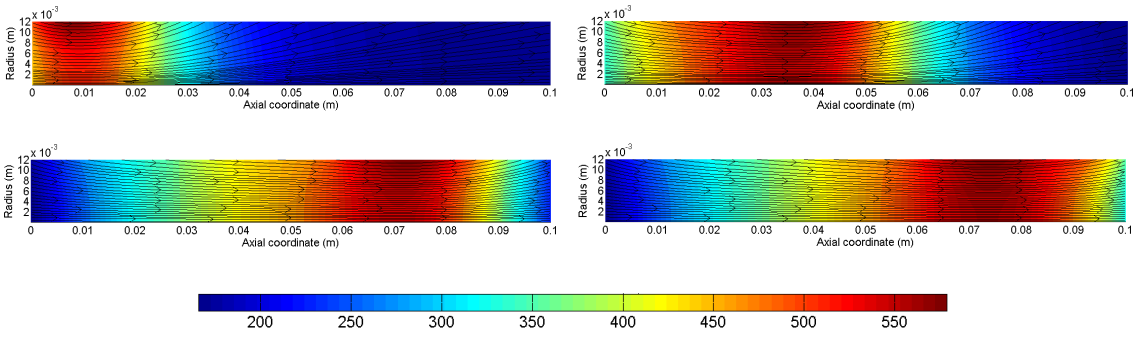


Figure 5.5: Example of magnetic field (in G) generated by a current pulse propagating along a transmission line at different time frames: 1, 3, 5, 7 $\mu$s. The propagation velocity is 17500 m/s.

As mentioned in the introduction, the system we designed is able to produce a propagating magnetic field with an estimated traveling velocity of 21500 m/s. The transmission line can be either continuously powered by a 280kHz - 300W RF generator or operated in a pulsed mode discharging a 1$\mu$F capacitor giving energy pulses in the range 0.7–2 J. The channel of the accelerator is made of a quartz tube with a diameter of 25 mm. The tube

narrows on the plasma injection side to house the Evenson microwave cavity [91] used as the primary ionization stage. The microwave source operates at 2.45 GHz with a power of 50–100 W. Neon is used as the propellant.

## 5.2 1D Analysis of the Plasma Acceleration Mechanism

A preliminary investigation of the physical acceleration mechanism has been performed through the 1D PIC code described in section 2.2.1. The aim is to highlight possible physical mechanisms caused by the different dynamics of the two species when forced by a magnetic pulse. The effect of the propagating magnetic field is comprised in the 1D model through the magnetic mirror term $-\mu\nabla B$, which represents the effect of a converging or diverging magnetic field on the particle motion. The magnetic moment $\mu$ is considered invariant in the case of slowly varying magnetic fields relative to the cyclotron period. We believe that only electrons are directly affected by the traveling field for the strength and velocity ranges considered, due to their higher mobility. On the other hand the direct effect of the magnetic field on ion motion is negligible since $\tau_{ci} >> w/2v_t$, where $\tau_{ci}$ is the ion cyclotron period, $w$ is the magnetic pulse spatial width and $v_t$ is its propagation velocity. The different dynamics of the two species create a charge separation and a consequent electric field which accelerates ions. A similar consideration has been pointed out by Jones [45]. The fully kinetic PIC code simulates the ion and electron motion and solves self-consistently the electric field arising from the local charge distribution, and therefore is a good candidate to highlight this effect.

### 5.2.1 Definition of the Numerical Problem

The numerical domain consists of a 2.5cm-diameter 10cm-length plasma cylinder in which a Gaussian-shaped magnetic pulse propagates with a traveling velocity of 30000 m/s. The pulse intensity is 400 G and its width 6 mm. A fully ionized collisionless plasma consisting of two species (ions and electrons) is simulated. The electron temperature is set to 4 eV and the ion temperature to 0.1 eV. The unperturbed plasma density is $6 \cdot 10^{13}$ m$^{-3}$. The ion species consists of hydrogen ions. The weight of a numerical macroparticle is 20000, i.e. 20000 physical particles are aggregated in a numerical macroparticle. For each ion crossing a boundary a new ion-electron pair is loaded in the domain. The overall number of simulated particles is 120000, giving an average number of particles per cell equal to 400. The cells dimension spatially resolves the Debye length with $\lambda_{De}/\Delta x \approx 3$. The time step has been chosen to satisfy the conditions required by particle-in-cell codes, i.e. the solution of characteristic plasma frequencies. For the aforementioned parameters the plasma period is 14.4 ns, the ion cyclotron period is 1.64$\mu$s, the electron cyclotron period is 0.9 ns (considering the peak magnetic field), whereas the time scale of the magnetic pulse is 0.1 $\mu$s. Both the boundaries are represented with a Dirichlet type condition, imposing a null voltage. In the simulations presented here we assume magnetized electrons and non-magnetized ions since only electrons are mobile enough to dynamically respond to the

traveling magnetic pulse. We consider the magnetic moment of electrons a good adiabatic invariant, since the rate of change of the magnetic field is much slower than the electrons cyclotron period $w/2v_t >> \tau_{ce}$.

### 5.2.2 Simulation Results

The simulation is run for about $10\mu$s in order to allow the sheath formation at the boundaries and to reach a steady unperturbed condition. Subfigures 5.6-5.11,a) represent the plasma properties before the action of the traveling magnetic field. In the central region the plasma is macroscopically quasi-neutral, whereas in the regions close to the boundaries a positive net charge takes place, due to the higher ion density in comparison to the electron density. Moreover, in the sheaths the ions are accelerated above the Bohm velocity satisfying the Bohm criterion. The potential in the bulk plasma relative to the wall is about 13 V in good agreement with that calculated through the analytical formula Eqn. 2.46, which gives 13.35 V.

At 10 $\mu$s the traveling magnetic field is launched and travels through the plasma from the left edge to the right edge of the domain. In all the figures below the position of the field is reported in order to give a reference during its motion.

Figures 5.6 and 5.7 illustrate the electron and ion phase spaces at different time steps. The propagating magnetic field locally affects both the ion and electron velocity distribution functions even if through different driver mechanisms. As the field runs through the plasma it pushes electrons downstream whereas ions are initially unperturbed since the time scale of their kinetic response is slower. As a consequence, a charge separation forms at the moving front of the magnetic field, with an electron rich region followed by an ion rich region (see Fig. 5.8), i.e., a double layer formation.

Since the net charge is no longer null a potential hill and associated electric field arise, holding electrons and accelerating ions. The ions are then dragged downstream by an electron sheath created by the traveling magnetic field. It is worth mentioning that this effect is local and takes place on the magnetic field front. The ion velocity is initially close to the traveling magnetic field velocity as we can observe from the plots in $11\mu$s (B) and $11.4\mu$s (C).

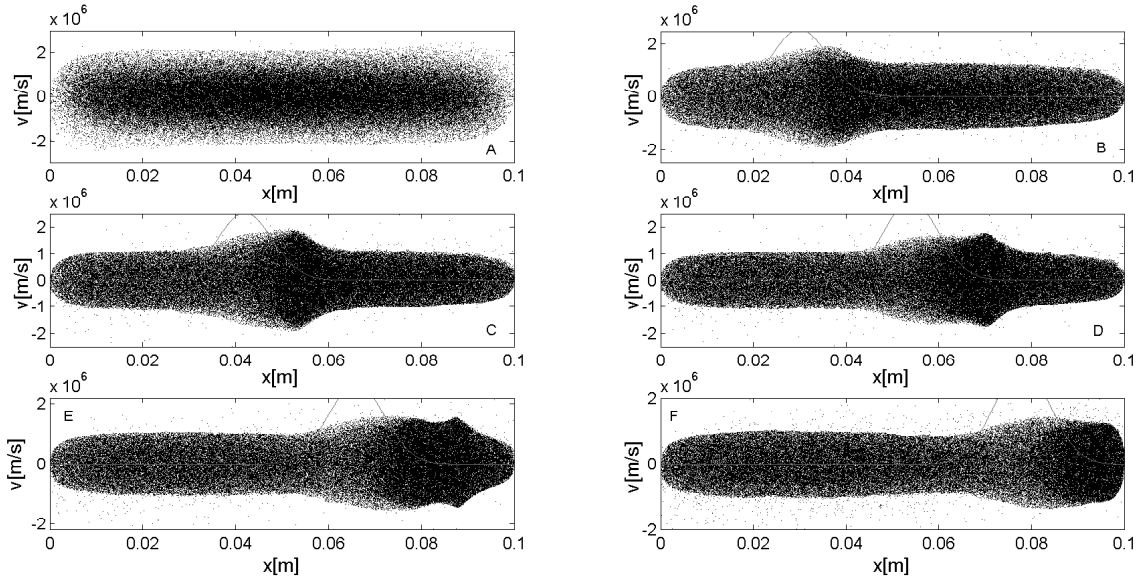


Figure 5.6: Electron phase space at different time steps. A: 10$\mu$s. B: 11$\mu$s. C: 11.4$\mu$s. D: 11.8$\mu$s. E: 12.2$\mu$s. F: 12.6$\mu$s.

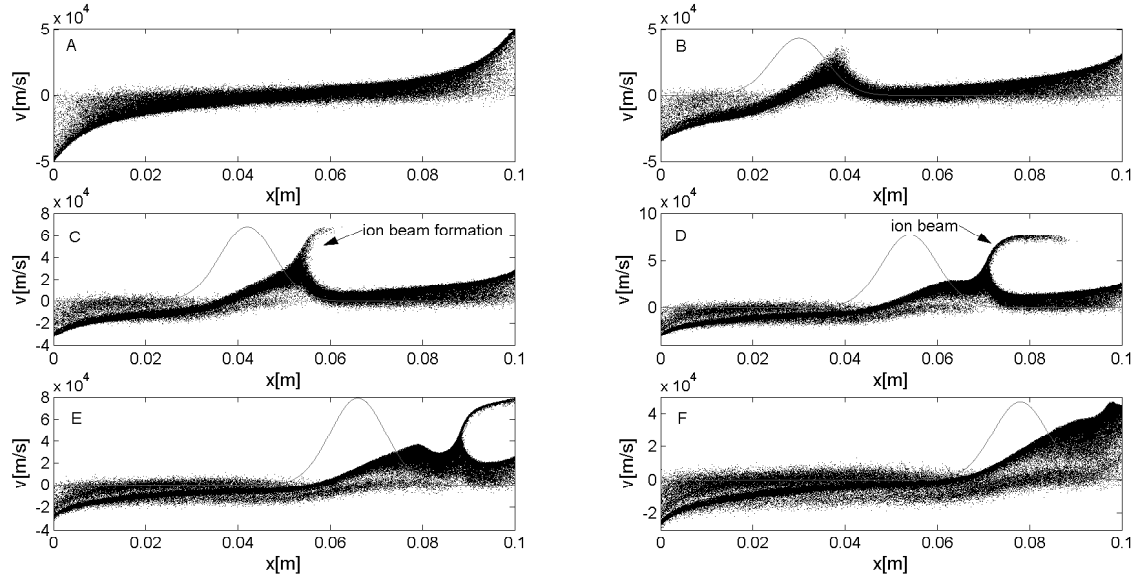


Figure 5.7: Ion phase space at different time steps. A: 10$\mu$s. B: 11$\mu$s. C: 11.4$\mu$s. D: 11.8$\mu$s. E: 12.2$\mu$s. F: 12.6$\mu$s.

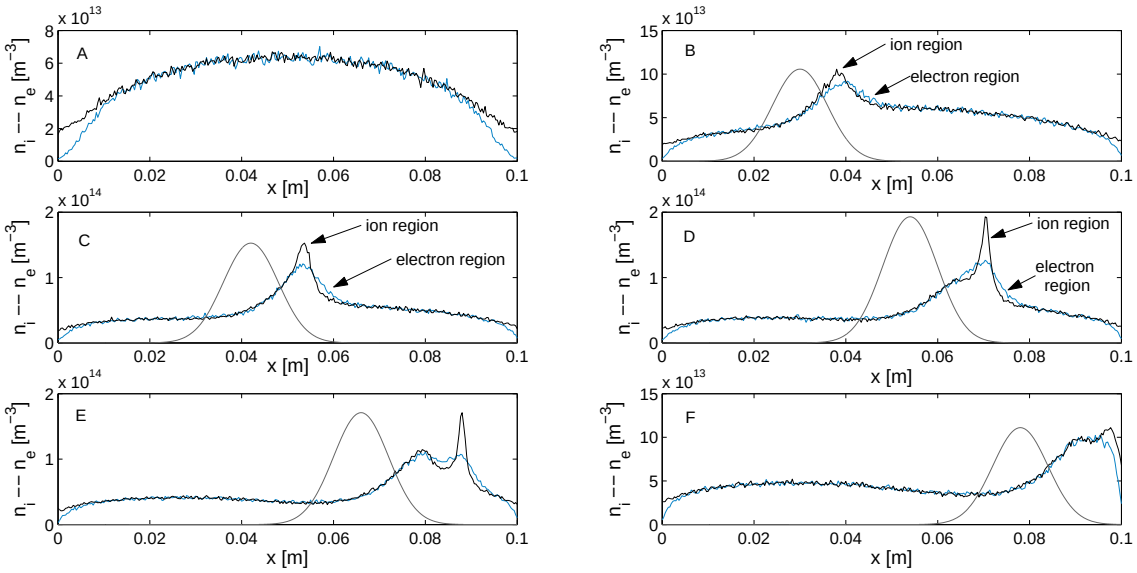


Figure 5.8: Ion (black) and electron (blue) densities at different time steps. A: 10$\mu$s. B: 11$\mu$s. C: 11.4$\mu$s. D: 11.8$\mu$s. E: 12.2$\mu$s. F: 12.6$\mu$s.

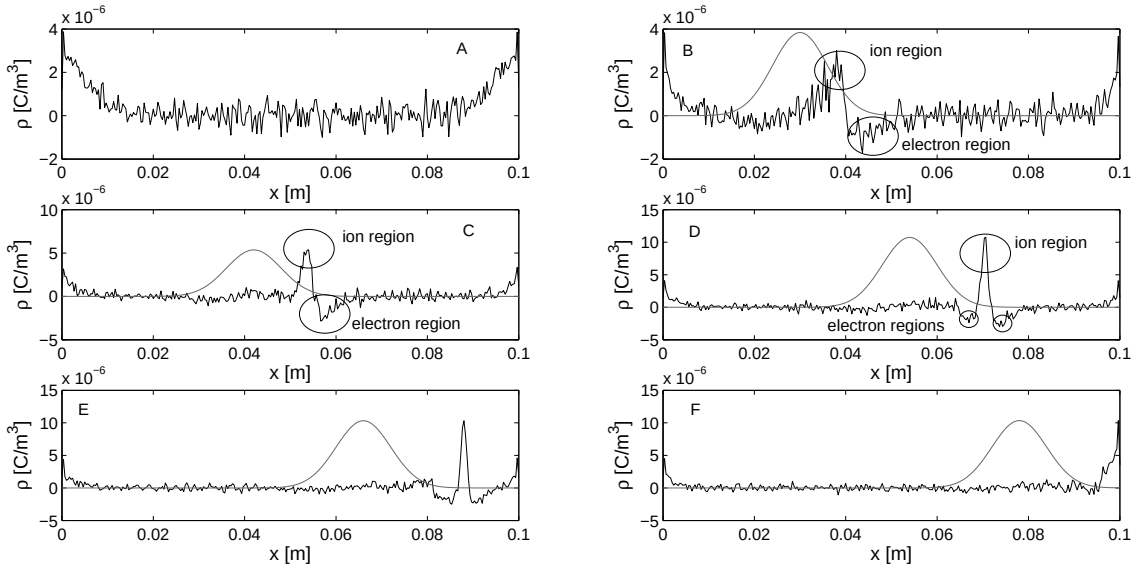


Figure 5.9: Charge density at different time steps. A: 10$\mu$s. B: 11$\mu$s. C: 11.4$\mu$s. D: 11.8$\mu$s. E: 12.2$\mu$s. F: 12.6$\mu$s.

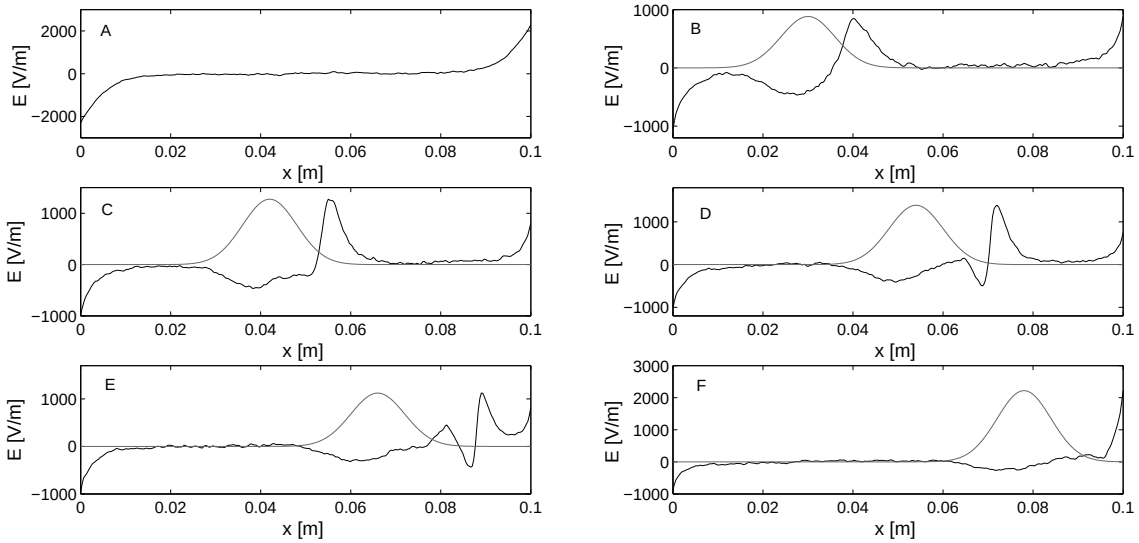


Figure 5.10: Electric field at different time steps. A: 10$\mu$s. B: 11$\mu$s. C: 11.4$\mu$s. D: 11.8$\mu$s. E: 12.2$\mu$s. F: 12.6$\mu$s.

During the propagation of the magnetic field through the plasma, the electrostatic structure formed at the magnetic front changes its characteristics. The positively charged region becomes surrounded by negatively-charged sheaths on both sides. A high velocity ion population forms and propagates downstream with a velocity higher than the traveling velocity of the magnetic field. The time evolution of the electrostatic structure is illustrated in Figure 5.12. The plot highlights the space propagation of the potential hill moving together with the magnetic field.

The simulations presented here, although performed with a 1D model with simplifying assumptions, point out a possible mechanism of plasma acceleration induced by a traveling magnetic field. The results show the fundamental role of electrons as carriers of the acceleration. A more complete picture requires additional simulations in order to explore different ion species, magnetic field strengths and velocities. Particularly, if the magnetic field is sufficiently high, even the ion motion can be directly affected by the magnetic pulse (since $\tau_{ic} < w/2v_t$), above all in case of light ions, creating a different physical frame.

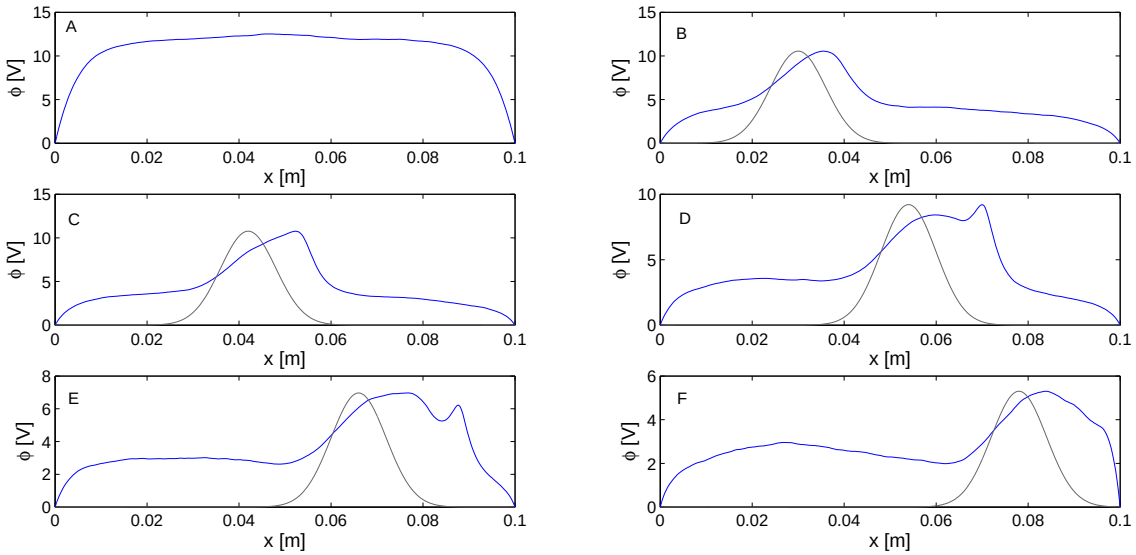


Figure 5.11: Electrostatic potential at different time steps. A: 10$\mu$s. B: 11$\mu$s. C: 11.4$\mu$s. D: 11.8$\mu$s. E: 12.2$\mu$s. F: 12.6$\mu$s.

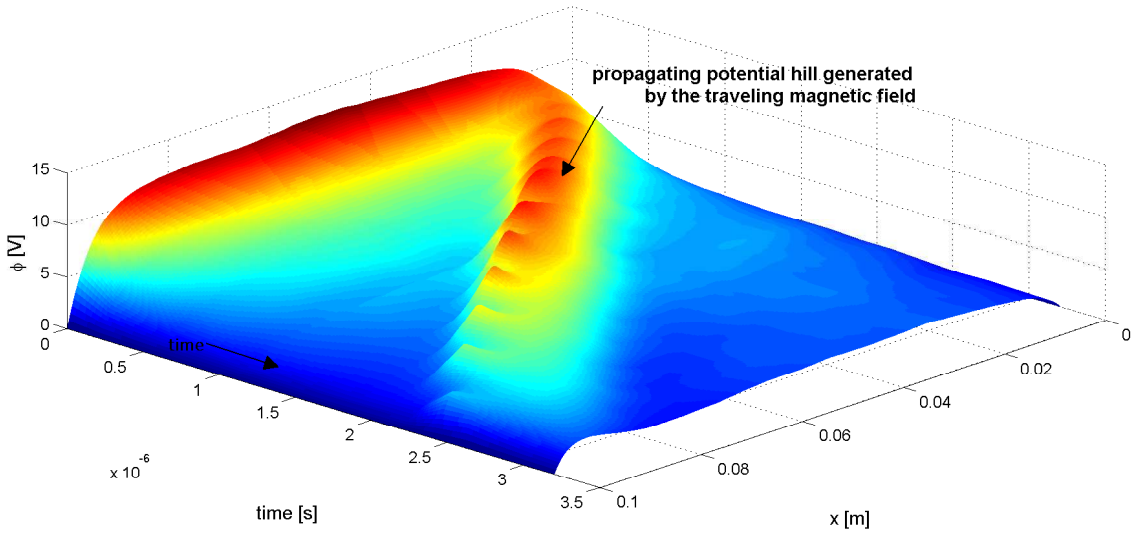


Figure 5.12: Time evolution of the potential along the simulation domain.

## 5.3 Preliminary Experimental Setup

### 5.3.1 Accelerator Configuration

We have designed and built an accelerator prototype based on a transmission line configuration. The accelerator is an array of ten coils connected in series and presents an inner diameter of 26 mm and a length of (110 ±3) mm. Each coil is made of 9 windings, arranged in 3 rows and 3 columns. The inductance of each coil as measured through an impedance meter is equal to $(2.68 \pm 5\%)$ $\mu$H. The transmission line consists of $(0.1 \pm 5\%)$ $\mu$F ceramic capacitors connected in parallel, according to the scheme illustrated in Fig. 5.13. The circuit is terminated by a $(5 \pm 1\%)$ $\Omega$ non-inductive resistive load. The estimated propagating velocity of the traveling magnetic field (using Eqn. 5.4) is $(21.25 \pm 4.06)$ km/s. The circuit has been designed with the support of Matlab and Simulink models.

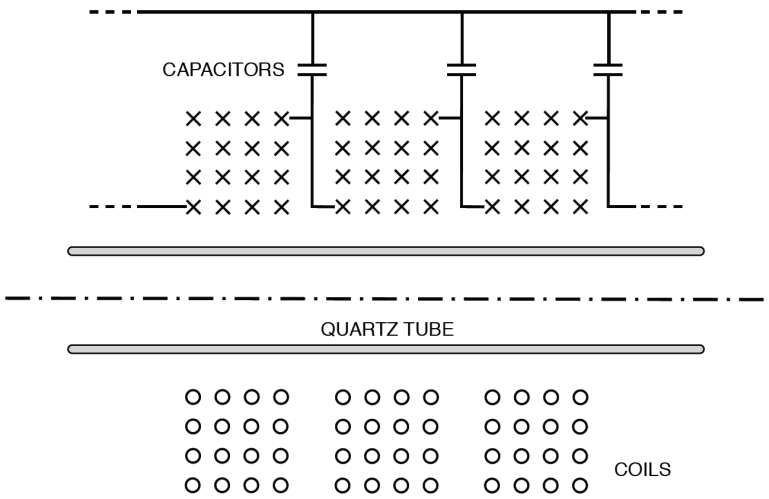


Figure 5.13: Schematic of the designed prototype.

We designed the transmission line to be powered by a 280kHz - 300W RF power supply for continuous operation. According to this frequency, the current in each coil is phase shifted by about 50° relative to the previous coil. At a given time step, the currents in the coils shape a sinusoidal profile in space with a wavelength of $v_t/f = 75$ mm. The system has been designed to have 1.5 spatial wavelengths along the accelerator length.

In order to verify the correct behavior of the transmission line we have measured the voltage at each connection between the coils and compared to the analytical predictions. The phase shifts relative to the first coil are plotted in Fig. 5.14.

If operating in the pulsed mode, a 1 $\mu$F capacitor is discharged generating a current pulse propagating along the transmission line. A hammer relay is used for connecting the capacitor to the transmission line. The applied voltage ranges between 1–2 kV giving pulse

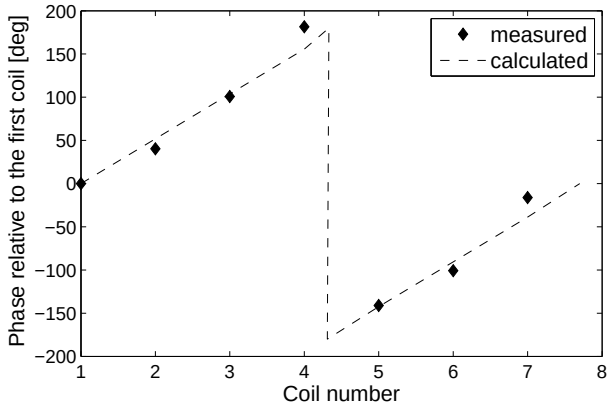


Figure 5.14: Predicted and measured phase shifts of the coils relative to the first one.

energies of 0.5–2 J.

The currents flowing through the first and last coil are measured using Pearson probes located at the beginning and at the end of the accelerator. The Pearson probes have a gain of 0.1 V/A, a 3dB bandwidth from 1 Hz to 20 MHz, a midband accuracy of 1% and a useable time rise of 20 ns. The 6.45 $\mu$s time delay between the two currents rises gives a propagation velocity of $\sim$ 17000 m/s.

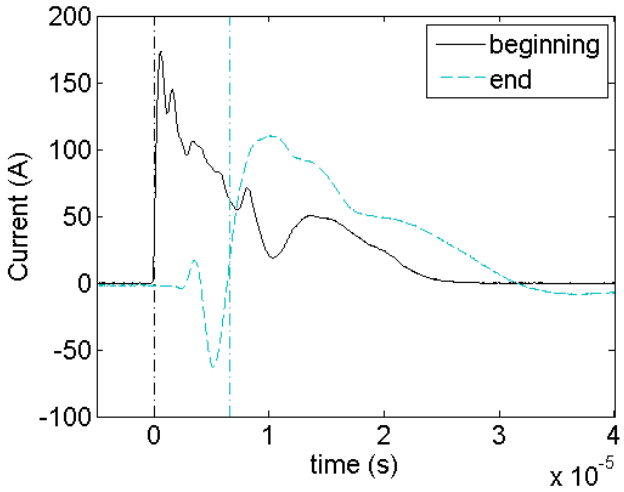


Figure 5.15: Currents flowing at the beginning and at the end of the accelerator. The latter is 6.45$\mu$s delayed relative to the former.

### 5.3.2 Experimental Testing

In these preliminary experiments the accelerator has been operated in the pulsed mode.

The 2.45 GHz Evenson microwave cavity used as the primary ionization stage is installed upstream of the accelerator and is operated continuously at 100 W generating a neon plasma. The quartz tube is mounted outside the vacuum chamber and connected to it through a flange. The pumping is provided by a cryogenic panel, leading to a background pressure of $5 \times 10^{-6}$ mbar and a pressure of $1 \times 10^{-4}$ mbar during the accelerator operation.

In order to detect the accelerated plasma sheet, a time-of-flight (TOF) probe has been built and installed downstream the accelerator. The probe is made of two copper conductors spaced 1.25 cm apart. Only the end of the conductors is exposed to the plasma while the remaining part is encased in an alumina tube. When a plasma sheet run into the electrodes, it causes a change of their potential relative to the ground. The propagating plasma sheet is sensed at first by the upstream electrode and then by the downstream one; the time delay provides an estimation of the propagating velocity. We have modified this classical configuration introducing a third conductor, completely insulated, in order to determine the signal generated by possible electromagnetic interferences. This encased conductor is located between the exposed ones (Fig. 5.16). This method allows for the identification of the component of signal picked-up by the exposed conductors which is actually produced by a propagating plasma sheet.

A photograph of the experimental facility while in operation is shown in Fig. 5.17.

The upstream electrode of the TOF probe is located at the exit plane of the accelerator. A Pearson probe, located at the beginning of the transmission line, is used to monitor the current flowing through the first coil and to trigger the scope acquisition.

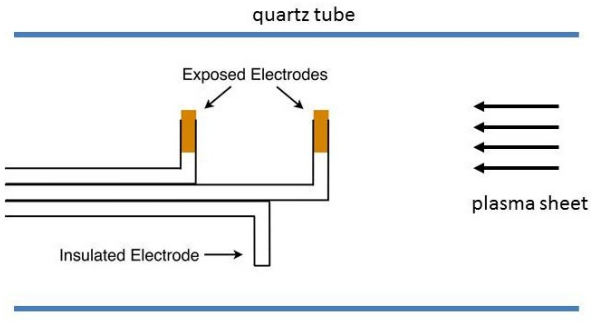


Figure 5.16: Scheme of the time-of-flight probe with two exposed electrodes and an insulated one.

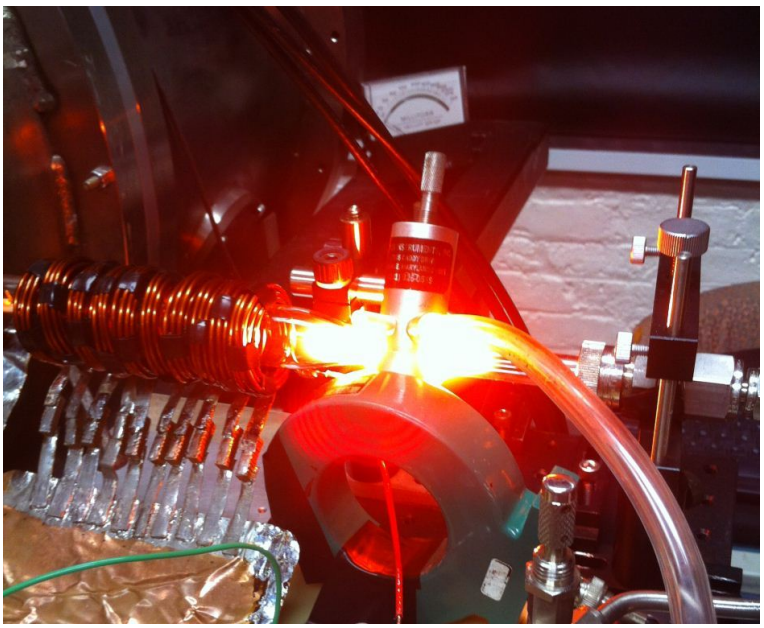

Figure 5.17: Photograph of the experimental arrangement with the coil system that generates the traveling magnetic field. The circuit is a transmission line. The plasma source which injects ions into the accelerator stage is an Evenson cavity operating at 2.45 GHz and about 100 W of power (neon feed).

Fig. 5.18a and 5.18b show the signals sensed by the upstream and downstream exposed electrodes and by the encased one for a 1.8 J (1900 V) pulse. The peak current value is $\sim$ 150 A. For these acquisitions, the first coil is negatively polarized relative to the common conductor closing the circuit. The time relative to the current peak detected by the Pearson probe is used as the time reference.

Fig. 5.18a illustrates the TOF profiles in the absence of plasma: the electromagnetic fields generated by the pulse induce a spurious signal with a peak at $\sim$ 7.06 $\mu$s which is consistent with the pulse traveling time along the accelerator. Fig. 5.18b shows the same signals with the microwave source switched on. The profiles are different from the previous ones, indicating an effect of the plasma on the system. Particularly the strength of the signals peaks increases by a factor of 3 respect to the case without plasma. We exclude the possibility that this effect is produced by a propagating plasma sheet since it is observed also by the encased electrode. However the plasma-circuit interaction generates a change in the equivalent impedance of the circuit and, as a consequence, of the generated electromagnetic fields.

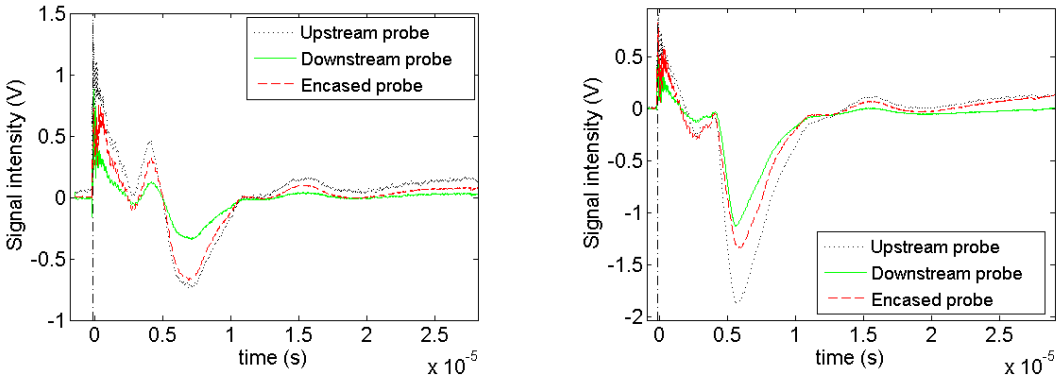


(a) without plasma

(b) with plasma

Figure 5.18: TOF probe measurements obtained with a negative polarization of the first coil relative to the transmission line closing conductor: a) signals in the absence of plasma, b) signals with the microwave source switched on.

Different features are observed in the TOF traces when the first coil is positively polarized. The plots reported in Fig. 5.19 refer again to a 1.8 J pulse. The signals in the absence of plasma (Fig. 5.19c) are similar to those obtained with negative polarization being characterized by a peak at 6.8 $\mu$s. However the profiles with plasma generation significantly change since they present two peaks: the usual peak at 6.7 $\mu$s and a second peak at 26 $\mu$s with opposite sign. The first peak is observed by all the electrodes, including the encased one, thus can be associated to an electromagnetic interference. As previously observed, its strength increases of a factor of 2 respect to the case without plasma. The second peak is observed only by the uncovered electrodes while the signal detected by the encased electrode in this time interval is much lower. Also, recall that this peak takes place only when the microwave plasma source is operating. These characteristics indicate that this peak can be produced by a plasma sheet. The time delay between the trigger of the pulse and the sheet detection suggests a charged-particles cloud traveling along the accelerator with a velocity lower than the pulse velocity, thus the plasma is not dragged downstream by the magnetic field. The 26 $\mu$s delay is compatible with a velocity of 4100 m/s to cover the accelerator length. We can suppose this cloud is generated in the region under the first coil when the pulse is triggered and then propagates downstream but separately from the pulse itself. However, the time delay between the upstream and downstream electrodes of the TOF probe (Fig. 5.19a) is in conflict with this hypothesis: the peaks almost coincide even when they should be spaced-in-time of $\sim 3$ $\mu$s considering the aforementioned velocity value (4100 m/s).

Finally, if the acceleration mechanism were a magnetic piston, the effect would not be

polarization-dependent as observed in these measurements. The polarization dependence is symptomatic of another mechanism such as the electric field generated by the high voltage associated with the pulse. These results indicate that this preliminary pulsed-mode operation produces an effect different that the target one. Additional experiments and modeling are needed to provide a final assessment on the plasma acceleration concept.

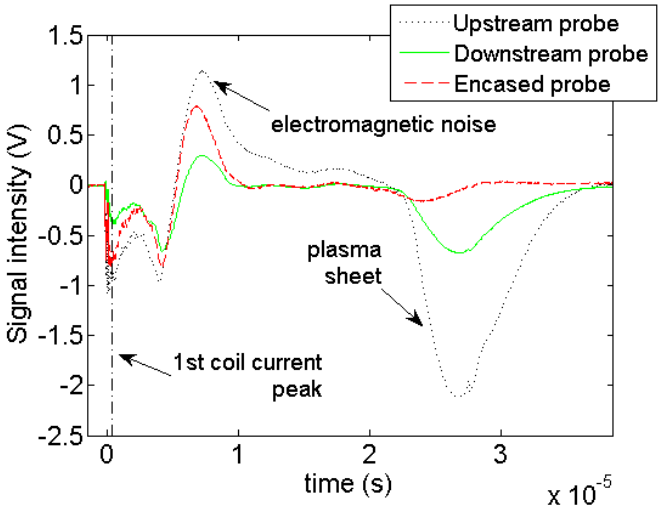


(a) with plasma

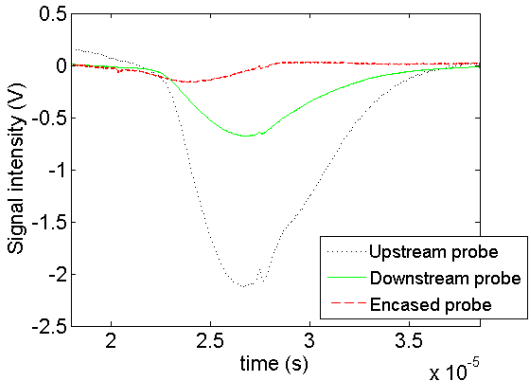


(b) with plasma

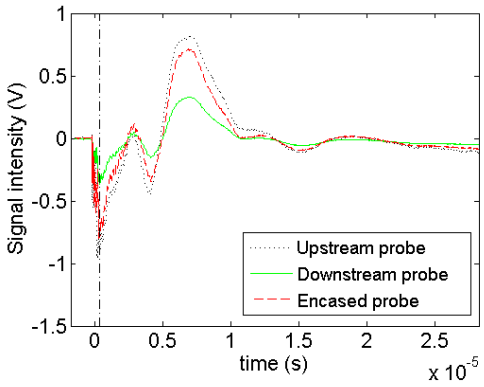


(c) without plasma

Figure 5.19: TOF probe measurements obtained with a positive polarization of the first coil relative to the transmission line closing conductor: a) signals with the microwave source switched on; b) detailed view of the 1.8 - 4 $\times$ $10^{-5}$s time interval; c) signals in the absence of plasma.

CHAPTER 6

# Conclusions

The following sections summarize the analysis and results obtained in this thesis and provide suggestions for future research.

## 6.1 Electrodeless RF Plasma Thruster

This work aimed to develop a RF plasma thruster working in the 1 - 3 mN range, with an input electrical power of 50 - 90 W and a target specific impulse of at least 1000 s.

An experimental apparatus has been designed and built in order to explore effects of critical plasma discharge parameters on thruster performance. Particularly, the setup allows the antenna type and position, magnetic field configuration and strength, ejection orifice diameter and plasma source length to all be varied. The magnetic field can be produced by either electromagnets or permanent magnets. The operating frequency has been varied between 3 - 13 MHz. The source diameter, of 19 mm, was determined in a previous study [84] through a numerical optimization process. We have carried out experiments in the 40 - 100 W power range at mass flow rates between 0.1 - 0.3 mg/s. The plasma source performance is monitored through a microwave interferometer that measures the plasma density and optical spectrometers that capture the emission spectrum. The latter, coupled with a collisional-radiative model, provides an estimation of the electron temperature. A current probe and a Retarding Potential Analyzer have determined the ejected plume's ion current and energy, respectively.

Numerical simulations have supported the experimental work by further investigating the physical phenomena that determine thruster behavior. The simulations are performed with the 3D code F3MPIC, entirely developed by the CISAS space propulsion group. The code solves for the electron and ion dynamics forced by the electric and magnetic fields. The electrostatic field is obtained at each time step through the solution of the Poisson equation; in this process, both the instantaneous charge density and polarized elements within the

domain are included. The code provides particle density distributions, charge density and electrostatic potential in the simulated volume and velocity distribution functions through user-defined surfaces.

Initial tests with traditional RF antennas coupled to a standard matching network did not achieve the plasma density and temperature levels expected to produce the target thrust. The maximum measured plasma density was 3.5 $\times 10^{18}$ m$^{-3}$ (at 80 W - 0.27 mg/s - 5 mm outlet diameter) and the electron temperature never exceeded 2 eV.

These results led to a change in the development strategy, focusing on a novel type of antenna invented by RESIA[1] during the HPH.com project, now undergoing the patent process. The new source, based on this antenna combined with a peculiar magnetic field pattern, produced a maximum plasma density of $\sim 2 \times 10^{19}$ m$^{-3}$ (at 75 W - 0.2 mg/s - 5 mm outlet diameter) and an electron temperature of $\sim$ 4.5 eV. Additionally, RPA measurements in the ejected plume have shown an ion energy above 100 eV. The magnetic configuration is critical: proper power coupling in the plasma is achieved only in the case of particular magnetic field configurations. The final arrangement is comprised of two circular arrays of radially-oriented permanent magnets. Finally, tests with the thruster mounted inside the vacuum chamber demonstrated the repeatability of the discharge conditions in a space-like environment.

F3MPIC simulations pictured the plasma dynamics in this novel thruster. The numerical results show an ion acceleration up to $\sim$5 times the Bohm velocity. The acceleration is generated by the combined effects of a potential drop, taking place at the interface between the plasma source and vacuum, and the oscillating electrostatic fields produced by the antenna. An oscillation at the RF frequency is observed in the ejected mass flow as well.

The experimental and numerical results determined the guidelines for the design of the HPH.com thruster prototype, built and characterized through a pendulum thrust balance by the KhAI[2] electric propulsion group. It achieved a thrust of 0.5 mN, a specific impulse of 420 s, and an efficiency of 13% while operating at 8 W and 0.12 mg/s xenon propellant flow rate (the power level was limited below 10 W to avoid spurious interference effects on the thrust balance electronics).

[1] Realizzazioni Elettroniche Selmo ing. Antonio, San Bonifacio, Verona, Italy - HPH.com project partner
[2] Kharkiv Aviation Institute, Kharkiv, Ukraine - HPH.com project partner

## 6.2 Magnetized DC Discharge

This work aims to provide new insight into the physical mechanisms occurring in the discharge channel and ejection region of the Stanford Cylindrical Cusped Field Thruster through a combined experimental and computational approach. Xenon laser induced fluorescence measurements have determined total ion velocities (both magnitude and direction) at several points near the thruster exit plane. The velocity field is correlated to the ion beam current profile, measured through a current probe, and the electrostatic potential field, obtained by a floating emissive probe in a previous work [37]. The thruster has also been simulated using the 3D particle-in-cell code F3MPIC. Agreement between simulation and experimental results highlights the capability of the code to reproduce several physical features of the thruster.

The CCFT is operated with a xenon mass flow rate of 0.586 mg/s and applied anode potential of 300 V, drawing 0.4 A of current (120 W of power). Ion acceleration is localized in a narrow region ($\sim 3-5$ mm) close the thruster exit plane where a strong potential drop ($\sim 180-200$ V) occurs. The mean velocity of 17000 m/s measured in the accelerated ion flow is consistent with this drop in potential. The acceleration front follows the magnetic separatrix and directs ions on a divergent trajectory into the plume with observed increases in ion density at the outer radii of the exit plane. The simulations show that the electrons are strongly magnetized and that their density distribution coincides with the cusped magnetic field structure. We believe that the magnetic field topology, which directly shapes the spatial electron density distribution and the electrostatic potential structure, indirectly affects ion dynamics in the discharge channel, particularly at the exit plane, through the creation of ionization and acceleration zones.

The plasma plume exhibits a hollow conical shape with a dense layer of ions observed at 30° half angle. This characteristic can be visually observed and appears in the LIF measurements and current probe traces. LIF measurements in the outer radii region show a mean velocity vector angle of 36.6°, which is consistent with the peak in the beam current profile observed at 35.5°. The hollow conical shape is reproduced in the PIC simulation as well, with a divergence angle in agreement with the experimental measurements. A possible future analysis can use F3MPIC simulations to explore the effects of altering the magnetic field structure to reduce the plume divergence.

We also propose a novel method to measure the ion velocity in a DC plasma thruster plume using the optogalvanic effect. Preliminary testing shows that excitation of the XeI - 834.62 nm and XeII - 834.72 nm spectral lines in a hollow cathode lamp discharge may be detected through the optogalvanic technique. We have also provided an intermodulated Doppler-free measurement of the XeI - 834.62 nm line. However, an attempt to generate a laser-induced optogalvanic perturbation in the thruster was unsuccessful and we did

not observe any consequent variations in the discharge current. Improvements of the optogalvanic sensing circuit will be implemented in future tests.

## 6.3 Traveling Magnetic Wave Plasma Accelerator

We have proposed a new dual-stage propulsion system based on a traveling magnetic field accelerator. The plasma produced in a primary ionization source is injected into the second stage where it is accelerated by means of a traveling magnetic field. Previous studies [43]-[50] have shown that the magnetic field acts as a piston, pushing the plasma downstream and accelerating it at velocities close to the traveling velocity of the field. A 1D numerical investigation of the system has been performed and a preliminary experiment aims to validate the concept.

The 1D particle-in-cell analysis highlights a possible acceleration mechanism induced by a magnetic pulse propagating in a uniform plasma. The results particularly emphasize the role of electrons as carriers of the acceleration. The field preferentially acts on electrons whereas its direct effect on ions is negligible for the field strengths employed because of their heavier mass. Due to the different dynamics of ions and electrons, a charge separation arises at the magnetic front, breaking the plasma quasi-neutrality in the surrounding region. The resulting potential drop and associated electric field then also accelerates the ions. This electrostatic structure propagates together with the field, inducing ion acceleration at the magnetic front.

A prototype of the system has been designed and built using a microwave cavity operating on neon as the primary ionization source and a transmission line circuit to generate the propagating magnetic field. The accelerator can be operated either in continuous or pulsed mode, and preliminary tests have been performed in the pulsed mode. The measured velocity of the propagating pulse is $\sim 17000$ m/s. A time-of-flight probe is used to detect the accelerated plasma sheet downstream of the accelerator. A signal that can be associated with a charged particle cloud has been identified only in the case of a positive pulse polarization. However, the time delay between the pulse trigger and the eventual detection of the charged sheet indicates that the plasma is not being dragged downstream by the magnetic field as expected. Moreover, the dependence of the sheet on the pulse polarization indicates a different mechanism other than the traveling magnetic field is responsible of the sheet generation. Future experiments will be dedicated to extend these studies and to investigate the continuous mode operation. Additional numerical analysis will be performed using F3MPIC, aiming to provide a final assessment on the plasma acceleration concept.

# Bibliography


[1] Jahn, R., *Physics of Electric propulsion, $2^{nd}$ edition*, Dover Publications, 2006.

[2] Martinez-Sanchez, M. and Pollard, J. E., "Spacecraft electric propulsion-an overview," *Journal of Propulsion and Power*, Vol. 14, No. 5, 1998, pp. 688–699.

[3] Gascon, N., Dudeck, M., and Barral, S., "Wall material effects in stationary plasma thrusters. I. Parametric studies of an SPT-100," *Physics of Plasmas*, Vol. 10, 2003, pp. 4123.

[4] Chen, F. F. and Boswell, R. W., "Helicons-the past decade," *IEEE Transactions on Plasma Science*, Vol. 25, No. 6, 1997, pp. 1245–1257.

[5] Lieberman, M. and Boswell, R., "Modeling the transitions from capacitive to inductive to wave-sustained rf discharges," *Le Journal de Physique IV*, Vol. 8, No. PR7, 1998, pp. Pr7–145.

[6] West, M. D., Charles, C., and Boswell, R. W., "High density mode in xenon produced by a Helicon Double Layer Thruster," *Journal of Physics D: Applied Physics*, Vol. 42, No. 24, 2009, pp. 245201.

[7] Merino, M. and Ahedo, E., "Simulation of plasma flows in divergent magnetic nozzles," *IEEE Transactions on Plasma Science*, Vol. 39, No. 11, 2011, pp. 2938–2939.

[8] Charles, C. and Boswell, R., "Laboratory evidence of a supersonic ion beam generated by a current-free helicon double-layer," *Physics of Plasmas*, Vol. 11, 2004, pp. 1706.

[9] Charles, C., Boswell, R., Alexander, P., Costa, C., Sutherland, O., Pfitzner, L., Franzen, R., Kingwell, J., Parfitt, A., Frigot, P., et al., "Helicon double layer thrusters," *42nd. AIAA/ASME/SAE/ASEE Joint Propulsion Conference*, 2006.

[10] Bering, E., Longmier, B., Ballenger, M., Olsen, C., Squire, J., and Diaz, F., "Performance studies of the VASIMR® VX-200," *Proceedings of 49$^{th}$ AIAA Aerospace Sciences Meeting and Exhibit, Orlando, FL, USA*, 2011.

[11] Hooper, E., "Plasma detachment from a magnetic nozzle," *Journal of Propulsion and Power*, Vol. 9, No. 5, 1993, pp. 757–763.

[12] Ahedo, E., "Double-layer formation and propulsive assessment for a three-species plasma expanding in a magnetic nozzle," *Physics of Plasmas*, Vol. 18, 2011, pp. 033510.

[13] Batishchev, O. V., "Minihelicon plasma thruster," *IEEE Transactions on Plasma Science*, Vol. 37, No. 8, 2009, pp. 1563–1571.

[14] Ziemba, T., "High Power Helicon Thruster," *Proceedings of AIAA/ASME/SAE/ASEE 41$^{st}$ Joint Propulsion Conference, Tucson, AZ, USA*, July 2005.

[15] Pavarin, D., Ferri, F., Manente, M., Lucca Fabris, A., Trezzolani, F., Faenza, M., Tasinato, L., Tudisco, O., Deangelis, R., Loyan, A., Protsan, Y., Tsaglov, A., Selmo, A., Katsonis, K., Berenguer, C., Packan, D., Jarrige, J., Blanchard, C., Elias, P. Q., and Bonnet, J., "Thruster Development Set-up for the Helicon Plasma Hydrazine Combined Micro Research Project," *Proceedings of 32$^{nd}$ International Electric Propulsion Conference, Wiesbaden, Germany*, September 2011, IEPC-2011-241.

[16] Takahashi, K., Oguni, K., Yamada, H., and Fujiwara, T., "Ion acceleration in a solenoid-free plasma expanded by permanent magnets," *Physics of Plasmas*, Vol. 15, 2008, pp. 084501.

[17] Motomura, T., Shinohara, S., Tanikawa, T., Hada, T., Funaki, I., Nishida, H., Shamrai, K. P., Matsuoka, T., Otsuka, F., Rudenko, T. S., Ohno, E., Yokoi, K., and Nakamura, T., "Development of electrodeless electric propulsion systems using high-density helicon plasmas: The HEAT project," *Proceedings of General Assembly and Scientific Symposium*, 2011.

[18] Cox, W., Charles, C., Boswell, R., and Hawkins, R., "Spatial retarding field energy analyzer measurements downstream of a helicon double layer plasma," *Applied Physics Letters*, Vol. 93, No. 7, 2008, pp. 071505–071505.

[19] Pavarin, D., Ferri, F., Manente, M., Lucca Fabris, A., Trezzolani, F., Faenza, M., Tasinato, L., Curreli, D., Melazzi, D., Rondini, D., Tudisco, O., Deangelis, R., Loyan, A., Protsan, Y., Tsaglov, A., Selmo, A., Katsonis, K., Berenguer, C., Pessana, M.,

and Lancellotti, V., "Characterization of the Helicon Plasma Thruster of the EU FP7 HPH.com Program," *Space Propulsion Conference, Bordeaux, France*, May 2012.

[20] West, M. D., Charles, C., and Boswell, R. W., "Testing a helicon double layer thruster immersed in a space-simulation chamber," *Journal of Propulsion and Power*, Vol. 24, No. 1, 2008, pp. 134–141.

[21] Takahashi, K., Charles, C., and Boswell, R., "Performance characterization of a permanent-magnet helicon plasma thruster," *Bulletin of the American Physical Society*, Vol. 57, 2012.

[22] Khayms, V. and Martinez-Sanchez, M., "Design of a Miniaturized Hall Thruster for Microsatellites," *Proceedings of the 32$^{nd}$ AIAA/ASME/SAE/ASEE, Joint Propulsion Conference & Exhibit, Lake Buena Vista, FL*, July 1996, AIAA Paper 96-3291.

[23] Schmidt, D. P., Meezan, N. B., Hargus Jr, W. A., and Cappelli, M. A., "A Low-Power, Linear-Geometry Hall Plasma Source with an Open Electron-Drift," *Plasma Sources Science and Technology*, Vol. 9, 2000, pp. 68–76.

[24] Kim, V., "Main Physical Features and Processes Determining the Performance of Stationary Plasma Thrusters," *Journal of Propulsion and Power*, Vol. 14, No. 5, 1998, pp. 736–743.

[25] Raitses, Y. and Fisch, N. J., "Parametric Investigations of a Nonconventional Hall Thruster," *Physics of Plasmas*, Vol. 8, No. 5, 2001, pp. 2579–2586.

[26] Courtney, D. G. and Martinez-Sanchez, M., "Diverging Cusped-Field Hall Thruster (DCHT)," *Proceedings of the 30$^{th}$ International Electric Propulsion Conference, Florence, Italy*, September 2007, IEPC-2007-039.

[27] Young, C. V., Smith, A. W., and Cappelli, M. A., "Preliminary Characterization of a Diverging Cusped Field (DCF) Thruster," *Proceedings of the 31$^{st}$ International Electric Propulsion Conference, Ann Arbor, MI*, September 2009, IEPC-2009-166.

[28] Koch, N., Harmann, H., and Kornfeld, G., "Status of the THALES High Efficiency Multi Stage Plasma Thruster Development for HEMP-T 3050 and HEMP-T 30250," *Proceedings of the 30th International Electric Propulsion Conference*, 2007.

[29] Koch, N., Harmann, H., and Kornfeld, G., "Development and test status of the THALES high efficiency multistage plasma (HEMP) thruster family," *Proceedings of the 29th International Electric Propulsion Conference, Princeton, NJ*, 2005, pp. 2005–297.

[30] Keller, A., Kohler, P., Gartner, W., Hey, F. G., Berger, M., Braxmaier, C., Feili, D., Weise, D., and Johann, U., "Feasibility of a down-scaled HEMP-Thruster as possible $\mu$N-propulsion system for LISA," *Proceedings of the 32nd International Electric Propulsion Conference (IEPC'11)*, 2011.

[31] Raitses, Y., Granstedt, E., Smirnov, A., Merino, E., and Fisch, N. J., "Effects of Cathode Electron Emission on Hall Thruster Discharge," *Proceedings of the $44^{th}$ AIAA/ASME/SAE/ASEE Joint Propulsion Conference & Exhibit, Hartford, CT*, July 2008, AIAA Paper 2008-5188.

[32] Raitses, Y., Smirnov, A., and Fisch, N. J., "Cylindrical Hall Thrusters," *Proceedings of the $37^{th}$ AIAA Plasmadynamics and Lasers Conference, San Francisco, CA*, June 2006, AIAA Paper 2006-3245.

[33] Smirnov, A., Raitses, Y., and Fisch, N. J., "Plasma Measurements in a 100 W Cylindrical Hall Thruster," *Journal of Applied Physics*, Vol. 95, No. 5, 2004, pp. 2283–2292.

[34] Smirnov, A., Raitses, Y., and Fisch, N. J., "Experimental and Theoretical Studies of Cylindrical Hall Thrusters," *Physics of Plasmas*, Vol. 14, 2007, pp. 057106.

[35] Courtney, D. G., Lozano, P., and Martinez-Sanchez, M., "Continued Investigation of Diverging Cusped Field Thruster," *Proceedings of the $44^{th}$ AIAA/ASME/SAE/ASEE Joint Propulsion Conference & Exhibit, Hartford, CT*, July 2008, AIAA Paper 2008-4631.

[36] Young, C. V., "The Stanford Diverging Cusped Field Thruster: Design, Construction, and Initial Testing," Undergraduate Honors Thesis, Stanford University, Jun 2010.

[37] MacDonald, N. A., Young, C. V., Cappelli, M. A., and Hargus Jr, W. A., "Ion Velocity and Plasma Potential Measurements of a Cylindrical Cusped Field Thruster," *Journal of Applied Physics*, Vol. 111, No. 9, 2012, pp. 093303.

[38] Meeker, D., "Finite Element Method Magnetics," www.femm.info, Jun 2011.

[39] Gardineer IV, B., Jorns, B., and Choueiri, E., "Simulations of Direct Ion Acceleration with Beating Electrostatic Waves," *Proceedings of the $32^{th}$ International Electric Propulsion Conference, Wiesbaden, Germany*, September 2011, IEPC-2011-212.

[40] Nakamura, T., K., Y., and et al., "Experimental Investigation of Plasma Acceleration by Rotating Electric field for Electrodeless Plasma Thruster," *Proceedings of the $32^{th}$ International Electric Propulsion Conference, Wiesbaden, Germany*, September 2011, IEPC-2011-279.

[41] Lovberg, R. and Dailey, C., "Large inductive thruster performance measurement," *AIAA Journal*, Vol. 20, No. 7, 1982, pp. 971–977.

[42] Choueiri, E. Y. and Polzin, K. A., "Faraday acceleration with radio-frequency assisted discharge," *Journal of propulsion and power*, Vol. 22, No. 3, 2006, pp. 611–619.

[43] Covert, E., Haldeman, C., and Sullivan, J., "A variable phase velocity traveling wave pump," *AIAA Journal*, Vol. 9, No. 7, 1971, pp. 1389–1395.

[44] Jones, R. and Palmer, R., "Traveling Wave Plasma Engine Program at NASA Lewis Research Center," *Third Annual Conference on Engineering Magnetohydrodynamics, Wiesbaden, Rochester, NY, USA*, March 1962.

[45] Jones, R. and Palmer, R., "Experimental Investigation a Constant-Velocity Traveling Magnetic Wave Plasma Engine," 1965, NASA TN D-2676.

[46] Jones, R., Palmer, R., and Seikel, G., "Analytical Investigation of Coils-System Design Parameters for a Constant-Velocity Traveling Magnetic Wave Plasma Engine," 1964, NASA TN D-2278.

[47] Light, C., "Magnetic Insulation Experiments with a Traveling Magnetic Piston Plasma Accelerator," Aerospace Corporation, El Segundo, California, 1963, report prepared for Commander Space Systems Division US Airforce.

[48] Penfold, A., Seemann, G., and Thornton, J., "Experimental study of a traveling-wave accelerator." *AIAA Journal*, Vol. 4, No. 10, 1966, pp. 1870–1872.

[49] Heflinger, L., Ridgway, S., and Schaffer, A., "Transverse traveling wave plasma engine," *AIAA Journal*, Vol. 3, No. 6, 1965, pp. 1028–1033.

[50] Schaffer, A., "Plasma propulsion with a pulsed transmission line," *ARS Journal*, Vol. 31, No. 12, 1961, pp. 1718–1722.

[51] Katsonis, K., Berenguer, C., Pavarin, D., Lucca Fabris, A., Trezzolani, F., Faenza, M., Tsekeris, P., Cohen, S., and Cornille, M., "Optical diagnostics of a low temperature argon thruster," *Proceedings of the 32nd International Electric Propulsion Conference (IEPC'11)*, 2011.

[52] Berenguer, C. and Katsonis, K., "Plasma Reactors and Plasma Thrusters Modeling by Ar Complete Global Models," *International Journal of Aerospace Engineering*, Vol. 2012, 2012.

[53] Cappelli, M. A., Gascon, N., and Hargus Jr, W. A., "Millimetre wave plasma interferometry in the near field of a Hall plasma accelerator," *Journal of Physics D: Applied Physics*, Vol. 39, No. 21, 2006, pp. 4582.

[54] Ohler, S. G., Gilchrist, B. E., and Gallimore, A. D., "Nonintrusive electron number density measurements in the plume of a 1 kW arcjet using a modern microwave interferometer," *IEEE Transactions on Plasma Science*, Vol. 23, No. 3, 1995, pp. 428–435.

[55] Swanson, D., *Plasma Waves, $2^{nd}$ edition*, IOP Publishing, 2003.

[56] Akhtar, K., Scharer, J. E., Tysk, S. M., and Kho, E., "Plasma interferometry at high pressures," *Review of Scientific Instruments*, Vol. 74, No. 2, 2003, pp. 996–1001.

[57] Tudisco, O., Lucca Fabris, A., Falcetta, C., Accatino, L., De Angelis, R., Manente, M., Trezzolani, F., Florean, M., Neri, C., Mazzotta, C., et al., "A microwave interferometer for small and tenuous plasma density measurements," *Review of Scientific Instruments*, Vol. 84, No. 3, 2013, pp. 033505–033505.

[58] Heald, M. A. and Wharton, C. B., *Plasma diagnostics with microwaves*, J. Wiley and Sons, 1965.

[59] Herrador, M., Asuero, A. G., and González, A. G., "Estimation of the uncertainty of indirect measurements from the propagation of distributions by using the Monte-Carlo method: An overview," *Chemometrics and intelligent laboratory systems*, Vol. 79, No. 1, 2005, pp. 115–122.

[60] Bohm, C. and Perrin, J., "Retarding-field analyzer for measurements of ion energy distributions and secondary electron emission coefficients in low-pressure radio frequency discharges," *Review of scientific instruments*, Vol. 64, No. 1, 1993, pp. 31–44.

[61] Baloniak, T., Reuter, R., Flötgen, C., and von Keudell, A., "Calibration of a miniaturized retarding field analyzer for low-temperature plasmas: geometrical transparency and collisional effects," *Journal of Physics D: Applied Physics*, Vol. 43, No. 5, 2010, pp. 055203.

[62] Sinenian, N., *Propulsion mechanisms in a helicon plasma thruster*, Ph.D. thesis, Massachusetts Institute of Technology, 2008.

[63] Hutchinson, I. H., *Principles of plasma diagnostics*, Cambridge university press, 2005.

[64] Harvey, Z., Chakraborty Thakur, S., Hansen, A., Hardin, R., Przybysz, W., and Scime, E., "Comparison of gridded energy analyzer and laser induced fluorescence

measurements of a two-component ion distribution," *Review of Scientific Instruments*, Vol. 79, No. 10, 2008, pp. 10F314–10F314.

[65] MacDonald, N. A., *Laser Induced Fluorescence Characterization of Cusped Field Plasma Thrusters*, Ph.D. thesis, Stanford University, June 2012.

[66] Mazouffre, S., Gawron, D., and Sadeghi, N., "A Time-Resolved Laser Induced Fluorescence Study on the Ion Velocity Distribution Function in a Hall Thruster After a Fast Current Disruption," *Physics of Plasmas*, Vol. 16, No. 4, 2009, pp. 043504.

[67] Goldsmith, J. and Lawler, J., "Optogalvanic spectroscopy," *Contemporary Physics*, Vol. 22, No. 2, 1981, pp. 235–248.

[68] Jackson, D., Gerhardt, H., and Hänsch, T., "Doppler-free optogalvanic spectroscopy using an infrared color center laser," *Optics Communications*, Vol. 37, No. 1, 1981, pp. 23–26.

[69] Lawler, J., Ferguson, A., Goldsmith, J., Jackson, D., and Schawlow, A., "Doppler-free intermodulated optogalvanic spectroscopy," *Physical Review Letters*, Vol. 42, No. 16, 1979, pp. 1046.

[70] Djulgerova, R. and Mihailov, V., "Laser optogalvanic effect from Ar positive ions in a hollow-cathode discharge," *EPL (Europhysics Letters)*, Vol. 36, No. 8, 1996, pp. 571.

[71] Verboncoeur, J., "Particle Simulation of Plasmas: Review and Advances," *Plasma Physics and Control Fusion*, Vol. 47, 2006, pp. A231–A260.

[72] Fife, J. and Martinez-Sanchez, M., "Two-Dimensional Hybrid Particle-In-Cell (PIC) Modeling of Hall Thrusters," *Proceedings of 24$^{th}$ International Electric Propulsion Conference, Moscow, Russia*, September 1995, IEPC-95-240.

[73] VanGilder, D., Font, G., and Boyd, I., "Hybrid Monte Carlo Particle-in-Cell Simulation of an Ion Thruster Plume," *Journal of Propulsion and Power*, Vol. 15, No. 4, 1999, pp. 530–538.

[74] Gildea, S. R., *Development of the Plasma Thruster Particle-in-Cell Simulator to Complement Empirical Studies of a Low-Power Cusped-Field Thruster*, Ph.D. thesis, Massachusetts Institute of Technology, Oct 2012.

[75] Collodo, A., "Development of one-dimensional particle codes for the simulation of plasmas for aerospace propulsion," Tesi per la "Laurea Magistrale in Ingegneria Aerospaziale", Università degli Studi di Padova, 2011.

[76] Meige, A., Boswell, R. W., Charles, C., and Turner, M. M., "One-dimensional particle-in-cell simulation of a current-free double layer in an expanding plasma," *Physics of plasmas*, Vol. 12, 2005, pp. 052317.

[77] Carlsson, J., Manente, M., and Pavarin, D., "Implicitly charge-conserving solver for Boltzmann electrons," *Physics of Plasmas*, Vol. 16, 2009, pp. 062310.

[78] Lieberman, M. and Lichtenberg, A., *Principles of Plasma Discharges and Material Processing, $2^{nd}$ edition*, Wiley, 2005.

[79] Chen, F. F., *Introduction to plasma physics and controlled fusion, volume 1: Plasma Physics*, Springer, 1984.

[80] Pavarin, D., Ferri, F., Manente, M., Curreli, D., Melazzi, D., Rondini, D., and Cardinali, A., "Development of Plasma Codes for the Design of Mini-Helicon Thrusters," *Proceedings of $32^{nd}$ International Electric Propulsion Conference, Wiesbaden, Germany*, September 2011, IEPC-2011-240.

[81] Manzolaro, M., Manente, M., Curreli, D., Vasquez, J., Montano, J., Andrighetto, A., Scarpa, D., Meneghetti, G., and Pavarin, D., "Off-Line Ionization Tests Using the Surface and the Plasma Ion Sources of the SPES Project," *Review of Scientific Instruments*, Vol. 83, No. 2, 2012, pp. 02A907.

[82] Chen, F. F., "Physical mechanism of current-free double layers," *Physics of plasmas*, Vol. 13, 2006, pp. 034502.

[83] Ahedo, E. and Martínez-Sánchez, M., "The role of current-free double-layers in plasma propulsion," *Proceedings of the $44^{th}$ AIAA/ASME/SAE/ASEE Joint Propulsion Conference & Exhibit, Hartford, CT*, 2008, AIAA paper 2008-5005.

[84] Curreli, D., *Analysis, Simulation and Testing of Advanced Electrodynamics Systems for Space Propulsion*, Ph.D. thesis, University of Padova, January 2011.

[85] Loyan, A. and Maksymenko, T., "Performance investigation of SPT-20M low power hall effect thruster," *Proceedings of the 30th Int. Electric Propulsion Conference, Florence, Italy*, 2007.

[86] Geuzaine, C. and Remacle, J., "Gmsh: a three-dimensional finite element mesh generator with built-in pre- and post-processing facilities," http://geuz.org/gmsh/.

[87] Hargus Jr, W. A. and Charles, C. S., "Near-Plume Laser-Induced Fluorescence Velocity Measurements of a Medium Power Hall Thruster," *Journal of Propulsion and Power*, Vol. 26, No. 1, 2010, pp. 135–141.

[88] Gawron, D., Mazouffre, S., Sadeghi, N., and Heron, A., "Influence of Magnetic Field and Discharge Voltage on the Acceleration Layer Features in a Hall Effect Thruster," *Plasma Sources Science and Technology*, Vol. 17, No. 2, 2008, pp. 025001.

[89] MacDonald, N. A., Cappelli, M. A., Gildea, S. R., Martinez-Sanchez, M., and Hargus Jr, W. A., "Laser-Induced Fluorescence Velocity Measurements of a Diverging Cusped-Field Thruster," *Journal of Physics D: Applied Physics*, Vol. 44, No. 29, 2011, pp. 295203.

[90] Matlock, T. S., Hu, F., and Martinez-Sanchez, M., "Controlling Plume Divergence in a Cusped Field Thruster," *Proceedings of the 32nd International Electric Propulsion Conference (IEPC'11)*, 2011.

[91] Fehsenfeld, F., Evenson, K., and Broida, H., "Microwave discharge cavities operating at 2450 MHz," *Review of scientific Instruments*, Vol. 36, No. 3, 1965, pp. 294–298.

## Acknowledgments

Vorrei innanzitutto ringraziare i miei supervisori; anzi più che supervisori posso chiamarli amici, Daniele, Marco e Mark. E' un piacere lavorare insieme a voi.

Ci sono poi tutti i compagni di questi anni: Fabio, Franco, Martina, Marta, Federico, Francesco, Nicolas, Davide, Davide, Alberto, Enri, Bros al CISAS; Chris e Ben a Stanford. Un ringraziamento particolare a Fabio e Chris per le ore passate a fare esperimenti e per il lavoro svolto insieme. Ringrazio Luca per il supporto ed Antonio per gli insostituibili insegnamenti.

Dedicato alla mia famiglia e a Martina.